Nucleosynthesis in Massive Rotating Stars

Inauguraldissertation

zur
Erlangung der Würde eines Doktors der Philosophie
vorgelegt der
Philosophisch-Naturwissenschaftlichen Fakultät
der Universität Basel
von

Urs Stefan Frischknecht

aus Schwellbrunn, AR

Basel, 2012

Genehmigt von der Philosophisch-Naturwissenschaftlichen Fakultät

auf Antrag von

Prof. Dr. Friedrich-Karl Thielemann, Dr. Raphael Hirschi, Prof. Georges Meynet

Basel, den 13. Dezember 2011

Prof. Dr. Martin Spiess

This work is dedicated to my parents, Bruno and Margrit

Namensnennung-Keine kommerzielle Nutzung-Keine Bearbeitung 2.5 Schweiz

---

Sie dürfen:

das Werk vervielfältigen, verbreiten und öffentlich zugänglich machen

Zu den folgenden Bedingungen:

Namensnennung. Sie müssen den Namen des Autors/Rechteinhabers in der von ihm festgelegten Weise nennen (wodurch aber nicht der Eindruck entstehen darf, Sie oder die Nutzung des Werkes durch Sie würden entlohnt).

Keine kommerzielle Nutzung. Dieses Werk darf nicht für kommerzielle Zwecke verwendet werden.

Keine Bearbeitung. Dieses Werk darf nicht bearbeitet oder in anderer Weise verändert werden.

- Im Falle einer Verbreitung müssen Sie anderen die Lizenzbedingungen, unter welche dieses Werk fällt, mitteilen. Am Einfachsten ist es, einen Link auf diese Seite einzubinden.
- Jede der vorgenannten Bedingungen kann aufgehoben werden, sofern Sie die Einwilligung des Rechteinhabers dazu erhalten.
- Diese Lizenz lässt die Urheberpersönlichkeitsrechte unberührt.

Quelle: http://creativecommons.org/licenses/by-nc-nd/2.5/ch/ Datum: 3.4.2009

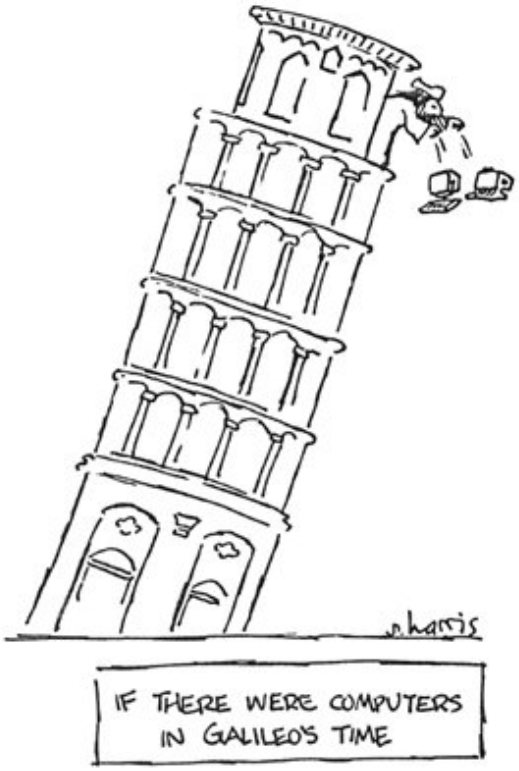
IF THERE WERE COMPUTERS
IN GALILEO'S TIME

Abstract

Most stars we see in the sky produce the energy they radiate away by central fusion. Most of them are fusing hydrogen to helium. After a star has exhausted hydrogen in its centre it contracts and can eventually start the fusion of helium to carbon. Massive stars are defined as stars with at least eight times the mass of the Sun, which is the critical mass for a star needed to start the carbon fusion after central helium has been exhausted. After three further fusion phases an iron core is formed and no further energy can be gained. When this core reaches a critical mass, the Chandrasekhar mass, it collapses and many of them explode in a Supernova, a stellar explosion, which is one of the most energetic events known in the universe. During such an explosion parts of the newly synthesised chemical elements are ejected and leads to an enrichment of heavy elements in the interstellar gas from which later generations of stars are formed. Massive stars are important for the formation and structure of the observed universe as well as for its chemical enrichment. They are therefore also fundamental physical constituents of our solar system and of life on earth.

Massive stars have surface temperatures higher than 10′000 K and are over ten-thousand times more luminous than the Sun, but their life is much shorter. The way how massive stars evolve, depends mainly on three different parameters, namely their initial mass, composition and rotation rate. It was shown by the research in the past 50 years of modelling massive stars, that rotation can strongly affect the way how massive stars evolve. Not only their fate can be changed by rotation effects, but also the chemical signature in the Supernova and wind ejecta. Still, the transport of matter and angular momentum, an essential part of physics inside rotating stars, is not yet fully understood.

In this project, I worked, on the one hand, on constraining the rotation induced mixing by looking at the surface evolution of the light element boron. On the other hand, I focussed in the main part of my work on the nucleosynthesis of heavy elements beyond iron by neutron captures during the helium and carbon burning phases in massive stars, the so-called slow neutron capture process or s process. An interesting and not yet fully studied question is, how stellar rotation may affect the s process.

In this work, the Geneva stellar evolution code (GenEC) and the Basel nuclear reaction network (BasNet) have been combined. It was found that the combination of meridional circulations toghether with shear mixing can well explain the depletion of boron at the surface of massive stars in the vicinity of the Sun. With a grid of massive star models including the effects of rotation, it was found that rotation induced mixing can enhance the production of nuclei by the s process strongly. This might be a solution for some yet unexplained features in the chemical pattern of very old stars in the Milky Way.

Contents

Acknowledgements

The results obtained in this dissertation would not have been possible without the close collaboration and support of a variety of persons. My thanks go to

- My parents for supporting me mentally and financially and encouraged me throughout my whole educational path, in good and in bad times.
- Dr. R. Hirschi (Keele University, UK) for advising the course of my Ph.D. thesis, his steady and patient support and encouragement. To him I would like to express my sincere gratitude!
- Prof. Dr. F.-K. Thielemann (University of Basel) for co-supervising my dissertation and giving me the possibility to do this thesis in the very stimulating working environment of his Astrophysics group.
- Prof Dr. G. Meynet (Geneva Observatory) for the collaboration from which I could profit a lot, for his always helpful and extensive feedbacks. Moreover, I appreciate his willingness to be the external expert for my dissertation.
- PD Dr. T. Rauscher (University of Basel) for the collaboration on the development of a thermo-nucler reaction network, allowing us to make reaction rate sensitivity studies.
- Prof Dr. C. Chiappini (Geneva Observatory, Institute of Astrophysics Potsdam) for the collaboration on Galactic chemical evolution from which I could profit extensively.
- Dr. R. Käppeli & Dr. S. Scheidegger (University of Basel) for loads of useful, useless and entertaining discussions. It was a unique time of sharing with them a "research outpost" for three years at Oetlingerstrasse 194, 4057 Basel.
- Dr. C. Winteler, A. Perego (University of Basel) for discussions on astrophysics and non-astrophysics related subjects, and sharing the office. Also a special thank to C. Winteler for sharing his extensive work on nuclear reaction networks.
- Dr. A. Arcones, Dr. Marco Pignatari, Dr. M. Hempel, Dr. T. Fischer, M. Horras, present and past members of the Astrophysics group of the University of Basel, for a cordial work ambiance.
- Dr. Simone Jeger for proof-reading, and for the always interesting philosophical and non-philosophical discussions and for her friendship.
- Sam Jones (Keele University) for proof-reading.

- the National Science Foundation for granting financial support for my Ph.D. project.
- the Royal Science Foundation providing financial travel support.
- the EuroGENESIS, a research networking programme of the European Science Foundation for financial travel support.

List of Figures

List of Tables

1 Introduction

1.1 Why are massive stars important?

Most of the objects we can observe in the sky are stars, the most critical for life on Earth is the Sun. Compared to more massive stars, the sun has a very long, calm and normal life. Massive stars live a turbulent and a relatively short life, ejecting a large fraction of their mass back to the Inter Stellar Medium (ISM) before and during their "death". Massive stars are defined as stars with masses $\gtrsim 8\ M_{\odot}$[1]. On the Main Sequence (MS), when the stars burn[2] hydrogen (H) to helium (He), massive stars have surface temperatures higher than $10'000$ K, while our sun has $5'780$ K. Massive stars are classified as O and early B-type stars, using the Harvard spectral classification. Since massive stars have very high luminosities, typically 10^4-$10^6\ L_{\odot}$[3].

The lower mass limit above which a star is considered as a massive star (around 8 $M_{\odot}$) is determined by whether the central conditions will evolve accordingly for the star to ignite the burning of carbon and heavier elements. Consequently, such a star burns the initial gas mixture of mainly H and He, via hydrogen, helium, carbon, neon, oxygen and silicon-burning phases to iron group elements[4] (mainly nickel (Ni) and iron (Fe) respectively). Massive stars end their lifes in one of the most powerful explosions in the universe, a Supernova (SN), or collapse to black holes. Another such energetic phenomenon, long Gamma Ray Bursts (GRBs), were also recently linked to SNe from stars in this mass range (Woosley & Bloom 2006). Massive stars can also trigger strong star formation activity by radiation (Getman et al. 2009), winds or SN shocks (Preibisch & Zinnecker 2007), affect planet formation (Bally et al. 2005) and the structure and formation of galaxies (Kennicutt 2005). Their metal-free[5] counterparts were main agents re-ionising the universe at the end of the "dark age" after the big bang. The high luminosities of massive stars result in relatively short lifetimes, and ultimately the lifetime τ depends on the initial mass of the star

$$\tau \propto M^{1-\alpha}$$

with $\alpha \approx 4$ for stars with initial masses $M = 0.6$ to 2 $M_{\odot}$, with $\alpha \approx 1.7$ for stars with $M > 60\ M_{\odot}$, and an average exponent of $\alpha = 3$ (Maeder 2009). While a 2 $M_{\odot}$ star lives about 10^9 years, a 20 $M_{\odot}$ stars lifetime is 100 times shorter, i.e. around 10^7 years. The shorter life explains the more immediate influence on their environment and why the early universe

[1] One solar mass $M_{\odot}$ is 1.99×10^{30} kg. The solar value of a quantity X is written as $X_{\odot}$ hereafter.
[2] Burning is used throughout this text as synonym for fusion.
[3] $L_{\odot}$ is the solar luminosity of 3.839×10^{33} erg s^{-1} and 3.839×10^{26} W, respectively.
[4] Elements from chromium (Cr) to nickel (Ni).
[5] In astrophysical/astronomical context all elements heavier than helium are called metals.

was dominated by massive stars. Besides the much shorter life compared to low mass stars, massive stars live after their MS evolution in different phases that are much more vivid and turbulent, with strong and varying mass loss and luminosities. During these phases, they are observed as peculiar objects such as Wolf-Rayet (WR) stars, Luminous Blue Variables (LBV) and Red or Blue-Super-Giants (RSG/BSG). Other special astronomical objects like pulsars, neutron stars or black holes are remnants of massive stars. Even though massive stars are much less common than stars like the sun, they dominate the visible spectrum of galaxies, especially those of very young galaxies, and are inevitably linked to galactic formation and evolution through their winds, ionizing radiation and SNe. The injection of matter by mass loss and SNe has not only an influence on the energetics of the ISM, but also means that massive stars contribute heavily to the chemical enrichment of the universe.

The synthesis of heavy elements in massive stars provides an important source for the chemical enrichment of their surrounding ISM and hence of the universe. Massive stars are responsible for the bulk of α-elements (isotopes clustering in multiple of α's, ^{16}O, ^{20}Ne, ^{24}Mg, ^{28}Si, ^{32}S, ^{36}Ar, ^{40}Ca, ^{48}Ti). Additionally, they also return some Fe to the ISM, which is ejected from the innermost part of the stars when they blow up in SN explosions. Assuming a Salpeter initial mass function (IMF) (Salpeter 1955), only 14% of the matter involved in star formation is going into massive stars and 25% into intermediate mass stars[6]. In contrary to low mass stars, however, a large fraction of the matter which was incorporated into massive stars, is returned to the ISM. The nucleosynthesis due to fusion of charged particles proceeds only up to the iron group nuclei, which is explained by the maximum of binding energy per nucleon at around ^{56}Fe. Different nucleosynthesis processes were discovered to produce chemical elements beyond iron. The νp, s, r and γ processes were found to occur in the interiors of massive stars and SNe, respectively. Therefore massive stars are main contributors of rare elements with atomic masses heavier than iron. How much of which element a star contributes to the chemical enrichment of its galaxy does not only depend on the stellar mass but also on other parameters. Two additional major properties defining the fate of a star are rotation and metallicity Z[7]. The impact of both on the yields of massive stars and subsequently their impact on Galactic Chemical Evolution (GCE) was studied extensively in the recent past, but there are still some major gaps remaining in our knowledge about stellar lives and their galactic enrichment.

In conclusion, massive stars are important for the formation and structure of the observed universe as well as for its chemical enrichment. They are therefore also fundamental physical constituents of our solar system and of life on earth.

1.2 Birth, life and death of massive stars

Massive stars have their origin in cold dense clumps inside of giant molecular clouds. These clumps have typical masses of a few 100 to a few 1000 $M_\odot$, molecular number densities of 10^5 cm^{-3} and temperatures of 10-20 K. They are also called infra-red dark clouds (IRDCs), because they are opaque against background radiation in the infra-red (Zinnecker & Yorke 2007). Gravitational instabilities or shock waves, from supernovae for example, are thought to trigger the collapse of such clouds of interstellar gas into proto-stars. In the state of a proto-star, the gas becomes opaque and the released gravitational binding energy is kept

[6]Stars with masses between 1 to 8 $M_\odot$.

[7]The metallicity is the sum of all mass fractions of elements heavier than helium.

inside. The proto-star is accompanied by an accretion disc and bipolar outflows of matter, therefore not all of the in-falling matter is kept by the proto-star. Once the star reaches the pre-main sequence, it contracts more slowly on the Kelvin-Helmholz time scale. This means that the gravitational binding energy released during contraction and the energy lost at the surface by radiation are about equal. Furthermore, some energy is released by the destruction of deuterium (^{2}H) and lithium (Li) in this phase. Massive proto and pre-MS stars do not keep all accreted mass, but loose also mass over the bipolar outflows (Zinnecker & Yorke 2007). High mass stars can, contrary to low mass stars, still accrete matter from their environment while their central temperature increases towards that required to initiate the fusion of hydrogen into helium. During the early stages of H burning, massive stars finally destroy their "parent" cloud by strong radiation and winds. Characteristic for massive star-forming regions are so-called HII-regions, i.e. gas clouds of ionized radiating hydrogen. The end products of massive star formation are OB-type star clusters and associations, but there are also field stars found, which seem to have formed in isolation (e.g. de Wit et al. 2005). Well known examples of star-forming regions include Orion, located in close proximity to the sun on a galactic distance scale and the Tarantula nebula (30 Doradus), where the most massive stars ever to be discovered reside, boasting masses of up to 300 $M_\odot$ (Crowther et al. 2010).

Massive stars start to fuse hydrogen into helium once their centre has reached temperatures $T_c \gtrsim 3 \times 10^7$ K and densities of a few g cm^{-3}. The start of central H burning is the start of the main sequence, also called the Zero Age Main Sequence (ZAMS). The release of nuclear energy by fusion then prevents further contraction of the star. The needed energy is released by nuclear reactions of the carbon-nitrogen-oxygen-cycles (hereafter CNO-cycles) and proton-proton chains (hereafter pp-chains). The central conditions in massive stars favour the CNO-cycles, in which C, N and O act as catalysts for fusing H to He. The central energy release establishes a temperature and pressure gradient, falling from centre to surface, creating a force acting in the opposite direction to gravity and keeping the star stable. During the MS massive stars have an inner convective core and a radiative envelope, i.e. in the core the energy is mainly transported outwards by flows of matter while in the envelope by outward diffusion of photons. Stars in general stay about 90% of their lifetime on the MS with a rather constant surface temperature and luminosity. Massive stars have MS-lifetimes of a few to a few tens of millions of years. The reasons for the H-burning phase being the longest are: First the change in average binding energy per nucleon is the highest compared to later stages (see discussion in Section 2.3 and Fig. 1.3); second, the convective core is largest during this phase resulting in the amount of available fuel also being larger; third, from C-burning stage onwards most of the energy produced in nuclear reactions is lost by neutrinos, resulting in a shortened lifetime, because neutrinos do not support the star agains its own gravity. On the one hand, the size of the convective core shrinks in the course of the MS-evolution, driven by the change of central composition. On the other hand, the radius determined by the envelope usually slightly expands on the MS, but shrinks in case of very strong mass loss occurring in very massive stars ($\gtrsim 50$ $M_\odot$). Typical radii of massive stars are between 3.5 $R_\odot$ for 8 $M_\odot$ stars and 15 $R_\odot$ for 100 $M_\odot$ stars. Stars with such strong winds reach a phase, in which they lose their entire H-rich envelope and become WR-stars already on the MS. How much mass a massive star loses during its life depends strongly on its initial mass, rotation rate and metallicity (Meynet & Maeder 2005). High metallicity and rotation rate boost mass loss. In contrast stars with low metallicity lose only considerable mass if they have high rotation velocities.

The end of the MS is marked by the exhaustion of H in the stellar centre. The missing energy production leads to a short contraction phase of the whole star, until the H burning ignites in a shell around the core, leading to an expansion of the envelope, while the core still contracts until He burning starts. The fusion of He to C begins once $T_c \approx 1.5 \times 10^8$ K is reached. How much the envelope expands will depend on the metallicity and its opacity at lower temperatures, respectively. At solar metallicity, the expansion leads to strong mass loss, if the envelope was not blown away before, which is the case for $M < 50\ M_\odot$. The expansion of the envelope leads to a drop in the surface temperature, and these stars become RSGs. They can extend their radii to more than 2000 $R_\odot$ in some cases. Lower mass stars ($M \lesssim 20\ M_\odot$) end their life as such, but more massive stars lose much more mass during their central He-burning phase, at solar metallicity. In the Hertzsprung-Russel diagram (hereafter H-R diagram) they go back to the blue stage, i.e. hotter layers are uncovered and the surface temperatures increase to more than 10^4 K. These stars become BSGs, eventually completely losing their hydrogen envelope to become WR-stars. Stars in the mass range of 3-12 $M_\odot$ go back to the hotter side of the H-R diagram for a fraction of their He-burning lifetime, spending it in the Cepheid phase. A Cepheid is a variable star with a pulsation period of about 1-100 days. The central He-burning phase lasts about 10% of the MS-lifetime, and a star is therefore more than 99% of its total lifetime either in the H- or He-burning phase. Observers thus usually see stars in their H- or He-burning stage.

Even if a star was further advanced in its evolution, it would not be recognised, since the envelope does not change much after He burning. The ashes of He burning consist of C and O. Massive stars with $M \gtrsim 10\ M_\odot$ will proceed to burn C to Ne and Mg during a C-burning phase; Ne to O and Mg during a Ne-burning phase; O and Mg to Si and S during an O-burning phase and finally in Si burning, Si and S are built into iron group elements like Ni, Fe and Cr. These burning phases ignite in this order with increasing temperatures, from $T_c \gtrsim 6 \times 10^8$ K for C burning to $T_c \gtrsim 3.5 \times 10^9$ K for Si burning. With increasing ignition temperatures also the time scales of the burning phases decrease, so while C burning is of the order of 1000 years, Si is exhausted in the centre in a couple of days. The shorter time scales of the later burning phases are related to the increasing energy loss by neutrinos with increasing temperatures. Because the maximum of nuclear binding energy is around Fe, stars cannot gain energy by fusion after Si burning. As a consequence, the iron core grows until it reaches the critical mass, the Chandrasekhar mass, and it collapses marking the death of the star. The preceding burning phases migrated outwards from central to shell burning phases. This gives a massive star an onion shell like structure at the time of iron core collapses, which is schematically shown in Fig. 1.1. Stars with 8-10 $M_\odot$ evolve differently in their interior after central C burning and undergo the transformation of nuclei to mainly iron group elements during the collapse of the degenerate O-Ne-Mg core.

The O-Ne-Mg core collapse of 8 to 10 $M_\odot$ stars is caused by electron (e^-) captures mainly on ^{20}Ne and ^{24}Mg (Miyaji et al. 1980). Resulting supernovae are therefore also called electron capture supernovae. The e^- captures lead to a quick drop of e^--degeneracy pressure and thus to a contraction. With increasing central densities an oxygen deflagration front starts to burn outwards and once $\rho_c > 10^{10}$ g cm^{-3} the matter goes into nuclear statistical equilibrium (NSE), and further e^- captures on heavier nuclei accelerate the collapse (Nomoto 1987). For stars more massive than about 10 $M_\odot$, the core reaches NSE in hydrostatic conditions, but starts to contract after central Si exhaustion. In all collapsing massive stars the inverse of the neutron decay into a proton occurs transforming the collapsing centre into very neutron rich matter. A stellar core halts its collapse and bounces back once it reaches

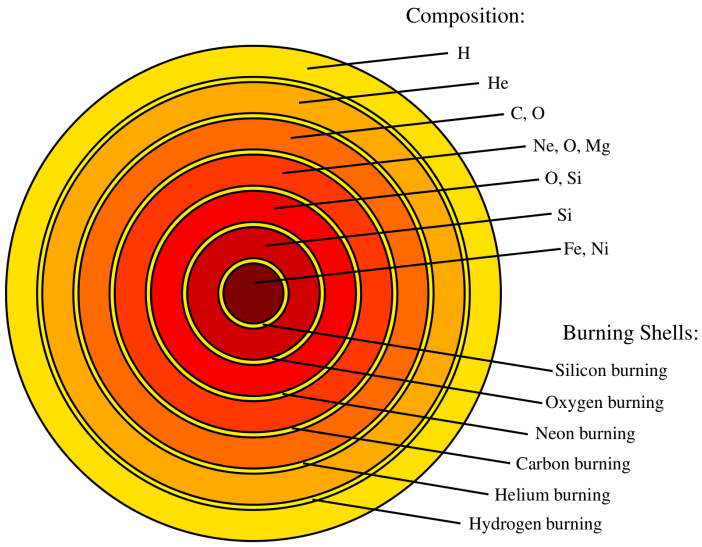

Figure 1.1: Schematic stellar structure of massive stars before their death. On the upper right the most abundant elements of the different layers are shown, while at the lower right the burning shells are indicated. Figure courtesy of C. Winteler.

nuclear matter density of about 10^{14} g cm^{-3}. The shock-front created by the bounce of the proto-neutron star, however, has not enough energy to explode the star. It loses its energy by dissociating the heavy nuclei of in-falling matter into protons, neutrons and α's[8]. Neutrino heating and/or hydrodynamic instabilities are necessary to explode the star. A review on the current understanding of the SN-explosion mechanism can be found in Mezzacappa (2005). Stellar cores of stars with initial masses $\gtrsim$ 25-30 $M_\odot$ collapse even further to black holes. While stars beyond 40 $M_\odot$ progenitors collapse directly to black holes, neutron stars of 25-40 $M_\odot$ progenitors only collapse beyond the black hole event horizon after some time, after enough matter falls back (Heger et al. 2003). In a SN-event gravitational binding energy of about 10^{53} erg is liberated, of which most is transported away by neutrinos, the kinetic (explosion) energy is about 10^{51} erg, and the energy released in photons only about 10^{49} erg, but they can still outshine their host galaxies.

Supernovae are classified according to their spectra and the absorption lines found therein (Filippenko 1997). In Fig. 1.2, a scheme of this classification is shown. SNe type II show strong H-absorption lines while type I do not. The H-lines of type II come from the H-rich envelopes of SN progenitor stars and are therefore related to the SN-explosion during the supergiant phase of massive stars. The lightcurves of SN IIP show a plateau during several weeks caused by massive hydrogen-rich envelopes, whereas the decay of SN IIL light curves is steeper, indicating a less massive H envelope. Recent observations suggest that SN IIP occur for stars with masses between $8.5^{+1.5}_{-1.0}$ and 16.5 ± 1.5 $M_\odot$ (Smartt 2009). This is in good agreement to recent stellar evolution models including rotation (Ekström et al. 2012), showing a transition to WR-stars around 20 $M_\odot$. WR-stars, having lost their whole H-envelope, are linked to SN Ib and Ic, which do not show H-absorption lines. In SN Ib, strong He-lines are present instead, implying that the SN-progenitor still had its He-rich shell in contrary to progenitors of SN Ic. Type IIn is a class of SN having narrow H emission lines, originating

[8]Hereafter, α is taken as a synonym for a ^{4}He nucleus.

from the interaction between the ejecta and the surrounding gas from the preceding stellar phase with strong mass loss. SN IIn are very luminous SN with kinetic energies $\gtrsim 10^{52}$ erg (Nomoto et al. 2010), also called hypernovae. Long gamma-ray bursts are linked to such hypernovae. Type Ia has Si absorption features and are associated to the thermonuclear explosions of white dwarfs (WD) in binary systems, and are therefore not related to massive stars. Because of their origin, Type II/Ibc SNe and long GRBs occur only in populations of young stars, while Type Ia SNe occur in older populations. Most of the SNe observed today are far away outside of the local group, because the typical SN rate of galaxies is in the order of one per century. The Galactic supernovae rate was estimated by different methods, such as from historical records and SN rates in similar other galaxies (Tammann et al. 1994) or from the amount of radioactive Al^{26} (Diehl et al. 2006), and was found to be one in every 30 to 50 years.

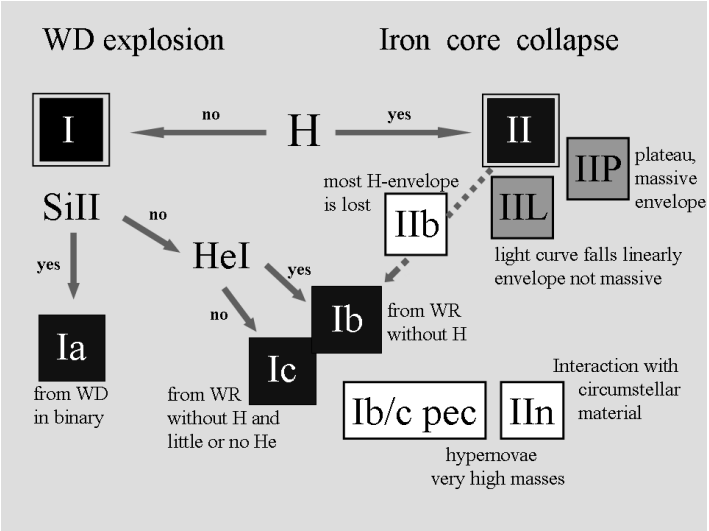

Figure 1.2: Supernova classification with the stellar progenitors associated with the different supernova classes. Figure of Maeder (2009) adapted from Turatto (2003).

1.3 Nucleosynthesis and galactic chemical enrichment

1.3.1 Nuclear burning phases

Stars have to support themselves against their energy loss, otherwise they would collapse. To compensate for self-gravity, stars need a steep pressure gradient that counteracts the gravity. Since usually pressure is density and temperature dependent, and stars loose energy via radiation, they have to produce energy to compensate for the energy loss and keep the pressure gradient stable. Nuclear fusion is the energy source stars can access. Energy is provided in nuclear reactions, if the parent nuclei have more mass than the daughter nuclei. Thus, nuclear reactions are providing the energy that is essential for the stars to shine in the sky for millions to billions of years; however, the chemical composition will have been altered at the expense of providing this energy, which will ultimately affect the evolution of the structure of the star over time.

The difference between the mass of the separated constituents of an atomic nucleus, i.e. protons and neutrons, and the mass of the nucleus itself is the so-called binding energy. In Fig. 1.3, the average binding energy per nucleon is shown for stable nuclei. It increases from light towards heavier isotopes up to a maximum around iron, from where on it decreases again. Thus, the binding energy curve explains why stars can gain energy by fusion only up to iron. The large jump of binding energy from hydrogen to helium explains the high energy release in hydrogen burning. This burning phase is the longest in a stellar life, considering that a star only produces as much energy as it radiates away.

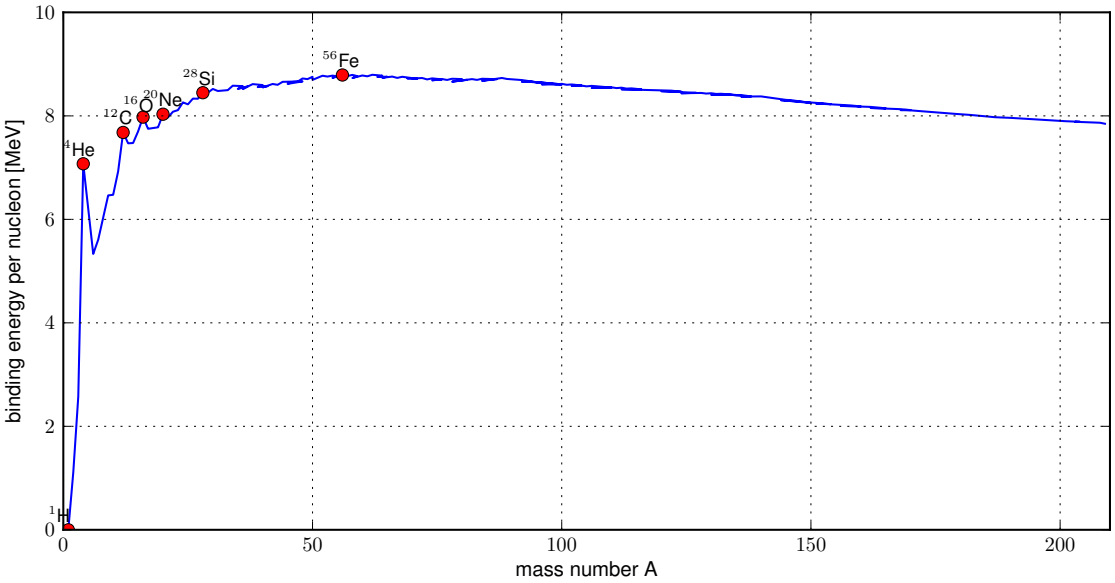

Figure 1.3: Average nuclear binding energy per nucleon of stable isotopes (data: Audi et al. 2003)

Nucleosynthesis is therefore a "by-product" of stellar energy generation, and the stellar burning phases involved explain the origin of the majority of the elements between carbon and iron, by the reactions involved in the energy generation. The different energy generation phases that massive stars experience and the associated nucleosynthesis are discussed, respectively, in the following paragraphs.

Hydrogen burning The fusion of hydrogen to helium is the longest phase in stellar evolution. The energy released in the conversion of four protons (^{1}H) into one ^{4}He is 26.7 MeV. Compared to later burning stages this is at least 10-times more energy per involved nucleon. The pp-chains and the CNO-cycles participate in the transformation of ^{1}H to ^{4}He. The CNO-cycles become more efficient than the pp-chains at temperatures $T_7 \approx 1.7$[9]; this corresponds to H-burning temperatures in a 1.2 $M_\odot$ star. When CNO-elements are available, the CNO-cycles dominate in massive stars. The most efficient cycle in H burning of massive stars is CNOI denoting the following reaction sequence:

$$^{12}\mathrm{C}(p,\gamma)^{13}\mathrm{N}(e^{+}\nu_e)^{13}\mathrm{C}(p,\gamma)^{14}\mathrm{N}(p,\gamma)^{15}\mathrm{O}(e^{+}\nu_e)^{15}\mathrm{N}(p,\alpha)^{12}\mathrm{C} \tag{1.1}$$

[9]Temperatures T_n are given in units of 10^n Kelvin.

^{14}N(p,γ) is the slowest reaction in this cycle and thus determines the time scale of H burning. It means also that most of the C, N and O nuclei of the initial gas is converted to ^{14}N, assuming a steady flow equilibrium. For example additional ^{12}C, mixed into the H-burning zone in massive stars, leads to the production of ^{14}N. Elemental and isotopic CNO equilibrium ratios of N/C and ^{12}C/^{13}C are used as indicators for H burning in massive stars. They indicate mixing in the envelopes of massive stars (e.g. Przybilla et al. 2010), because they differ from the ratios usually found in the ISM. Further CNO-cycles branching from ^{15}N and ^{17}O increase in importance with increasing burning temperatures, i.e. with increasing stellar mass.

If in H burning of massive stars $T_7 \gtrsim 2.5$ is reached ^{26}Al is efficiently produced from pre-existing ^{25}Mg via ^{25}Mg(p,γ) in the MgAl cycle. By this proton capture the unstable but long-living ground-state ^{26}Al$_g$ (half-life $t_{1/2} = 7.17 \times 10^5$ yrs) and the short-living isomeric state ^{26}Al$_m$ ($t_{1/2} = 6.35$ s) are produced. ^{26}Al$_g$ is important because it decays to ^{26}Mg with the emission of a positron (e^+). The subsequent e^+e^--annihilation releases observable γ-rays with a typical energy of 1.8 MeV. Observations showed a patchy emission-map throughout the Galaxy matching with recent star forming regions, and thus regions with massive star activity (Diehl et al. 2010). Doppler-shifts of the 1.8 MeV γ-rays display the large-scale movement of the ISM showing the rotation of the Galaxy (Diehl et al. 2008).

The NeNa cycle is activated at similar temperatures to the MgAl cycle, producing ^{23}Na out of pre-existing Ne isotopes. NeNa and MgAl each lead to an anti-correlation (Na vs. O and Al vs. Mg) in an ISM enriched with H-burning ashes, ejected by mass loss of massive stars. These anti-correlations are observed in in Galactic globular clusters (Decressin et al. 2007).

Helium burning Helium burning is special because there are no stable isotopes with mass number $A = 8$. Proton and neutron captures therefore do not allow the production of heavier nuclei. The only way to bridge this gap at temperatures $T_8 \gtrsim 1.5$ is the reaction converting three ^{4}He to ^{12}C (3α-reaction). Besides the 3α-reaction, ^{12}C$(\alpha,\gamma)^{16}$O contributes to the energy generation, which becomes efficient towards the end of He burning. It essentially determines the ^{12}C/^{16}O ratio in the He-burning ashes, which determines whether the subsequent C burning is convective or not. This ratio is typically 0.25 for a 20 $M_\odot$ star and decreases with increasing stellar mass. The rate of ^{12}C$(\alpha,\gamma)^{16}$O is very uncertain at the moment and consequently the C/O ratio after central He burning, which has a big impact on the subsequent stellar structure and evolution respectively, and therefore also on the nucleosynthesis in the later burning.

Important for the nucleosynthesis of elements heavier than iron at the end of He burning is the conversion of ^{14}N to ^{22}Ne at the start of He burning via

$$^{14}\mathrm{N}(\alpha,\gamma)^{18}\mathrm{F}(e^+\nu_e)^{18}\mathrm{O}(\alpha,\gamma)^{22}\mathrm{Ne} \tag{1.2}$$

since ^{22}Ne is the main neutron source of the s process (see Section 1.4) in massive stars.

Carbon burning The main reaction during C burning is the fusion of two ^{12}C to the compound nucleus ^{24}Mg*. It has three different major decay channels,

$$\begin{aligned} &^{12}\mathrm{C}(^{12}\mathrm{C},\alpha)^{20}\mathrm{Ne} \\ &^{12}\mathrm{C}(^{12}\mathrm{C},p)^{23}\mathrm{Na} \\ &^{12}\mathrm{C}(^{12}\mathrm{C},n)^{23}\mathrm{Mg}\ . \end{aligned} \tag{1.3}$$

The neutron emission channel is endothermic and thus much weaker than the other two. However, the liberation of protons and α-particles allows a wealth of other reactions. ^{23}Na is efficiently converted to ^{20}Ne and ^{24}Mg by $^{23}\mathrm{Na}(p,\gamma)^{24}\mathrm{Mg}$ and $^{23}\mathrm{Na}(p,\alpha)^{20}\mathrm{Ne}$ respectively; the $^{12}\mathrm{C}(\alpha,\gamma)^{16}\mathrm{O}$ reaction is also active, leaving the main products ^{16}O, ^{20}Ne and ^{24}Mg in the burning ashes. Many other reactions are important to produce minor abundances of isotopes like ^{26}Mg and ^{27}Al (Arnett & Thielemann 1985). Some s process occurs also at the very start of C burning if some ^{22}Ne remained from He burning, but its products are only ejected for the shell burning phases since the central 1.5 to 3 $M_\odot$ are ending up either in a black hole, neutron star or are photodisintegrated before ejection.

Neon burning After C burning one would expect ^{16}O nuclei to start burning next, but it is very stable since it is at proton and neutron magic number $N = Z = 8$. Therefore ^{20}Ne starts to photodisintegrate first at $T_9 \approx 1.2$ K, by $^{20}\mathrm{Ne}(\gamma,\alpha)^{16}\mathrm{O}$. A major fraction of liberated α-particles are captured on ^{20}Ne and ^{24}Mg producing ^{24}Mg and ^{28}Si, by

$$^{20}\mathrm{Ne}(\alpha,\gamma)^{24}\mathrm{Mg}(\alpha,\gamma)^{28}\mathrm{Si}\ .$$

Neutrons are released via different reaction chains and lead to the production of heavier elements (Thielemann & Arnett 1985), but it does not produce a typical s-process signature since it acts on a shorter time scale, and many neutron poisons are present.

Oxygen burning Finally at around $T_9 = 1.9$, the fusion of two ^{16}O begins producing the compound nucleus $^{32}\mathrm{S}^*$. It decays into ^{28}Si and ^{31}P through the three channels

$$^{16}\mathrm{O}(^{16}\mathrm{O},\alpha)^{28}\mathrm{Si}$$
$$^{16}\mathrm{O}(^{16}\mathrm{O},p)^{31}\mathrm{P}$$
$$^{16}\mathrm{O}(^{16}\mathrm{O},n)^{31}\mathrm{S}(e^+\nu_e)^{31}\mathrm{P}\ .$$

Again the protons, neutrons and α-particles liberated allow a wealth of other reactions and the main burning products are, beside ^{28}Si, ^{30}Si, ^{34}S, ^{38}Ar, ^{42}Ca and ^{46}Ti (Thielemann & Arnett 1985). For oxygen burning in high density conditions ($\rho \gtrsim 10^7$ g cm^{-3}) electron captures on ^{33}S and ^{35}Cl become important leading to a reduction of the electron abundance Y_e, and hence of the electron degeneracy pressure.

Silicon burning The final burning phase of stars is Si burning, but fusion via ^{28}Si+^{28}Si or ^{28}Si+^{32}S is unlikely because of the high Coulomb barrier. Instead, photodisintegration destroys nuclei and heavier nuclei are produced via the capture of the liberated protons, neutrons or α-particles. With increasing temperature several groups of nuclei start to be linked by forward and reverse reactions and form groups of nuclei in quasi-statistical equilibrium (QSE), when forward and reverse reactions occur at the same rate. The two main QSE-clusters are around ^{28}Si ($12 \leq Z \leq 20$) and ^{56}Ni ($22 \leq Z \leq 28$) separated by the proton magic number $Z = 20$ (Thielemann & Arnett 1985). With increasing temperatures ($T_9 \gtrsim 4$) the bottleneck at $Z = 20$ can be bridged and all the nuclei come into equilibrium via strong and electromagnetic interactions, which is called the nuclear-statistical equilibrium (NSE). At this stage the production of the isotopes with the highest binding energy are favoured, which are the iron group nuclei and in particular ^{56}Ni. Naturally weak interactions (e^--captures, β-decays) are not in equilibrium with their reverse, i.e. Y_e still changes in the course of Si burning.

1.3.2 Nucleosynthesis of heavy nuclei

In Fig. 1.4 the solar system abundances are shown with the three double peak structures between mass number $A = 60$ and 209. Hydrogen, helium and lithium originate mainly from the big-bang nucleosynthesis and are the starting point for the chain of nucleosynthesis processes producing all the other elements. The primordial gas consists (in mass fractions) of about 0.75 ^{1}H, 0.25 ^{4}He and traces of deuterium (^{2}H), ^{3}He and ^{7}Li. Starting from this primordial composition the production of elements up to the iron-group mainly happens by fusion reactions, occurring in the hydrostatic burning phases of massive stars (see yellow region in Fig. 1.4), as discussed in the previous section. It is other nucleosynthesis processes, however, that are responsible for the production of elements beyond iron for two main reasons: firstly, the temperatures have to be very high ($T_9 \gtrsim 4$) to overcome the Coulomb barrier in charged particle reactions and secondly, at such high temperatures photodisintegration is very efficient. However, neutron capture processes are not hindered by a Coulomb barrier and can produce heavy elements at lower temperatures. The slow and the rapid neutron capture process (s process and r process hereafter) are distinguished. Their names refer to the time scale on which they occur. Both processes are responsible for about half of the heavy elements beyond iron (see e.g. Sneden et al. 2008). The white regions in Fig. 1.4, however, can not be attributed to a single process.

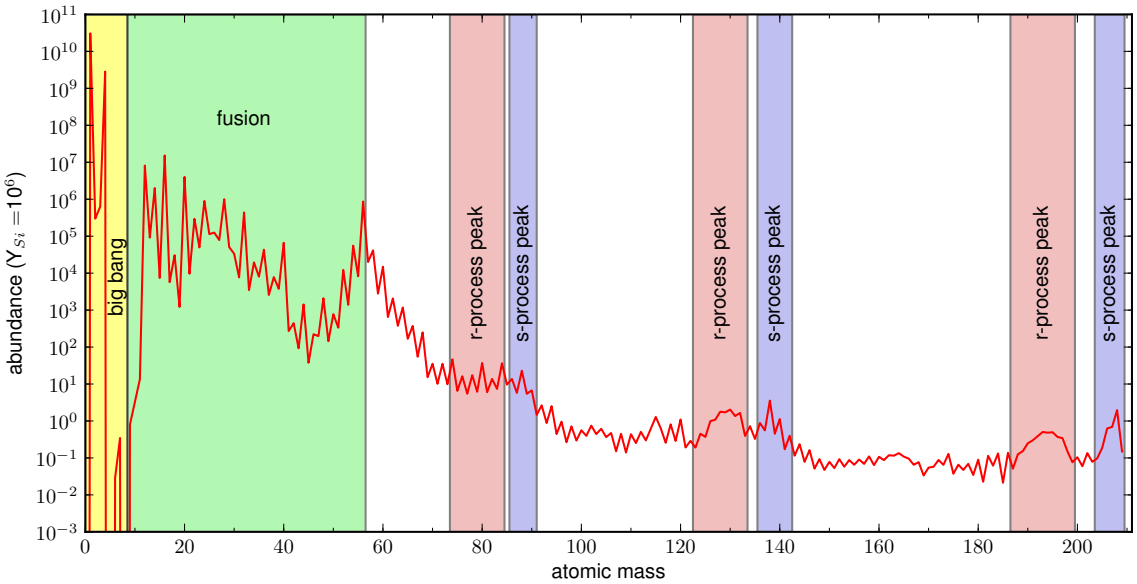

Figure 1.4: Solar system abundances of Asplund et al. (2005) with silicon normalised to 10^6.

The s process as a distinguished nucleosynthesis process was introduced by Cameron (1957) and Burbidge et al. (1957) as the process responsible for the production of the narrow abundance peaks (blue regions in Fig. 1.4) in the solar system abundances beyond Fe at mass numbers $A = 90$, 138, and 208. The broader abundance peaks (red regions in Fig. 1.4), which are shifted to lower mass numbers, are produced by the r process. The r process takes place on a much shorter time scale of seconds. Its production path reaches the neutron magic numbers at lower atomic masses on the neutron rich side, at unstable isotopes in the chart of nuclides by virtue of much higher neutron densities. Other processes are the νp process, thought to

occur in SNe under the influence of the high neutrino flux (Fröhlich et al. 2006) and the (classical) p process[10] which produces the p nuclei on the proton-rich side of the valley of stability by photodisintegration of heavier nuclei. The p process occurs in hydrostatic burning phases in the O-Ne layers of massive stars and in the same layer when the SN-shockwave runs through (e.g. Rauscher et al. 2002).

The s process in massive stars is the subject of this work and will be introduced in more detail in Section 1.4. The other nucleosynthesis are beyond the scope of this work. More about the r process can be found in recent reviews about the solved and unsolved problems by Arnould et al. (2007) and Thielemann et al. (2011) and about r, p and νp process by Thielemann et al. (2010).

1.4 S process

The s process was defined as "the process of neutron capture with the emission of gamma radiation" (Burbidge et al. 1957) taking place on long time scales from 100 to 10^5 years, that means the β-decay time scales t_β (seconds to days) of unstable isotopes involved are much shorter than the time t_n between two successive neutron captures on a nucleus ($t_\beta \ll t_n$). Because of the difference in these time scales, unstable isotopes decay before another neutron is captured with the exception of the so-called branching nuclei for which $t_\beta \approx t_n$. The production path of heavy isotopes runs therefore along the stable isotopes - the valley of stability. This "s-process path" splits at the branching points. When the s-process path meets the neutron magic numbers ($N = 50$, 82, and 126) the neutron capture cross section becomes low. This in turn leads to higher abundances for isotopes with the magic numbers, creating the characteristic peaks in the solar chemical composition (see Fig. 1.4).

Figure 1.5 shows the section of the chart of nuclides from iron to zirconium (Zr); in this diagram squares are stable isotopes with the exception of the ones marked in red, but in the latter case the isotope have a long enough half-life to be significant branching points. Some stable isotopes (marked yellow in Fig. 1.5), the r-only isotopes, are shielded from the s-process path (red dashed line) by fast decaying isotopes and are only produced by the r process. Similarly some isotopes (marked blue), the s-only isotopes, are shielded by stable isotopes against the production from the r process. And on the proton-rich side the orange marked isotopes cannot be produced by a neutron capture processes at all but only the νp or γ process (classical p process).

1.4.1 Classical s process

Even though there were hints that the s process occurs in He-burning zones of red giant stars (Cameron 1955) at first it was described by a heuristic model and not by full nucleosynthesis calculations. This "classical" s-process model was introduced by Burbidge et al. (1957) to describe together with the r process the observed abundances beyond iron.

The change in abundance Y[11] of an isotope with mass A, due to neutron captures and β

[10] More correctly it is called γ process in recent publications (e.g. Rauscher 2010).

[11] The abundance of a particular particle specie is defined as $Y := \frac{n}{\rho N_A}$, with n the number density of the element, ρ the total mass density, and N_A the Avogadro number. The mass fraction X is related to Y by $X = AY$, with A the molar mass.

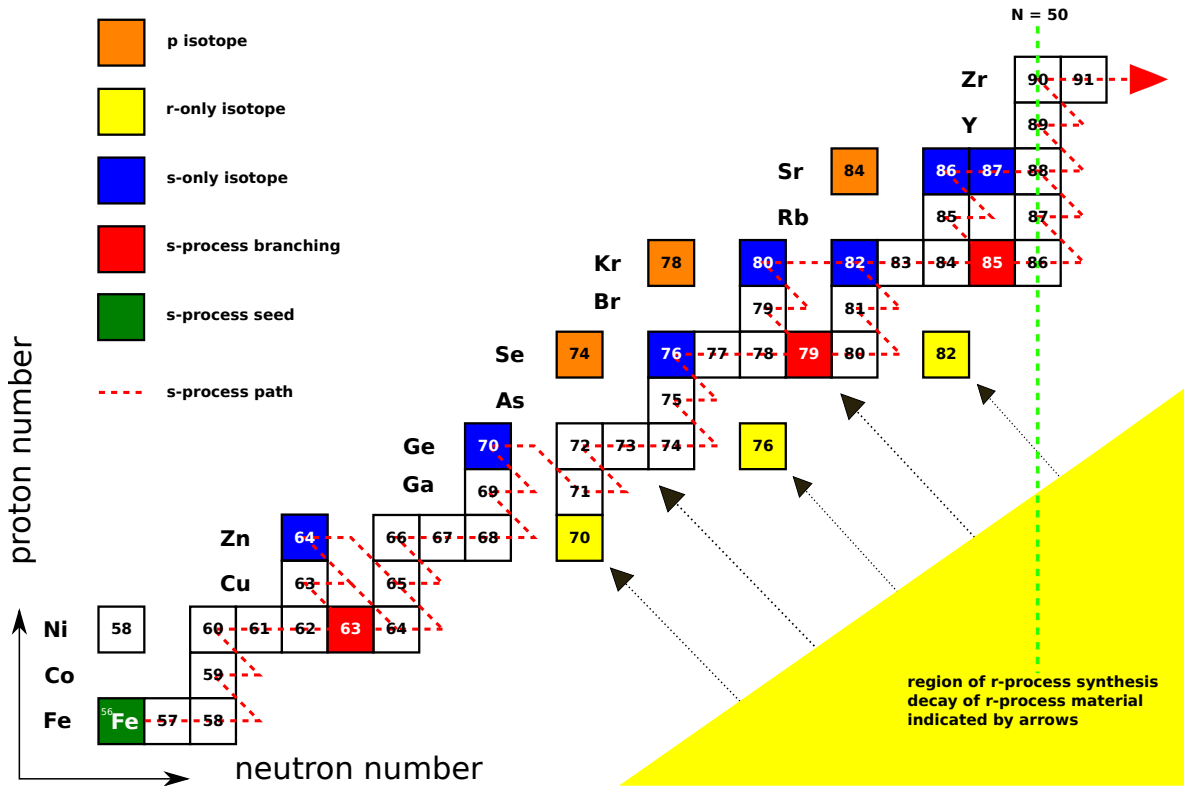

Figure 1.5: The s-process path (red dashed line) in a section of the nuclear chart (proton vs. neutron number) starting with iron as the seed of the slow neutron capture process. The isotopes shown are either stable or unstable but long-living (red squares). Figure adopted from Käppeler et al. (1989).

decays, is

$$\frac{dY(A)}{dt} = \lambda_n(A-1)Y(A-1) - (\lambda_n(A) + \lambda_\beta(A))Y(A) \tag{1.4}$$

with $\lambda_n(A) = \sigma \upsilon_T n_n$ the neutron capture rate[12] on isotope A[13] and $\lambda_\beta(A)$ the β-decay rate, with $\upsilon_T = \sqrt{2kT/m_n}$ the thermal neutron velocity, n_n the neutron density and σ the neutron capture cross section. In the classical model two further assumptions, were made

1. Isotopes are treated as stable or very fast decaying, i.e. the time scale t_n for a neutron capture is short ($t_n \ll t_\beta$) or long ($t_n \gg t_\beta$) compared to the decay of an isotope.

2. The neutron capture rates and the temperature are constant.

The first is true for all isotopes involved in the s process, with the exception of the branching points. The second is also good, since when considering only s-waves the neutron capture cross sections $\sigma \propto \upsilon^{-1}$, i.e. $\langle \sigma \upsilon \rangle \approx$constant. With the definition of the neutron exposure

$$\tau = \int \upsilon_T n_n dt \tag{1.5}$$

[12]Using i as identifier for the isotope instead of A, the more general $\lambda_{n,i} = \rho N_A \langle \sigma \upsilon \rangle_{n,i} Y_n$ - see also Chapter 3.

[13]When branchings are not considered in the s-process path it is unique and the mass A can also be used as identifier for isotopes.

and the two assumptions, Eq. 1.4 can be rewritten

$$\frac{dY(A)}{d\tau} = \sigma(A-1)Y(A-1) - \sigma(A)Y(A). \tag{1.6}$$

The situation of a constant s-process flow would occur, if the production and destruction term were equal (see also Käppeler et al. 1989), i.e. the σY = constant. In Fig. 1.6 σY of s-only isotopes in solar system is shown as red dots and it is clear that such a condition is only closely reached for regions $90 < A < 135$ and $140 < A < 205$. This two regions where a constant σY is approximately reached are divided by the isotopes with neutron magic number $N = 50$, and have nuclei with magic numbers $N = 82$ and 126 at their lower and upper boundary, respectively. Neutron magic numbers correspond to nuclear shell closures, meaning a gap in the nuclear potential. Isotopes with such a number of neutrons have a low neutron capture cross sections σ, because it is energetically unfavourable to add another neutron. It was recognised early that a single exposure is not sufficient for explaining the s-process abundances (Clayton et al. 1961). Seeger et al. (1965) showed that the observed abundances can be explained by exponential distributions of neutron exposures.

$$\rho(\tau) = \frac{GY_{\odot}(^{56}\mathrm{Fe})}{\tau_0} \exp(\tau/\tau_0) \tag{1.7}$$

where ^{56}Fe is the main s-process seed, and G specifies the fraction of the observed ^{56}Fe, which is irradiated by an exponential neutron exposure distribution and with the mean exposure τ_0.

Clayton & Ward (1974) derived with such an exponential distribution of exposures for σY_s[14] the smooth relation:

$$\sigma Y_s(A) = \frac{GY_{\odot}^{56}}{\tau_0} \prod_{i=56}^{A} \left(1 + \frac{1}{\sigma_i \tau_0}\right)^{-1} \tag{1.8}$$

where σ_i are the neutron capture cross sections. By using this mathematical formulation of the classical s process, it was found that at least three components are necessary to fully reproduce the observed solar system abundances: The *weak* component accounting for the atomic mass region $A < 90$, the *main* component producing the s-process isotopes with $A > 90$ and the *strong* component, which accounts for a fraction of the observed lead (Pb).

In Fig. 1.6 σY_s is shown for s-only isotopes of solar system abundances of Asplund et al. (2005) (red dots) and for the classical s process (blue continuous and green dashed lines). The theoretical curves were calculated using Eq. 1.8 and the Maxwellian averaged cross sections of the KADoNiS (Dillmann et al. 2008) database. For both curves the parameters G and τ_0 were chosen to fit the data[15]. For most of the isotopes a single theoretical curve (blue line) is sufficient to explain the observations within their uncertainties in the mass region $A > 90$. These main and strong components corresponds to the s-process contribution from AGB stars (see Section 1.4.3). The mass region $A < 90$ is characterised by a lower mean neutron exposure τ_0 but higher G (green dashed line). However, Beer & Macklin (1989) found that this *weak* component is better described by a single irradiation than an exponential as used here. Helium burning in massive stars was found as a further astrophysical site where s process occurs (Peters 1968). It is discussed in further detail in Section 1.4.2.

[14] Subscript s stands for s process.

[15] For simplicity I did not consider the branching points.

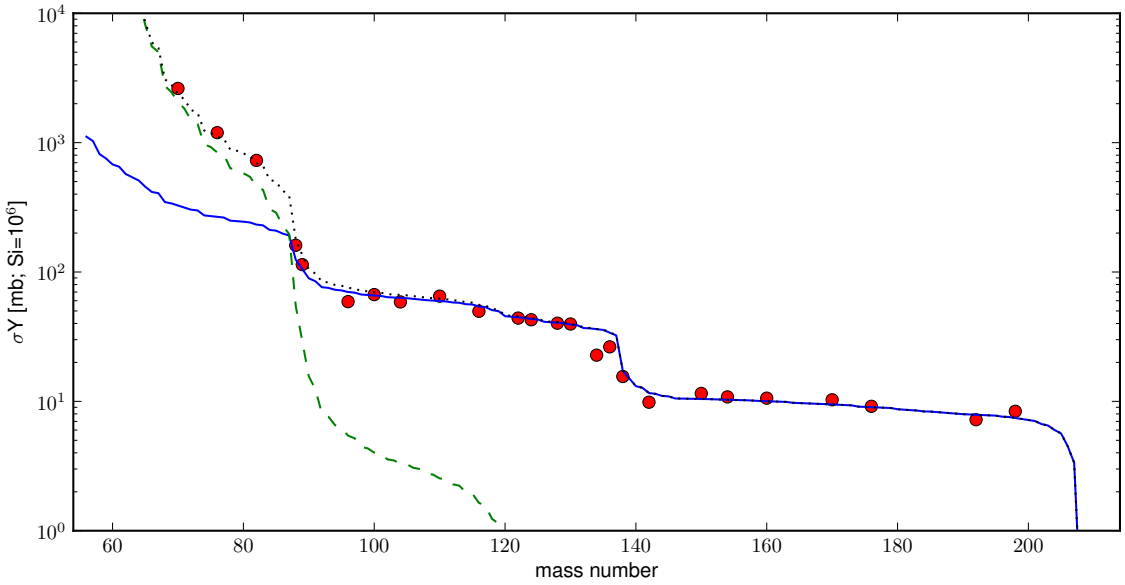

Figure 1.6: σY_s - cross section times solar system abundances (Asplund et al. 2005) of s-only isotopes. The black dotted curve is the sum of the *weak* (green dashed line) and the *main* (blue continuous line) component.

The branching points are an important feature of the s process. An s-process branching is a split of the s-process path, which emerges if the mean neutron capture time and the decay time of an isotope are of the same magnitude $t_n \approx t_\beta$ (see red marked isotopes in 1.5). From the abundance pattern one can derive the strength of such a branching and it is then possible to calculate the neutron density n_n and the temperature, which were present during the s process, when a constant neutron flux is additionally assumed. For the *weak* component ($A < 90$) there are only three branching points, located at ^{63}Ni, ^{79}Se and ^{85}Kr (see Fig. 1.5).

The branching factor f_β is defined in terms of β-decay rate λ_β and neutron capture rate λ_n of the branching point,

$$f_\beta = \frac{\lambda_\beta}{\lambda_\beta + \lambda_n} \tag{1.9}$$

where $\lambda_\beta = \ln(2)/t_{1/2}$, $t_{1/2}$ is the half life of the branching isotope. If the abundances of the s-only isotopes are known and there are at least two of them, the branching ratio f_β can be calculated as well in terms of the σY-values of the involved s-only isotopes. For instance at the ^{79}Se branching point

$$f_\beta = \frac{\lambda_\beta}{\lambda_\beta + \lambda_n} \approx \frac{\sigma Y\left(^{80}\mathrm{Kr}\right)}{\sigma Y\left(^{82}\mathrm{Kr}\right)} \tag{1.10}$$

The Equation 1.10 can be solved for the neutron density, which shows how to calculate the conditions during the s process.

$$n_n = \frac{1 - f_\beta}{f_\beta} \cdot \frac{1}{v_T < \sigma >_{^{79}Se}} \cdot \frac{ln(2)}{t_{1/2}(^{79}\mathrm{Se})} \tag{1.11}$$

The neutron capture cross section varies only slightly with temperature. Hence, only the third factor can vary strongly with the temperature of stellar plasma, due to the temperature

dependence of the β-decay rates. These rates can differ from the terrestrial rates by up to several magnitudes. Thus, for the calculation of n_n and T two branching points are needed, because of this temperature dependence in equation 1.11.

There are several branching points that may be used to characterise the *main* component but only two that are feasible for the *weak* component: those at ^{79}Se and ^{85}Kr. For more information about branching points analysis and its importance the reader is referred to Käppeler et al. (1992) and Käppeler (1996).

In the framework of the classical s process the analysis of the branching points allows the determination of conditions (temperature and the neutron densities) of s-process nucleosynthesis. In the past determination of the allowed regions of s-process conditions helped to find the corresponding astrophysical production site and the neutron source for the *weak* and *main* component. For both components the neutron density was found to be between $n_n = 10^7$ and 10^9 cm^{-3}, and at temperatures around of 2.5×10^8 K for the *main* and 2.5 to 5.8×10^8 K for the *weak* component (see e.g. Käppeler et al. 1989).

1.4.2 S process in massive stars

The *weak* component of the classical s process is associated with the nucleosynthesis of heavy elements in He burning and shell C burning of massive stars with initial solar-like metallicity and $M \gtrsim 13\ M_\odot$. This component contributes a considerable amount of atomic nuclei with masses between $A = 65$ and 90 (from copper, Cu, to zirconium, Zr) to the galactic chemical enrichment. Massive stars produce mainly nuclei up to the neutron magic number peak $N = 50$ at strontium (Sr), yttrium (Y) and Zr (e.g. Käppeler et al. 2011).

It was first recognised by Cameron (1960), that massive stars can produce ^{22}Ne via the reaction sequence 1.2 from secondary ^{14}N produced in H burning via the CNO-cycles. Peters (1968) identified the s process in the convective He-burning core of massive stars, where the neutrons are released by the

$$^{22}\mathrm{Ne}(\alpha, n)^{25}\mathrm{Mg} \tag{1.12}$$

reaction. Other neutron sources such as ^{13}C(α, n) do not play a major role in He burning (e.g. Rayet & Hashimoto 2000). ^{22}Ne begins to be destroyed by α-captures when $T \approx 2.5 \times 10^8$ K, resulting in neutron densities n_n reaching as high as 10^6 to 10^7 cm^{-3}. Both match very well the conditions derived in the classical s process for the *weak* component from branching ratios. These conditions are reached only close to exhaustion of helium in the centre of massive stars.

Couch et al. (1974) realised early that not all of ^{22}Ne is converted to magnesium at the end of He burning in stars with $M \lesssim 30\ M_\odot$ with solar metallicity and therefore enables s process by the same neutron source at the beginning of carbon burning. There, the α-particles for the ^{22}Ne-neutron source, come from the α-emission channel of ^{12}C+^{12}C (see reaction sequence 1.3). The s-process elements from central carbon burning, however, do not survive the later burning phases and the explosion, because of photodisintegration (Thielemann & Arnett 1985). The only way to avoid this destruction would be outward mixing of products of central carbon burning, which would only be the case if the rates for ^{12}C+^{12}C of Caughlan & Fowler (1988) currently used, was higher by about a factor 100 (Bennett et al. 2012). The ^{22}Ne remaining from He burning is destroyed at the very beginning of the multiple convective shell C-burning phases, releasing a short burst of neutrons with neutron densities $n_n \approx 10^{11}$ cm^{-3}. It alters the s-process yields significantly (Raiteri et al. 1991a) and produces typically 20 to 30% of the s-process yields from massive stars (The et al. 2007). Compared to central He burning and shell C burning, the He-shell burning contributes the least, i.e. at most

about 10%, to the s-process yields (The et al. 2007) because the temperatures reached in the convective shell are never high enough to efficiently activate ^{22}Ne$(\alpha,n)^{25}$Mg in the remaining lifetime of the stars. The ^{22}Ne surviving in these outer layers was thought to provide a neutron source during the explosion of the star (e.g. Thielemann et al. 1979; Truran et al. 1978), but recent explosion models do not find important nucleosynthesis there (Rauscher et al. 2002).

The neutron economy of the s process is determined by the neutron sources and sinks. The ^{22}Ne$(\alpha,n)^{25}$Mg reaction is the main source in massive stars, and it is in direct competition with ^{22}Ne$(\alpha,\gamma)^{26}$Mg. The ratio of both reaction rates determines how many neutrons are released and available for captures on heavy isotopes. In He-burning sources such as ^{13}C$(\alpha,n)^{16}$O and ^{17}O$(\alpha,n)^{20}$Ne are only important for recycling previously captured neutrons on light isotopes of ^{12}C and ^{16}O, by ^{12}C$(n,\gamma)^{13}$C and ^{16}O$(n,\gamma)^{17}$O. In carbon core burning ^{13}C(α,n) acts as an important neutron source, but such a nucleosynthesis signature is only ejected if the ^{12}C+^{12}C is more efficient than what currently is used in stellar models, and an extended convective core evolves (Bennett et al. 2012). ^{13}C is produced via ^{12}C$(p,\gamma)^{13}$N$(e^{+}\nu_e)^{13}$C in shell C burning, and thus is a real neutron source, but is not produced efficiently enough to boost the s process (The et al. 2007). ^{13}C(α,n) is not an efficient neutron source in shell C burning, because the high temperatures lead to a increased ^{13}N(γ,p) competing with the ^{12}C(p,γ). This keeps the available ^{13}C low. Other sources such as the neutron emission channel of ^{12}C+^{12}C (see Section 1.3.1) are not efficient enough to contribute substantially to the s process during carbon burning or are just acting to recycle neutrons in the same fashion as the (α,n) reactions on ^{17}O and ^{21}Ne.

Only a fraction of the neutrons are captured by the seed nuclei of the iron group. Other important sinks are the so-called neutron poisons, meaning light elements which compete for the neutrons and thus reduce the s-process efficiency. The most abundant neutron absorbers in He burning are ^{12}C and ^{16}O, but they are only moderate poisons at solar metallicity, since most of the neutrons are released again by the subsequent (α,n) reactions. Even though the (α,γ) reaction rate on ^{17}O is lower than the (α,n) rate it can remove a major fraction of neutrons in stars with sub-solar iron content. ^{16}O can reduce the s-process efficiency, in particular at low metallicity (Rayet & Hashimoto 2000; Hirschi et al. 2008), because the ratio of ^{16}O to s-process seeds is higher. What is unfortunate for the s-process efficiency is the fact that the most important neutron poisons in He burning are ^{22}Ne (at the start of s processing) and ^{25}Mg (later on), independent of the metallicity (Prantzos et al. 1990). In C burning important additional neutron poisons ^{20}Ne and ^{24}Mg are built up by fusion, reducing the s process after the initial neutron release from ^{22}Ne to a minimum.

Knowing the details of the neutron economy, it is possible to predict how the s-process efficiency depends on the stellar mass and composition. More massive stars have higher central temperatures but somewhat lower densities in the same burning stage than the lower mass stars, owing to the higher energy production due to higher mass loss. As a consequence the ^{22}Ne neutron source ignites earlier in more massive stars and is thus also earlier exhausted. As expected, Langer et al. (1989) found an increase of the s-process efficiency in core He burning with increasing stellar mass, reaching a saturation at around 40 $M_\odot$ in stars with solar metallicity. Since a higher mass fraction of ^{22}Ne is burned in the core He burning, the C-shell contribution to the s process decreases with increasing stellar mass (The et al. 2007). The more efficient destruction of ^{22}Ne in more massive stars in He burning means also that the peak neutron densities are reached earlier in massive stars and only at the very end for stars with $M \approx 15\ M_\odot$.

S process in massive stars is a secondary process, meaning that its products are not

formed from the light elements H and He but from heavier seeds, as opposed to primary nucleosynthesis processes. Its secondary nature has direct consequence for the metallicity dependence and originates from the need for iron seeds and CNO-nuclei, which have to be present in the initial star-forming gas cloud. The knowledge about the s-process dependence on the initial stellar composition is important to estimate the massive star contribution to the galactic enrichment in s-process elements and was studied by several authors (Prantzos et al. 1990; Baraffe et al. 1992; Raiteri et al. 1992; Rayet & Hashimoto 2000). On the one hand the neutron to seed ratio increases with decreasing metallicity Z, but on the other hand most of the neutron poisons are primary and thus increase in strength towards lower Z. With lower Z also the C-shell contribution vanishes, since the lower available ^{22}Ne is burnt already in He burning. All in all, the s-process yields do not scale with [Fe/H] as a typical secondary process as suggested earlier with either the secondary sources or seeds, but instead are negligible below [Fe/H]≈ -2, because seeds, sources and neutron poisons all depend in a negative way on Z for the s process in (Prantzos et al. 1990).

1.4.3 S process in AGB stars

The s process in low and intermediate mass stars is described here only for completeness, but the following work focuses only on massive stars. In the mass range of $1 \lesssim \mathrm{M/M_\odot} \lesssim 8$, stars undergo the He-core and short pulsed He-shell burning. They are running up to higher luminosities but lower surface temperatures to the asymptotic giant branch (AGB) in the H-R diagram. The increasing mass loss during the AGB phase end the life of these stars after typically 5 to 20 pulses (Herwig 2005).

It was suggested early-on that s-process elements are produced in He-burning shell of red giant stars (Cameron 1955). It was first found by Weigert (1966) and Schwarzschild & Härm (1967) that the low and intermediate mass stars develop a convective He-burning shell, which reaches far enough outward to mix in protons and produces ^{13}C via

$$^{12}\mathrm{C}(p,\gamma)^{13}\mathrm{N}(\beta^+)^{13}\mathrm{C} \tag{1.13}$$

However Iben (1976) found in his stellar models that mixing above this convective zone is prohibited due to a strong gradient in the mean molecular weight.

Figure 1.7 shows schematically the stellar structure versus time of an AGB star around the pulse-driven convection zones (PDCZ), where convective regions are green. The squared density dependence of the 3α-rate leads to a thermonuclear runaway whenever He-shell burning in AGB stars ignites, because the thin helium burning shell can not expand against the outer layers shortly after the ignition. Thus during the He-shell burning a strongly growing convective He burning zone, the PDCZ, develops during which the star expands. As a consequence of expansion the density and temperature drop and helium and hydrogen burning cease. Thereafter the star contracts again and the convective envelope extends below its original level bringing up freshly processed material into the envelope and to the surface (third dredge-up). The contraction heats up the material and the H shell reignites. The helium shell burning reignites after inter-pulse phases of typically 100′000 years and a new cycle begins. The He-burning pulses last only for a few hundred years.

Two different reactions, $^{13}\mathrm{C}(\alpha,n)$ and $^{22}\mathrm{Ne}(\alpha,n)$, were considered historically as possible neutron sources for s process in AGB stars, but today only one of them is known to be the main neutron source in these stars ($^{13}\mathrm{C}(\alpha,n)$). In H burning ^{14}N is produced from CNO

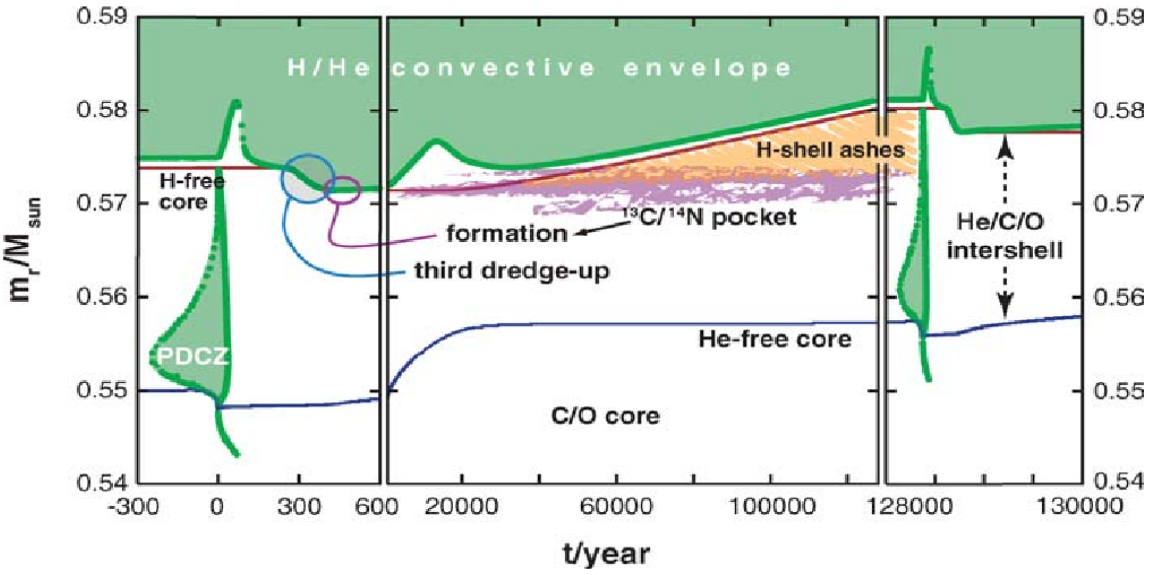

Figure 1.7: Schematic diagram from Herwig (2005) which shows where the third dredge-up and the ^{13}C-pocket in AGB stars appears.

nuclei as in massive stars. At the beginning of He burning this ^{14}N is transformed to ^{22}Ne by the reaction chain 1.2.

Unfortunately, accounting for the s process in AGB stars with ^{22}Ne alone becomes problematic. On the one hand the evidence points out that the most s-enriched AGB stars have masses of 1 to 3 $M_\odot$, but the activation temperatures of a few times 10^8 K are only reached for stellar evolution models of masses higher than approximately 5 $M_\odot$. Although the ^{22}Ne source can be (briefly) activated at the peak of each pulse with quite high neutron densities of $n_n \approx 10^{11}$, the neutron exposures are low, $\tau \approx 10^{-2}$ mb^{-1}, and it does not contribute much to s-process production. On the other hand a change in the ratio of Mg isotopes would be evidence for the contribution of this neutron source, however such a ratio has not been found in s-enriched low mass stars to date. So these facts seem to point out that the ^{22}Ne$(\alpha, n)^{25}$Mg neutron source does not operate in low mass AGB stars, although it is the main neutron source for intermediate mass stars (Lattanzio 1992). This distinction is important because the main s-process contribution from AGB stars is produced by 1-3 $M_\odot$ stars (Lattanzio & Lugaro 2005). The second and more efficient neutron source for AGB stars is the ^{13}C$(\alpha, n)^{16}$O-reaction. After each pulse protons are mixed down below the hydrogen envelope into the ^{12}C enriched helium shell, where these protons can be captured by ^{12}C to form ^{14}N and ^{13}C by the same reactions involved in the CNOI cycle, producing ^{14}N from ^{12}C. But only if the amount of protons mixied into the ^{12}C-rich shell is limited, ^{13}C can be produced without producing ^{14}N. This is essential, because ^{14}N is a very strong neutron poison via ^{14}N(n, p) and would suppress the s process.

The contraction after each such He-shell flash raises the temperature again until the hydrogen shell burning reignites. The H-shell burning and contraction heats up the ^{13}C

enriched zone[16]. When the temperature rises to about $T_8 = 1$ the reaction

$$^{13}\mathrm{C}(\alpha, n)^{16}\mathrm{O} \tag{1.14}$$

starts to release neutrons at low neutron densities $n_n \approx 10^7$ cm^{-3}. These neutrons mainly capture onto iron and heavier elements, and are released during the inter-pulse phase. How the above described down-mixing of protons into the helium layer really works, i.e. what mechanism produces the ^{13}C-pocket, is not yet fully understood (Lattanzio & Lugaro 2005).

With relatively high neutron exposures by the ^{13}C neutron source 1 to 3 $M_\odot$ AGB stars assemble the *main* component of the classical s process and it was also found that the *strong* component is produced by low metallicity AGB stars (Gallino et al. 2000). They favour the production of Pb because they are short of seeds. More detailed information about the evolution of AGB stars and nucleosynthesis in AGB stars can be found in reviews written by Herwig (2005), Busso et al. (1999) and a recent study of s process in low metallicty AGB stars in (Bisterzo et al. 2010).

1.4.4 Diagnostics

There are several useful quantities which specify the efficiency of the s-process nucleosynthesis. One such quantity is the neutron exposure as defined already in Eq. 1.5. The number density of the neutrons depends in general on time and the mass coordinate in a star, but in the case of a one-zone model the latter evidently becomes void. For the investigation of s process in convective zones one can define a mean neutron exposure

$$\langle \tau_n \rangle = \int \langle n_n(t) \rangle v_T dt \tag{1.15}$$

In this equation as well as in Eq. 1.5, usually the themal velocity $v_T = \sqrt{2kT/m_n}$ at $kT =$ 30 keV is chosen. However, Eq. 1.15 does not describe the efficiency in convective zones very well, since the neutrons are captured locally during core He burning, near the centre of the star and later the products are mixed outwards. This is the reason why Woosley & Weaver (1995) introduced a different kind of exposure defined by a nucleus, which can only be destroyed by the s process. They chose ^{54}Fe for this definition

$$\tau_{54} = -\frac{1}{\sigma_{54}} \ln\left(\frac{X_{54}}{X_{54}^0}\right)$$

where σ_{54} is the Maxwellian averaged neutron capture cross section. X_{54} and X_{54}^0 are the final and the initial mass fractions of ^{54}Fe.

Another quantity for the s-process characterisation is the average number of neutron captures per iron seed (e.g. Käppeler et al. 1990)

$$n_c = \frac{\sum_{A=56}^{209} (A-56)\,(Y(A) - Y_0(A))}{\sum_{A=56}^{209} Y_0(A)} \approx \frac{\sum_{A=56}^{209} (A-56)\,(Y(A) - Y_0(A))}{Y_0(56)} \tag{1.16}$$

[16] also called ^{13}C-pocket.

$Y(A)$ and $Y_0(A)$ are the final and the initial abundance respectively of a nucleus with nuclear mass number A. The maximum of this number is defined by the amount of main neutron source ^{22}Ne burned (or ^{13}C in case of AGB stars) $\Delta Y(^{22}\mathrm{Ne})$

$$n_{c,max} = \frac{\Delta Y(^{22}\mathrm{Ne})}{Y_0(56)} \tag{1.17}$$

describing the case where all neutron source nuclei are destroyed trough a neutron emission channel and all neutrons are absorbed by heavy nuclei. The ratio $n_c/n_{c,max}$ gives an integrated quantity describing the fraction of neutrons available for heavy element production.

The relative strength of neutron poisons and neutron absorber in general can also be investigated by the more detailed quantity

$$p_i(t) = \frac{\sum\limits_j \lambda_j(t) Y_i(t)}{\sum\limits_l \lambda_l(t) Y_{i_l}(t)} = \frac{\sum\limits_j \rho N_A \langle \sigma v \rangle_j Y_n Y_i}{\sum\limits_l \rho N_A \langle \sigma v \rangle_l Y_n Y_{i_l}} \tag{1.18}$$

where the λs are the neutron capture rates and Y_n and Y_i the number abundances of neutrons and nuclear species i. The sum of the nominator includes the (n,γ), (n,p), and (n,α) rate on the nucleus i and the sum in the denominator includes the neutron captures on all nuclei or only the neutron poisons if only their relative strength is wanted. If many captured neutrons are recycled by a subsequent neutron source it is more accurate to take the effective reaction rate which removes the neutrons definitely from the neutron economy. For example ^{16}O captures a lot of neutrons, but a high fraction of it is recycled by $^{17}\mathrm{O}(\alpha,n)$; to measure the strength of ^{16}O as a neutron poison therefore the $^{17}\mathrm{O}(\alpha,\gamma)$ rate should be taken.

1.5 Stellar rotation

From the principle of the conservation of angular momentum it is expected that stars or at least their precursors rotate. Even though a high fraction of rotation energy is lost during star formation in winds and disc-like structures around proto-stars (e.g. Zinnecker & Yorke 2007), massive stars are observed to have considerable rotation rates (e.g. Dufton et al. 2006). Because stars are not solid bodies, they are flattened due to centrifugal forces, becoming ellipsoid-like shapes with bigger equatorial than polar radii. The most oblate star observed today has a ratio of equatorial to polar radius of at least 1.5 (Domiciano de Souza et al. 2003). Such a deformation has also observable impact on the distribution of the surface temperature; it makes stars appear cooler around their equator than at their poles (see Von Zeipel theorem in Maeder 2009), an effect also observed for different stars (e.g. Domiciano de Souza et al. 2005; McAlister et al. 2005). Fast rotation has also effects on the stellar mass loss by winds. It becomes not only anisotropic, but can also remove a considerable amount of angular momentum by equatorial mass loss depending on the spectral type of the star (Maeder & Meynet 2000, see for a review).

Rotation affects also the stellar interiors, meaning the physical and chemical structures of the stars and therefore quantities such as lifetime, luminosity, or stellar yields. Recent stellar models including rotation reproduce a wide range of observations better than those without. For example: the Wolf-Rayet to O-type star number ratio (Meynet & Maeder 2003, 2005; Vázquez et al. 2007), the variation with metallicity of the number ratio of type Ibc to

type II supernovae (Georgy et al. 2009), or the ratio of blue to red supergiants in the Small Magellanic Cloud (Maeder & Meynet 2001).

The observation of CNO-cycled material, in particular increased nitrogen abundances at the surface of massive stars, is a strong indicator for internal mixing. Models including rotation induced mixing (Meynet & Maeder 2000; Heger & Langer 2000) seem to be in good agreement with observed nitrogen surface enrichments (Przybilla et al. 2010). Mixing induced by rotation can also be constrained by the depletion of light elements such as lithium (Li), beryllium (Be) and boron (B), which can also help to distinguish between single stars and mass transfer binaries (Brott et al. 2009); boron is destroyed at relatively low temperatures ($\approx 6 \times 10^6$ K) where the CNO-cycles are not yet efficient. Therefore, modest mixing due to rotation leads to a depletion of light elements at the surface without considerable nitrogen enrichment. This effect can not be explained by mass transfer in a binary system, since there the accreted material is depleted in B and enriched in N (Fliegner et al. 1996), but can be explained by single rotating stars (Frischknecht et al. 2010) in particular if strong mixing occurs due to magnetic braking of the outer stellar layers (Meynet et al. 2011).

Massive stars in the early universe are different from the ones observed today. Due to their low metal content, they are more compact and rotate faster than their equivalents found in the Milky Way. This view is supported by observations of an increasing Be/B-type star ratio with decreasing metallicity (Martayan et al. 2007) and by faster rotating massive stars in the SMC compared to the Milky Way (Hunter et al. 2008) and by recent hydrodynamic models of the first stars (Stacy et al. 2011).

Faster rotation and therefore more mixing at low Z has an impact on the early galactic chemical enrichment. Fast rotating stellar models at low Z have been calculated by Meynet et al. (2006) and Hirschi (2007). In these rotating models, primary nitrogen yields are much larger than in non-rotating models. When yields from these rotating models are used as input ingredients in chemical evolution models, a nice fit of the N/O in very metal poor halo stars (see e.g. Spite et al. 2005) can be obtained (Chiappini et al. 2006) shown in Fig. 1.5). Also the $^{12}C/^{13}C$ ratio found in low Z stars can be reproduced by stellar models including rotation-induced mixing (Chiappini et al. 2008). Rotation provides also an explanation for the abundance patterns, such as O-Na anti-correlation, observed in globular clusters (Decressin et al. 2007).

Finally, even though the treatment of transport of angular momentum and chemical species is thought to be one of the main uncertainties in stellar evolution models, it is necessary to reproduce all the different observables. Rotation is thus, beside the mass and the composition, the most important initial parameter of stellar models.

1.6 This work

From the discussion in Section 1.5 it became obvious that rotation has a high impact on the stellar evolution, and seems to be important to describe many astronomical observations. In an ideal case, a stellar evolution code is able to follow the evolution of many different isotopes involved in hydrostatic nucleosynthesis, in particular for the s process but also the γ-process (e.g. Rauscher et al. 2002). The main purpose of this work was thus to produce a numerical stellar evolution code able to follow the effects of rotation on nucleosynthesis in a consistent but computationally efficient manner. Thus the investigation of rotational effects on s process in massive stars was the main goal.

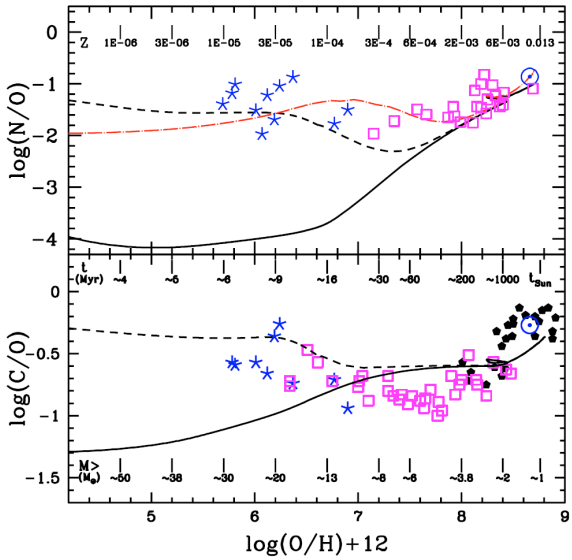

Figure 1.8: N/O and C/O evolution of observations and GCE models of Chiappini et al. (2006) including yields of massive stars with (dashed lines) and without (continuous lines) rotation.

We chose thus on the one hand the Geneva stellar evolution code (Eggenberger et al. 2008, hereafter GenEC, e.g.), which is one of the few codes worldwide available that is able to model stellar rotation in a comprehensive and consistent way, and on the other hand the nucleosynthesis network BasNet[17], used for example in Arnett & Thielemann (1985), Thielemann & Arnett (1985) and Fröhlich et al. (2006), to form a efficient numerical unit to gain new scientific insights into synthesis of atomic nuclei in rotating stars. Both codes were applied in countless astrophysical research projects and have helped to achieve very significant scientific results in the field.

[17]Since there exists no official name for the nuclear reaction network code, originally developed by F.-K. Thielemann, we use this name here standing for Basel Network.

2 Stellar evolution code

In this chapter the physical principles and the methods of stellar evolution are described. Details given here mainly refer to the Geneva stellar Evolution Code (GenEC). It is based on the Kippenhahn code (Kippenhahn et al. 1967), and methods and improvements were described e.g. in Meynet & Maeder (1997) and Eggenberger et al. (2008). We summon the main aspects of GenEC.

2.1 Stellar structure

The fundamental equations to calculate stellar models are based on basic physical principles, and describe the distribution of luminosity L, temperature T, mass M, pressure P and the chemical composition with respect to the radius and their evolution with time. At the moment it is computationally too expensive to calculate the numerical problem of a star in three spacial dimensions (3D), thus the problem is reduced to the radial dimension in all current codes, which are able to follow the full stellar evolution. This is a well justified assumption, because stars are more or less spherical objects as long as they do not rotate. Moreover instead of spacial usually the enclosed mass is used as independent coordinate, because it changes less drastically over the stellar lifetime and poses therefore a smaller numerical challenge.

However, in case of rotation the stellar shape is deformed and not spherical any more. But with slow to moderate rotation rates the structure is still axial symmetric as long as the rotational energy does not exceed a considerable fraction of gravitational binding energy (Tassoul 1978). Kippenhahn & Thomas (1970) found that stellar structure equations can be kept in similar form as in the spherical symmetric case with cylindrical rotation and a conservative potential respectively. This is not a very general case, but Meynet & Maeder (1997) showed that for a stellar structure with constant rotation rate on isobars, called "shellular rotation", the structure equations can keep the same form, if appropriate mean values are used. Such shellular rotation is enforced, if the horizontal turbulence is much faster than the vertical turbulence, which is expected in stars as a consequence of gravity acting as restoring force only in vertical direction (Zahn 1992). Here the stellar structure equations are given directly in this form, with the unknown variables defined on isobaric surfaces. For a comprehensive derivation and discussion of the stellar structure equation see e.g Kippenhahn & Weigert (1990); Maeder (2009).

Mass conservation The continuity equation means that the infinitesimal mass dM_P on an isobar with radius r_P and density $\overline{\rho}$ is $4\pi r_P^2 \overline{\rho} dr_P$, thus

$$\frac{\partial r_P}{\partial M_P} = \frac{1}{4\pi r_P^2 \overline{\rho}}. \tag{2.1}$$

The radius r_P is defined as the radius of a sphere with the same volume as the isobar, $V_P = \frac{4}{3}\pi r_P^3$. Here and in the subsequent equations a quantity x on an isobar with pressure P is written as $\langle x \rangle$ when averaged on the isobaric surface S_P, and $\overline{x}$ if averaged in the volume between two isobars.

Hydrostatic equilibrium In most phases of stellar evolution it is a good assumption, that gravity and pressure force are in equilibrium and thus

$$\frac{\partial P}{\partial M_P} = -\frac{GM_P}{4\pi r_P^4} f_P. \tag{2.2}$$

G is the gravitational constant, and f_P is a geometrical factor due to deformation by rotation and given in Eq. 2.7.

Energy conservation The change of luminosity L_P over a small mass shell dM_P is given by the energy produced by nuclear reactions ϵ_{nuc}, the energy lost by neutrinos ϵ_ν and the change in gravitational energy ϵ_{g}.

$$\frac{\partial L_P}{\partial M_P} = \epsilon_{\mathrm{nuc}} - \epsilon_\nu + \epsilon_{\mathrm{g}} = \epsilon_{\mathrm{nuc}} - \epsilon_\nu - c_P \frac{\partial T}{\partial t} + \frac{\delta}{\rho}\frac{\partial P}{\partial t} \tag{2.3}$$

ϵ_ν contains the neutrinos emitted by nuclear reactions and produced by several other processes in the stellar plasma, e.g. pair-, photo-, and plasma-neutrinos. ϵ_{g} is the energy released per time and mass unit by expansion or contraction of the star.

Energy transport The transport of energy from the stellar interior to the surface is usually dominated in different regions by either, radiation, convection, or in rare cases of strongly degenerate cores also conduction. It is described by

$$\frac{\partial \ln \overline{T}}{\partial M_P} = -\frac{GM_P}{4\pi r_P^4} f_P \min\left[\nabla_{\mathrm{ad}}, \nabla_{\mathrm{rad}} \frac{f_T}{f_P}\right] \tag{2.4}$$

with the adiabatic gradient, describing the energy transport in convective zones

$$\nabla_{\mathrm{ad}} = \left(\frac{\partial \ln T}{\partial \ln P}\right)_{\mathrm{ad}} = \frac{P\delta}{\overline{T}\overline{\rho} c_P}, \tag{2.5}$$

being the internal gradient when a moving blob of matter (eddy) does not exchange heat with its surrounding. c_P is the specific heat at constant pressure. ∇_{rad} is the thermal gradient necessary to transport the total energy by radiation only,

$$\nabla_{\mathrm{rad}} = \frac{3}{16\pi acG} \frac{\kappa L_P P}{M_P \overline{T}^4} \tag{2.6}$$

with a the radiation constant, c the speed of light and κ the opacity (see Section 2.6). f_P and f_T are defined as following, and are solved iteratively together with the stellar structure equations (Endal & Sofia 1976).

$$f_P = \frac{4\pi r_P^4}{GM_P S_P} \frac{1}{\langle g^{-1} \rangle} \tag{2.7}$$

and

$$f_T = \left(\frac{4\pi r_P^2}{S_P} \right)^2 \frac{1}{\langle g \rangle \langle g^{-1} \rangle} \tag{2.8}$$

with the effective gravity $\mathbf{g}$ perpendicular to the isobaric surface and $g \equiv |\mathbf{g}|$. Hereafter the subscript $_P$ is omitted.

To solve the structure equations 2.1-2.4 additional physical quantities must be known and calculated respectively, which is discussed in the subsequent sections.

- Mixing, i.e transport of angular momentum and matter inside the star, modifies the angular velocity Ω and the abundance distributions of chemical species, described by mass fractions X_i (see Section 2.2).
- Nuclear reactions, mainly responsible for the changes in X_i, define the nuclear energy generation $\epsilon_{\rm nuc}$, which is discussed in Section 2.3.
- Neutrino energy loss ϵ_ν becomes very important in the late burning stages (see sec 2.4).
- Mass loss determines the evolution of the total stellar mass, M^*, with time (see sec 2.5).
- The opacities are needed to calculate $\nabla_{\rm rad}$ (see Section 2.6).
- Density ρ is calculated from the equation of state (see Section 2.7).
- A stellar structure calculation can only be started with an initial structure and an initial composition, both are described in Section 2.8.

2.2 Mixing

2.2.1 Transport of angular momentum

Inside a rotating star angular momentum is transported by convection, meridional circulation and turbulent diffusion. The transport of angular momentum in the vertical direction is described by the following advection-diffusion equation (Chaboyer & Zahn 1992),

$$\rho \frac{d}{dt} \left(r^2 \Omega \right)_{M_r} = \frac{1}{5r^2} \frac{\partial}{\partial r} \left(\rho r^4 \Omega U(r) \right) + \frac{1}{r^2} \frac{\partial}{\partial r} \left(\rho D r^4 \frac{\partial \Omega}{\partial r} \right), \tag{2.9}$$

where ρ is the density, Ω the angular velocity of a shell, D the diffusion coefficient due to several turbulent diffusion processes and $U(r)$ the amplitude of the radial component of the meridional velocity, which is expressed by $u(r, \theta) = U(r) \cdot P_2(\cos\theta)$. The expression of $U(r)$ and its derivation can be found in Maeder & Zahn (1998). Without any transport mechanisms for angular momentum, i.e. with $D = U = 0$, both terms on the right hand side of Eq. 2.9

vanish corresponding to specific angular momentum conservation. In such a situation the angular velocity would only change due to contraction or expansion.

At the moment it is not clear how rotation evolves in convective regions. On the one hand magnetic fields could enforce solid body rotation (Maeder & Meynet 2004), meaning angular velocity Ω =constant. But it is not clear whether magnetic fields generated by dynamo action (Spruit 1999) are strong enough to do so. On the other hand mixing length theory (Böhm-Vitense 1958) suggests that rising plumes of matter conserve their angular momentum before they dissolve again leading to uniform specific angular momentum. In GenEC convective regions are currently treated as a solid body rotator.

For a general rotation law stars cannot be in hydrostatic and radiative thermal equilibrium (Baker & Kippenhahn 1959), because isobaric and isothermal surfaces are not identical. As a consequence large scale circulations, called meridional circulation, can develop. These large scale circulations are described by the first term on the right hand side of Eq. 2.9. Meridional circulation transports angular momentum outwards when the matter flow is rising at the equator and descending at the poles ($U(r) < 0$), and angular momentum is transported inward when the circulation goes the other way round ($U(r) > 0$). In GenEC the advection-diffusion Eq. 2.9 is solved, however it is very challenging and only done for the main sequence, because the lagest changes by meridional circulation occur during the main sequence. Most other stellar evolution codes treat meridional circulation as diffusion process (e.g. Heger et al. 2000), which is not appropriate since meridional circulation is an advective and not a diffusiive process.

Various rotation induced instabilities go into D in the second term on the right hand side of Eq. 2.9. The instabilities responsible for angular momentum transport are also the cause for the transport of chemical elements and are described in the Section 2.2.4.

2.2.2 Transport of chemical elements

The chemical composition inside a star is changed by transport processes and nuclear reactions. It is homogenised by strong horizontal diffusion on isobars and can therefore as the stellar structure be treated as constant on shells (Chaboyer & Zahn 1992). Within a mass shell at coordinate M, the mass fraction X_i of nuclear specie i changes with time according to

$$\left(\frac{\partial X_i}{\partial t}\right)_M = \left(\frac{\partial}{\partial M}\right)_t \left[\left(4\pi r^2 \rho\right)^2 D \left(\frac{\partial X_i}{\partial M}\right)_t\right] + \left(\frac{dX_i}{dt}\right)_{\text{nuc}} \tag{2.10}$$

Since there is no transport across the inner and outer boundary ($M = 0$ and $M = M^*$) the abundance and mass fraction respectively cannot be changed by diffusive transport, which is equivalent to the boundary conditions

$$\left(\frac{\partial X_i}{\partial M}\right)_{M=0} = \left(\frac{\partial X_i}{\partial M}\right)_{M=M^*} = 0$$

Similar boundary conditions are valid for angular momentum transport. In convective regions the diffusion coefficient is very high and the mixing time scale very short compared to the burning time scale. Nuclear burning, the second term on the right hand side of Eq. 2.10, is treated separately and discussed in Chapter 3.

2.2.3 Convection and overshooting

A radiative stellar layer is unstable against convection, if the buoyancy on an upward displaced eddy is stronger than the restoring gravitational force or a downward displaced eddy is more strongly accelerated by gravity than buoyancy can drive it back. The stability criterion including the stabilising effect of a mean molecular weight gradient ∇_μ is

$$\nabla_{\rm ad} - \nabla + \frac{\varphi}{\delta}\nabla_\mu > 0 \tag{2.11}$$

with

$$\nabla \equiv \left(\frac{d\ln T}{d\ln P}\right) \qquad \nabla_\mu \equiv \left(\frac{d\ln \mu}{d\ln P}\right)$$
$$\delta \equiv -\left(\frac{\partial \ln \rho}{\partial \ln T}\right)_P \qquad \varphi \equiv \left(\frac{\partial \ln \rho}{\partial \ln \mu}\right)_{P,T}$$

Equation 2.11 is the so-called *Ledoux criterion*. Usually $\nabla_\mu > 0$, meaning ∇_μ is stabilising the stellar plasma against convection, because nuclear reactions produce heavier nuclei in the stellar interiors. The Ledoux criterion is valid, if convection is perfectly adiabatic. However, real fluid elements would loose some energy by radiation leading to a growth of the convective region. It is thus common to use the less strict *Schwarzschild criterion*,

$$\nabla_{\rm ad} - \nabla > 0. \tag{2.12}$$

The zone, in which Eq. 2.11 is fulfilled but Eq. 2.12 not, defines the semi-convective region. Upto now there is no definite answer how much mixing occurs therein.

I used for all models the Schwarzschild criterion to determine the boundaries of convective zones. Additionally, the upper boundary of convective core with radius $r_{\rm conv}$ is moved outwards in GenEC by a distance $d_{\rm over}$, to consider the effect of overshooting of a fluid element over their equilibrium position. $d_{\rm over}$ is defined by

$$d_{\rm ov} \equiv \alpha_{\rm ov} \min\left[H_P, r_{\rm conv}\right]$$

where $\alpha_{\rm ov} = l/H_P$ is a dimensionless free parameter and $H_P = \frac{dr}{d\ln P}$ the pressure scale height. $\alpha_{\rm ov} = 0.1$ is used as standard, since models including effects of rotation reproduce the main-sequence width best, when this parameter choice is adopted (Ekström et al. 2012).

The diffusion coefficient, describing the mixing of chemical elements in convective zones, is taken from the mixing-length theory (Böhm-Vitense 1958)

$$D_{\rm conv} = \frac{1}{3}\alpha_{\rm MLT} H_P v_{\rm conv}$$

with $v_{\rm conv}$ the average velocity of the eddies (see e.g. Kippenhahn & Weigert 1990), $\alpha_{\rm MLT} = l_m/H_P$ the unit free mixing length parameter and l_m the mixing length. In GenEC $\alpha_{\rm MLT} = 1.5$ is used by default for massive stars.

2.2.4 Rotation induced mixing

Beside structural changes, rotation can also cause mixing in zones, which are otherwise stable against convection. The rotation induced instabilities considered in GenEC are discussed in the following paragraphs.

Dynamical shear

On the one hand velocity gradients in the stellar interior causes shear between the layers, on the other hand density gradients can stabilise the plasma. Mixing is prevented as long as the available kinetic energy δK is smaller than the energy needed to exchange two fluid cells against gravity δW. The stability criterion is known as the Richardson criterion. When thermal effects are not considered the Richardson criterion is

$$Ri \equiv \frac{g\delta}{H_P}\left(\nabla_{\rm ad} - \nabla - \frac{\varphi}{\delta}\nabla_\mu\right)\left(\frac{\partial r}{\partial V}\right)^2 > Ri_c$$

where V is the horizontal velocity and Ri_c the critical Richardson number. $Ri_c = \frac{1}{4}$ appears for the critical case of $\delta K = \delta W$, but Brüggen & Hillebrandt (2001) and Canuto (2002) found that mixing occurs already for $Ri \lesssim Ri_c = 1$. In this work we applied therefore $Ri_c = 1$.

The following diffusion coefficient for dynamical shear is used throughout this work.

$$D_{d-shear} = \frac{1}{3} r d\Omega dr,$$

where $d\Omega$ is the variation of the angular velocity Ω over a stellar zone with radial extension dr (Hirschi et al. 2004). Dynamical shear operates only at and smooths very steep velocity gradients, which appear only in advanced burning phases, usually at the edge of convective zones.

Solberg-Høiland instability

The stability criterion against convection in a star with rotation and density stratification is

$$R_{SH} \equiv \frac{g\delta}{H_P}\left(\nabla_{\rm ad} - \nabla + \frac{\varphi}{\delta}\nabla_\mu\right) + \frac{1}{\omega^3}\frac{d}{d\omega}\left(\omega^2\Omega\right)^2 \sin\vartheta > 0,$$

(e.g. Maeder 2009), with ϑ being the colatitude and ω the distance from the rotation axis. Without rotation, this criterion reduces back to the Ledoux and Schwarzschild criterion, respectively, depending weather ∇_μ is considered or not. The Solberg-Høiland instability appears only in regions with strongly decreasing specific angular momentum, meaning that stellar rotation favours convective stability and decreases the size of convective regions slightly when there is no or just a moderate gradient in the specific angular momentum. In GenEC it is implicitly accounted for R_{SH} by using Schwarzschild criterion and dynamical shear in radiative zones, because it can be shown that dynamical shear always appear before Solberg-Høiland instabilities (Hirschi 2004). Also the stabilising effect due to rotation is very weak and thus using the usual stability criterion for convective zones (Schwarzschild or Lexoux) is a good assumption.

Secular shear

In the criterion for dynamical shear given above the thermal adjustment of an eddy is not considered. This, however, weakens the stabilising effect of the thermal stratification and allows shear to operate on a thermal time scale. For the vertical shear diffusion coefficient we use the expression of Talon & Zahn (1997), which accounts for the effects of horizontal

turbulence in contrast to the prescription of Maeder (1997):

$$D_{\rm shear} = \frac{(K + D_{\rm h})}{\left[\frac{\varphi}{\delta}\nabla_{\mu}(1 + \frac{K}{D_{\rm h}}) + (\nabla_{\rm ad} - \nabla_{\rm rad})\right]} \frac{\alpha H_{\rm p}}{g\delta} \left(0.8836\Omega \frac{d\ln\Omega}{d\ln r}\right)^2,$$

where K is the thermal diffusivity, the diffusion coefficient $D_{\rm h}$ describes the horizontal turbulent transport. We used the $D_{\rm h}$ derived by Maeder (2003) in Frischknecht et al. (2010) and $D_{\rm h}$ of Zahn (1992), which we used in the s-process grid models (see Chapter 4), where the former is much stronger than the latter. Strong horizontal turbulence favours the vertical transport by secular shear in this prescription of Maeder (1997).

Meridional circulation

It was shown by Chaboyer & Zahn (1992) that the vertical transport of chemical elements by meridional circulation can be treated as diffusion, if the horizontal turbulence is very strong, i.e. when horizontal layers are homogenised on a smaller than the meridional circulation time scale. In this case the effective diffusion coefficient accounting for the combined effect of meridional circulation and horizontal turbulence is

$$D_{\rm eff} = \frac{|rU(r)|^2}{30 D_{\rm h}}.$$

It is rather low compared to $D_{\rm shear}$ when there is a gradient in Ω, but dominates mixing in regions with shallow $\nabla\Omega$, i.e. in layers rotating almost like a solid body.

The final diffusion coefficient D used in Equations 2.9 (angular momentum) and 2.10 (chemical elements) contains the effects of shear for the former, shear and meridional circulation for the latter. During the early burning phases, H and He burning, only $D_{\rm eff}$ and $D_{\rm shear}$ are relevant. Other possible instabilities are not considered in GenEC, but have probably rather small effects as for example the Goldreich-Schubert-Fricke instability (Hirschi & Maeder 2010). Magnetic fields could strongly affect the transport of angular momentum and chemical elements (see e.g. Maeder & Meynet 2005; Heger et al. 2005), but since there are high uncertainties in the implementation of magnetic fields, no models including magnetic fields are presented here. Another big uncertainty in these diffusion coefficients is the strength of the horizontal turbulence D_h and poses therefore also an important source of uncertainty for the mixing of chemical elements and the transport of angular momentum.

2.3 Nuclear energy production

In a nuclear fusion reaction, energy is either released (exothermic) or absorbed (endothermic), depending on whether the mass of parent or daughter nuclei are larger. The this energy difference is the so-called Q-value. This energy released by a nuclear reaction, is taken away by electron neutrinos ν_e, kinetic energy of nuclei and photons γ. But only the fraction of energy released in the latter two energy forms is available to heat the stellar material and keep up the pressure gradient, which stabilises the star, since neutrinos interact only very weakly with the stellar matter. Therefore only an effective Q-value, $Q_{\rm eff} = Q - Q_{\nu_e}$, is relevant for the star and used in stellar evolution calculations.

The energy produced in the stellar interior can be calculated from the reaction rates. The energy delivered by a particular reaction i per unit mass and time has the form

$$\epsilon_i = N_A R_i Q_i \tag{2.13}$$

where the form of the reaction rate R_i depends on the reaction type, $Q_i = Q_{\mathrm{eff},i}$ and N_A is the Avogadro number. For β-decays, e^--captures and γ-disintegrations it has the following form

$$R_i = \lambda_i Y_{j_i} \tag{2.14}$$

with Y_i the abundance of nuclear specie i. λ depends only on the temperature for β-decays and γ-disintegrations, for e^--captures it additionally depends on the density ρ. In case of two-body reactions (Eq. 2.15) and three-body reactions (Eq. 2.16) the reaction rate is determined by the temperature dependent reactivity $\langle \sigma v \rangle$ and the density ρ.

$$R_i = \rho N_A \langle \sigma v \rangle_{j;k} Y_{j_i} Y_{k_i} f_i \tag{2.15}$$

$$R_i = \rho^2 N_A^2 \langle \sigma v \rangle_{j;k;l} Y_{j_i} Y_{k_i} Y_{l_i} f_i \tag{2.16}$$

where $f_i = \exp(h)$ is the screening factor and h the screening function describing the screening effect on the repulsive nuclear Coulomb potential by the surrounding electron plasma. The released total energy per unit mass and time ϵ within a mass shell, with density ρ and temperature T, is therefore the sum over all occuring reactions. Usually this quantity is given in *cgs* units, i.e. in [erg g^{-1} s^{-1}].

$$\epsilon = N_A \sum_i R_i Q_i \tag{2.17}$$

The derivatives $\partial\epsilon/\partial\rho$ and $\partial\epsilon/\partial T$ are needed in the Jacobian of the Henyey method. More details about this are given in Section 3.7.1.

Another possibility is to calculate the energy production from the change of mass due to abundance changes, by using the mass excess m_j (e.g. Thielemann et al. 1998).

$$\epsilon = N_A \sum_j \dot{Y}_j m_j c^2 \tag{2.18}$$

We however use this second method only to calculate models with BasNet (see Chapter 3) during Si burning, because it is numerically more stable. For this methods the neutrino energy lost in nuclear reactions has to be calculated separately.

2.4 Neutrino energy loss

Beside nuclear reactions there are various other processes which can create neutrinos and remove in this way energy from the stellar interior. From electron scattering there is a branching with neutrino pair creation (photo neutrinos), as well as from e^-e^+-pair annihilation (pair neutrinos). Further neutrino production occurs from bremsstrahlung on nuclei and plasmon annihilation (plasma neutrinos). Neutrino energy loss dominates the total energy loss of massive stars from the onset of C burning, i.e from $\rho \gtrsim 10^5$ g cm^{-3} and $T \gtrsim 6 \times 10^8$ K. The different processes dominate in different regions of the ρ-T plane (see e.g. figures 11 and 12 of Itoh et al. 1996). For high temperatures ($T \gtrsim 0.5 \times 10^8$ K) and low densities ($\rho \lesssim 10^6$ g cm^{-3})

pair neutrinos dominate, while in degenerate conditions at low temperatures ($T \lesssim 0.5 \times 10^8$ K) and high densities ($\rho \gtrsim 10^7$ g cm^{-3}) bremsstrahlung neutrinos. In between these two regions plasma neutrinos dominate. The high neutrino energy loss in the center is also the reason why the evolution of envelope and the core decouple in the late stages. In GenEC the ν-energy loss of Itoh et al. (1989) is adopted.

2.5 Mass loss

Mass loss is an important ingredient for determining how stars evolve in particular for stars with $M \gtrsim 15\ M_\odot$. For a review about the wind of massive stars see Kudritzki & Puls (2000). All stars with luminosities $L \gtrsim 10^4\ L_\odot$ and AGB-stars with $L \gtrsim 10^{3.6}\ L_\odot$ show spectroscopic evidence of winds. For the most massive stars, stellar winds can remove more than 90% of initial mass before their explosion. Momentum of the mainly out-flowing photons is transferred to the matter at the stellar surface by continuum and line absorption, accelerating the matter away from the star. The stellar winds are driven mainly by the absorption of UV-photons in resonance lines of Fe and CNO elements, thus very strong winds are mainly expected in metal rich and hot stars.

We use for models of stars with $M > 15\ M_\odot$ the mass loss prescription of Vink et al. (2001). For the regions in HRD not described by this work, the prescription of de Jager et al. (1988) is used. For the winds in WR-phase modified mass loss rates of Nugis & Lamers (2000) are applied taking into account the metallicity dependence of Eldridge & Vink (2006). Mass loss depends on metallicity as $\dot{M} \propto Z^\alpha$, with α between 0.5 and 0.85 depending on the evolutionary phase. For models with rotation a correction factor F_Ω is applied to the mass loss rate, $\dot{M}(\Omega) = F_\Omega \dot{M}(\Omega = 0)$ (see Meynet & Maeder 2000; Ekström et al. 2012).

2.6 Opacities

In the radiative energy transport (see Eq. 2.6) the opacity κ describes the absorption and scattering of photons in the stellar plasma. The opacity depends on temperature, density, and composition. Several different processes contribute to the opacity, as line absorption, electron scattering, bound-free, and free-free transitions. In different temperature regimes other processes are the main contributors to the opacity.

We used tabulated Rosseland mean opacities computed with the OPAL tool (opalopacity.llnl.gov, Iglesias & Rogers 1996). The matching low temperature opacity tables were provided by Jason Ferguson (priv. communication and Ferguson et al. 2005). For both regimes the opacities were calculated to match the solar and α-enhanced initial composition, used in the models of this work and described in Section 2.8. In this work the solar composition from new hydrodynamic models of Asplund et al. (2005) are used. This new composition is in disagreement with helioseismic measurements. A possible solution for this problem is an upward correction of stellar opacities which could be caused by several different sources (see Pradhan & Nahar 2009). Another possible source could also be the too low neon abundance in the new solar abundance (Drake & Testa 2005). This is the reason why we applied the neon elemental abundance of (Cunha et al. 2006), which is 0.27 dex higher than the value of Asplund et al. (2005).

2.7 Equation of state

In most regions where the stellar plasma is fully ionized a simple equation of state (EoS) is sufficient. It is the sum of pressure components by the electron gas and the different nuclear species and the radiation pressure,

$$P(\rho, T, Y_1, \ldots, Y_n) = \rho N_A k T \left(Y_e + \sum_{i=1}^{n} Y_i \right) + \frac{1}{3} a T^4 = \frac{1}{\mu} \rho N_A k T + \frac{1}{3} a T^4 \qquad (2.19)$$

Y_e is the electron abundance[1]. In GenEC the pressure is used as unknown variable, hence, $\rho = \rho(P, T, Y_1, \ldots, Y_n)$ is used instead of $P = P(\rho, T, Y_1, \ldots, Y_n)$. Below the photosphere at relatively low temperatures the stellar gas is only partially ionised, and EoS becomes more complex because the ionization equilibrium of the elements depend on the number of free electrons. The calculation of the EoS in partially ionised stellar regions is describe in Baker & Kippenhahn (1962). When in the stellar center the matter becomes degenerate, it can no longer be described as an ideal gas. For a partial degenerate gas with the degeneracy parameter $\Phi < 7$ the approximations of Kippenhahn et al. (1967) are used and for more degenerate matter the complete degeneracy approximations of Chandrasekhar (1939). Hirschi (2004) was not able to go through the final collapse stage before the SN and suspected the limited reaction network to be the main cause of it. But this limitation should be solved with the implementation of BasNet and in a future project SN progenitors can be calculated. A future project is therefore to implement an EoS, which is accurate also for completely degenerate and relativistic matter up do densities close to nuclear matter density ($\rho = 10^{14}$ g cm^{-3}), to allow a smooth transition from stellar 1D progenitor models to multi-D hydrodynamic SN simulations. The Helmholz EoS of Timmes & Swesty (2000) (available on cococubed.asu.edu) would be a good solution with very good thermodynamic consistency. However, in our calculations such conditions were not reached, which is why we did not yet replace the EoS.

2.8 Initial structure and composition

Our models were started from the ZAMS. The initial structure, i.e. the initial L, P, T and M profiles, was taken from pre-calculated ZAMS models. As initial composition for models at solar metallicity ($Z = 0.014$), the elemental composition of Asplund et al. (2005) was adopted, with the Ne abundance modified according to Cunha et al. (2006). The isotopic ratios from Lodders (2003) are used. At all three sub-solar metallicities, we assumed an α-enhanced composition with the α-elements (^{12}C, ^{16}O, ^{20}Ne, ^{24}Mg, ^{28}Si, ^{32}S, ^{36}Ar, ^{40}Ca, and ^{48}Ti) enhanced with respect to iron, i.e. [X/Fe]$= -A$[Fe/H] for $-1 \geq$[Fe/H]> 0 and [X/Fe]$= A$ =constant for [Fe/H]≤ -1 where $A = +0.562$, $+0.886$, $+0.500$, $+0.411$,$+0.307$, $+0.435$, $+0.300$, $+0.222$, and $+0.251$ for the different α-enhanced isotopes. This α-enhanced composition was derived by fitting the abundance trends [X/Fe] vs [Fe/H] derived from halo and thick disk F- and G-dwarfs (Reddy et al. 2006) between [Fe/H]$= 0$ and -1. The linear fits were fixed to the solar value, i.e. [X/Fe]$= 0$ at [Fe/H]$= 0$, and below [Fe/H]$= -1$ a plateau was assumed. The values for the noble gases were adopted from the galactic chemical evolution models of Kobayashi et al. (2006). This α-enhancement gives a Fe/Z ratio which is

[1]The electron abundance is $Y_e = \sum Y_i Z_i$ in a fully ionized plasma, with Z_i the charge number of the different nuclear species.

a factor 4.6 lower than solar for [Fe/H] ≤ -1. All other elements were scaled from the solar composition. A more detailed description, about how the initial abundances were determined, can be found in Appendix B.

2.9 Numerical methods

The stellar structure (Eqs. 2.1 to 2.4), the nuclear reaction network (see Chapter 3) and mixing are solved sequentially in iterative steps in GenEC. Other codes solve the equations for mixing and burning (e.g. FRANEC, see Limongi & Chieffi 2006) or for structure, mixing, and burning (e.g. MESA, see Paxton et al. 2011) in a fully coupled way, but as long as the time steps are small enough GenEC displays similar results as other stellar evolution codes.

The method, how to the structure equations are disceretized and solved in GenEC, is described in Kippenhahn et al. (1967). This so-called Henyey method (Henyey et al. 1964) is an implicit finite difference method and therefore relatively stable compared to explicit methods, allowing large time steps. This allows to follow the early evolutionary stages, H and He burning, without high computational effort. The time scales of later stages are getting smaller due to neutrino energy loss and it becomes problematic to follow the inner part of a star by this implicit method when the time step is smaller than the time scale of conduction through a particular layer. Hirschi (2004) therefore implemented the method of Sugimoto (1970) modifying the discretisation of Eqs. 2.3 and 2.4, allowing to solve the structure equations in a numerically more stable way.

To solve the diffusion equation for either chemical species (Eq. 2.10) or angular momentum (Eq. 2.9 without the advection term) the implicit finite difference method is applied in GenEC. It was found by Meynet et al. (2004) to be the most robust method to follow the secular evolution of chemical elements and angular momentum. The advection equation (Eq. 2.9) is of fourth order, since $U(r)$ includes derivatives up to the third order, and is therefore very hard to solve. In GenEC a Henyey scheme is applied to do this (Meynet & Maeder 2000).

3 Nuclear reaction network and nuclear burning

The basics of a nuclear reaction network and in particular the code BasNet are described in this chapter. It was originally developed by F.-K. Thielemann and extensively used in the past 30 years in the research of astrophysical nucleosynthesis.

3.1 Thermonuclear reaction rates

Nuclei in an astrophysical plasma can interact with each other, with leptons[1], and photons. It is of particular interest for finding the answer to many problems in astrophysics to follow the abundance changes of nuclear species, either for calculating the sources and sinks of nuclear energy (see Section 2.3) or understanding the nucleosynthesis.

The quantity which describes the probability that the reaction

$$i + j \rightarrow o + m$$

occurs is the nuclear cross section

$$\sigma_{i;j,o} = \frac{\text{number of reactions/target/second}}{\text{flux of incoming projectiles}} = \frac{r_{i;j,o}/n_i}{n_j v},$$

where n_i and n_j are the number densities of projectile and targets, $v = |v_i - v_j|$ the relative velocity between i and j, and $r_{i;j,o}$ the number of reactions per cm^3 and second between the two kind of particles, hence can be expressed as $r_{i;j,o} = \sigma_{i;j,o} v n_i n_j$. In general, however, the relative velocity v is not constant but both kind of particles have a velocity distributions. In this case

$$r_{i;j,o} = \int \sigma_{i;j,o}\left(|v_i - v_j|\right) \cdot |v_i - v_j| dn_i dn_j \tag{3.1}$$

and for its evaluation the velocity distributions, obeyed by the particle types i and j have to be known. In an astrophysical plasma, when both i and j are nuclei, they can be described by Maxwell-Boltzmann distribution, hence by

$$dn_j = n_j \left(\frac{m_j}{2\pi kT}\right)^{3/2} \exp\left(-\frac{m_j v_j^2}{2kT}\right) d^3 v_j = n_j \phi\left(\vec{v}_j\right) d^3 n_j \tag{3.2}$$

[1] i.e. mainly electrons and neutrinos.

and analogue for dn_i. And subsequently we find

$$\begin{aligned} r_{i;j,o} &= n_i n_j \int \sigma_{i;j,o}\left(|v_i - v_j|\right) \phi\left(\vec{v}_i\right) \phi\left(\vec{v}_j\right) d^3 n_i d^3 n_j \\ &= n_i n_j \langle \sigma v \rangle_{i;j,o}. \end{aligned}$$

Changing to the centre of mass system and using the reduced mass $\mu = m_i m_j/(m_i + m_j)$, the relative coordinates and relative velocity v respectively, $\langle \sigma v \rangle_{i;j,o}$ becomes

$$\langle \sigma v \rangle_{i;j,o}(T) = \left(\frac{\mu}{2\pi kT}\right)^{3/2} \int \sigma_{i;j,o}(v) v \exp\left(-\frac{\mu v^2}{2kT}\right) d^3 v$$

or when using $d^3 v = 4\pi v^2 dv$ and the energy $E = \frac{1}{2}\mu v^2$ instead of the relative velocity v

$$\langle \sigma v \rangle_{i;j,o}(T) = \left(\frac{8}{\mu\pi}\right)^{1/2} \frac{1}{(kT)^{3/2}} \int_0^\infty \sigma_{i;j,o}(E) E \exp\left(-\frac{E}{kT}\right) dE \tag{3.3}$$

Thus if the involved particles obey the Maxwell-Boltzmann distribution, the *reactivity* can easily be evaluated knowing the cross section.

Not all reactivities for thermonuclear reactions have to be evaluated from Eq. 3.3. The total cross section $\sigma_{m;o,j}$ of reverse rate $m(o,j)i$ at energy E_{om} is given by the *detailed balance*, meaning it is related to $\sigma_{i;j,o}$ at energy $E_{ij} = E_{om} + Q_{o,j}$ of the forward reaction $i(j,o)m$, with a positive Q-value $Q_{o,j}$, by

$$\sigma_{i;j.o}\left(E_{ij}\right) = \frac{1+\delta_{ij}}{1+\delta_{om}} \frac{g_o g_m}{g_i g_j} \frac{k_o^2}{k_j^2} \sigma_{m;o,j}\left(E_{om}\right)$$

δ is the Kronecker-Delta, $k_j = \sqrt{2\mu_{ij} E_{ij}}/\hbar$ (k_o analogue), and $g_x = (2I_x + 1)$, with I_x being the particle spins. Applying this expression in Eq. 3.3, and the expression for the reactivities follows

$$\langle \sigma v \rangle_{i;j,o}(T) = \frac{1+\delta_{ij}}{1+\delta_{om}} \frac{g_o G_m}{G_i g_j} \left(\frac{\mu_{om}}{\mu_{ij}}\right)^{3/2} \exp\left(-\frac{Q_{o,j}}{kT}\right) \langle \sigma v \rangle_{m;o,j}(T). \tag{3.4}$$

g_m and g_i were also replaced by

$$G_x = \sum_n (2J_n + 1) exp(-E_n/kT) \tag{3.5}$$

to account for the possibility that excited states of the nuclei i and j are thermally populated. Therefore whenever the cross section and the reactivity of a reaction respectively is known, these quantities can easily be calculated for the reverse reactions.

3.2 Photodisintegration

When a high-energy photon is captured a nucleus is excited, this excited state decays under the emission of a p, n or α-particle, such a reaction $i(j,o)m$, in which j is a photon γ, is called photodisintegration reaction. The reaction rate can be evaluated from Eq. 3.1 as for

thermonuclear reactions. The nucleus i obeys again the Boltzmann distribution as given in Eq. 3.2, but the photons the Planck distribution,

$$dn_\gamma = \frac{1}{\pi^2(c\hbar)^3}\frac{E_\gamma^2 dE_\gamma}{\exp\left(E_\gamma/kT\right)-1}.$$

The integral over dn_i can easily be evaluated, because the relative velocity between the photons and the target i is constant and the photodisintegration cross section depends only on E_γ. Subsequently the following expression is found for the reaction rate, which is only linearly dependent on the number densities.

$$r_{i;\gamma,o} = \lambda_{i;\gamma,o}(T)n_i, \tag{3.6}$$

where

$$\lambda_{i;\gamma,o}(T) = \frac{1}{\pi^2 c^2\hbar^3}\int_0^\infty \sigma_{i;\gamma,o}(E_\gamma)\frac{E_\gamma^2}{\exp\left(E_\gamma/kT\right)-1}dE_\gamma$$

But usually the photodisintegration reaction rates are determined from the rate $m(o,\gamma)i$ by a similar expression as in Eq. 3.4,

$$\lambda_{i;\gamma,o}(T) = \frac{1}{1+\delta_{om}}\frac{g_o G_m}{G_i}\left(\frac{\mu_{om}kT}{2\pi\hbar^2}\right)^{3/2}\exp\left(-\frac{Q_{o,\gamma}}{kT}\right)\langle\sigma v\rangle_{m;o,\gamma}(T).$$

3.3 Decays

Beta- and alpha-decay rates of a nucleus i can be described by a similar form as Eq. 3.6,

$$r_i = \lambda_i n_i$$

$\lambda = \ln(2)/\tau_{1/2}$ is constant in case of normal decays and $\tau_{1/2}$ is the terrestrial half-life. But in stellar plasmas the thermal excitation of nuclear energy levels, which have different decay half-lives, modify the total decay rate and λ becomes temperature dependent, with

$$\lambda_i(T) = \frac{\sum_n \lambda_{n,i}(2J_n+1)\exp(-E_n/kT)}{G_i} \tag{3.7}$$

3.4 Electron, positron captures

The Fermi-energy of a degenerate non-relativistic electron gas is increasing with electron density n_e. As a consequence, the electron captures become possible, which were prohibited before because of negative Q-values. An electron capture of a nucleus i leads to the transformation of a proton to a neutron and the emission of an neutrino ν, meaning a reaction $i(e^-,\nu_e)m$. The "neutronisation" of the astrophysical plasma by electron captures is essential in the late phase of evolution of massive stars. With the knowledge that electrons are much lighter than nuclei Eq. 3.1 can be simplified showing

$$\begin{aligned} r_{i;e} &= n_i\int \sigma_{i;e}(v_e)v_e dn_e \\ &= \lambda_{i;e}(\rho Y_e, T)n_i \end{aligned}$$

The temperature determines whether dn_e has to be treated as Fermi distribution or can be approximated by a Maxwell-Boltzmann distribution. When the temperatures are high enough e^-e^+-pairs are produced and also positron captures occur. $i(e^+, \overline{\nu}_e)m$ reaction rates are evaluated in an analogous way.

3.5 Nuclear Reaction network

From the previous sections one can see that the number of reactions per unit volume and time has either the form

$$r_{i;j} = \frac{1}{1+\delta_{ij}} \langle \sigma v \rangle_{i;j} n_i n_j \tag{3.8}$$

for thermonuclear reactions or

$$r_i = \lambda_i n_i$$

for photodisintegration, decays, electron and positron captures. In the first equation the term $1/(1+\delta_{ij})$ is added to prevent double counting if particle i and j are identical. Number densities can change either due to reactions or density changes. The change of number densities of nuclei due to reaction $i(j,o)m$ are then given by

$$\left(\frac{\partial n_i}{\partial t}\right)_\rho = \left(\frac{\partial n_j}{\partial t}\right)_\rho = -r_{i;j}$$
$$\left(\frac{\partial n_m}{\partial t}\right)_\rho = \left(\frac{\partial n_o}{\partial t}\right)_\rho = +r_{i;j}$$

To avoid counting the change of number density due to density changes, the (number) abundance defined as

$$Y := \frac{n}{\rho N_A}$$

is used. The change of Y over time then becomes

$$\frac{\partial Y_i}{\partial t} = N^i_{j;k} r_{j;k}$$

In a more general form a nuclear specie i can interact with all other nuclear species present in the plasma and a variety of reactions can either produce or destroy nucleus i. Therefore to get the abundances at time $t + \Delta t$ the following system of ordinary differential equations has to be solved, when $Y_i(t)$ are known.

$$\begin{aligned} \dot{Y}_i &= \sum_j N^i_j \lambda_j Y_j + \sum_{j,k} N^i_{j,k} \rho N_A \langle \sigma v \rangle_{j;k} f_{j;k} Y_j Y_k \\ &\quad + \sum_{j,k,l} N^i_{j,k,l} \rho^2 N_A^2 \langle \sigma v \rangle_{j;k;l} f_{j;k;l} Y_j Y_k Y_l, \end{aligned} \tag{3.9}$$

with

$$\begin{aligned} N^i_j &= N_i \\ N^i_{j,k} &= \frac{N_i}{1+\delta_{jk}} \\ N^i_{j,k,l} &= \frac{N_i}{1+\Delta_{ijk}} \\ \Delta_{ijk} &= \delta_{jk} + \delta_{jl} + \delta_{kl} + 2\delta_{jkl} \end{aligned}$$

and the N_i are the numbers of particles i destroyed or produced in a particular reaction, they are negative in case of destruction and positive in case of formation of the particular isotope i (Fowler et al. 1967). The denominator contains statistical factors preventing double counting. The first term on the right hand side of Eq. 3.9 describes photo-disintegrations, β-decays and ν-, e^-- and e^+-capture reactions, whereas the second and third term contains the thermonuclear two and three-body reactions respectively. As seen before, λ_j depends on density and temperature in case of ν-, e^-- and e^+-captures, but only on the temperature in case of decays and photo-disintegration. $f_{j;k}$ and $f_{j;k;l}$ are so called screening factors accounting for the electron screening of the positively charged nuclei against the Coulomb repulsion, meaning that they have values of ≥ 1. For more details about electron screening see Section 3.7.2. Equation 3.9 describes therefore the change of mass fractions $\dot{X}_i = A_i\dot{Y}_i$ due to nuclear reactions (the second term on the right-hand side of Eq. 2.10 in Section 2.2.2).

In BasNet the set of stiff differential equations 3.9 are solved in a implicit manner by the backward Euler method. Therein the set of coupled ordinary differential equations,

$$\frac{dY_i}{dt} = f_i(t, Y_1, \ldots, Y_n),$$

with $i = 1, \ldots, n$, is solved to evaluate the abundances $Y_i(t+\Delta t)$ at time $t+\Delta t$ starting from the initial values $Y_i(t)$ at time t, by calculating the new abundances $Y_i(t+\Delta t)$ from

$$Y_i(t+\Delta t) = Y_i(t) + h f_i(t+\Delta t, Y_1(t+\Delta t), \ldots, Y_n(t+\Delta t)). \tag{3.10}$$

In both equations above the functions f_i are the right hand sides of equations 3.9. Equations 3.10 can also be written in a vector notation

$$\boldsymbol{Y}(t+\Delta t) = \boldsymbol{Y}(t) + \Delta t \boldsymbol{f}\left(t+\Delta t, \boldsymbol{Y}(t+\Delta t)\right),$$

where $\boldsymbol{Y} = (Y_1, \ldots, Y_n)$ and $\boldsymbol{f} = (f_1, \ldots, f_n)$. Solving this problem is then equivalent to finding the root of

$$\frac{\boldsymbol{Y}(t+\Delta t) - \boldsymbol{Y}(t)}{\Delta t} - \boldsymbol{f}(t+\Delta t, \boldsymbol{Y}(t+\Delta t)) = 0.$$

The root finding is done in BasNet in an iterative way by the Newton-Raphson method. Which means a repetitive evaluation of

$$\boldsymbol{Y}_{n+1}(t+\Delta t) = \boldsymbol{Y}_n(t+\Delta t) - \left(\frac{\boldsymbol{Y}_n(t+\Delta t) - \boldsymbol{Y}(t)}{\Delta t} - \boldsymbol{Y}_n(t+\Delta t)\right) \cdot \boldsymbol{J}^{-1} \tag{3.11}$$

until a certain convergence criterion is reached. The subscript n refers to the n-th iteration. $\boldsymbol{J}$ is the Jacobian

$$\boldsymbol{J} \equiv \frac{1}{\Delta t} - \frac{\partial \dot{\boldsymbol{Y}}(t+\Delta t)}{\partial \boldsymbol{Y}(t+\Delta t)} = \frac{1}{\Delta t} - \frac{\partial \boldsymbol{f}(t+\Delta t)}{\partial \boldsymbol{Y}(t+\Delta t)}.$$

Hence the matrix $\boldsymbol{J}$ has to be inverted to calculate the new abundances, which is computationally the most expensive part of this method. As initial guess the abundance at the time t is taken, i.e. $\boldsymbol{Y}_0(t+\Delta t) = \boldsymbol{Y}(t)$. In this case the first term in brackets on the right hand side of Eq. 3.11 cancels. Then Jacobian is still calculated with $\rho(t+\Delta t)$ and $T(t+\Delta t)$, but $\boldsymbol{Y}(t)$, which makes the method *semi-implicit* for $n = 0$. However, with sufficiently small time steps the convergence is usually reached even in this very first iteration step ($n = 0$).

$S = \sum_{i=1}^{n} X_i = 1$ by definition, but this cannot be strictly fulfilled, because of round-off and numerical error. As a convergence criterion, the method requires that the mass conservation has to obey $\varepsilon = |S(t+\Delta t) - S(t)| \leq 10^{-7}$. Usually, when the time step is small enough this is fulfilled after the first iteration step ($n = 0$) and far better than the criterion used. The time steps are first given by the stellar evolution time step $\Delta t_{\rm ss}$ from solving the stellar structure. The time scale on which the nuclear abundances change is

$$\Delta t_{{\rm nuc},i} = \left| \frac{Y_i}{\dot{Y}_i} \right|$$

It is therefore defined by the biggest relative change of nuclear abundance Y_i. Finally, the applied time step Δt is

$$\Delta t = \min \left[\Delta t_{\rm ss}, \alpha \Delta t_{{\rm nuc},i} \right]$$

with the parameter $\alpha = 0.1$ and $\Delta t_{{\rm nuc},i}$ is only checked for $Y_i \geq 10^{-7}$. For the first sub-time step of the network, $\alpha = 0.1$. The network is typically doing 1 to 5 sub-time steps, but in most cases only a single sub-time step is needed.

A more detailed description of the methods to solve a nuclear reaction network set of differential equations is given in Hix & Thielemann (1999) and in the Ph.D. thesis of C. Winteler (2011).

3.6 Nuclear input data

3.6.1 Reaclib format

REACLIB is a reaction library containing the reactions not in tabular but in analytical form, which is used by BasNet. It allows the fast computation of large nuclear reaction networks, and additionaly an easy calculation the reaction rate derivatives with respect to T and ρ.

The REACLIB-format is an analytical function where seven parameters determine the reaction rate and the reactivity respectively,

$$\langle \sigma v \rangle_{i;j,o} N_A = e^{[a_0 + a_1 T_9^{-1} + a_2 T_9^{-1/3} + a_3 T_9^{1/3} + a_4 T_9 + a_5 T_9^{5/3} + a_6 log(T_9)]}. \tag{3.12}$$

In most cases a single seven parameter fit cannot describe a real reaction rates accurately. Nevertheless features due to resonances can be described by additional functions of the same form. Thus the total reaction rate is defined by n sets of these seven parameters $a_0,\ldots,a_6$, i.e.

$$\langle \sigma v \rangle_{i;j,o} N_A = \sum_{k=1}^{n} e^{[a_0(k) + a_1(k) T_9^{-1} + a_2(k) T_9^{-1/3} + a_3(k) T_9^{1/3} + a_4(k) T_9 + a_5(k) T_9^{5/3} + a_6(k) log(T_9)]} \tag{3.13}$$

Equation (3.12) and (3.13) are only valid for two-body reactions. For three-body reactions the left side of this equation is equal to $\langle \sigma v \rangle_{i,j,k} N_A^2$ and in case of decays or photodisintegration it is equal to λ_β and λ_γ respectively. This REACLIB format however only works for rates where the ρ-dependency only originate from the number density $n = \rho N_A Y$. For rates where the reactivity is density dependent as for example for e^--captures this format does not work any more. Such rates are treated differently in BasNet.

3.6.2 Calculation of reverse rates

As seen in sections 3.1 and 3.2 reverse reaction rates can be calculated from the forward rate by detailed balance. As a consequence the REACLIB parameters of the reverse rates can be calculated from the seven parameter fit of the forward rates.

2-body reactions and photodisintegration

For a reaction of the form $i(j,o)m$ it is thus possible to calculate the reverse rate $m(o,j)i$ (Rauscher & Thielemann 2000) from detailed balance, by

$$\langle \sigma v \rangle_{m;o,j} = C_1 \frac{\tilde{G}_i(T)}{\tilde{G}_m(T)} e^{-Q/kT} \langle \sigma v \rangle_{i;j,o} \tag{3.14}$$

where

$$C_1 = \left(\frac{A_i A_j}{A_o A_m} \right)^{3/2} \frac{(2J_i+1)(2J_j+1)}{(2J_o+1)(2J_m+1)} \tag{3.15}$$

and $\tilde{G}_x(T) = G_x(T)/(2J_x+1)$ is the temperature-dependent partition function normalised to the ground state, A the atomic mass number, J the ground state spin and Q the Q-value. For photodisintegrations this looks quite similar.

$$\lambda_\gamma = C_2 T^{3/2} e^{-Q/kT} \frac{\tilde{G}_i(T)}{\tilde{G}_m(T)} \langle \sigma v \rangle_{i;j,\gamma} \tag{3.16}$$

where

$$C_2 = \left(\frac{A_i A_j}{A_m} \right)^{3/2} C \frac{(2J_i+1)(2J_j+1)}{(2J_m+1)} \tag{3.17}$$

and $C = 9.8685 \times 10^9$ mol cm^{-3}. The ratio of the partition functions is multiplied in the network code itself. Thus it is easy to calculate the REACLIB coefficients for the reverse reaction rates. In case of photodisintegration the coefficients a_0, a_1 and a_6 change in the following way.

$$\begin{aligned} a_0^{rev} &= a_0 + log(C_2) \\ a_1^{rev} &= a_1 - 11.6045Q \\ a_6^{rev} &= a_6 + 1.5 \end{aligned}$$

All other coefficients stay the same as in the forward rate. The factor 11.6045 (units: [10^9 K/MeV]) comes from the relations $T = 10^9 \times T_9$ and $1/k_B$, with $k_B = 8.617343 \times 10^{-11}$ MeV/K the Boltzmann constant (source: CODATA). In case of all the other two particle reactions only the parameters a_0 and a_1 has to be changed to

$$\begin{aligned} a_0^{rev} &= a_0 + log(C1) \\ a_1^{rev} &= a_1 - 11.6045Q \end{aligned}$$

Thus most of the work is done when the coefficients of the forward rate are calculated.

3-body reactions

For the reverse rates of 3-body reactions the calculation of the coefficients is similar. We assume a 3-body exoergic reaction of the form

$$N_i(A_i, Z_i) + N_j(A_j, Z_j) \rightarrow N_o(A_o, Z_o) + N_m(A_m, Z_m) \quad (N_i + N_j = 3, N_i \geq 2) \tag{3.18}$$

with N_x the number of particles of specie x involved in the reaction. According to Wagoner (1969) the connection to its reverse (endoergic) reaction is

$$[rate]_{m;o} = C^N \left(\frac{N_o! N_m!}{N_i! N_j!}\right) \left(\frac{(2J_i+1)^{N_i}(2J_j+1)^{N_j}}{(2J_o+1)^{N_o}(2J_m+1)^{N_m}}\right) \left(\frac{\tilde{G}_i^{N_i}}{\tilde{G}_m^{N_m}}\right) \left(\frac{A_i^{N_i} A_j^{N_j}}{A_o^{N_o} A_m^{N_m}}\right)^{\frac{3}{2}} \times \rho^{-N} T_9^{\frac{3N}{2}} exp\left(-11.6045 \frac{Q}{T_9}\right) [rate]_{i;j} \tag{3.19}$$

where $N = N_i + N_j - N_o - N_m$. The $G_i(T)$ are again applied in the program. Therefore only the spins of the ground states are involved when the reverse rate is evaluated. $[rate]_{i;j}$ is defined in the following way

1. For photodisintegrations, i.e. reactions between photons γ and a nucleus i $[rate]_{i;\gamma} = \lambda_{i,\gamma}$.

2. For two particle reactions $[rate]_{i;j} = \rho N_A \langle \sigma v \rangle_{i;j}$

3. And for 3-body reactions between a particle of specie i and two particles of specie j $[rate]_{i;j} = \rho^2 N_A^2 \langle \sigma v \rangle_{i;j}$

Example: reverse rate of 3α-reaction With these formulae it is now simple to calculate for example the reverse rate of 3α-reaction, which is the photodisintegration of ^{12}C to three α-particles. So $N_i = 3$, $N_j = 0$, $N_m = 1$, $N_o = 0$, $N = 2$ and the ground state spins $J_\alpha = J_{^{12}C} = 0$ which implies then that the photodisintegration-rate is

$$\lambda_\gamma(^{12}\mathrm{C}) = e^{[a_{0,rev} + a_{1,rev} T_9^{-1} + a_{2,rev} T_9^{-1/3} + a_{3,rev} T_9^{1/3} + a_{4,rev} T_9 + a_{5,rev} T_9^{5/3} + a_{6,rev} log(T_9)]}$$

with

$$\begin{aligned} a_{0,rev} &= a_0(3\alpha) + log\left(C^2 \frac{1}{6} \left(\frac{4^3}{12}\right)^{\frac{3}{2}}\right) \\ a_{1,rev} &= a_1(3\alpha) - 11.6045 Q(3\alpha) \\ a_{6,rev} &= a_6(3\alpha) + 3 \\ a_{n,rev} &= a_n(3\alpha), n = 2, 3, 4, 5 \end{aligned}$$

In case there are more than one contributions one has to calculate the coefficients for all contributions in this way.

3.6.3 Reaction rates

The basic set of reaction rates was taken from the REACLIB of Rauscher & Thielemann (2000), which can be found on nucastro.org. Also the normalised partition functions and the nuclear data were obtained from the same source. REACLIB was updated with the rates for charged particle reactions from NACRE (Angulo et al. 1999).

The reaction determining the efficiency of the CNO cycle, $^{14}\mathrm{N}(p,\gamma)^{15}\mathrm{O}$, was updated to the rate of Imbriani et al. (2005). Essential for the energy generation in He burning are the 3α and $^{12}\mathrm{C}(\alpha,\gamma)^{16}\mathrm{O}$ reactions and their rates were adopted from Fynbo et al. (2005) and Kunz et al. (2002), respectively. The rates for the different channels of $^{12}\mathrm{C}+^{12}\mathrm{C}$ and $^{16}\mathrm{O}+^{16}\mathrm{O}$ are taken from Caughlan & Fowler (1988), and the photodisintegration rates initiating the Ne burning are the reverse reaction rates from NACRE rates.

For the s process, important rates are those which affect the neutron economy, i.e neutron sources, the seeds and the neutron poisons. In Table 3.1, the most important reactions with their rate source are listed. The rate for the main neutron source in massive stars in He and in C burning, $^{22}\mathrm{Ne}(\alpha,n)^{25}\mathrm{Mg}$, was updated by Jaeger et al. (2001). In Fig. 3.1 the ratio of upper and lower limits normalised to the NACRE rate are shown from three different publications. The lower limit is for all three rates the same, and does not include the contributions of a 635 keV resonance. The uncertainty of a 635 keV resonance to this reaction rate was reduced in the past years, which allowed to reduce the upper limits strongly. As seen in Fig. 3.1 the upper limit of the rate determined by Jaeger et al. (2001), is even below the adopted NACRE rate in the temperature region above $T_9 = 0.3$, which is relevant for the s process. The recommended rate of Jaeger et al. (2001) is about a factor 1.5 lower than the adopted NACRE rate at in the s-process relevant temperature range. We used therefore the rate of Jaeger et al. (2001) instead of the one from the NACRE compilation. The $^{22}\mathrm{Ne}(\alpha,\gamma)^{26}\mathrm{Mg}$ is the competing reaction for ^{22}Ne nuclei to the s-process neutron source, and was taken from NACRE as other neutron sources, mainly involved in neutron recycling.

Neutron capture reactions are essential ingredients for the s-process network. Depending on their rate they can define bottle necks along the s-process path or being weak or strong neutron poisons. The (n,γ)-rates from the compilation of Bao et al. (2000) are used with recent updates listed in Karlsruhe Astrophysical Database of Nucleosynthesis in Stars (KADoNiS, Dillmann et al. 2006) version 0.3. Fig. 3.2 illustrates the differences of KADoNiS v0.3 to Bao et al. (2000) compilation. It shows that the neutron capture rates important for the *weak* s process were downward corrected by the expweriments in the past years. The neutron captures on unstable nuclei for which no experimental data was available, were taken from Rauscher & Thielemann (2000).

The β-decays and (n,γ)-rates are important in s process. The missing experimental β-decays in the Rauscher & Thielemann (2000)-REACLIB of nuclei from palladium (Pd) on towards higher proton number were added from Nuclear Wallet Cards 7th Ed, if there was only the information about λ_β of the ground state. As mentioned in Section 3.3, decay reaction rates can vary with temperature due to thermal excitation. It is essential to know the temperature dependence of a decays to predict the branching ratios. If available we took the data from NETGEN website (Aikawa et al. 2005), which correspond to the temperature dependent decay rates of Takahashi & Yokoi (1987) or Goriely (1999). Otherwise if there was λ_n available in the NNDC database for the low-lying excited states the decay rates were calculated according to Eq. 3.7.

The REACLIB parameters for 3α, $^{12}\mathrm{C}(\alpha,\gamma)^{16}\mathrm{O}$, $^{14}\mathrm{N}(p,\gamma)^{15}\mathrm{O}$, and the constant β-decays

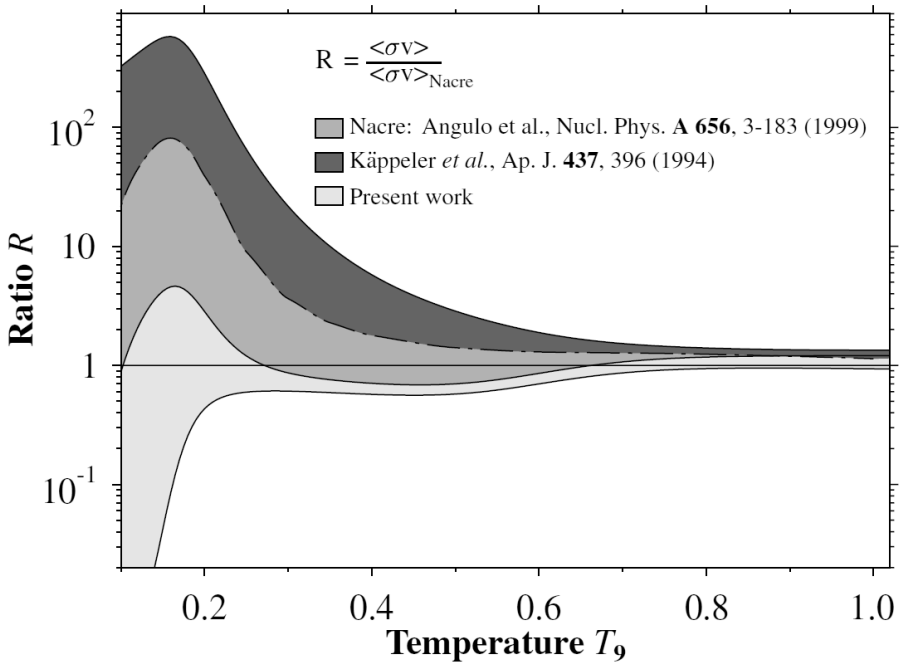

Figure 3.1: Uncertainty bands (shaded areas) of ^{22}Ne$(\alpha, n)^{25}$Mg reaction from different sources. The rates are normalised to the NACRE rate. Figure from Jaeger et al. (2001).

rates beyond Pd were obtained from the JINA database. The 7-parameter fits for the updated n-captures from KADoNiS v0.3, temperature-dependent β-decays, and the charged particle reaction rates from NACRE were fitted with our own fitting tool, for which a "How to" can be found in Appendix C. The total Q-values in our REACLIB were replaced by $Q_{\rm eff}$ without the neutrino energy to gain the relevant nuclear energy for the star (see Section 2.3). $Q_{\rm eff}$ values were also obtained from the NETGEN database, and concerned mainly β-decays.

3.6.4 Size of reaction network

How many nuclear species have to be included in the reaction network for modelling the s process properly? To answer this question we followed with BasNet a single zone trajectory with He-core and C-shell conditions, with different network sizes. The default network contained 2303 nuclei. The trajectory was derived from a 25 $M_{\odot}$ model of Hirschi et al. (2005). For He burning the conditions of a mass shell inside the convective core was chosen in a way to reproduce the amount of burned ^{22}Ne. For the C burning the conditions corresponding to the bottom of the shell C burning were adopted.

When comparing the final abundances using the default network and a smaller network, I found that the networks listed in Table 3.6.4 well reproduce ($\Delta Y_i/Y_{i,\rm def} < 0.01$) the result of the default network. The network for the s process in He burning contains 613 nuclei and the one for shell C burning 737 nuclear species. Concerning the different network sizes, the larger network in shell C burning is necessary, because the neutron densities reached during this stage are about 10^5-times higher than in He burning, allowing the s-process path to reach nuclei further away from the stability on the neutron rich side. The He-burning network is also similar in size to the one used by The et al. (2000).

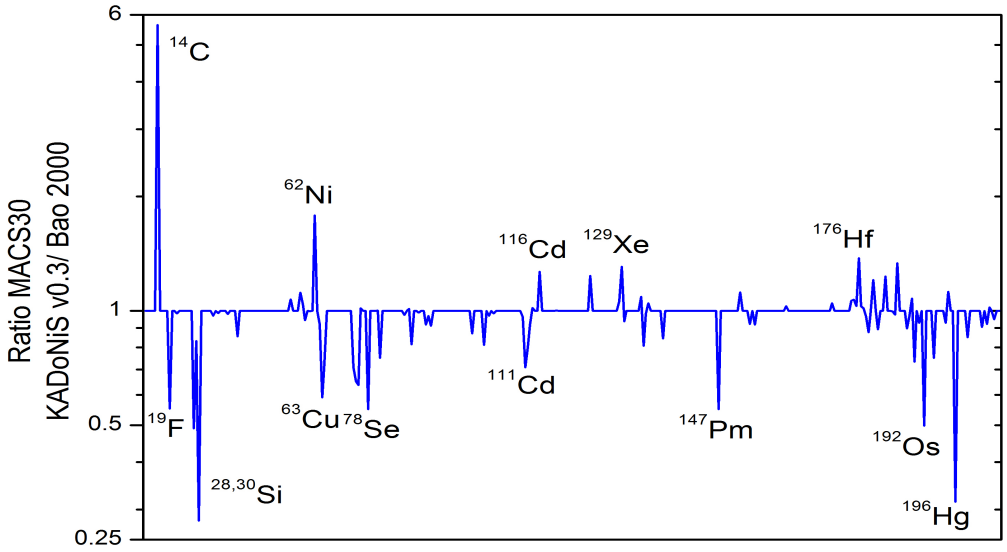

Figure 3.2: Ratios of Maxwellian averaged neutron capture cross sections at 30 keV of KADoNiS v0.3 to Bao et al. (2000). Figure by courtesy of Iris Dillmann

Table 3.1: Important reaction rates for the s process

Nuclear reaction	Rate source
^{22}Ne$(\alpha,n)^{25}$Mg	Jaeger et al. (2001)
^{22}Ne$(\alpha,\gamma)^{26}$Mg	NACRE
^{14}N$(\alpha,\gamma)^{18}$F	NACRE
^{18}O$(\alpha,\gamma)^{22}$Ne	NACRE
^{17}O$(\alpha,n)^{20}$Ne	NACRE
^{17}O$(\alpha,\gamma)^{21}$Ne	Caughlan & Fowler (1988)
^{13}C$(\alpha,n)^{16}$O	NACRE
^{12}C$(\alpha,\gamma)^{16}$O	Kunz et al. (2002)
^{4}He$(2\alpha,\gamma)$	Fynbo et al. (2005)
(n,γ) - experimental	KADoNiS v0.2/v0.3
(n,γ) - theoretical	Rauscher & Thielemann (2000)
β^- - constant	bet-/Nuclear Wallet Cards 7th Ed.
β^- - T-dependent	Takahashi & Yokoi (1987)/Goriely (1999)

Table 3.2: Nuclei included in the s-process network.

	Z	A_{min}	A^a_{max}	A^b_{max}		Z	A_{min}	A^a_{max}	A^b_{max}		Z	A_{min}	A^a_{max}	A^b_{max}
n	0	1	1	1	Cu	29	56	66	68	Ce	58	136	144	145
H	1	1	2	2	Zn	30	59	71	72	Pr	59	141	144	147
He	2	3	4	4	Ga	31	69	72	75	Nd	60	142	151	152
Li	3	7	7	7	Ge	32	70	77	79	Pm	61	144	151	153
Be	4	7	7	7	As	33	75	77	80	Sm	62	144	155	157
B	5	8	11	11	Se	34	74	83	84	Eu	63	151	157	159
C	6	11	15	15	Br	35	79	83	85	Gd	64	152	161	162
N	7	13	16	16	Kr	36	78	87	89	Tb	65	156	162	163
O	8	15	19	19	Rb	37	85	88	90	Dy	66	156	165	168
F	9	17	20	20	Sr	38	84	91	93	Ho	67	162	166	169
Ne	10	20	23	24	Y	39	89	91	95	Er	68	162	171	173
Na	11	21	24	25	Zr	40	90	97	98	Tm	69	168	172	175
Mg	12	23	27	28	Nb	41	93	97	98	Yb	70	168	177	178
Al	13	25	28	29	Mo	42	92	101	102	Lu	71	174	180	180
Si	14	26	31	33	Tc	43	97	101	102	Hf	72	174	183	184
P	15	27	34	34	Ru	44	96	105	108	Ta	73	179	184	186
S	16	30	37	38	Rh	45	103	105	108	W	74	180	188	190
Cl	17	33	38	39	Pd	46	102	111	113	Re	75	184	189	191
Ar	18	34	41	43	Ag	47	107	111	115	Os	76	184	195	196
K	19	37	42	45	Cd	48	106	117	119	Ir	77	190	195	197
Ca	20	38	49	49	In	49	113	117	119	Pt	78	190	199	200
Sc	21	40	49	50	Sn	50	112	127	127	Au	79	195	200	201
Ti	22	42	51	52	Sb	51	121	127	130	Hg	80	196	205	205
V	23	44	52	53	Te	52	120	131	132	Tl	81	203	206	206
Cr	24	46	55	56	I	53	125	131	135	Pb	82	204	209	210
Mn	25	48	56	57	Xe	54	124	137	137	Bi	83	209	210	212
Fe	26	50	61	62	Cs	55	131	137	139	Po	84	210	210	212
Co	27	52	61	63	Ba	56	130	139	141					
Ni	28	54	65	67	La	57	137	141	143					

Notes. $^{(a)}$ Network up to the end of central He burning. $^{(b)}$ Enlarged network after central He burning.

3.7 Details of BasNet implementation into GenEC

The major results of this work was obtained with GenEC (see Chapter 2) including the network code BasNet. Merging the two codes GenEC and BasNet was one of the major parts of this work. In the following sections the modifications are discussed.

In Fig. 3.3 the flow chart of GenEC is shown with the modified parts marked in red. Essentially two parts had to be modified. On the one hand the nuclear reaction network was replaced by BasNet, and on the other hand a routine was written, calculating the released nuclear energy ϵ (discussed in Section 2.3) and its derivatives with respect to T and P, which is discussed in Section 3.7.1. In BasNet abundances Y_i are used but in GenEC mass fractions X_i, so for the information exchange between network and stellar evolution code only the relation $X_i = A_i Y_i$ has to be known.

3.7.1 Energy derivatives

The energy derivatives $\partial\epsilon/\partial\rho$ and $\partial\epsilon/\partial T$ are needed for solving the stellar structure equations (see e.g.. Henyey et al. 1964), and have thus to be calculated for a specific model[2] for every mass shell. Since the nuclear energy production is defined by Eq. 2.17 and the reaction rates therein depend on temperature T and density ρ, the new network implementation has to deliver besides the nuclear energy ϵ, its derivatives with respect to T and pressure P. In GenEC P is used instead of the density ρ as unknown variable, thus $\rho = \rho(P, T, ...)$ is given by the equation of state. The logarithmic form of the unknown variables is used in GenEC, to avoid them crossing several orders of magnitude (Kippenhahn et al. 1967). The derivatives which have to be also calculated in the energy routine are therefore

$$\begin{aligned} \frac{\partial \ln(\epsilon)}{\partial \ln(T)} &= \frac{T}{\epsilon}\frac{\partial \epsilon}{\partial T} = \frac{T}{\epsilon}\sum_i \frac{\partial \epsilon_i}{\partial T} \\ \frac{\partial \ln(\epsilon)}{\partial \ln(P)} &= \frac{P}{\epsilon}\frac{\partial \epsilon}{\partial P} = \frac{P}{\epsilon}\sum_i \frac{\partial \epsilon_i}{\partial P} \end{aligned}$$

where the sum runs over all reactions, i.e. i is the reaction index. For the reactions with one particle in the incoming channel, as e^--capture, decays and photodisintegration reactions, the rate is given by Eq. 2.14 and the contribution to these derivatives are simply given by

$$\begin{aligned} T\frac{\partial \epsilon_i}{\partial T} &= N_A Y_{k_i} Q_i T \left(\frac{\partial \lambda_i}{\partial T} + \frac{\partial \lambda_i}{\partial \rho}\left(\frac{\partial \rho}{\partial T}\right)_{P,\boldsymbol{Y}} \right) \\ P\frac{\partial \epsilon_i}{\partial P} &= N_A Y_{k_i} Q_i P \frac{\partial \lambda_i}{\partial \rho}\left(\frac{\partial \rho}{\partial P}\right)_{T,\boldsymbol{Y}} \end{aligned}$$

When we use the REACLIB format as defined in Eq. 3.12, λ_i is a function defined by the seven fit parameters. λ_i is independent of ρ for decays and photodisintegration, the derivatives with respect to P and ρ, respectively, vanish naturally. Its derivative with respect to the temperature is then easily calculated,

$$T\frac{\partial \lambda_i}{\partial T} = \lambda_i T \frac{\partial \ln(\lambda_i)}{\partial T} = \lambda_i \left(-a_0 T^{-1} - \frac{a_1}{3}T^{-1/3} + \frac{a_2}{3}T^{1/3} + a_3 T + \frac{5a_4}{3}T^{+5/3} + a_6 \right) \quad (3.20)$$

[2] Time t is constant.

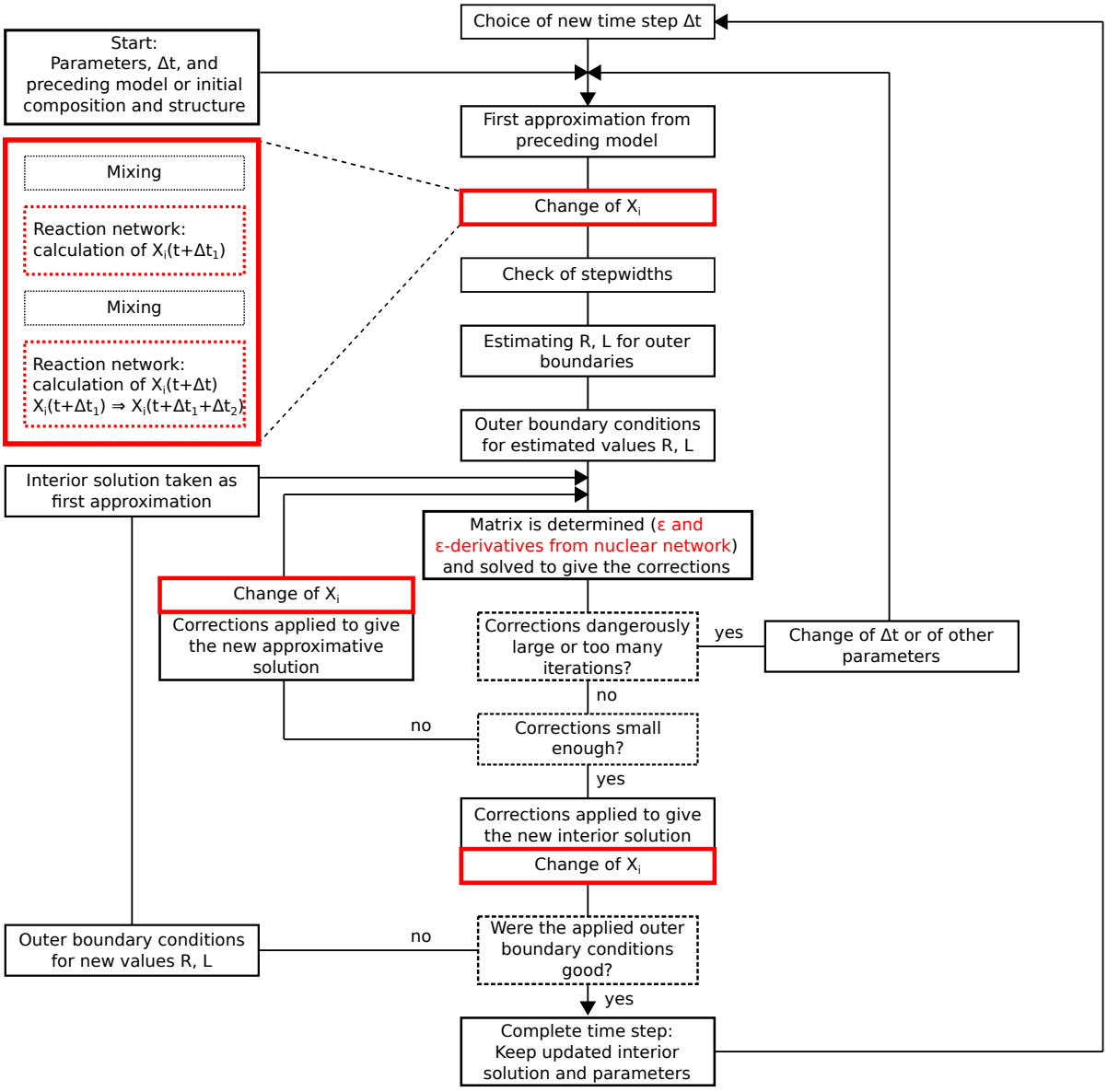

Figure 3.3: Flow chart of GenEC adopted from Kippenhahn et al. (1967). The red marked areas were modified in this work.

If we define

$$\Lambda_i(T) := \left(-a_0 T^{-1} - \frac{a_1}{3} T^{-1/3} + \frac{a_2}{3} T^{1/3} + a_3 T + \frac{5a_4}{3} T^{+5/3} + a_6\right),$$

and use Eq. 3.20, the energy derivative with respect to temperature for a single fit of (ρ-independent) "one-body" reactions becomes simply

$$T\frac{\partial \epsilon_i}{\partial T} = N_A Y_{k_i} Q_i T \left(\frac{\partial \lambda_i}{\partial T}\right) = \epsilon_i \Lambda_i(T)$$

The derivatives for two and three-body reactions can be obtained in the same way. But for reactions with two particles in the incoming channel $\lambda_i Y_i$ is replaced by $N_A \rho \langle \sigma v \rangle f Y_k Y_l$ and for three particles with $N_A^2 \rho^2 \langle \sigma v \rangle f_1 f_2 Y_k Y_l Y_m$. The density dependence adds additional terms, as well as the temperature and density dependent screening factor $f_i(\rho, T) = \exp\left(h_i(\rho, T)\right)$ in case of charged particle reactions (see Section 3.7.2). If Eq. 2.15 is used, the derivatives for two-body reactions are

$$T\frac{d\epsilon_i}{dT} = \epsilon_i \left[\Lambda_i(T) + \left(1 + \rho\frac{\partial h_i}{\partial \rho}\right)\left(\frac{\partial \ln \rho}{\partial \ln T}\right)_{P,\boldsymbol{Y}} + T\frac{\partial h_i}{\partial T}\right]$$
$$P\frac{d\epsilon_i}{dP} = \epsilon_i \left[1 + \rho\frac{\partial h_i}{\partial \rho}\right]\left(\frac{\partial \ln \rho}{\partial \ln P}\right)_{T,\boldsymbol{Y}}$$

and for three-body reactions from Eq. 2.16 follows

$$T\frac{d\epsilon_i}{dT} = \epsilon_i \left[\Lambda_i(T) + \left(2 + \rho\left(\frac{\partial h_{1,i}}{\partial \rho} + \frac{\partial h_{2,i}}{\partial \rho}\right)\right)\left(\frac{\partial \ln \rho}{\partial \ln T}\right)_{P,\boldsymbol{Y}} + T\left(\frac{\partial h_{1,i}}{\partial T} + \frac{\partial h_{2,i}}{\partial T}\right)\right]$$
$$P\frac{d\epsilon_i}{dP} = \epsilon_i \left[2 + \rho\left(\frac{\partial h_{1,i}}{\partial \rho} + \frac{\partial h_{2,i}}{\partial \rho}\right)\right]\left(\frac{\partial \ln \rho}{\partial \ln P}\right)_{T,\boldsymbol{Y}}$$

The derivatives of ρ with respect to T and P, are the partial derivatives keeping the other quantities constant, and are given by the equation of state. The derivatives of h_i are calculated by the screening routine. For three-body reactions $h_{1,i}$ describes the electron screening between nuclei (A_1, Z_1) and (A_2, Z_2) and $h_{2,i}$ the screening between $(A_1 + A_2, Z_1 + Z_2)$ and (A_3, Z_3).

3.7.2 Screening

In the dense plasmas of stars, nuclei are surrounded by a gas of free electrons. This lead on the one hand to a modification of Coulomb repulsion between the positively charged nuclei, i.e. the Coulomb barrier is reduced by the electron gas. On the other hand it changes the Q-value of reactions and would therefore not only modify the charged particle reactions, but also photodisintegration reactions. The electron screening leads to a modification of thermonuclear charged particle reactions, which is described by the screening factor f, and the true rate in an astrophysical plasma is given by

$$\langle \sigma v \rangle_{i;j,screen} = \langle \sigma v \rangle_{i;j} f \tag{3.21}$$

with

$$f = exp(h) \tag{3.22}$$

and h the so-called "screening function", which depends on the density ρ, temperature T, composition Y and of course the nuclear charges Z_i and Z_j. However, Mochkovitch & Nomoto (1986) show that the effect on photodisintegration reactions can be neglected. We therefore apply such a correction in the network only on the charged particle reactions.

The "weak" screening regime is defined by a small Coulomb interaction energy between the target nucleus i and the nearest electrons compared to the thermal energy kT (Salpeter 1954). In this case the effect of the electrons can be approximated as a weak correction to the Coulomb potential between the reacting nuclei. In cgs-units the screening function is then (see e.g. Salpeter 1954; Graboske et al. 1973)

$$h = \frac{V_0}{kT} = 0.188 \cdot Z_i Z_j \frac{(\zeta\rho)^{1/2}}{T_6^{3/2}}. \tag{3.23}$$

Z_i and Z_j are the charge numbers of the colliding nuclei, T_6 the temperature in units of 10^6 Kelvin and

$$\zeta = \sum_i Y_i Z_i (Z_i + 1). \tag{3.24}$$

Equation 3.23 is the so-called Debye-Hückel form of the screening function.

In the "strong" screening regime on the other hand defined the Coulomb interaction energy between the target i and the nearest electrons compared to the thermal energy kT is small (Salpeter 1954). In the most extreme case called "pycno-nuclear" screening the Coulomb barrier for charged particle reactions is negligible. However this regime appears only for a very dense but cool environment ($\rho \geq 10^6$ g cm^{-3} and $T \leq 10^7$ K). The "intermediate" regime is the most important one for astrophysical application, but was addressed by only a few authors in the past (e.g. Graboske et al. 1973).

The energy derivatives with respect to temperature and density (see Section 2.3) are needed for solving the stellar structure equations. It means that the first derivatives of the screening factor are necessary, making an analytical screening function for all regimes desirable. I therefore applied the analytical screening function of Chugunov et al. (2007) (Eq. 20 therein),

$$h(\tilde{\Gamma}) = \tilde{\Gamma}^{3/2} \left(\frac{A_1}{\sqrt{A_2 + \tilde{\Gamma}}} + \frac{A_3}{1 + \tilde{\Gamma}} \right) + \frac{B_1 \tilde{\Gamma}^2}{B_2 + \tilde{\Gamma}} + \frac{B_3 \tilde{\Gamma}^2}{B_4 + \tilde{\Gamma}^2} \tag{3.25}$$

which was fitted to their results of the screening function, calculated by assuming WKB Coulomb barrier penetration through radial mean-field potential for "strong" screening regime. The A's and B's are fitting constants, $\tilde{\Gamma} = \tilde{\Gamma}(\zeta, \Gamma)$ is defined in Eq. 21, the screening parameter Γ in Eq. 1 and ζ in Eq. 3 of Chugunov et al. (2007). Importantly for our application, this fit also reproduces the assymptotic behaviour of the Debye-Hückel form of the screening function in case of "weak" screening, which leaves the "intermediate" screening as not verified region for this fit.

In Fig. 3.4 the screening factor given by the fit of Chugunov et al. (2007)(see Eq. 3.25) is plotted. It shows $f_c = \exp(h)$ for the ^{12}C+^{12}C collisions in a carbon-rich plasma. The yellow line divides the weak from the intermediate screening regime ($\Gamma = 0.1$) and the red line the intermediate from the strong regime ($\Gamma = 1$). In the weak screening regime the factor is very close to 1. In the intermediate regime it increases to $f \approx 3$, while in the strong regime it reaches very large values ($f \approx 10^3$).

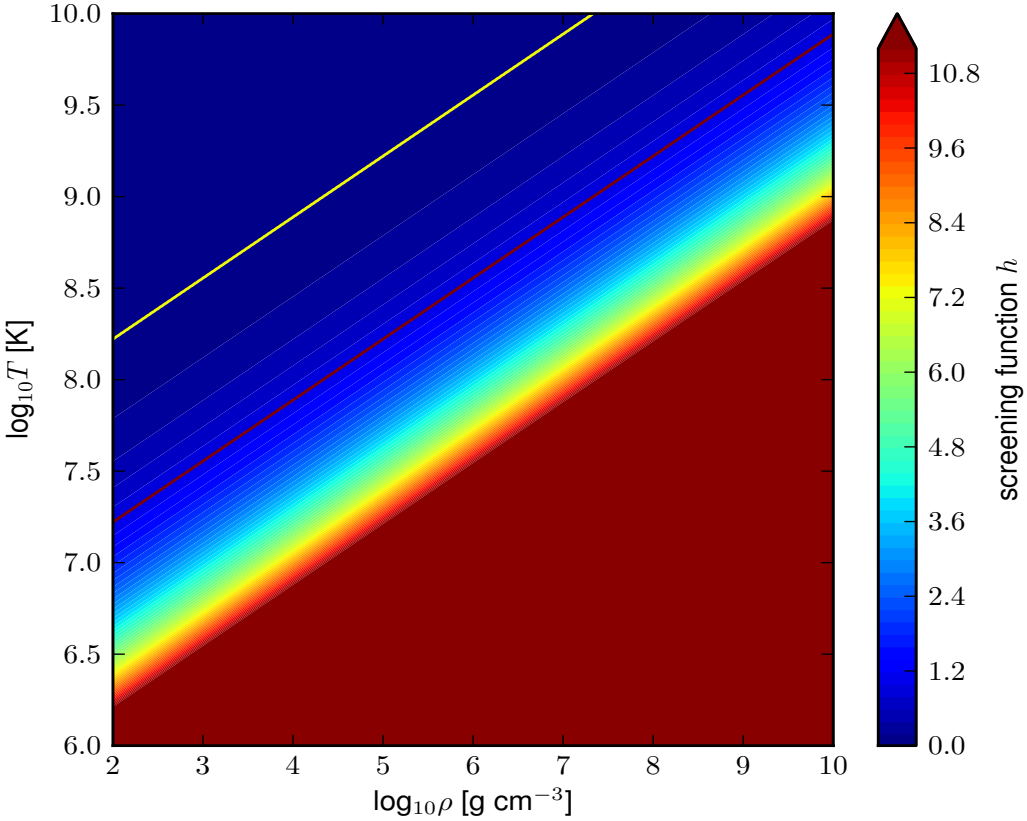

Figure 3.4: Screening factor f_c for $^{12}C+^{12}C$ reactions in a C-rich plasma.

In Fig. 3.5 the ratio of the screening factors used originally in BasNet f_{gi} and the newly adopted screening factor f_c is plotted. The lines show again the division between the regimes as in Fig. 3.4 (see previous paragraph). f_{gi} are the screening prescriptions for weak and intermediate regime of Graboske et al. (1973) and of Itoh et al. (1979) for the strong regime. The largest difference is naturally found for the strong regime. There f_{gi} systematically larger, as long as it is valid, which was already found in Itoh et al. (1990). We favour f_c in the strong screening regime over f_{gi}, since it is based on more recent and more sophisticated methods and matches also results found by other authors (e.g. Ogata 1997; Itoh et al. 1990). In the weak regime $f \approx 1$ and both factors converge against the Debye-Hückel solution making the difference negligible. In the intermediate regime the difference is up to 30%. We decided to use f_c also there even though it was not developed for this regime, but f_c allows a continuous transition between the regimes. f_{gi} as given in Graboske et al. (1973) and Itoh et al. (1979) respectively shows discontinuities between the "intermediate-weak" and the "intermediate-strong" regimes, which can also be seen in Fig. 3.5. For f_c the derivatives are continuous functions also across the regime boundaries.

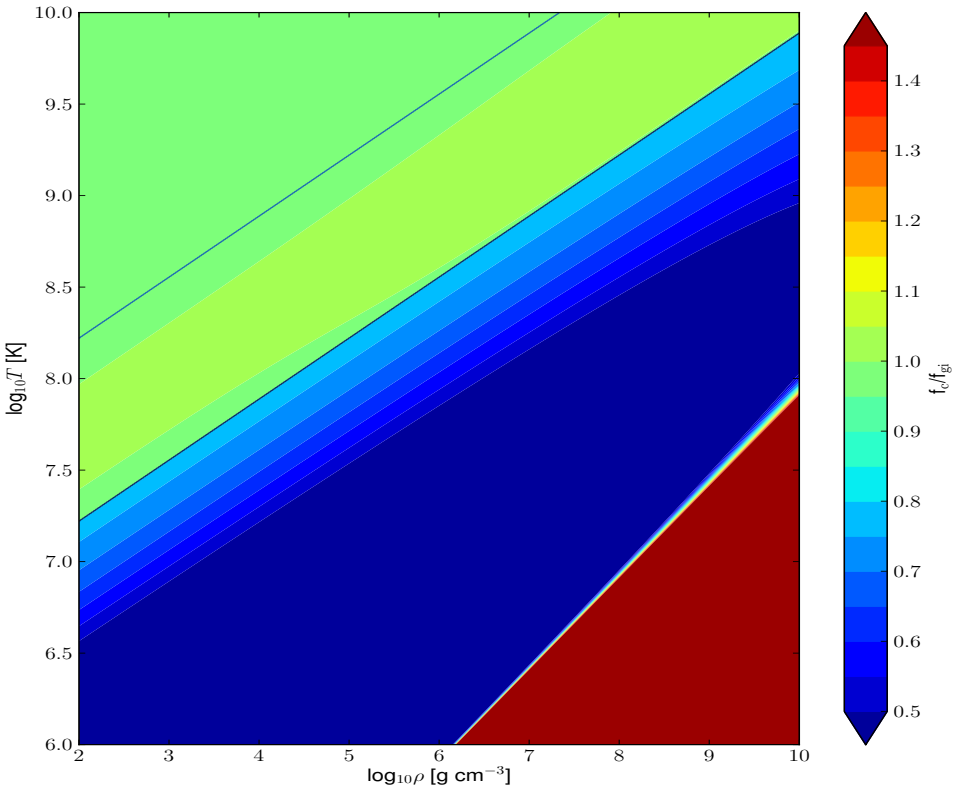

Figure 3.5: Screening factor ratio f_c/f_{gi} for $^{12}C+^{12}C$ reactions in a C-rich plasma.

3.7.3 Mixing

The convective mixing time scale $t_{conv} \approx r^2/D_{conv}$ is during the early burning stages much smaller than the nuclear time scale of the most important isotopes $t_{nuc,i} = X_i/\dot{X}_i$. In GenEC structure, transport, and nuclear burning is solved sequentially. In this case, and as long as $t_{conv} \ll t_{nuc}$, it is possible to homogenise the convective zones, which is equivalent to instantaneous mixing and a constant isotopic mass fractions over the convective regions. The mass fraction X_i of a nucleus i is then after its adjustment by the nuclear network, calculated by

$$X_{i,conv} = \frac{1}{M_{up} - M_{lo}} \int_{M_{lo}}^{M_{up}} X_i(m) dm. \tag{3.26}$$

where M_{lo} and M_{up} are the lower and upper boundaries of the convective zone. Only from the onset of O burning the diffusion Eq. 2.10 (only first term on the right hand side) is used with $D = D_{conv}$. In the previous versions of GenEC abundance change was therefore calculated by the sequence of mixing for time Δt_1[3], burning[4] for Δt and again mixing for Δt_2, with

[3]The time step has only to be known, if the diffusion equation is solved.
[4]Here, "burning" means the solving of the network equations 3.9.

$\Delta t = \Delta t_1 + \Delta t_2$. From O burning onwards this was extended to the sequence mixing (for Δt_1), burning (for Δt_1), mixing (for Δt_2) and burning (for Δt_2) with $\Delta t_1 = \Delta t_2 = \Delta t/2$. This treatment is similar to what is shown schematically by the red box in the upper left of Fig. 3.3.

The homogenisation by Eq. 3.26 is basically not correct, when isotopes are present for which $t_{\rm conv} \gtrsim t_{\rm nuc}$. It can lead to wrong energy distribution by transporting short-lived nuclei to an upper edge of a convective zone. Because BasNet includes also the unstable nuclei explicitly, such troubles occur in particular in H burning by the unstable isotopes involved in the CNO-cycles, in particular by ^{13}N, ^{15}O and ^{17}F. We solved this problem by adding an additional short burning sequence for H to Ne burning phases over a time $\Delta t_{2,\rm net} = \min[20\ \text{yrs}, 0.5\Delta t]$, while the main burning sequence is done on a time step $\Delta t_{1,\rm net} = \Delta t - \Delta t_{2,\rm net}$. With such a treatment the gradient in the abundance of unstable nuclei is maintained without producing a considerable gradient in the stable nuclei. Such a treatment was done before already from O burning. Figure 3.3 thus illustrates the default method for all burning phases using BasNet.

3.7.4 Treatment of initial composition at ZAMS

Starting on the ZAMS with an initial composition containing isotopes like deuterium, ^{7}Li or ^{9}Be, pose a problem as these isotopes would be destroyed already on the pre-main sequence. A unnatural energy boost would appear as a consequence. This problem only appeared with BasNet since those isotopes were not included in the original network. With BasNet this problem is circumvented, by including a pre-burning phase, to allow the composition to adjust to the temperatures T and densities ρ inside the star before the energy is calculated for the first time.

The pre-burning is done as following: The initial structure of the star ($T(r)$,$P(r)$ profiles) provides $T_{\rm ini,m}$ and $\rho_{\rm ini,m}$[5], of the discrete shells with index m. However, to start with the high temperatures close to the centre would be numerically difficult for the network. The network is thus called for all shells $n = 10$ times with time steps $\Delta t_{\rm net} = \Delta t_{\rm ini}/n$ and for each shell the conditions are linearly adjusted from the surface conditions $\rho_{\rm net,m} = \rho_{\rm ini,0}$, $T_{\rm net,m} = T_{\rm ini,0}$ to the correct shell conditions $\rho_{\rm net,m} = \rho_{\rm ini,m}$, $T_{\rm net,m} = T_{\rm ini,m}$. In this way the surface can still contain isotopes of Li, Be and B while in the hotter regions they are burned away without affecting the released nuclear energy at ZAMS.

[5]The density is determined from the ideal gas EoS, see Eq. 2.19.

4 Grid of stellar models with rotation including s process

The motivation to reinvestigate the s process in massive stars is the fact that stars with rotation can enable mixing between the H-burning shell and the convective He-burning core. In case if such mixing is present ^{22}Ne is produced, which is the main s-process neutron source in massive stars. Hirschi (2007) and Meynet et al. (2006) found in their models, calculated with GenEC, an important primary production of ^{22}Ne and ^{14}N at low metallicity, Z. Chiappini et al. (2006) explained the nitrogen enrichment in metal poor halo stars, by including yields of these models in galactic chemical evolution models. A comprehensive study of the s process in massive rotating stars might therefore shed some light on the production of heavy elements and possible impacts of rotation.

4.1 Model grid

The stellar models were calculated with GenEC including BasNet from ZAMS up into O burning for the grid of models, which is shown in Table 4.1. Therein the following quantities are tabulated: the stellar mass, model name, the ratio of the initial equatorial velocity to the critical velocity $v_{\rm ini}/v_{\rm crit}$, the time averaged equatorial main-sequence velocity $\langle v\rangle_{\rm MS}$, the initial angular momentum $J_{\rm ini}$, the metallicity Z, the initial [Fe/H][1] and the life time τ.

The mass range from 15 and 40 $M_\odot$ was investigated, with models of 15, 20, 25 and 40 $M_\odot$ and for each mass a model without rotation and at least one with rotation was chosen. Models with masses below 15 $M_\odot$ were not followed, because the temperatures are not high enough to efficiently activate the neutron source. The observed s-process nuclei are usually also not considered to originate from stars beyond 40 $M_\odot$, because more massive stars are thought to collapse directly to black holes at the end of their life without an explosion, while stars between 25 and 40 $M_\odot$ lead to black hole formation by matter falling back on the remnant neutron star (e.g. Woosley et al. 2002). In the latter case an explosion still happens, ejecting fractions of the synthesised elements.

All masses were calculated at initial metallicities, $Z = 0.014, 10^{-3}$, and 10^{-5}, to investigate the metallicity dependence of the s process in massive rotating stars. Additionally 25 $M_\odot$ stars at $Z = 10^{-7}$ were modelled. The [Fe/H]-values corresponding to these four metallicites are 0, -1.8, -3.8 and -5.8. For $Z = 0.014$ we have adopted the elemental composition of Asplund et al. (2005), with the modified Ne abundance of Cunha et al. (2006), and the isotopic ratios from Lodders (2003). At all three sub-solar metallicities, we assumed an α-enhanced

[1]The bracket ratio of chemical elements A and B is defined as $[A/B] := \frac{\log Y(A)}{\log Y(B)} - \frac{\log Y_\odot(A)}{\log Y_\odot(B)}$.

Table 4.1: Model parameters

Mass [$M_\odot$]	Model	$v_{\rm ini}/v_{\rm crit}$	$\langle v\rangle_{\rm MS}$ [km s^{-1}]	$J_{\rm ini}$ [10^{52}erg s]	Z	[Fe/H]	τ [Myr]
15	A15s0	0.0	0	0.00	0.014	0.0	12.6
	A15s4	0.4	200	1.83	0.014	0.0	14.9
	B15s0	0.0	0	0.00	10^{-3}	−1.8	13.0
	B15s4	0.4	234	2.00	10^{-3}	−1.8	15.3
	C15s0	0.0	0	0.00	10^{-5}	−3.8	12.8
	C15s4	0.4	277	1.81	10^{-5}	−3.8	14.9
20	A20s0	0.0	0	0.00	0.014	0.0	8.8
	A20s4	0.4	216	3.21	0.014	0.0	10.5
	B20s0	0.0	0	0.00	10^{-3}	−1.8	9.3
	B20s4	0.4	260	3.46	10^{-3}	−1.8	11.0
	C20s0	0.0	0	0.00	10^{-5}	−3.8	9.2
	C20s4	0.4	305	3.11	10^{-5}	−3.8	10.7
25	A25s0	0.0	0	0.00	0.014	0.0	7.1
	A25s4	0.4	214	4.83	0.014	0.0	8.4
	B25s0	0.0	0	0.00	10^{-3}	−1.8	7.6
	B25s4	0.4	285	5.24	10^{-3}	−1.8	8.8
	C25s0	0.0	0	0.00	10^{-5}	−3.8	7.5
	C25s4	0.4	333	4.70	10^{-5}	−3.8	8.6
	C25s5	0.5	428	5.70	10^{-5}	−3.8	8.8
	D25s0	0.0	0	0.00	10^{-7}	−5.8	7.1
	D25s4	0.4	383	4.05	10^{-7}	−5.8	8.2
	D25s6	0.6	588	5.68	10^{-7}	−5.8	8.7
40	A40s4	0.4	186	11.30	0.014	0.0	5.7
	B40s4	0.4	334	12.27	10^{-3}	−1.8	6.0
	C40s4	0.4	409	10.83	10^{-5}	−3.8	5.9

composition with the α-elements (^{12}C, ^{16}O, ^{20}Ne, ^{24}Mg, ^{28}Si, ^{32}S, ^{36}Ar, ^{40}Ca, and ^{48}Ti) enhanced with respect to iron (the [α/Fe] values are given in Section 2.8 and Appendix B). All other elements were scaled from the solar composition. More details about the initial composition can be found in Section 2.8 and Appendix B.

As standard initial rotation rate 40% of critical velocity ($v_{\rm ini}/v_{\rm crit} = 0.4$) was used. For 15 to 25 $M_\odot$ stars at solar Z, it corresponds to an average equatorial rotation velocity on the main sequence $\langle v\rangle_{\rm MS} = 200$ to 220 km s^{-1}. This is slightly lower than the peak of the velocity distribution, at $v_{\rm MW,peak} = 225$ km s^{-1}, found for O and B-type stars in the Milky Way (Dufton et al. 2006; Hunter et al. 2009). Due to their low metal content, low-Z massive stars are more compact and have a higher surface velocity than their equivalents found in the Milky Way. With $v_{\rm ini}/v_{\rm crit}$ =constant, $\langle v\rangle_{\rm MS}$ increases with decreasing Z up to about 400 km s^{-1}. This view of faster rotating massive stars at low Z is supported by observations of an increasing Be/B-type star ratio with decreasing metallicity (Maeder et al. 1999; Martayan et al. 2007), by faster rotating massive stars in the SMC compared to the Milky Way (Hunter et al. 2008), and hydrodynamic models of the first generation of stars (Stacy et al. 2011). Thus, $v_{\rm ini}/v_{\rm crit}$ being constant might turn out to be even too slow to reproduce the peak

velocity of the velocity distribution at low Z, which is unknown. We asses the possible impact of faster rotation at low Z by models C25s5 and D25s6 with $\upsilon_{\rm ini}/\upsilon_{\rm crit} = 0.5$ and 0.6, respectively.

For ^{17}O(α,γ) and ^{17}O(α,n) reaction rates we used the rates of Caughlan & Fowler (1988) (hereafter CF88) and Angulo et al. (1999) (hereafter NACRE), respectively. Their ratio determines the strength of ^{16}O as a neutron poison and is very uncertain at the moment. Indeed, Descouvemont (1993) predicts that the ^{17}O(α,γ) should be a factor of 1000 smaller than the CF88 rate. This huge uncertainty strongly affects the s process in massive stars at low Z (Hirschi et al. 2008), where ^{16}O is known to be a strong neutron absorber/poison (Rayet & Hashimoto 2000). Recently, two independent groups measured the ^{17}O(α,γ) rate (Taggart et al. 2011; Best et al. 2011) but it is not yet clear if the new rate will be lower than the CF88-rate at the relevant energies (priv. comm. A. Laird). In order to assess the impact of a decreased rate, we also calculated the rotating 25 $M_\odot$ models at $Z = 10^{-5}$ (C25s4, C25s5) and 10^{-7} (D25s4, D25s6) with the CF88 rate divided by a factor 10, which will probably still be inside the uncertainties of the new measurements in the relevant energy range. These models are in the following text labeled by and additional "b" at the end of their name.

The network used in all models is described in Section 3.6.4 and the set of adopted reaction rates in Section 3.6.3.

4.2 Mixing and production primary ^{22}Ne and ^{14}N

4.2.1 He-core burning

Meynet et al. (2006) and Hirschi (2007) found that rotating stars could produce important amounts of primary ^{14}N and ^{22}Ne by rotation induced mixing. In a basic picture, the production of these nuclei originates in the transport of matter between the He-burning core and the H-burning shell. If the He-burning products ^{12}C and ^{16}O reach the proton-rich layers, they are transformed immediately to ^{14}N by the CNO-cycles. A ^{14}N-pocket is produced in this way at the lower edge of the H-burning shell. Some of this nitrogen can be transported back into the He-burning core, where it is further transformed to ^{22}Ne by the α-captures (see reaction chain 1.2). In the following section a detailed analysis of all the stellar evolution models listed in Table 4.1 shed some light on questions such as: Under which conditions is transport of chemical elements efficient? How much of ^{22}Ne and ^{14}N is produced in massive stars? What observable features would rotational mixing introduce in the light elements?

In Fig. 4.1 the abundance profile of the 25 $M_\odot$ model with rotation at $Z = 10^{-3}$ illustrates the transport of chemical elements. The rotation induced mixing, which is the source for primary ^{14}N and ^{22}Ne production, occurs in the region above the convective He core ($M_{\rm r} \approx$ 7.5-10.5 $M_\odot$). The core itself is identifiable by the flat abundance profile between $M_{\rm r} = 0$ and 7.5 $M_\odot$. Differential rotation develops between convective He core and H shell by core contraction and envelope expansion. It induces secular shear in this radiative zone, which is otherwise stable against convection assuming the Schwarzschild criterion. Diffusion makes primary ^{12}C and ^{16}O (blue dashed and black continuous lines) appear above the convective core. The ^{14}N-pocket appears in this zone ($M_{\rm r} \approx$ 7.5-10.5 $M_\odot$) and the ^{14}N is produced at $M_{\rm r} \approx 10.5$ $M_\odot$, where the hydrogen abundance (red dashed line) drops. In all our models the transport of ^{14}N back to the centre appears mainly by the growth of the convective core, incorporating parts of the ^{14}N-pocket. The diffusive transport is not fast enough to produce

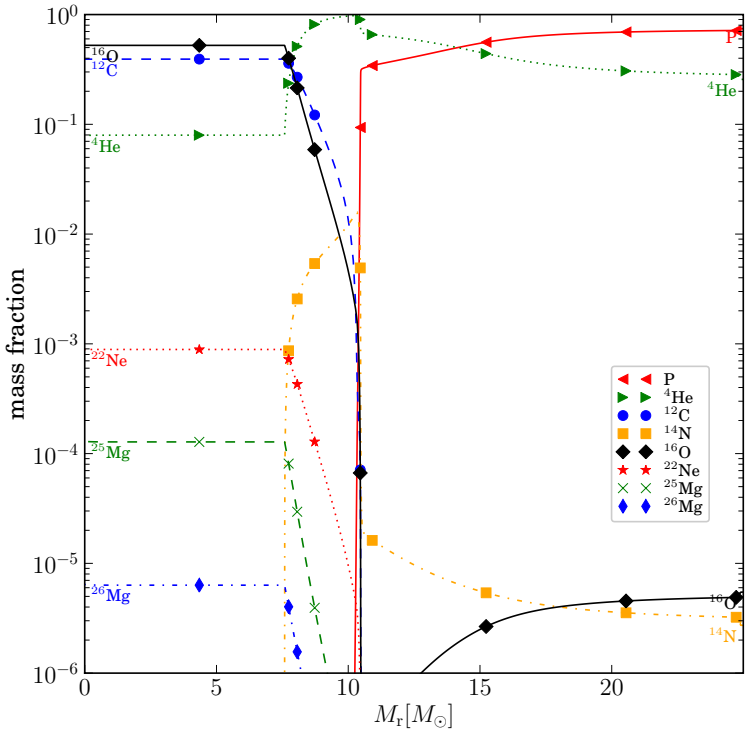

Figure 4.1: Abundance profiles of the main light isotopes during central He burning (X_c(He) $\approx$ 0.08) for the 25 $M_\odot$ model with rotation and $Z = 10^{-5}$. The convective He-burning core presents itself by the flat abundance profiles from the center to about $M_r = 7.5$. The appearance of primary ^{12}C above the convective core, illustrates the presence of rotation induced mixing.

a ^{22}Ne mass fraction, $X(^{22}\mathrm{Ne})$, of 10^{-3} to 10^{-2} in the core, necessary to boost the s process efficiently. As can be seen in Eq. 2.10 the transport of chemical elements is not only driven by a large diffusion coefficient, but also appears stronger when gradients in the chemical composition are present. In this respect the situation favours mixing, because steep gradients exist in the abundances of all involved nuclei.

Secular shear is the essential mechanism for the transport between He-core and H-envelope. The diffusion coefficient D_{shear}, used in our models of Talon & Zahn (1997) is given in by

$$D_{\mathrm{shear}} = \frac{(K + D_{\mathrm{h}})}{\left[\frac{\varphi}{\delta}\nabla_{\mu}(1 + \frac{K}{D_{\mathrm{h}}}) + (\nabla_{\mathrm{ad}} - \nabla_{\mathrm{rad}})\right]} \frac{\alpha H_{\mathrm{p}}}{g\delta} \left(0.8836\Omega \frac{d\ln\Omega}{d\ln r}\right)^2 .$$

Naturally, a high Ω-gradient favours shear. Additionally, this choice of D_{shear} suppresses the mixing across the mean molecular weight gradient, $\nabla\mu$. Such a $\nabla\mu$ is present between H-burning shell and He-rich core and is most prominent at the lower edge of the H-burning zone. D_{shear} is lowered most efficiently for high $\nabla\mu$, in case the thermal diffusivity is larger than the horizontal turbulence ($K > D_h$). This suppression of mixing by $\nabla\mu$ is in this case stronger than in other prescrition available in GenEC of Maeder (1997), in which the prefactor $(1 + \frac{K}{D_{\mathrm{h}}})$ is missing. The efficient lowering of mixing by $\nabla\mu$ is the case in all our models just above the convective He-core, where K/D_h has typical values between 10 and 100, and where $\nabla\mu$ is highest it reaches often values towards 10^3. This can also be seen on the left hand side in Figures 4.2, 4.3 and 4.4 at $M_{\mathrm{r}} \approx 5-10\ M_{\odot}$, where K is the black dotted line and D_h is the blue dash-dotted line. The K/D_h ratio does not change significantly in the relevant regions in the course of central He burning.

There are basically three different configurations of the stellar structure during central He burning, which appear in the different models including the effects of rotation. These cases are illustrated with the help of three evolutionary snap-shots of a rotating 25 $M_{\odot}$ $Z = 10^{-3}$ star during central He burning:

- In case **(a)**, shown in Fig. 4.2, the convective shell at the bottom of the H-rich envelope including the H-burning shell rotates considerably slower than the regions below. The angular velocity Ω is plotted as orange dashed line on the left hand side. It shows a steep gradient at the lower boundary of the convective shell which compensates for the inhibiting effect of $\nabla\mu$ and D_{shear} has values between 10^4 and 10^7 cm^2 s.

- Case **(b)** is shown Fig. 4.3 which is identical to case (a), but with the important difference that the convective H-shell is retracting away from its lowest mass coordinate. It leaves a flat Ω-profile behind, showing up at $M_{\mathrm{r}} \approx 9.5\ M_{\odot}$ on the left hand side in Fig. 4.3. For this reason the steep Ω-gradient and the μ-gradient do not coincide, and a gap with low values of D_{shear} appears, i.e. D_{shear} between 10 and 10^4 cm^2 s. On the right hand side of Fig. 4.3 the slope of the proton abundance $X(^1\mathrm{H})$ (red dash-dotted line) is representative of $\nabla\mu$. On the one hand the comparison of cases (a) and (b) reveals a much higher value of $\nabla\mu$ for case (b), explaining together with the low $\nabla\Omega$ the low value D_{shear}. On the other hand the steeper $\nabla X(^1\mathrm{H})$ in case (b) keeps the transport of hydrogen across $\nabla\mu$ alive and compensates partially for the higher $\nabla\mu$ and the lower values of $\nabla\Omega$.

- Case **(c)** is shown in Fig. 4.4. There is no convective zone in the H-rich layers and only a moderate $\nabla\Omega$ across the H-burning shell and the μ-barrier. The latter therefore

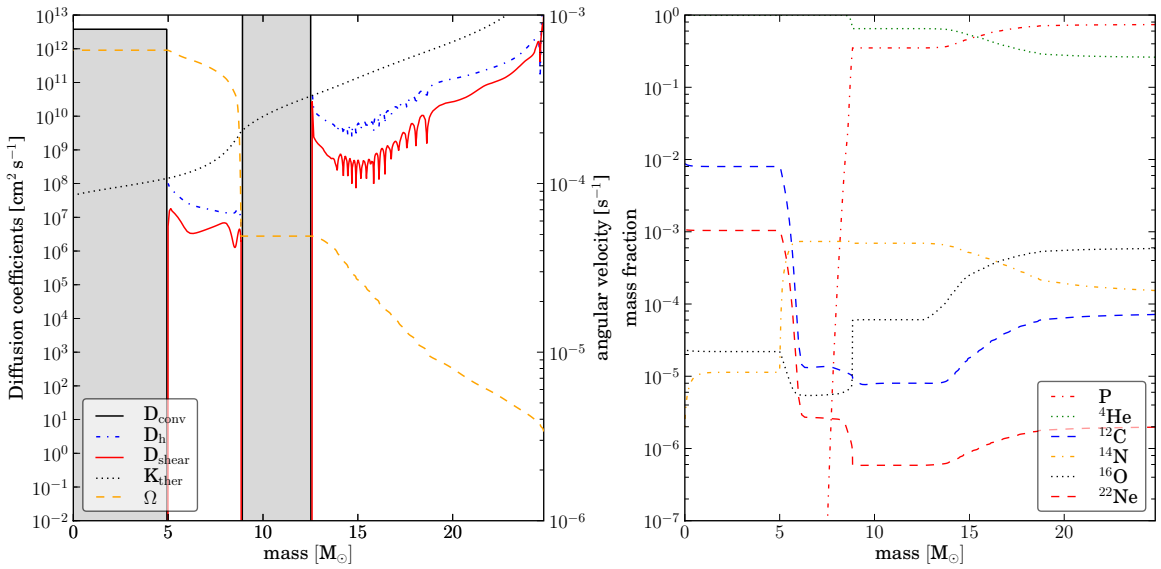

Figure 4.2: Diffusion coefficient profiles on the left hand side and abundance profiles on the right hand side during central He burning, when a convective H shell is present, inside the 25 $M_\odot$ star with rotation at $Z = 10^{-3}$. The shear diffusion coefficient (red continuous line) describes the mixing between He core and H-burning shell. The convective regions are represented by the grey shaded areas.

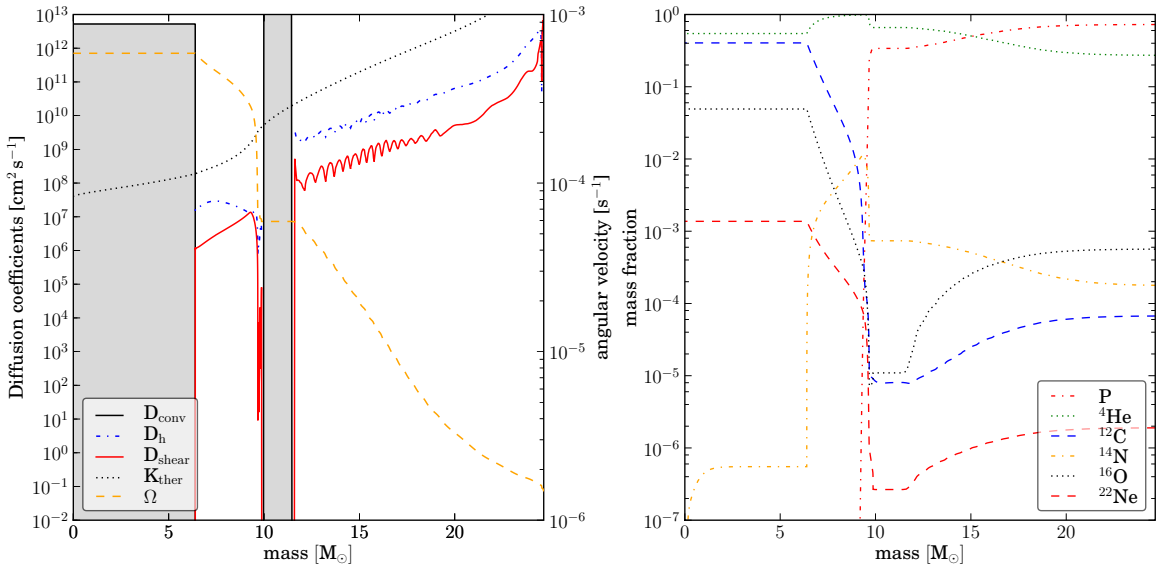

Figure 4.3: Diffusion coefficient profiles on the left hand side and abundance profiles on the right hand side during central He burning, when a retracting convective H shell is present, inside the 25 $M_\odot$ star with rotation at $Z = 10^{-3}$. The shear diffusion coefficient (red continuous line) describes the mixing between He core and H-burning shell. The convective regions are represented by the grey shaded areas.

brakes the transport of hydrogen into carbon-rich layers and the mixing is relatively weak, with $D_{\rm shear}$ between 1 and 10^3 cm^2 s. Case (c) can also appear as a successor of case (b). In this situation $\nabla\Omega$ is even lower at the bottom of the H-burning shell and $D_{\rm shear}$ displays the lowest values of all cases. Compared to (a) again a steeper $\nabla X(^1{\rm H})$ compensates partially the reduced $D_{\rm shear}$, at the interface between H-burning shell and subjacent layers. But this is the case of weakest mixing when the convective shell just disappeared.

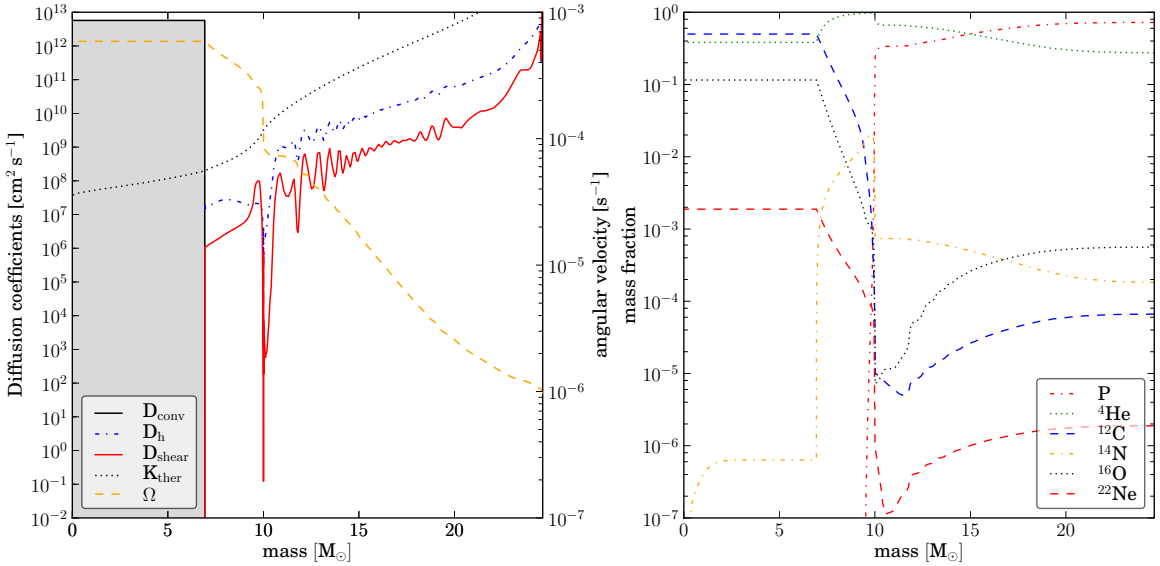

Figure 4.4: Diffusion coefficient profiles on the left hand side and abundance profiles on the right hand side during central He burning, when no convective H shell is present, inside the 25 $M_\odot$ star with rotation at $Z = 10^{-3}$. The shear diffusion coefficient (red continuous line) describes the mixing between He core and H-burning shell. The convective core is represented by the grey shaded areas.

The rotating solar metallicity 15, 20 and 25 $M_\odot$ models, as well as the 15 $M_\odot$ with sub-solar Z do not develop a convective zone at the inner edge of the H-rich layers during central He burning. Thus, the mixing proceeds in these models in configuration (c). The rotating sub-solar Z models with 20, 25 and 40 $M_\odot$, as well as the 40 $M_\odot$ $Z = Z_\odot$ model develop before the start of central He burning a convective H-shell where the H-shell burning occurs. It shrinks and retreats when the convective He-core grows. These models follow therefore the sequence (abc), but with a basic difference between the models at $Z = 10^{-5}$ and those at higher metallicity. While the latter develop case (b) with a very low $D_{\rm shear}$ as soon as the convective shell starts to shrink, the former show strong angular momentum transport at the steep $\nabla\Omega$, which is fast enough to follow the retreating convective zone and therefore develops rather a hybrid case between (a) and (b) when the convective shell shrinks.

To ensure that the mixing is not overestimated by our choice of resolution parameters a 25 $M_\odot$ $Z = 10^{-3}$ rotating model was performed with a much higher resolution, i.e. doubled resolution in the He-core[2] and five times the resolution in the radiative layers between the

[2]The critical value of the luminosity gradient $\nabla L_{\rm crit}$, used to split a mass shell when $\nabla L > \nabla L_{\rm crit}$, was

convective core and H-burning shell[3]. There is essentially one considerable difference, by the smoother growth of the convective core. But it did not affect the ^{14}N and ^{22}Ne production strongly. For example the mass factions $\Delta X(^{22}\mathrm{Ne})$ of burned ^{22}Ne during central He burning decreased only by 2.5% in the high resolution model compared to the standard resolution. The mass fraction $X_{\mathrm{shell}}(^{22}\mathrm{Ne})$ of ^{22}Ne in the He-shell at the pre-SN stage differs more, meaning that the high resolution case is about 22% lower. Still this value originates from $X(^{22}\mathrm{Ne}) = 0.0246$ and 0.0314, for the high and the default resolution model, respectively. The slight decrease of transport efficiency by higher resolution would therefore not change the s process and only moderately lower the yields of ^{14}N and ^{22}Ne.

In Table 4.2 the mass factions $\Delta X(^{22}\mathrm{Ne})$ of burned ^{22}Ne during central He burning, $X_{\mathrm{r}}(^{22}\mathrm{Ne})$ of remaining ^{22}Ne after He burning, $X_{\mathrm{shell}}(^{22}\mathrm{Ne})$ of ^{22}Ne in the He-shell at the pre-SN stage, and the yields of ^{22}Ne and ^{14}N are tabulated for all models. $\Delta X(^{22}\mathrm{Ne})$ characterises to a certain extent the neutron source in He burning, while $X_{\mathrm{r}}(^{22}\mathrm{Ne})$ is the same for C burning.

Mixing is strong enough at all metallicities in our models including rotation effects to produce the pocket of primary ^{14}N above the convective core $X(^{14}\mathrm{N})$. The amount of primary ^{22}Ne in the convective He-core at the end of He burning, when s process is active, is between 0.1 and 1% in mass fractions. Considering a constant value of $\upsilon_{\mathrm{ini}}/\upsilon_{\mathrm{crit}} = 0.4$ at all metallicities, the primary ^{22}Ne in the He-core decreases slightly with decreasing metallicity. Thus, we can see from Table 4.2 ($\Delta X(^{22}\mathrm{Ne}, \mathrm{burn})$) that rotating models at all metallicities produce and burn significant amounts of ^{22}Ne, confirming the results of previous studies (Meynet et al. 2006; Hirschi 2007). There is, however, theoretical and observational support to consider a slight increase of $\upsilon_{\mathrm{ini}}/\upsilon_{\mathrm{crit}}$ with decreasing metallicity. Considering models with 25 $M_{\odot}$ and $\upsilon_{\mathrm{ini}}/\upsilon_{\mathrm{crit}} = 0.4$ at $Z = Z_{\odot}$ and 10^{-3}, $\upsilon_{\mathrm{ini}}/\upsilon_{\mathrm{crit}} = 0.5$ at $Z = 10^{-5}$ and $\upsilon_{\mathrm{ini}}/\upsilon_{\mathrm{crit}} = 0.6$ at $Z = 10^{-7}$, which correspond to an increase of $\upsilon_{\mathrm{ini}}/\upsilon_{\mathrm{crit}}$ with decreasing metallicity. In this case we see that rotating models produce and burn a constant quantity of ^{22}Ne, around 0.5% in mass fraction. However in our solar metallicity models the ^{22}Ne is mainly secondary, because the He-core does not grow as much as at sub-solar metallicity. The largest cores are found (see Table 4.3) and also core grows at $Z = 10^{-3}$. Towards lower metallicites the core sizes decrease with decreasing opacity. At solar Z the core size is smaller for all masses. It is related to a slow activation of CNO cycle above the core during the main sequence and a small energy release in these layers. Another effect which hinders the core growth is the strong mass loss at solar Z, in particular for the 40 $\mathrm{M}_{\odot}$ stars. We can see from these results that rotating models produce significant amounts of ^{22}Ne in a primary way over the entire range of masses and all metallicities computed, except at $Z = Z_{\odot}$ where the secondary ^{22}Ne is more significant.

The convective He-shell, which follows on the ^{14}N-pocket, transforms most of this ^{14}N into ^{22}Ne. While the ^{22}Ne in the He-shell of non-rotating model is purely secondary, in rotating models it is primary at the pre-SN stage and almost independent of metallicity. It is only weakly destroyed during the He-shell burning and leaves a mass fraction of $X(^{22}\mathrm{Ne})$ between 0.7 and 3.2% in the He layers. This is very interesting in the context of the r-process in He-rich layers. This site was investigated by Truran et al. (1978) and Thielemann et al. (1979) in the context of r process, but later on found to be only a possible site for a weak r process

reduced by a factor two.

[3]The critical values of the mass fraction gradients of carbon and helium, $\nabla X_{\mathrm{crit}}(^{12}\mathrm{C})$ and $\nabla X_{\mathrm{crit}}(^{4}\mathrm{He})$, used to split a mass shell when $\nabla X(^{12}\mathrm{C}) > \nabla X_{\mathrm{crit}}(^{12}\mathrm{C})$ or $\nabla X(^{4}\mathrm{He}) > \nabla X_{\mathrm{crit}}(^{4}\mathrm{He})$, were reduced by a factor five.

Table 4.2: ^{14}N and ^{22}Ne production and destruction

Model	$\Delta X(^{22}\mathrm{Ne})^{a}$	$X_{\mathrm{r}}(^{22}\mathrm{Ne})^{a}$	$X_{\mathrm{shell}}(^{22}\mathrm{Ne})^{a}$	$m(^{22}\mathrm{Ne})^{a}$ [$\mathrm{M}_{\odot}$]	$m(^{14}\mathrm{N})^{a}$ [$\mathrm{M}_{\odot}$]
A15s0	3.06(-3)	9.70(-3)	9.23(-3)	9.11(-3)	3.19(-2)
A15s4	5.59(-3)	7.42(-3)	1.38(-2)	2.78(-2)	2.63(-2)
B15s0	3.54(-4)	8.02(-4)	9.24(-4)	1.28(-3)	2.91(-3)
B15s4	9.37(-4)	1.02(-3)	7.34(-3)	1.49(-2)	7.17(-3)
C15s0	3.75(-6)	7.70(-6)	1.02(-5)	6.42(-5)	4.77(-5)
C15s4	4.84(-4)	3.92(-4)	7.55(-3)	1.39(-2)	5.25(-3)
A20s0	5.34(-3)	7.43(-3)	1.14(-2)	2.50(-2)	3.76(-2)
A20s4	7.23(-3)	5.03(-3)	1.99(-2)	4.99(-2)	3.72(-2)
B20s0	6.16(-4)	5.46(-4)	1.15(-3)	2.68(-3)	4.06(-3)
B20s4	3.49(-3)	1.14(-3)	3.20(-2)	7.59(-2)	9.39(-3)
C20s0	5.66(-6)	5.74(-6)	1.32(-5)	1.21(-4)	5.80(-5)
C20s4	1.52(-3)	4.62(-4)	1.67(-2)	4.09(-2)	4.04(-3)
A25s0	7.68(-3)	5.10(-3)	1.27(-2)	3.39(-2)	4.76(-2)
A25s4	9.69(-3)	3.28(-3)	1.56(-2)	4.06(-2)	4.95(-2)
B25s0	7.52(-4)	4.16(-4)	1.15(-3)	3.36(-3)	5.90(-3)
B25s4	4.08(-3)	6.22(-4)	1.99(-2)	6.72(-2)	8.47(-3)
C25s0	7.21(-6)	4.14(-6)	1.13(-5)	2.38(-4)	9.38(-5)
C25s4	1.23(-3)	1.69(-4)	1.15(-2)	3.61(-2)	1.85(-3)
C25s4b[b]	1.27(-3)	1.82(-4)	1.17(-2)	3.49(-2)	9.33(-4)
C25s5	3.83(-3)	4.94(-4)	1.59(-2)	4.80(-2)	2.07(-3)
C25s5b[b]	3.75(-3)	4.85(-4)	1.61(-2)	4.81(-2)	1.99(-3)
D25s0	8.28(-7)	4.67(-7)	3.09(-7)	1.63(-4)	1.80(-5)
D25s4	1.05(-4)	3.81(-5)	1.46(-2)	3.81(-2)	1.10(-2)
D25s4b[b]	1.06(-4)	3.96(-5)	1.45(-2)	3.71(-2)	1.11(-2)
D25s6	4.57(-3)	2.68(-4)	1.95(-2)	5.52(-2)	3.43(-3)
D25s6b[b]	4.44(-3)	3.11(-4)	2.00(-2)	5.56(-2)	3.48(-3)
A40s4	1.23(-2)	5.29(-4)	1.21(-2)	3.34(-2)	2.23(-2)
B40s4	3.31(-3)	1.06(-4)	2.08(-2)	7.99(-2)	1.84(-2)
C40s4	2.70(-3)	1.93(-5)	8.75(-3)	3.21(-2)	2.07(-3)

Note. [(a)] Values in brackets are the exponents ($x(y) = x \times 10^{y}$). [(b)] This model was calculated with the same initial parameters as the model, on the line above, but with the $^{17}\mathrm{O}(\alpha,\gamma)$ reaction rate of CF88 divided by 10.

(Woosley et al. 2002) or n process (Rauscher et al. 2002). Given the large amounts of primary ^{22}Ne produced in the rotating models at all Z, it is worthwhile re-considering the He-shell as a site for explosive neutron capture nucleosynthesis.

4.2.2 C-shell burning

The carbon shell burning is the second efficient s-process production site inside massive stars at solar metallicity (The et al. 2007). It is active from the end of central C burning. One could think of rotation induced mixing appearing in the same way as in He burning, mixing

down some of the primary ^{22}Ne into the C shell and boosting the s process. However, the time scale of the secular shear mixing, which is still present between convective He and C shells, is of the same order as during central He burning. On the other hand the the burning time scale of Ne, O and Si burning are at least 5 to 6 orders of magnitude smaller than the one of He burning. This leaves C-shell burning just with the remaining ^{22}Ne from He burning.

Rotation has thus rather an effect on the stellar structure side changing the CO-core sizes and ^{12}C/^{16}O ratio after He burning and the impact this ratio has on all subsequent burning phases and their heavy element production.

4.3 Yields

In this work, a complete list of pre-SN yields is determined. We calculated the yields out of a wind and a SN-progenitor contribution. The pre-SN yield of a nucleus i is the net amount produced of it in $M_\odot$ and can easily be calculated by

$$m_i = \int_{M_{\rm rem}}^{M^*} (X_i(M) - X_{i,0})dM + \int_0^\tau \dot{M}(t)(X_{i,\rm s}(t) - X_{i,0})dt, \tag{4.1}$$

where M^* is the stellar mass before the explosion, $X_i(M)$ the mass fraction of nucleus i at Lagrangian mass coordinate M, $X_{i,0}$ the initial mass fraction, $X_{i,\rm s}$ the surface mass fraction and $\dot{M}$ the mass loss rate. The first term on the left hand side describes the mass produced or destroyed in the SN-progenitor and the second term describes what is ejected by the wind. The remnant mass $M_{\rm rem}$ was derived from the relation of $M_{\rm rem}$ to $M_{\rm CO}$, which was originally established in Maeder (1992). $M_{\rm CO}$ is the carbon-oxygen core mass determined as the part of the star for which the ^{4}He mass fraction is below 10^{-2}. Both, $M_{\rm rem}$ and $M_{\rm CO}$, are listed in Table 4.3 in units of $M_\odot$, as well as the final mass, $M_{\rm fin}$, the mass coordinate for which $X(^4{\rm He}) > 0.75$, M_α, the maximal extension of the convective He core $M_{\rm He}^{\rm max}$, and the maximal radius of convective C-burning shell $M_{\rm C}^{\rm max}$. The latter is given because, this is the maximal mass coordinate to which the s-process products can be mixed outwards.

The time scales of C burning and later evolutionary stages are much shorter than those of H and He-burning stages. Our models were calculated at least up to the onset of O burning, hence the wind contribution by the wind term in Eq. 4.1 can well be determined. The pre-SN term in Eq. 4.1 was calculated from the final profile during O burning. Changes in the chemical profile during the final phase appear only in the innermost part of the star. We compared our models with Hirschi et al. (2004) and even though our models do not use exactly the same mixing and wind prescription, the lower boundary and the extension of the C shell as well as the size of convective core during O burning, are similar. We therefore know that our models would evolve in a similar way as the one of Hirschi et al. (2004), up to the onset of core collapse. In this case we expect a only a weak modification of the yields for the 15 $M_\odot$ star. Thus we are confident that running the models only up to O burning is sufficient for a good approximation of the pre-explosive yields.

The yields from the SN progenitor are in reality modified by explosive nucleosynthesis activated by SN shock (Thielemann et al. 1996). Yields of s-process nuclei are not strongly modified by the explosion (Tur et al. 2009), but only by the γ-process just above $M_r = M_{\rm rem}$. The same is true for light nuclei up to ^{16}O. Isotopic yields of ^{20}Ne and ^{24}Mg will have the correct order of magnitude, even though they will be modified by the explosion. Hence, also

isotopic ratios for Ne and Mg can be estimated from the yields. The yields calculated here can therefore be taken as a good estimate and are well suited to investigate the galactic chemical enrichment in s-process nuclei and light nuclei by massive rotating stars.

Table 4.3: Different core masses of the models

Model	$M_{\rm fin}$	M_α	$M_{\rm He}^{\rm max}$	$M_{\rm C}^{\rm max}$	$M_{\rm CO}$	$M_{\rm rem}$
A15s0	13.01	4.27	2.24	2.19	2.35	1.49
A15s4	10.43	5.81	3.39	2.75	3.33	1.74
B15s0	14.80	4.74	2.60	2.33	2.62	1.56
B15s4	13.84	6.03	3.52	2.54	3.44	1.77
C15s0	14.99	4.54	2.41	2.02	2.49	1.52
C15s4	14.84	5.70	3.41	2.06	3.34	1.74
A20s0	9.02	6.17	3.84	3.23	3.76	1.85
A20s4	7.92	7.88	5.36	3.41	5.13	2.20
B20s0	19.85	6.65	4.15	3.75	4.11	1.94
B20s4	10.91	8.16	5.41	4.35	5.22	2.22
C20s0	20.00	6.26	3.93	3.54	3.88	1.88
C20s4	17.01	8.10	5.36	3.82	5.18	2.21
A25s0	10.86	8.23	5.74	4.87	5.53	2.30
A25s4	10.04	9.99	7.40	5.97	6.97	2.66
B25s0	24.73	8.63	5.92	4.97	5.79	2.36
B25s4	14.32	10.96	7.93	6.62	7.56	2.81
C25s0	25.00	8.03	5.61	4.47	5.57	2.31
C25s4	24.40	10.69	7.63	5.07	7.33	2.75
C25s5	24.72	10.49	7.38	5.59	7.08	2.69
D25s0	25.00	7.39	5.72	4.09	5.56	2.31
D25s4	25.00	8.77	5.78	4.97	5.61	2.32
D25s6	24.81	9.72	6.53	3.92	6.19	2.46
A40s4	19.01	19.01[a]	15.23	14.10	15.04	4.65
B40s4	25.15	19.30	15.40	13.90	14.76	4.57
C40s4	38.49	19.18	14.70	6.51	14.08	4.36

Note. [(a)] This star ends its life as WR star and as a consequence $M_\alpha = M_{\rm fin}$

We also calculated the yields separately for core He, shell C and shell He burning to distinguish between the s-process contributions. To do that besides the yields at the pre-SN stage they were also calculated just after core He burning for stellar regions with $M_{\rm r} > M_{\rm rem}$, this is illustrated in Fig. 4.5. The difference describes what the s process in shell He and shell C burning together produced from the end of He-core burning onward. If one splits this difference in the yields in two parts at mass $M_{\rm cut}$ (red horizontal line in Fig. 4.5), the separate contributions of shell He and shell C burning are obtained. ^{20}Ne is a C-burning product and its abundance drop at the outer boundary of the C-burning shell and was chosen to determine $M_{\rm C}^{\rm max}$, so we chose $M_{\rm cut} = M_{\rm C}^{\rm max} + 0.01$.

Beside the yields, the production factors, f, will be used in the subsequent discussion. The production factor of an isotope i is defined as

$$f_i = \frac{m_{i,\rm eject}}{m_{i,\rm ini}} = \frac{m_i + m_{i,\rm ini}}{m_{i,\rm ini}},$$

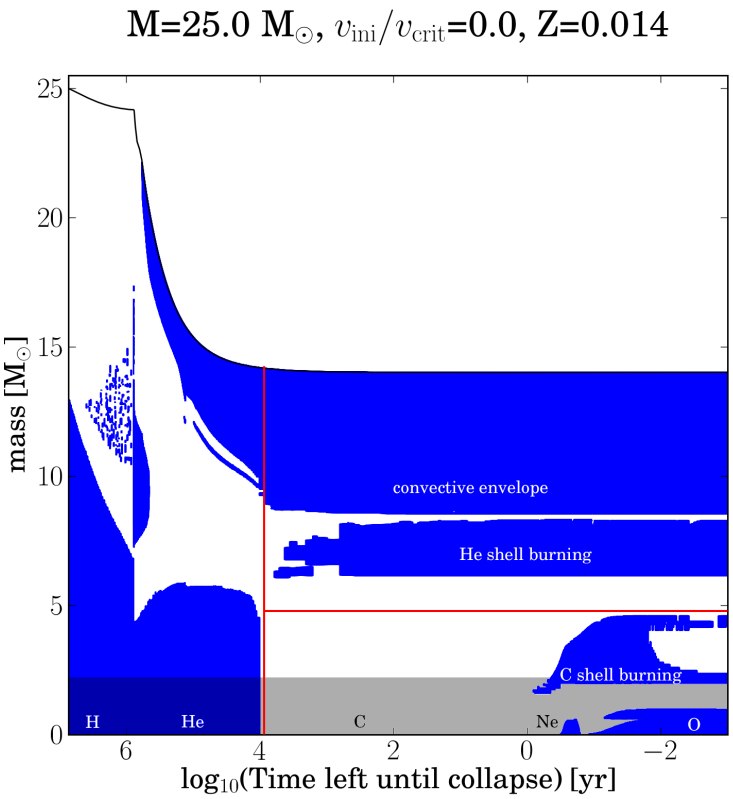

Figure 4.5: Kippenhan diagram of 25 $M_\odot$ star with $Z = Z_\odot$ and no rotation, to illustrate the $M_{\rm cut}$ (red horizontal line). The shaded area show the mass ending up inside $M_{\rm rem}$. The red vertical line marks the point in the stellar life where the He core s-process yields are calculated.

with m_i the yield, $m_{i,\rm eject}$ the ejected mass, and $m_{i,\rm ini}$ the initial mass of nucleus i in the star. The production factor quantifies if a star is a strong producer of an element or not.

The full set of yields for all models will be made available on forum.astro.keele.ac.uk.

4.4 Results and discussion

4.4.1 S process - rotation vs. no rotation

He core burning

Two of the most important nuclear reaction rates for s process in massive stars are ^{22}Ne(α, n) and ^{22}Ne(α, γ). The rates taken from Jaeger et al. (2001) and NACRE, respectively, result in an equal strength of both channels at $T_8 \approx 2.8$. Below this temperature the (α, γ)-channel dominates, while above the (α, n)-channel is stronger. The destruction of ^{22}Ne begins in our models already at temperatures around $T_8 = 2.2$ and when $T_8 \approx 2.8$ is reached, only $X(^{22}\text{Ne}) = 10^{-2}$, 6.8×10^{-3}, 5.7×10^{-3}, and 5.0×10^{-3} is left in models A15s0, A25s0, A25s4, and A40s4, respectively. All four models had about $X(^{22}\text{Ne}) = 1.3 \times 10^{-2}$ of secondary ^{22}Ne. Thus an important fraction of ^{22}Ne is burned, when ^{22}Ne(α, γ) dominates over the neutron source. The more recent rate determinations of ^{22}Ne(α, γ) from Karakas et al. (2006) or Iliadis et al. (2010) were not applied in this work, but both are considerably lower than the NACRE rate. This means, that the yields from He-core burning could be somewhat higher.

Only close to the end of central He burning, temperatures for an efficient activation of ^{22}Ne$(\alpha, n)^{25}$Mg are reached. At $T_8 \approx 3$, only $X(\alpha) = 4.5 \times 10^{-5}$, 1.2×10^{-3}, 2.4×10^{-3} and 8.5×10^{-3} is left in our models A15s0, A25s0, A25s4 and A40s4, respectively. These few numbers illustrate already that several well known parameters limit the s-process efficiency of He-core burning.

- Because only a small helium mass fraction, $X(^4\text{He})$, is left when ^{22}Ne$+\alpha$ is activated, the competition with other α-captures as the ^{12}C(α, γ) and 3α is essential at the end of He burning and will affect the s-process efficiency in core He burning. Unfortunately all the important reactions involved contain still large uncertainties. An extensive study of s-process uncertainties due to uncertainties in ^{12}C(α, γ) and 3α was done by Tur et al. (2009).

- The low amount of $X(^4\text{He})$, when the neutron source is activated, means also that not all of ^{22}Ne is burned and a part of it will be left for subsequent C-burning phase. This depends on the stellar core size. The more massive the core the more ^{22}Ne is burned and the more efficient is the s process in core He burning, as can be seen from the increasing number of neutron captures per seed n_c from 0.77, 2.42, 3.13 and 4.05 for the four models mentioned before, which have M_{CO} of 2.35, 5.53, 6.97, and 15.04 $M_\odot$, respectively (see Table 4.3).

- In this late phase during He burning the bulk of the core matter consists of ^{12}C and ^{16}O, which are both strong neutron absorbers, producing ^{13}C and ^{17}O. It is therefore important to know how many of the captured neutrons can be recycled by ^{13}C(α, n) and ^{17}O(α, n), and how many neutrons are either lost by further neutron captures on ^{13}C and ^{17}O or ^{17}O(α, γ). The strength of primary neutron poisons, like ^{16}O, increases towards lower metallicities, because of the decreasing ration of seeds to neutron poisons. In this study we used the ^{17}O(α, n) rate of NACRE and the ^{17}O(α, γ) rate of CF88. In at He burning temperatures $(\alpha, n)/(\alpha, \gamma)$ ratio increases from 6.6 (at $T_8 = 2.5$) to 16.5 (at $T_8 = 3.5$). This shows that most of the neutrons captured by ^{16}O are released again. But since ^{16}O is an efficient neutron absorber it makes the (α, γ) an important neutron

sink. Descouvemont (1993) proposed a 1000-times lower (α,γ)-channel, which would make the poisoning effect of ^{16}O disappear completely. To investigate the effect of lower $^{17}\mathrm{O}(\alpha,\gamma)$ on the s process at low Z, models C25s4b, C25s5b, D25s4b and D25s6b were calculated, with the CF88 rate reduced by a factor 10.

In Table 4.4 characteristic quantities for s process in He burning are presented. The central and the core-averaged neutron exposure, τ_c and $\langle\tau\rangle$, describe the amount of free neutrons. The average number of neutron captures per seed n_c describes how far up in the nuclear chart an iron seed is processed on average. These quantities are defined in Section 1.4.4. Additionally, the central and core averaged peak neutron density, $n_{n,c,\mathrm{max}}$ and $\bar{n}_{n,\mathrm{max}}$, the burned and the amount of ^{22}Ne left in the centre after core He exhaustion are tabulated.

For the non-rotating models, the typical picture of s process appears in the mass and the metallicty dependence. The values in Table 4.4, show a decrease with decreasing metallicity and at the same metallicity (A, B or C series) an increase with increasing mass. This is what we call here the *standard* s process in massive stars. It is a secondary process (see e.g. Prantzos et al. 1990; Raiteri et al. 1992), because the main neutron source (^{22}Ne) and the seeds (mainly iron) have a secondary origin. Indeed, in non-rotating models, the main neutron source, ^{22}Ne, comes only from the initial C, N, and O. During helium burning, the neutron poisons are a mixture of secondary (mainly ^{22}Ne and ^{25}Mg) and primary (mainly ^{16}O) elements, whereas during carbon burning the neutron poisons are primary elements (^{16}O, ^{20}Ne, ^{24}Mg). Thus, towards lower Z, the standard s process is neither scaling with seeds nor sources, but is even less efficient (Prantzos et al. 1990). Not only the contribution from the carbon shell becomes negligible, but also the one from core He burning below $Z/Z_\odot = 10^{-2}$ (Prantzos et al. 1990), which we confirm with our non-rotating models at $Z = 10^{-5}$ and $Z = 10^{-7}$ (C and D series).

At the first glance the very low metallicity model D25s0 seem to be astonishing, because it does not follow the trend. It shows a higher s-process efficiency than C25s0. This model shows a smooth transition between central H and He burning. When only fractions of hydrogen are left in the core temperatures of $T_8 = 1.4$ are reached and the 3α-reaction is weakly activated. It leads to the immediate transformation of produced ^{12}C by $^{12}\mathrm{C}(p,\gamma)^{13}\mathrm{N}(\beta^+)^{13}\mathrm{C}(p,\gamma)^{14}\mathrm{N}$ and therefore also the consumption of remaining protons. In this way $X(^{22}\mathrm{Ne}) = 1.2\times10^{-6}$ of primary ^{22}Ne is produced. Still as for non rotating $Z = 10^{-5}$ models, D25s0 produces negligible amounts of heavy elements. It therefore rather shows the transition to pop III (metal-free) stars, which cannot produce enough energy by the pp-chains and therefore go into a state of combined hydrogen and weak He burning, letting the ^{14}N gradually increase (Ekström et al. 2008; Heger & Woosley 2010).

Rotation significantly changes the structure and pre-SN evolution of massive stars (Hirschi et al. 2004) and thus also the s-process production. Rotating stars have central properties similar to more massive non-rotating stars. In particular they have more massive helium burning and CO cores (see Table 4.3), respectively, which is an effect of rotation also found by other studies (e.g. Heger & Langer 2000; Hirschi et al. 2004). Our models with rotation show typically 30% to 50% larger He cores and CO cores than the non-rotating models. A 20 $M_\odot$ star with rotation has thus a core size which is almost as large as the one of a 25 $M_\odot$ non-rotating star. The higher core size means higher central temperatures at the same evolutionary stage and consequently the $^{22}\mathrm{Ne}{+}\alpha$ is activated earlier. The latter means that the He-core s-process contribution increases at the expense of the C-shell contribution. But since the convective He core extends over a higher fraction of total stellar mass than the shell C burning, an overall increase of the s-process efficiency is expected.

Table 4.4: S-process parameters after central He exhaustion

Model[a]	τ_c[b]	$\langle\tau\rangle$[c]	n_c[d]	$\bar{n}^{e}_{n,\max}$	$n_{n,c,\max}$[f,g]	$\Delta X(^{22}\mathrm{Ne})$[g]	$X_r(^{22}\mathrm{Ne})$[g]
	[mb^{-1}]	[$10^{-1}\mathrm{mb}^{-1}$]		[cm^{-3}]	[cm^{-3}]	($\times 10^{-2}$)	($\times 10^{-2}$)
A15s0	1.52	0.581	0.77	3.04(5)	6.58(6)	3.06(-3)	9.70(-3)
A15s4	2.93	1.02	1.60	4.65(5)	1.17(7)	5.59(-3)	7.42(-3)
B15s0	0.883	0.427	0.53	2.32(5)	4.32(6)	3.54(-4)	8.02(-4)
B15s4	3.06	1.51	2.55	5.18(5)	1.07(7)	9.37(-4)	1.02(-3)
C15s0	0.0157	0.0561	0.04	2.85(3)	5.59(4)	3.75(-6)	7.70(-6)
C15s4	2.21	1.07	2.18	3.38(5)	7.33(6)	4.84(-4)	3.92(-4)
A20s0	2.97	0.971	1.52	5.17(5)	1.22(7)	5.34(-3)	7.43(-3)
A20s4	4.66	1.43	2.57	5.89(5)	1.54(7)	7.23(-3)	5.03(-3)
B20s0	1.88	0.761	1.13	4.11(5)	9.10(6)	6.16(-4)	5.46(-4)
B20s4	9.73	4.07	9.85	8.73(5)	2.22(7)	3.49(-3)	1.14(-3)
C20s0	0.0286	0.0401	0.05	6.00(3)	1.31(5)	5.66(-6)	5.74(-6)
C20s4	6.55	2.80	5.87	6.84(5)	1.69(7)	1.52(-3)	4.62(-4)
A25s0	4.42	1.33	2.42	5.85(5)	1.56(7)	7.68(-3)	5.10(-3)
A25s4	5.63	1.60	3.13	5.98(5)	1.72(7)	9.69(-3)	3.28(-3)
B25s0	2.65	0.970	1.64	4.99(5)	1.20(7)	7.52(-4)	4.16(-4)
B25s4	12.1	4.80	12.7	8.03(5)	2.31(7)	4.08(-3)	6.22(-4)
C25s0	0.0466	0.0829	0.08	9.36(3)	2.13(5)	7.21(-6)	4.14(-6)
C25s4	6.73	2.94	5.77	5.77(5)	1.53(7)	1.23(-3)	1.69(-4)
C25s4b[g]	16.4	7.15	23.1	8.02(5)	2.10(7)	1.27(-3)	1.82(-4)
C25s5	13.5	5.73	16.5	8.27(5)	2.26(7)	3.83(-3)	4.94(-4)
C25s5b[g]	20.3	8.67	31.8	1.01(6)	2.74(7)	3.75(-3)	4.85(-4)
D25s0	0.166	0.0866	6.31	9.61(2)	2.24(4)	8.28(-7)	4.67(-7)
D25s4	0.804	0.354	14.0	1.39(5)	3.38(6)	1.05(-4)	3.81(-5)
D25s4b[g]	2.29	1.048	16.5	3.85(5)	8.60(6)	1.06(-4)	3.96(-5)
D25s6	19.2	7.78	33.5	6.77(5)	2.03(7)	4.57(-3)	2.68(-4)
D25s6b[g]	24.6	10.0	48.5	9.77(5)	2.76(7)	4.44(-3)	3.11(-4)
A40s4	7.76	2.00	4.05	3.77(5)	1.42(7)	1.23(-2)	5.29(-4)
B40s4	12.1	4.12	10.6	6.38(5)	2.13(7)	3.31(-3)	1.06(-4)
C40s4	11.6	4.67	10.4	6.12(5)	1.97(7)	2.70(-3)	1.93(-5)

Notes. [a] The A-series models have metallicty of $Z = Z_\odot$, B-series $Z = 10^{-1}$, C-series $Z = 10^{-5}$, and D-series $Z = 10^{-7}$. [b] Central neutron exposure calculated according to Eq. 1.5. [c] Neutron exposure averaged over He core (see Eq. 1.15). [d] Number of neutron capture per seed calculated according to Eq. 1.16, averaged over the He-core mass. [e] Maximum of the mean neutron density. [f] Maximum of the central neutron density. [g] Values in brackets are the exponents ($x(y) = x \times 10^y$). [h] This model was calculated with the same initial parameters as the model, on the line above, but with $^{17}\mathrm{O}(\alpha,\gamma)$ reaction rate of CF88 divided by 10.

At solar metallicity the difference between rotating and non-rotating stars is only found in the core size, but not in the amount of available ^{22}Ne. This becomes clear if one compares $X(^{22}\mathrm{Ne}) = \Delta X(^{22}\mathrm{Ne}) + X_\mathrm{r}(^{22}\mathrm{Ne})$ of the A-series models in Table 4.4. In mass fraction, $X(^{22}\mathrm{Ne}) \approx 1.3 \times 10^{-2}$ is available for α-captures, which is therefore mainly secondary, and about the same independent of rotation. This means also that the mixing is not very efficient at $Z = Z_\odot$ and does not produce important amounts of primary ^{22}Ne. The difference in s-process efficiency is therefore mainly due to the rotation induced larger core size, which is caused by mixing during the main sequence. The difference in the neutron exposure therefore appears primarily, because of higher fraction of burned ^{22}Ne. The difference in s processing between rotating and non-rotating stars is the the smallest at 25 $M_\odot$ (A25s0 vs A25s4), when comparing 15 to 25 $M_\odot$ models. It is related to the saturation of the s process towards higher core masses, which was already found by Langer et al. (1989) and can be seen in Fig. 4.6. It shows n_c after He burning versus CO-core mass of rotating (blue squares) and non-rotating stars (red circles). The overall production of heavy elements is the most efficient for the 40 $M_\odot$ star with rotation, but saturates for $M_\mathrm{CO} > 7$ M$_\odot$ (initial mass > 25 $M_\odot$). The saturation is caused by the exhaustion of ^{22}Ne, and is illustrated by model A40s4, which has burned 96% of available ^{22}Ne after He burning. At the same time consumption of the iron seeds ranges from 35% (A15s0) to 80% (A40s4) in $Z = Z_\odot$ models.

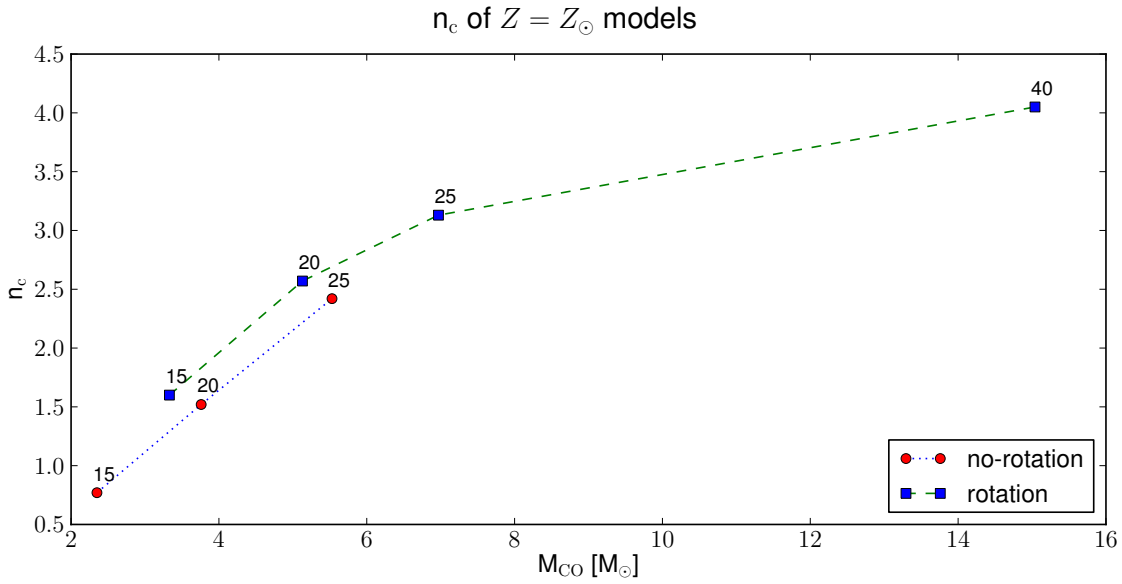

Figure 4.6: Average number of neutron captures per seed n_c versus M_CO for solar metallicity models after central He burning. Blue squares show rotating stars and red circles non-rotating stars. The initial mass of each star is written above the symbol.

In Fig. 4.7 the overproduction factors of 25 $M_\odot$ models (A25s0 and A25s4) with solar metallicity after the end of He burning are shown. Model A25s4 (circles) shows only a moderate increase of the s-process production with respect to A25s0 (diamonds). Both models produce heavy isotopes from iron seeds up to the Sr-peak ($A \approx 90$). In A25s0 model, 66% of Fe is destroyed, and in A25s4 73%. The varying overproduction factors ($\neq 1$) beyond $A = 90$ are only redistributed pre-existing heavy nuclei. This figure therefore illustrates that not only the s-process quantities given in Table 4.4 are similar, but also the abundances pattern

of rotating and non-rotating models at solar Z are almost identical. The difference in the efficiency is only caused by the larger core size of the rotating star.

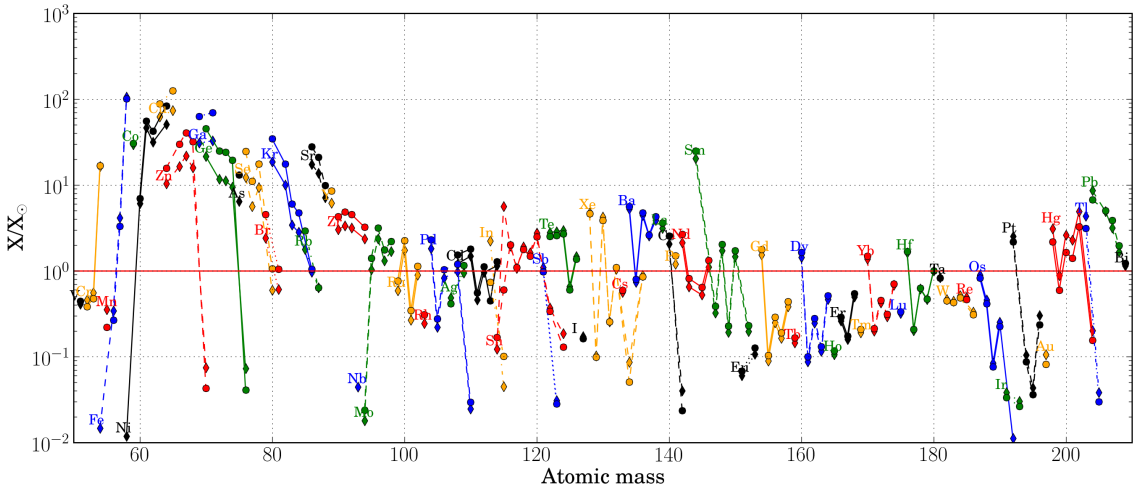

Figure 4.7: Isotopic overproduction factors (abundances over initial abundances) of 25 $M_\odot$ models with solar metallicity after He exhaustion. The rotating model (A25s4, circles) has slightly higher factors that the non-rotating model (A25s0, diamonds).

At sub-solar metallicity the differences between rotating and non-rotating models are much more striking. Rotating models have much higher neutron exposures compared to non-rotating stars, which is due to the primary ^{22}Ne produced and burned during central He burning (see Section 4.2). This is also illustrated by the 3 to 270 times higher amount of ^{22}Ne burned in rotating stars up to central He exhaustion, depending on the initial mass (or $M_{\rm CO}$) and metallicity. The s-process boosting effect of this primary ^{22}Ne is partially eaten away again by ^{22}Ne and ^{25}Mg, which are now primary neutron poisons (Pignatari et al. 2008). Figures 4.8, 4.9 and 4.10 show the abundance normalised to solar in the CO core of 25 $M_\odot$ stars with $Z = 10^{-3}$, $Z = 10^{-5}$ and $Z = 10^{-7}$ just after central He exhaustion, each for a rotating (circles) and a non-rotating model (diamonds). Going from $Z = Z_\odot$ (Fig. 4.7) to $Z = 10^{-3}$ and 10^{-5} (Fig. 4.8 and 4.9) the production of nuclei between $A = 60$ and 90 vanishes in the non-rotating models, which is what is expected from the combination of secondary neutron source, secondary seeds and primary neutron poisons. The non-rotating model at $Z = 10^{-7}$ (D25s0, diamonds in Fig. 4.10) is special with its small amount of primary ^{22}Ne. The rotating models at sub-solar Z produce efficiently up to Sr ($Z = 10^{-3}$), Ba ($Z = 10^{-5}$) and finally up to Pb ($Z = 10^{-7}$). At the same time the consumption of iron seeds increases from 74% at $Z = Z_\odot$ (A25s4) to 96% (B25s4), 97% (C25s4) and 99% (D25s6) at $Z = 10^{-3}$, $Z = 10^{-5}$ and $Z = 10^{-7}$, respectively. Also with the standard rotation rate $\upsilon_{\rm ini}/\upsilon_{\rm crit} = 0.4$ around 90% of initial Fe is destroyed in models with 25 $M_\odot$ and $Z < Z_\odot$. Hence already from the s process in He burning one can conclude, that the primary neutron source in the rotating models is sufficient to deplete all the seeds and the production is limited by the seeds (not the neutron source any more). The other stellar masses show similar trends towards lower Z. Except with the lower masses being in general less efficient, and heavier masses more efficient in burning ^{22}Ne during central He burning.

It is interesting to look at the rotation dependence of the non-standard s-process produc-

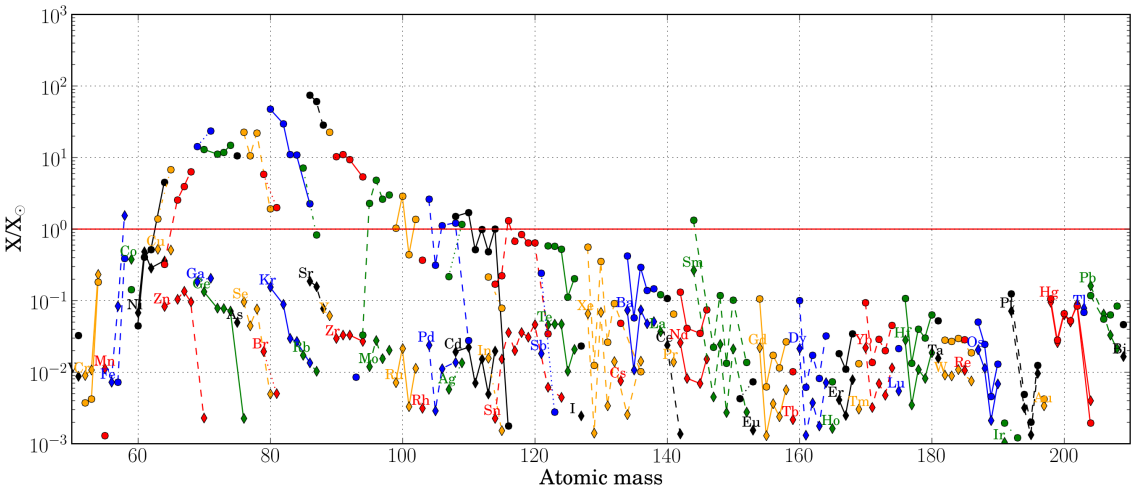

Figure 4.8: Isotopic abundances normalised to solar abundances of 25 $M_{\odot}$ models with with $Z = 10^{-3}$ after He exhaustion. The rotating model (B25s4, circles) has higher factors that the non-rotating model (B25s0, diamonds).

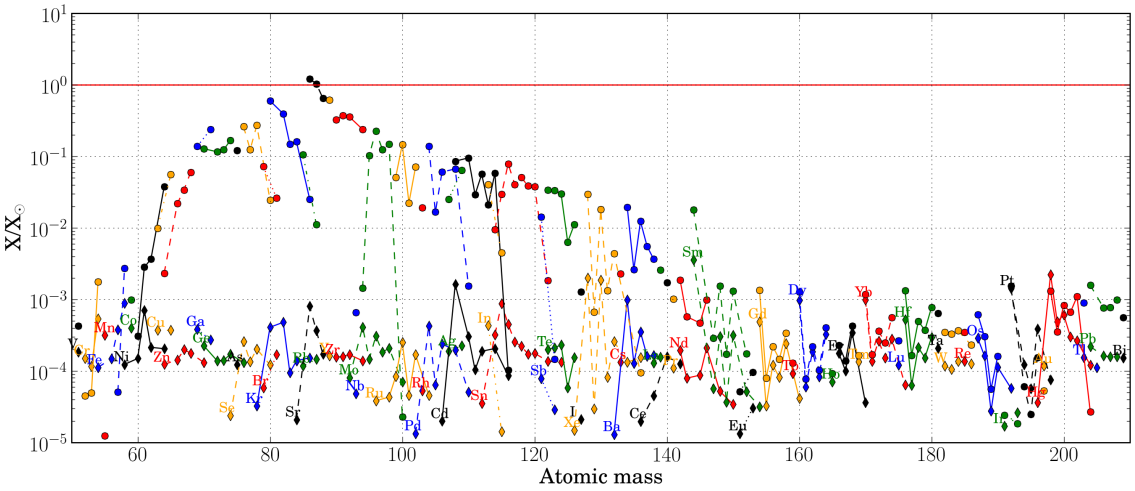

Figure 4.9: Isotopic abundances normalised to solar abundances of 25 $M_{\odot}$ models with with $Z = 10^{-5}$ after He exhaustion. The rotating model (C25s5, circles) has much higher factors that the non-rotating model (C25s0, diamonds).

tion. At $Z = 10^{-5}$ the faster rotating model (C25s5) does not produce more heavy isotopes beyond iron compared to the one with standard rotation (C25s4). Instead, what happens is that not only iron is depleted but elements up to Sr are partially destroyed (after being produced) and heavier elements like Ba are produced. Even at the lowest metallicities in a very fast rotating model (D25s6 and D25s6b, $\upsilon_{\rm ini}/\upsilon_{\rm crit} = 0.6$ instead of the standard 0.4), and thus with a larger primary neutron source, there is no additional production of s-process elements starting from light element seeds like ^{22}Ne. Indeed, going from [Fe/H] $= -3.8$ (C25s4) to [Fe/H] $= -5.8$ (D25s4), the Sr yield decreases by a factor of ~ 9, while the Ba yield increases

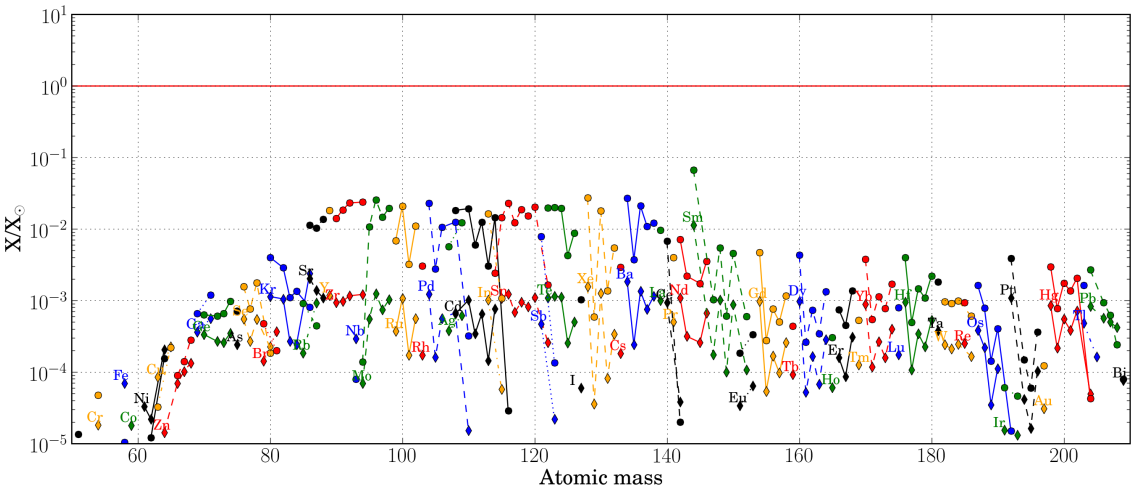

Figure 4.10: Isotopic abundances normalised to solar abundances of 25 $M_\odot$ models with with $Z = 10^{-7}$ after He exhaustion. The rotating model (D25s6, circles) has slightly higher factors that the non-rotating model (D25s0, diamonds).

by a factor of 5. Hence, the production is limited mainly by the iron seeds.

Models with a reduced $^{17}O(\alpha,\gamma)$ (C25s4b, C25s5b, D25s4b and D25s6b) are of course similarly limited by seeds. Therefore the higher number of available neutrons acts in a similar way as a higher amount of ^{22}Ne by faster rotation. Already a reduction of $^{17}O(\alpha,\gamma)$ by a factor 10 boosts the s process up to Ba more (model C25s4b) than going from standard (C25s4) to faster rotation (C25s5). Models C25s4b, C25s5b, D25s4b and D25s6b show [Sr/Ba] of about +1, +0.3, 0, and −0.6 which is rather "main" s-process-like. These models therefore emphasises the importance of ^{16}O as a neutron poison, when using the CF88 rate, and in general the uncertainties in the primary neutron poisons.

The normalisation to solar composition allows to compare the low Z models in Figures 4.8, 4.9, and 4.10 to the solar Z models in Fig. 4.7 with respect to their total production. Model B25s4 produces overall similar amounts of heavy nuclei in the range A = 60-90 as models A25s0 and A25s4. A closer look reveals that the solar metallicity models produce higher amounts beyond Fe up to Ge. For isotopes of As, Se, Br and Kr, A25s0, A25s4 and B25s4 produce similar amounts, while for Sr, Y and Zr B25s4 produces more. However, here one has to keep in mind, that for the final picture also the shell C burning contribution has to be taken into account. Models A25s0, A25s4 and B25s4 compared to C25s5 (Fig. 4.9) make it clear that rotating stars at $Z = 10^{-5}$ (initial [Fe/H] = −3.8) cannot contribute significantly to chemical enrichment at solar Z, because the $X/X_\odot$ values are only around 1 or lower for C25s5. This is even more true for D25s6 in Fig. 4.10. For the Sr, Y, and Zr, still a contribution from rotating stars with Z between 10^{-3} (initial [Fe/H] = −1.8) and 10^{-5} can be expected. For the non-rotating stars the s-process contribution is already negligible at 10^{-3}.

C shell burning

In carbon burning α particles are released by ^{12}C+^{12}C (see Reaction Sequence 1.3). Raiteri et al. (1991a) found that the free α particles can trigger major s-process nucleosynthesis by $^{22}Ne(\alpha,n)$. Other studies of the s process in shell C burning (The et al. 2007) and

evolution of massive stars including nucleosynthesis confirmed that ^{22}Ne(α, n) is the only important neutron source in C-shell burning (e.g. Limongi et al. 2000; Woosley et al. 2002). The remaining ^{22}Ne left after central He burning is consumed in a very short time (time scale ~ 1 yr). At shell C burning temperatures ($T_9 = 1$) the ratio of the ^{22}Ne(α, n) to ^{22}Ne(α, γ) rates is about 230. The ^{22}Ne(α, γ) is therefore not a strong competitor to the neutron emission channel any more. ^{13}C(α, n) recycles the neutrons captured on ^{12}C. Other neutron sources as ^{17}O(α, n) and ^{21}Ne(α, n) recycle only partially the neutrons absorbed by ^{16}O and ^{20}Ne (e.g. Limongi et al. 2000). The main neutron poisons are ^{16}O, ^{20}Ne, ^{23}Na, and ^{24}Mg, which are primary and the seeds are the remaining iron and heavier nuclei.

Shell C-burning occurs in the CO core (see Table 4.3) after central C burning. How the shells proceed depend on whether central C burning appears radiative or in a convective core. It is thus sensitive to the C/O ratio in the core after He burning and therefore on the ^{12}C(α, γ) rate. The uncertainty of this rate and its impact on the stellar structure evolution was studied for example in El Eid et al. (2004). In our models between one and three convective C-burning shells appear in the course of the evolution. The last shell has a maximal extension up to $M_r = M_{\rm C}^{\rm max}$. In most of the models, a large fraction of the He-burning s-process material is reprocessed. Comparing $M_{\rm C}^{\rm max}$ to $M_{\rm He}^{\rm max}$ in Table 4.3 shows that only 10 to 20% of the CO core is not reprocessed and keeps the pure signature of the He-burning s process.

The activation ^{22}Ne(α, n) at the start of C-shell burning shows up as a short neutron burst with relatively high neutron densities, compared to He burning. The efficiency of the s process mainly depends on the remaining iron seeds and ^{22}Ne left after He burning, $X_{\rm r}(^{22}{\rm Ne})$, in the CO core. All the remaining ^{22}Ne is burned quickly with maximal neutron densities between 6×10^9 and 10^{12} cm^{-3}, for the both extremes in models B15s4 and A40s4, respectively. The time scale of this s process is in our models of the order of a few tens of years in 15 $M_\odot$ stars to a few tenth of years in 40 $M_\odot$. Temperatures and densities at the start of C-shell burning show the same behaviour as the core burning conditions, i.e. the temperatures increase and the densities decrease with core mass. They vary between $T_9 \approx 0.8$, $\rho \approx 2 \times 10^5$ g cm^{-3} in 15 $M_\odot$ stars and $T_9 \approx 1.3$, $\rho \approx 8 \times 10^4$ g cm^{-3} in 40 $M_\odot$ model. These temperatures are higher than in the central C burning, where $T_9 = 0.6 - 0.8$.

In Figures 4.11 and 4.12 the ratio of abundances after shell C burning to the abundances after core He burning, $X_{\rm C}/X_{\rm He}$ is plotted, in a 25 $M_\odot$ star at $Z = Z_\odot$. Figure 4.11 illustrates the abundance modification in the non-rotating model (A25s0) and Fig. 4.12 the same by the rotating model (A25s4). In both models there is an overproduction of most isotopes from Zn to Rb. It is also found in the other models which have both,

1. $X_{\rm r}(^{22}{\rm Ne}) \gtrsim 10^{-3}$ and
2. $X(^{56}{\rm Fe}) \gtrsim 10^{-4}$, at the start of shell C burning

Therefore only 15 to 25 $M_\odot$ stars at solar Z have a considerable overall C-shell contribution. Since in our models with $Z < Z_\odot$ the s process in the helium core is already limited by the seeds. And as a consequence, the C-burning shell has a small contribution ($< 10\%$) at sub-solar metallicity.

In the mass range $A = 60$ to 90, ^{63}Ni, ^{79}Se, and ^{85}Kr are branching points. The high neutron densities modify the s-process branching ratios (see Section 1.4.1), in a way that the neutron capture on the branching nuclei are favoured (see e.g. The et al. 2007, for a discussion on the ^{79}Se branching). The relatively high neutron densities in shell C burning therefore change the s-process path and lower the branching ratios ^{64}Zn/^{66}Zn, ^{80}Kr/^{82}Kr, ^{86}Sr/^{88}Sr,

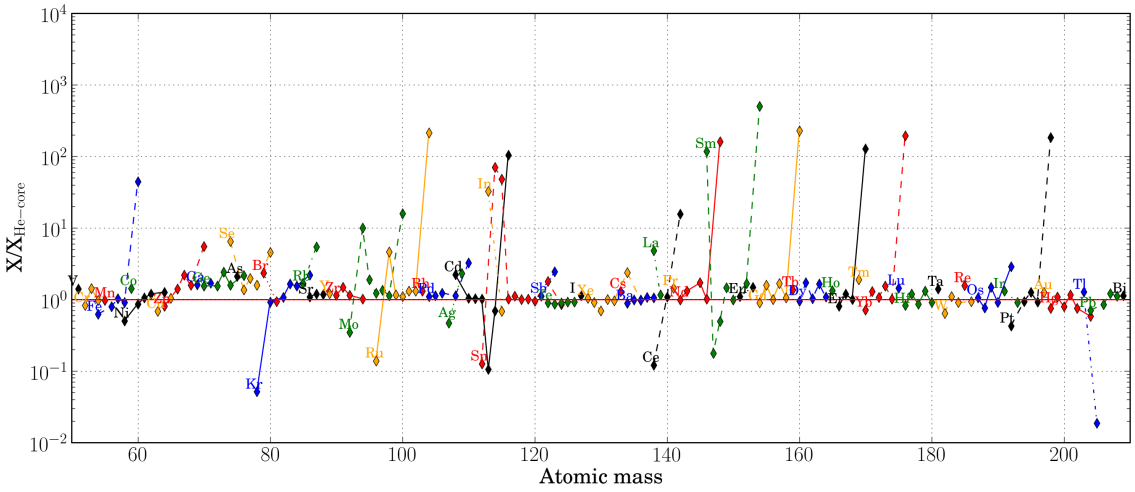

Figure 4.11: Ratio of abundances after shell C burning to the abundances after core He burning, X_C/X_{He}, in a non-rotating 25 $M_\odot$ star at $Z = Z_\odot$. It illustrates the modification of the abundances by s process in shell C burning.

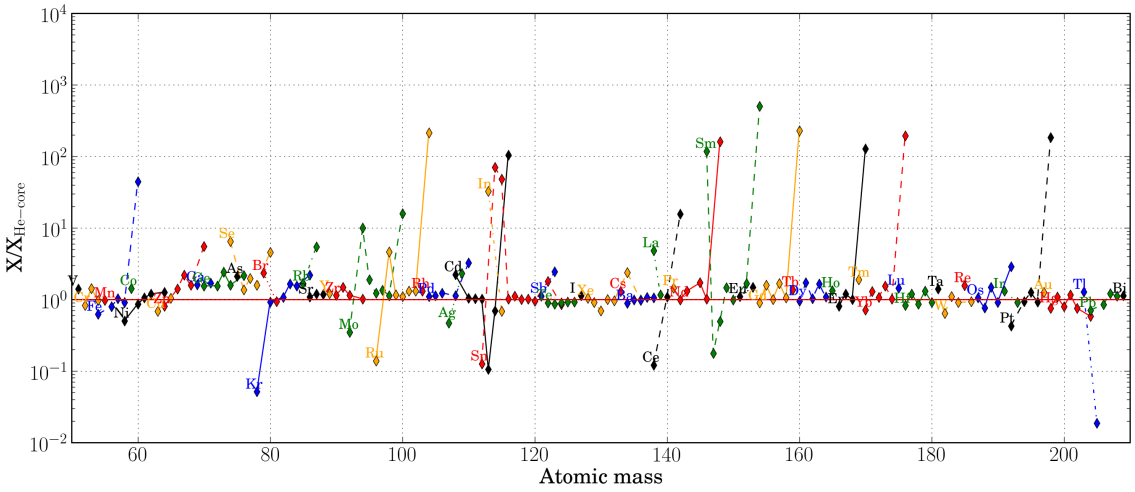

Figure 4.12: Ratio of abundances after shell C burning to the abundances after core He burning, X_C/X_{He}, in a rotating 25 $M_\odot$ star at $Z = Z_\odot$. It illustrates the modification of the abundances by s process in shell C burning.

as well as ^{79}Br/^{81}Br and ^{85}Rb/^{87}Rb. Since the neutron densities increase with core mass the different stars show very different final branching ratios. Stars with 15 $M_\odot$ and with 20 $M_\odot$ without rotation still produce ^{64}Zn, ^{80}Kr, ^{86}Sr in the C shell, while in 20 $M_\odot$ stars with rotation and heavier stars these isotopes are destroyed. Stars with rotation have higher neutron densities, because of the primary ^{22}Ne, and consequently the branching ratios drop more than in the non-rotating models. However, this effect occurs only at solar Z, since shell C burning is mainly efficient at solar metallicity ($Z = 0.014$) or higher.

The most obvious impact of C-shell s process in Figures 4.11 and 4.12 is also caused by the high neutron densities. It is the strong overproduction of some r-process only nuclei, such as ^{70}Zn, ^{76}Ge, ^{82}Se, or ^{96}Zr, which rebuilds at least partially what was destroyed before by the "slower" s process in He burning. ^{96}Zr is produced in shell C burning of all stars except the 15 $M_\odot$ with $Z < Z_\odot$. ^{70}Zn and ^{76}Ge are only created in 20 to 40 $M_\odot$ stars with rotation and in the non-rotating 25 $M_\odot$ $Z = Z_\odot$ star. ^{82}Se is only produced in the C shells with the highest neutron densities i.e. in 40 $M_\odot$ stars. The production of r-only nuclei in carbon burning compensates only the destruction in the He-core s process when looking at final the yields. Only for 40 $M_\odot$ stars ^{96}Zr has a weak overproduction.

In summary we can say, that rotating massive stars have higher neutron densities, because of their different structure and the primary ^{22}Ne. Thus the abundance pattern of He-core and C-shell s process are different, which is displayed by lowered branching ratios. The C-shell s-process contribution of massive rotating stars is also limited to solar-like metallicities, as found in previous studies, but with the difference that the limitation at sub-solar Z is coming from the missing seeds.

He shell burning

Shell He burning similar to the other burning shells appear at higher temperatures and lower densities than the equivalent central burning phase. In our models high temperature conditions of $T_8 \approx$ 3.5-4.5 and $\rho \approx$ 3-5.5 $\times 10^3$ g cm^{-3} are ideal for s process in shell He burning. Additionally the primary ^{22}Ne in rotating models is at the level of 10^{-2} at all metallicities.

However, the highest neutron densities are reached in all our models only in the layers below the convective shell helium burning. Therefore only a narrow range inside the stars is affected by the free neutrons, which extends over about 0.2 $M_\odot$ in non-rotating and 0.4 $M_\odot$ in rotating stars. In rotating stars the larger s-process shell arises from the smoother abundance profiles introduced by mixing. Other stellar models (Tur et al. 2009) have the ^{22}Ne burning layers included in the convective shell and can therefore have higher He-shell s-process yields.

The contribution to the total s-process yields is therefore low in our models, and only in the region of 5% for solar metallicity 25 $M_\odot$ stars with and without rotation. For less massive stars the He shell gains more weight and produces in 15 $M_\odot$ models with rotation up to 50% of the total yields. Thus for the 15 to 20 $M_\odot$ stars also the He-shell s-process contribution has to be considered.

Total and relative yields

In Fig. 4.13 the dependence of total ^{68}Zn yields on the mass and metallicity are displayed for rotating stars with standard rotation rate ($\upsilon_{\rm ini}/\upsilon_{\rm crit} = 0.4$) on the right hand side and non-rotating stars on the left hand side. The red circles display the location of our models in the mass-metallicity space. The values in between the data points are interpolated linearly

in $\log(m)$. We chose ^{68}Zn as a representative for the isotopes in range A = 60-80, because it is produced in the s process of core He burning, shell C, and shell He burning. A similar plot is given for ^{88}Sr in Fig. 4.14, to show the different dependence of the Sr-peak elements in stars with rotation (^{86}Sr, ^{87}Sr, ^{89}Y, and ^{90}Zr show the same trends as ^{88}Sr) compared to non-rotating stars. Several differences between the standard and rotation boosted s process become very obvious.

1. From the comparison of left and right hand side in both figures, the higher yield of rotating stars become clear for solar as well as for low metallicity stars.

2. The yields of non-rotating stars as well as the ^{68}Zn yields of rotating stars show a secondary-like behaviour, going from reddish to blueish colours towards lower Z.

3. While the ^{68}Zn yields of non-rotating stars drop by five orders of magnitude when the metallicity goes down by a factor 10^3, the yields from rotating stars drop only by a factor 10^3. The scaling with metallicty is less steep for rotating models. Strictly speaking, therefore only the boosted s process from rotating stars is a secondary process.

4. The Sr-peak isotopes do not show a secondary behaviour for stars with rotation and $M > 15\ M_\odot$ in the metallicity range between solar ($Z = 0.014$, $\log(Z/Z_\odot) = 0$) and about one hundredth ($Z = 1.4 \times 10^{-4}$, $\log(Z/Z_\odot) = -2$) of solar metallicity, but they eject maximal yields around one tenth of solar metallicity (dark red around $\log(Z/Z_\odot) = -1$) for 20 to 30 $M_\odot$ stars.

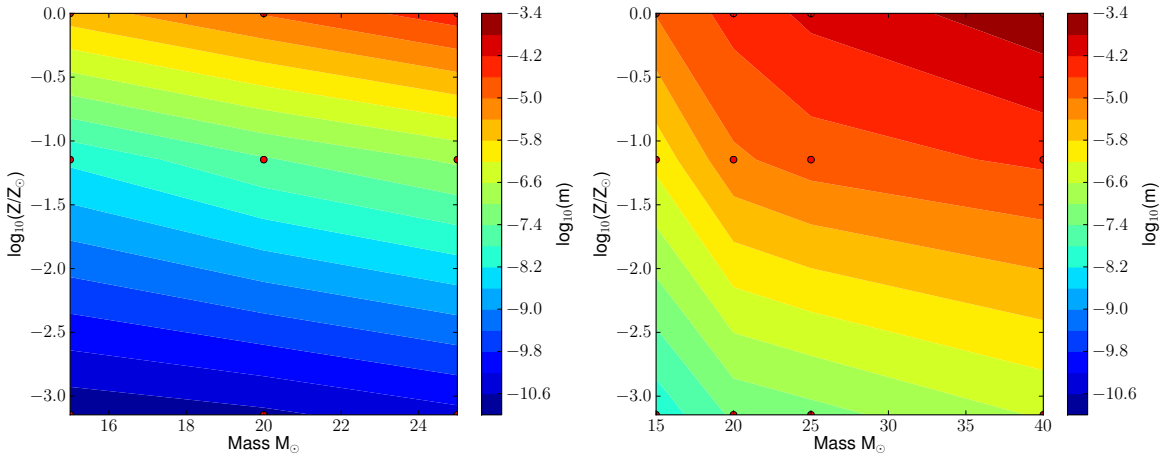

Figure 4.13: S-process yields, m, of ^{68}Zn in $M_\odot$ to illustrate the mass and metallicity dependence of the s process, without rotation on the left hand side and with rotation on the right hand side. The red circles display the location of our models in the mass-metallicity space. The values in between the data points are interpolated linearly in $\log(m)$.

In Fig. 4.15 the yields of ^{68}Zn of the three s-process sites normalised to the total yields are displayed, for non-rotating stars on the left hand side and rotating stars on the right hand side, and from top to the bottom for He-core, C-shell and He-shell burning yields. This figure allows a good comparison for which mass and metallicity the three different sites are contributing a lot to the total yields. The following points can be derived:

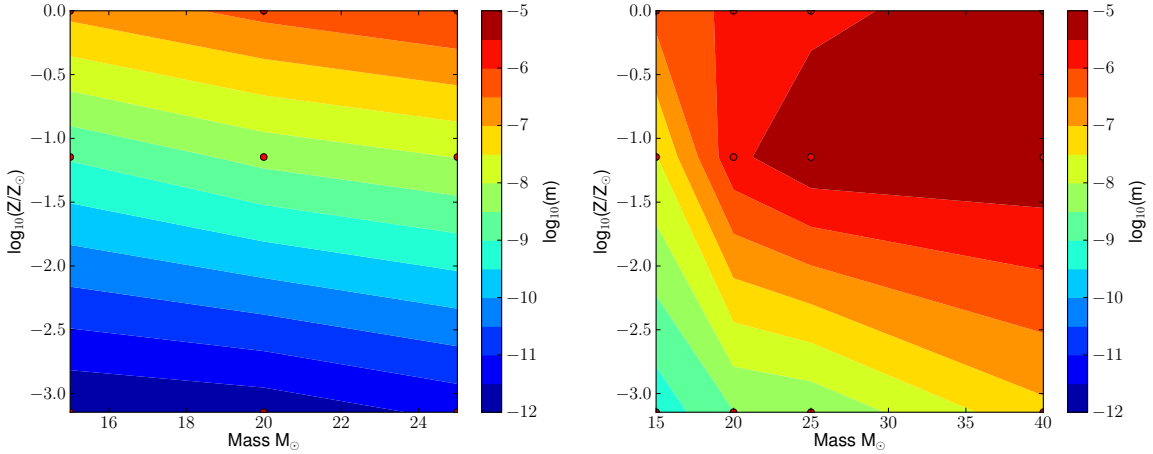

Figure 4.14: S-process yields, m, of ^{88}Sr in $M_\odot$ to illustrate the mass and metallicity dependence of the s process, without rotation on the left hand side and with rotation on the right hand side. The red circles display the location of our models in the mass-metallicity space. The values in between the data points are interpolated linearly in $\log(m)$.

1. The overall production is the largest from He-core burning (colours yellow to red in Fig. 4.15a and 4.15b). Surprisingly, at solar Z in non-rotating models the strongest contribution comes from carbon shell burning (see Fig. 4.15c), which is not seen in previous literature (e.g. The et al. 2007). This is not the case in stars with rotation. We suspect that this is the effect of the high $^{22}\mathrm{Ne}(\alpha,\gamma)$ rate of NACRE, which is in strong competition to the neutron source during central He burning. This is not that pronounced for rotating stars since they have higher central temperatures.

2. Shell carbon burning is, compared to the other two sites, only efficient at solar metallicity (see Fig. 4.15c and Fig. 4.15d), caused by the low amount of ^{22}Ne left, the missing seeds and the primary neutron poisons, which have an increased strength towards lower Z.

3. Shell He burning contributes only a small fraction but typically 5% to the final yields (see Fig. 4.15e and Fig. 4.15f). The exceptions are the rotating 15 to 25 $M_\odot$ stars at low Z and rotating 15 to 20 $M_\odot$ stars at solar Z. It is the effect of decreasing contribution from the He core towards lower masses and the higher burning temperatures in the shell compared to the He core, which allows also an efficient activation of $^{22}\mathrm{Ne}(\alpha,n)$ in the 15 $M_\odot$ models. Additionally the He shell is not limited by the missing iron seeds consumed by s process in He core but occurs in a region providing the initial iron content.

So as a final conclusion we can say: Massive rotating stars produce more heavy nuclei that non-rotating stars at all metallicities, especially at $Z = Z_\odot$. Massive non-rotating stars contribute to the chemical enrichment of "weak" s-process isotopes only for $Z > 10^{-3}$, while for rotating stars the same is true for isotopes with $A \lesssim 80$. But for Sr-peak isotopes produced by rotating stars the metallicity range of $Z \gtrsim 10^{-4}$ has to be considered.

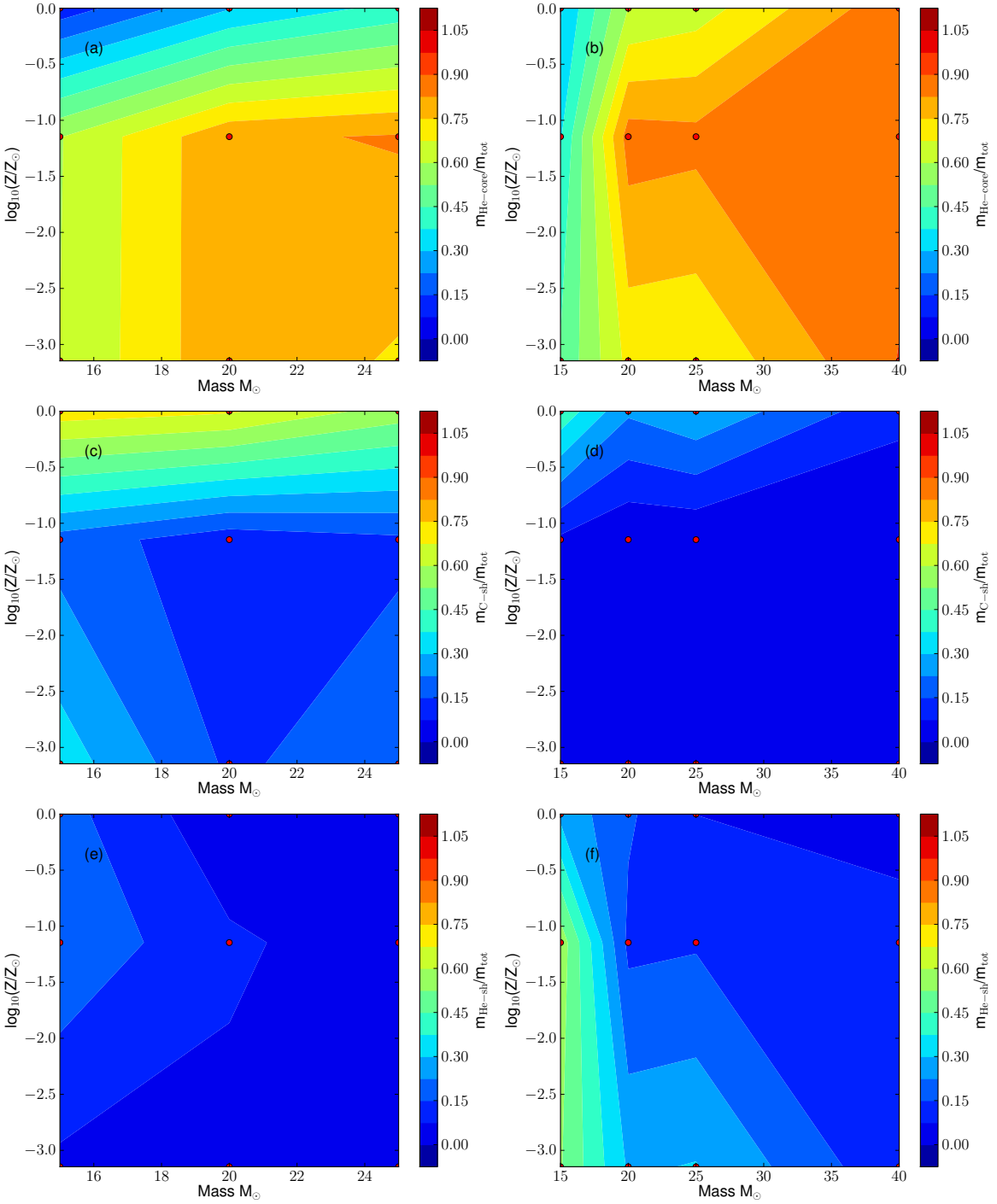

Figure 4.15: S-process site yields of ^{68}Zn normalised to the total yields to illustrate the different relative contributions as a function of mass and metallicity Z, for He core without (a) and with rotation (b), for C shell without (c) and with rotation (d), and the He shell without (e) and with rotation (f). The red circles display the location of our models in the mass-metallicity space.

4.4.2 Comparison to the literature

He-burning s process

In Table 4.5 the overproduction factors $X_i/X_{i,\mathrm{ini}}$ in the center of solar metallicity 25 $M_\odot$ models after the end of central He burning are presented. It shows $X_i/X_{i,\mathrm{ini}}$ for isotopes between Cu and Zr for the models with (A25s4) and without rotation (A25s0), as well as for models 1 and 2 from Pignatari et al. (2010), models 25K and 25C from The et al. (2007) which are based on stellar models of El Eid et al. (2004), and the model from Raiteri et al. (1991b).

First of all, the overproduction factors in Table 4.5 show a wide spread between the models. For the lighter nuclei as for example Cu and Zn isotopes, the most efficient models (Pi10-2, T07-25C, Ra91a) produce four to seven times more than the least efficient model (A25s0). This difference becomes even more pronounced for heavier isotopes, e.g. ^{86}Sr, where the difference from the least efficient (A25s0) to the most efficient models (T07-25C, Ra91a) can exceed a factor of twenty. Model Pi10-2 produces large amounts of Cu isotopes, while for heavier elements the production factors can not keep up with those of T07-25C and Ra91a.

In Table 4.6 we show the characteristic s-process parameters of the same models. The central neutron exposure τ_c and the convective core averaged neutron exposure $\langle\tau\rangle$ together with the average number of neutron captures per seed n_c describe the s-process efficiency. These s-process quantities show a similar picture as the overproduction factors in Table 4.5. The most efficient models are again Pi10-2 and T07-25C, Ra91a, and the least efficient model is A25s0.

There are several important differences between our models (A25s0, A25s4) and the others, namely in the initial composition and the nuclear reaction input, which explain the big differences. Here these differences are listed.

- We used for our models with solar-like composition the initial chemical composition from Asplund et al. (2005) with a metallicity $Z = 0.014$. The other authors used the solar composition from Anders & Grevesse (1989) with $Z \approx 0.019$. It means that in our models the secondary ^{22}Ne and the iron seeds are reduced by about 35%. From a reduction of the ^{22}Ne neutron source and the seeds a reduction of the s-process production is expected. However, if one uses a solar-like composition with lower Z, this is partially compensated in the overproduction factors by the normalisation to the smaller initial abundances. It is only partially compensated, because the source and the seeds are reduced while the primary poisons not, and the standard s process scales therefore less than secondary. The impact of a similar change, from Anders & Grevesse (1989) composition to the one of Lodders (2003) with $Z = 0.0149$, was investigated by Tur et al. (2009). They found that the change of initial composition can modify the final production factors by 0.2 to 0.5 dex for 25 $M_\odot$ stars. Since we used $Z = 0.014$ in our solar Z models, the reduction in the overproduction factors is even higher.

- In Table 4.7 the sources of the reaction rates used in the works, compared here, are listed. The neutron source and the $^{22}\mathrm{Ne}(\alpha,n)/^{22}\mathrm{Ne}(\alpha,\gamma)$ ratio, respectively, of our models is only similar in Pi10-1, but they use the lower rate for $^{22}\mathrm{Ne}(\alpha,\gamma)$ of Karakas et al. (2006), which is lower than the NACRE rate we used. The rates for the neutron source of CF88 and NACRE are both considerably higher (see discussion in NACRE and Jaeger et al. 2001). Therefore all other models used more favourable combinations

of ^{22}Ne+α rates for the s process. There is, however, an indication that our choice of rates lead to a too weak s process at solar metallicities, because in our models only Cu istopes are overproduced in a similar amount as ^{16}O but all other isotopes less (see Pignatari et al. 2010).

- In the mass region $A = 50 - 90$ many (n, γ) rates, relevant for the s process, were found to be lower by new measurements in the past 15 years, which is displayed in Fig. 3.2. Thus the neutron capture rates also changed over the time frame of the different studies. Pignatari et al. (2010) used the same rates of KADoNiS v0.3, as we did in our models. The rate reduction of several s-process path bottlenecks, in particular at ^{63}Cu hinder the s process and reduce the overproduction factors above the copper isotopes, when using the newer rate compilation.

- The ^{12}C$(\alpha, \gamma)^{16}$O rate sources are listed in table 4.7. The rate of Kunz et al. (2002) is the lowest and about 10 to 20% smaller than the NACRE rate in the relevant temperature region for core He burning. A higher rate means that the star can obtain the same amount of energy at lower temperatures. In this way a lower rate supports the s process. Tur et al. (2009) studied the impact of the uncertainty in the ^{12}C$(\alpha, \gamma)^{16}$O rate. And a reduction of this rate by 10 to 20% increases the overproduction factors on average by 0.1 to 0.2 dex.

- Neglecting mass loss for here the compared 25 $M_\odot$ models means that the core is larger during the core He-burning phase, and consequently has higher temperatures. The et al. (2007) point out the possible impact of such a change with their models 25N and 25NM. Pignatari et al. (2010) and Raiteri et al. (1991b) used stellar models calculated with the Frascati Raphson Newton Evolutionary Code (FRANEC), which did not include mass loss (Käppeler et al. 1994). The maximal core size of their model during He burning is $M_{\rm He}^{\rm max} = 6.17$ M$_\odot$ (priv. comm. M. Pignatari). It lies thus between the core sizes of our models A25s0 and A25s4 (see Table 4.3). The mass loss introduces therefore a rather moderate uncertainty, but still reduces the overproduction factors, n_c and $\langle\tau\rangle$ by about 10%.

These various differences in the nuclear reaction input as well as the stellar models make it very hard to disentangle the impact of the different parameters quantitatively. On the qualitative side, our models are consistent with the previous publications considering the above discussed differences.

If we compare the difference between our two models (A25s0, A25s4) and the other model we can also conclude, that the effect of rotation at solar metallicity is rather moderate and well within the nuclear reaction rate uncertainties. This is the case because ^{22}Ne production by rotation induced mixing does not play a role at $Z = Z_\odot$

Table 4.5: Production factors[a] of 25 $M_\odot$ models after central He exhaustion

Model	A25s0[b]	A25s4[b]	Pi10-1	Pi10-2	T07-25K	T07-25C	Ra91a
Isotope	Overproduction factors						
^{63}Cu	62.0	88.0	127	134	60.8	78.2	91.8
^{65}Cu	73.7	125	280	317	128	205	226.3
^{64}Zn	10.4	15.7	34.1	36.8	30.7	43.6	41.0
^{66}Zn	16.5	30.0	76.3	88.7	59.6	107	118.9
^{67}Zn	21.8	40.7	109	127	82.9	153	171.7
^{68}Zn	16.0	32.1	99.1	121	73.1	158	164.7
^{70}Zn	0.1	0.0	0.3	0.3	0.4	0.6	...
^{69}Ga	30.8	63.1	126	156	...	...	208.6
^{71}Ga	32.6	69.4	147	187	...	...	263.9
^{70}Ge	21.5	45.2	154	193	112	270	253.7
^{72}Ge	11.7	24.9	88.0	114	75.2	201	190.7
^{73}Ge	11.2	24.0	82.4	107	46.9	128	128.8
^{74}Ge	9.5	19.5	71.0	94.2	37.5	110	99.3
^{76}Ge	0.1	0.0	0.0	0.0	...	...	...
^{75}As	6.4	13.1	45.3	60.2	27.4	81.9	59.6
^{76}Se	12.3	24.6	99.4	133	78.2	241	212.2
^{77}Se	5.6	11.1	44.0	59.1	...	...	88.6
^{78}Se	9.3	17.6	67.4	91.7	...	...	108.9
^{80}Se	0.6	1.1	1.5	1.9	1.3	4.0	...
^{82}Se	0.3	0.3	0.1	0.1	...	...	...
^{79}Br	2.4	4.5	15.6	21.3	...	...	36.6
^{81}Br	0.6	1.0	15.4	21.1	...	...	...
^{80}Kr	18.7	34.6	169	232	183	618	480.7
^{82}Kr	9.8	17.4	79.1	108	77.9	277	210.3
^{83}Kr	3.4	6.0	25.9	35.5	...	...	63.0
^{84}Kr	2.8	4.7	22.0	29.9	...	...	52.6
^{86}Kr	1.0	1.1	0.7	0.8	2.6	5.7	...
^{85}Rb	1.8	2.9	14.8	20.0	...	...	28.6
^{87}Rb	0.6	0.6	0.8	0.8	1.3	3.0	...
^{86}Sr	17.5	27.8	79.9	107	60.7	232	147.3
^{87}Sr	13.8	21.1	68.8	91.4	50.4	190	129.2
^{88}Sr	7.2	9.9	21.5	26.8	14.9	45.3	34.8
^{89}Y	6.2	8.6	15.6	18.9	...	...	22.3
^{90}Zr	3.0	4.3	6.9	8.2	...	...	...
^{91}Zr	3.3	4.8	8.6	10.1	...	...	...
^{92}Zr	3.2	4.6	7.3	8.5	...	...	...
^{94}Zr	2.4	3.2	5.4	6.3	...	...	...

References. Pi10-x - model x from Pignatari et al. (2010), T07-25K/C - model 25K/C from The et al. (2007), Ra91a - Raiteri et al. (1991b).

Notes. [(a)] Production factors are defined as the mass fractions/abundances X normalised to the initial ones $X_{\rm ini}$. Since the are $Z = Z_\odot$ models, the production factors are $X/X_\odot$.

[(b)] The other authors used the solar abundances of Anders & Grevesse (1989), but we used the one of Asplund et al. (2005).

Table 4.6: S-process parameters in the center of 25 $M_\odot$ stars after central He exhaustion

Model	τ_c[a] [mb^{-1}]	$\langle\tau\rangle$[b] [mb^{-1}]	n_c[c]	$\bar{n}^{\rm d}_{n,\rm max}$ [10^5 cm^{-3}]	$n_{n,c,\rm max}$[e] [10^7 cm^{-3}]	$\Delta X(^{22}\mathrm{Ne})$ ($\times10^{-2}$)	$X_{\rm r}(^{22}\mathrm{Ne})$ ($\times10^{-2}$)
A25s0	3.80	0.133	2.34	5.85	1.56	0.77	0.51
A25s4	4.86	0.160	3.06	5.98	1.72	0.97	0.33
Pi10-1	...	0.197	4.95	11.4	3.22	1.03	1.14
Pi10-2	...	0.209	5.35	10.1	2.88	1.47	0.70
T07-25K	5.00	0.15	3.63	2.53	...	1.39[f]	0.78
T07-25C	5.43	0.30	5.14	1.95	...	1.19[f]	0.98
Ra91a	...	0.206	5.67	6.79	1.80	1.06	0.96

Notes. [(a)] Central neutron exposure calculated according to Eq. 1.5. [(b)] Neutron exposure averaged over He core (see Eq. 1.15). [(c)] Number of neutron capture per seed calculated according to Eq. 1.16, averaged over the He-core mass. [(d)] Maximum of the mean neutron density. [(e)] Maximum of the central neutron density. [(f)] Assuming for the secondary ^{22}Ne a mass fraction of $X(^{22}\mathrm{Ne}) = 2.17 \times 10^{-2}$ at the start of He burning as in Pignatari et al. (2010).

Table 4.7: Used reaction rates for 25 $M_\odot$ $Z = Z_\odot$ models in literature

Model	A25s0	A25s4	Pi10-1	Pi10-2	T07-25K	T07-25C	Ra91a
$^{22}\mathrm{Ne}(\alpha,n)$	Ja01	Ja01	Ja01	NACRE	NACRE	CF88	CF88
$^{22}\mathrm{Ne}(\alpha,\gamma)$	NACRE	NACRE	Ka06	NACRE	NACRE	K94	CF88
$^{12}\mathrm{C}(\alpha,\gamma)$	Ku02	Ku02	CFHZ85	CFHZ85	Ku02	CF88	CFHZ85
n-captures	K0.3	K0.3	K0.3	K0.3	Be92	Be92	

References. Pi10-x - model x of Pignatari et al. (2010), T07-25K/C - model 25K/C of The et al. (2007), Ra91a - Raiteri et al. (1991b), Ja01 - Jaeger et al. (2001), NACRE - Angulo et al. (1999), CF88 - Caughlan & Fowler (1988), Ka06 - Karakas et al. (2006), K94 - Käppeler et al. (1994), Ku02 - Kunz et al. (2002), CFHZ85 - Caughlan et al. (1985), K0.3 - KADoNiS v0.3, Be92 - Beer et al. (1992)

4.4.3 Comparison to observations

Observations of elemental abundances of Germanium (Ge) and Copper (Cu) are known to have a secondary trend with metallicity (Cowan et al. 2005; Bisterzo et al. 2005) in agreement with the theory, which predicts that a major part of these elements come from the s process in massive stars at solar metallicity. As mentioned before rotation would not change the secondary nature of the s-process production of these elements. It is also known that the Sr- peak elements Sr, Y, and Zr have trend with metallicity suggesting a primary production in massive stars. The unknown process responsible for the primary Sr-peak elements, called Light Element Primary Process (LEPP, Travaglio et al. 2004), cannot be explained by the rotation boosted s process. Our models do not produce the Sr-peak elements in a primary way and show only a primary-like production above $Z \approx 10^{-3}$, because the iron seeds are secondary. Still some of the missing Sr-peak nuclei from solar LEPP (Travaglio et al. 2004; Montes et al. 2007) might come from a rotation boosted s process in massive stars.

From the discussion above, we have seen a possible scatter in the production up to Ba, which is however also very uncertain due to uncertainties in neutron poisons. Additionally a scatter in Sr production is intrinsic to the rotation boosted s process, since a varying rotation rate would lead to a varying amount of primary ^{22}Ne and thus to a varying neutron exposure and s-process production, respectively. Typically the s process in massive stars produces only minor amounts of Ba and [Sr/Ba] is around +2, with an upper limit of $\approx +2.3$. However, due to the seed limitation the enhanced s process starts to produce a "main" s-process-like pattern at low Z, and as a consequence [Sr/Ba] ≈ 0. In this case also small amounts of Pb can be produced.

Isotopic ratios like ^{86}Sr/^{88}Sr are involved in branchings. They may constrain the s process and the ratios between the He-core and C-shell contribution. The solar value of ^{86}Sr/^{88}Sr ratio is 0.116 (Lodders 2003). But our models producing efficiently Sr show values between 0.22 and 0.28. A similar trend can be seen in the ^{85}Rb/^{87}Rb. Our stellar models show values between 2 and 10, but typically around 4.5 from the stars with the strongest contribution, which is higher than the solar value of 2.53. Of course for these branching ratios one has also to consider that the solar composition contains a major contribution from AGB stars, however, there only in the pulse driven convective zone high enough neutron densities ($n(n) \approx 10^{11}$ cm^{-3}, Herwig 2005) are reached to lower this ratio, assuming the same nuclear physics. The r-process contribution to ^{88}Sr is rather moderate (Sneden et al. 2008), therefore will reduce ^{86}Sr/^{88}Sr just slightly. For ^{85}Rb/^{87}Rb, the r-process would rather increasing the ratio, by producing more ^{85}Rb (Sneden et al. 2008). Both ratios show the same trend. A reason could be that the branching at ^{85}Kr has either a too low β^--decay half life, or the neutron capture rate is too low. The branching ratio of ^{80}Kr/^{82}Kr from the most efficient rotating stars, with values of 0.16 to 0.29, matches better the solar value of 0.195. Also the ^{79}Br/^{81}Br ratio, with model values of about 1.3 matches better the solar value (≈ 1.0). The ^{64}Zn/^{66}Zn ratio corresponds to the lowest branching point at ^{63}Ni involved in s process between Fe and Sr. The solar ratio is 1.69, while our models show values between 0.2 and 0.9, but Zn is also produced in explosive nucleosynthesis which produces more ^{64}Zn than ^{66}Zn by either the hypernovae (Nomoto et al. 2006) or neutrino induced nucleosynthesis (Fröhlich et al. 2006). Here again, it would be interesting to have post-explosive yields of our models.

The magnesium (Mg) isotopes ^{25}Mg and ^{26}Mg provide a possibility to constrain whether stars produce reasonable isotopic ratios. Yong et al. (2003) found that their data of ^{25}Mg/Mg and ^{26}Mg/Mg ratios was considerably higher than GCE models predicted (Timmes et al.

1995), and suggested as another source intermediate mass AGB stars. Rotating stars with mixing between H-burning shell layers and convective He core produce primary ^{25}Mg and ^{26}Mg and would therefore be another possible source for ^{25}Mg and ^{26}Mg. In Fig. 4.16, ^{25}Mg/Mg[4] versus [Fe/H] of rotating and non-rotating 20 and 25 $M_{\odot}$ stars is shown together with values of cool dwarfs and giants in the Galaxy (circles) from Yong et al. (2003) and the solar system value (yellow star). For the models, the initial values of [Fe/H] were used, but the abundance ratios would be finally observed in a low mass star forming from the ejected material, which is mixed with the ISM. Therefore iron ejection could move the model values to the right and dillution in the ISM again to the left. An additional uncertainty comes from the explosive Ne/C-burning producing magnesium isotopes (Woosley & Weaver 1995; Thielemann et al. 1996), which could well lower the ^{25}Mg/Mg and ^{26}Mg/Mg ratios. Still, between [Fe/H] = −2 and 0 the trend of models and observations is the same, showing a secondary production of ^{25}Mg. Below [Fe/H] = −2 where the trend of primary production from rotation models dominates, unfortunately only a few observations exist, which cannot constrain the models.

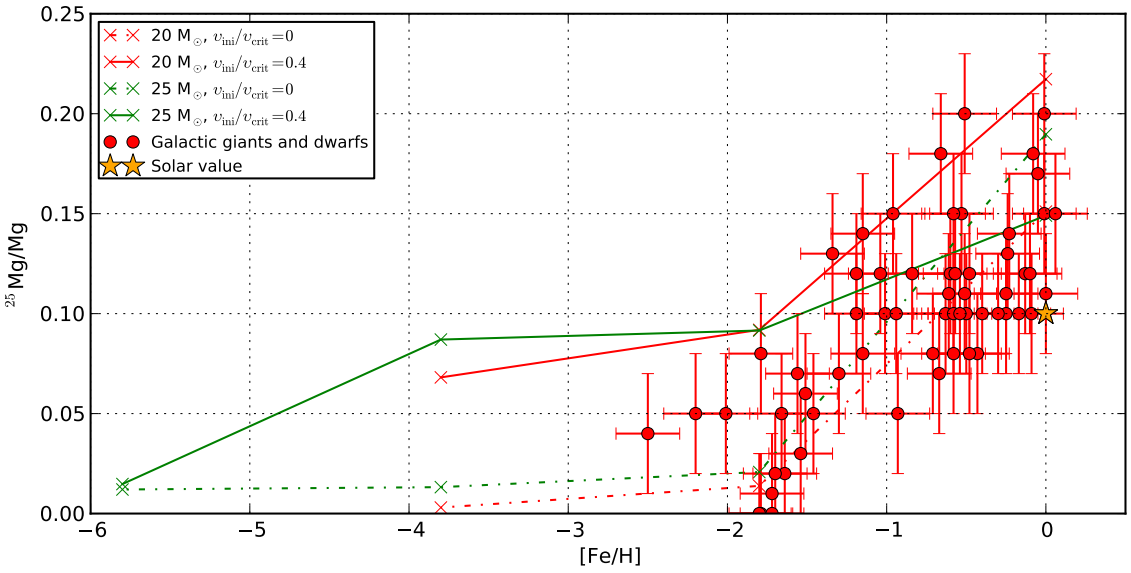

Figure 4.16: ^{25}Mg/Mg versus [Fe/H] of rotating and non-rotating 20 and 25 $M_{\odot}$ stars. The yellow star marks the position of the solar system ratio (Lodders 2003). The red circles are values determined from spectra of cool dwarfs and giants in the Galaxy by Yong et al. (2003).

A figure for ^{26}Mg would look about the same as Fig. 4.16, but the lines for the models are shifted up. This indicates a higher ^{26}Mg/^{25}Mg ratio from our models than in the observations. This can be caused by a too high ^{22}Ne(α,γ) rate in He-burning conditions. At first glance, the ^{25}Mg/Mg ratio of our models is consistent with observations, but the ^{26}Mg/^{25}Mg ratio is too high. For an accurate comparison we would have to calculate the explosive nucleosynthesis of our models.

[4] Mg = ^{24}Mg + ^{25}Mg +^{26}Mg in number abundances.

5 Imprints of fast rotating massive stars in the Galactic Bulge

This chapter was published as a short publication in Chiappini et al. (2011) and is kept here in the same form.

5.1 Letter

The first stars that formed after the Big Bang were probably massive (Bromm et al. 2009), and they provided the Universe with the first elements heavier than helium ('metals'), which were incorporated into low-mass stars that have survived to the present (Truran 1981; Cowan & Sneden 2006). Eight stars in the oldest globular cluster in the Galaxy, NGC 6522, were found to have surface abundances consistent with the gas from which they formed being enriched by massive stars (Barbuy et al. 2009) (that is, with higher α-element/Fe and Eu/Fe ratios than those of the Sun). However, the same stars have anomalously high abundances of Ba and La with respect to Fe (Barbuy et al. 2009), which usually arises through nucleosynthesis in low-mass stars (via the slow-neutron-capture process, or s process Sneden et al. 2008). Recent theory suggests that metal-poor fast-rotating massive stars are able to boost the s-process yields by up to four orders of magnitude (Pignatari et al. 2008), which might provide a solution to this contradiction. Here we report a reanalysis of the earlier spectra, which reveals that Y and Sr are also overabundant with respect to Fe, showing a large scatter similar to that observed in extremely metal-poor stars (Frebel 2010), whereas C abundances are not enhanced. This pattern is best explained as originating in metal-poor fast-rotating massive stars, which might point to a common property of the first stellar generations and even of the 'first stars'.

NGC 6522 has been confirmed to be older than any halo globular cluster, despite its metallicity being a tenth that of the Sun (Barbuy et al. 2009), and is therefore a witness of the early phases of the chemical enrichment of the Universe. Consistent with the age of this cluster, its stars show a chemical pattern typical of an interstellar medium enriched by core collapse supernovae (in which thermonuclear supernovae of type Ia and low- and intermediate-mass stars did not have time to contribute to the chemical enrichment). However, the large [Ba/Eu] ratios found (Barbuy et al. 2009) in five of the eight stars of NGC 6522 studied (Table 5.1) shows that the excess in Ba cannot be attributed to the rapid-neutron-capture (r) process, and so the s process must be invoked (Barbuy et al. 2009, see Supplementary Information in Section 5.2).

There are only two ways to explain the high Ba and La found in NGC 6522, namely:

Table 5.1: Abundances of the eight stars in NGC 6522

Element	Reference	B-8 (star 1)	B-107 (star 2)	B-108 (star 3)	B-118 (star 4)	B-122 (star 5)	B-128 (star 6)	B-130 (star 7)	F-121 (star 8)
[O/Fe]	B09	+0.25	+0.50	+0.70	+0.30	+0.70	–	+0.50	+0.50
[Mg/Fe]	B09	+0.10	+0.27	+0.33	+0.20	+0.20	+0.25	+0.40	+0.40
[Si/Fe]	B09	+0.34	+0.20	+0.20	+0.29	+0.13	+0.24	+0.35	+0.27
[Ca/Fe]	B09	+0.15	+0.04	+0.18	+0.21	+0.21	+0.16	+0.23	+0.16
[Ti/Fe]	B09	+0.12	+0.14	+0.21	+0.11	+0.19	+0.17	+0.21	+0.16
[Ba/Fe]	B09	+0.95	+0.50	+0.00	+1.00	+0.60	+0.90	+0.25	-0.25
[La/Fe]	B09	+0.50	+0.50	+0.30	+0.50	+0.30	–	–	+0.00
[Y/Fe]	This work	+1.20	+1.00	+1.50	+1.50	+1.20	+1.50	+1.20	+1.20
[Sr/Fe]	This work	+1.20	+1.30	+1.00	+0.50	+0.50	+1.50	–	–
[Eu/Fe]	B09	+0.50	+0.00	+0.50	+0.50	+0.30	+0.00	+0.80	+0.50
[Na/Fe]	B09	+0.35	-0.30	-0.15	+0.10	+0.15	+0.10	+0.15	-0.10
[C/Fe]	This work	$\lesssim 0$	$\lesssim 0$	$\lesssim 0$	$\lesssim 0$	$\lesssim 0$	$\lesssim 0$	$\lesssim 0$	$\lesssim 0$

Reference. B09 - Barbuy et al. (2009)

Notes. We present the abundances reported in B09 and the new [Y/Fe] and [Sr/Fe] abundances (shown in boldface) obtained here (where $[A/B] = \log(N_A/N_B) - \log(N_A/N_B)_\odot$ for the number N of atoms of elements A and B). The uncertainties in [X/Fe] =Mg, Si, Ca, Ti, Ba, Eu and Na are of 0.2 dex. The [O/Fe] ratios have larger uncertainties B09 (about 0.3 dex). The [Sr/Fe] and [La/Fe] abundances have larger uncertainties (about 0.3 dex) owing to the weakness of the available lines, and could be estimated only for six of the eight stars. Although the Sr I lines are weak and subject to non-LTE (local thermodynamic equilibrium) effects, a clear Y II line at $6'613.733$ Å was measured, leading to [Y/Fe] ratios with uncertainties around 0.15 dex (see Supplementary Information in section 5.2). In addition, from the C_2 band-head at wavelength $\lambda = 56'675.90$ Å we were able to estimate upper limits for the [C/Fe] ratios and found that all studied stars in NGC 6522 have $[C/Fe] \lesssim 0.0$. Hence, these stars are not strongly C-enhanced relative to Fe, as are many of the halo stars with $[Fe/H] < -3.0$.

(1) the original gas fromwhich the globular cluster formed had been pre-enriched in s-process elements by previous generations of massive stars, or (2) the original composition of the stars formed in the globular cluster was lately modified by mass transfer episodes taking place in binary systems involving low-mass asymptotic giant branch (AGB) stars within NGC 6522.

From re-inspection of the spectra of NGC 6522 (Barbuy et al. 2009), we were able to obtain the Y abundances for eight giant stars, and estimate the Sr abundances for six of them (Table 5.1 and the Supplementary Information 5.2). We find large overabundances of Y (and Sr) with respect to Fe and Ba in the NGC 6522 stars, with a similar scatter to that observed in extremely metal-poor halo stars (Frebel 2010), but now also observed for bulge stars with $[Fe/H] < -1$, a result not seen previously (see Fig. 5.1). In addition, from the C_2 band-head (see Supplementary Information), we were able to estimate upper limits for the [C/Fe] ratio. We found that all studied stars have $[C/Fe] \lesssim 0.0$, and hence are not enriched in C, as is the case in a significant fraction of very-metal-poor halo stars (Beers & Christlieb 2005).

Extremely metal-poor environments can produce noticeable effects on the properties of massive stars (more details can be found in the Supplementary Information in section 5.2). At very low metallicities, stars rotate faster (Martayan et al. 2007). Models of fast-rotating massive stars (hereafter 'spinstars') at very low metallicities (Hirschi 2007; Ekström et al. 2008; Meynet et al. 2006) have shown that rotational mixing transports ^{12}C from He-burning core into H-rich layers, where it is transformed to ^{14}N and ^{13}C. This primary ^{14}N is then transported back to the He-burning core where it is converted into ^{22}Ne, the main neutron source in massive stars for the s process beyond Fe. Hence, the amount of ^{22}Ne and of s-process products in the He core is enhanced with respect to non-rotating models (Pignatari

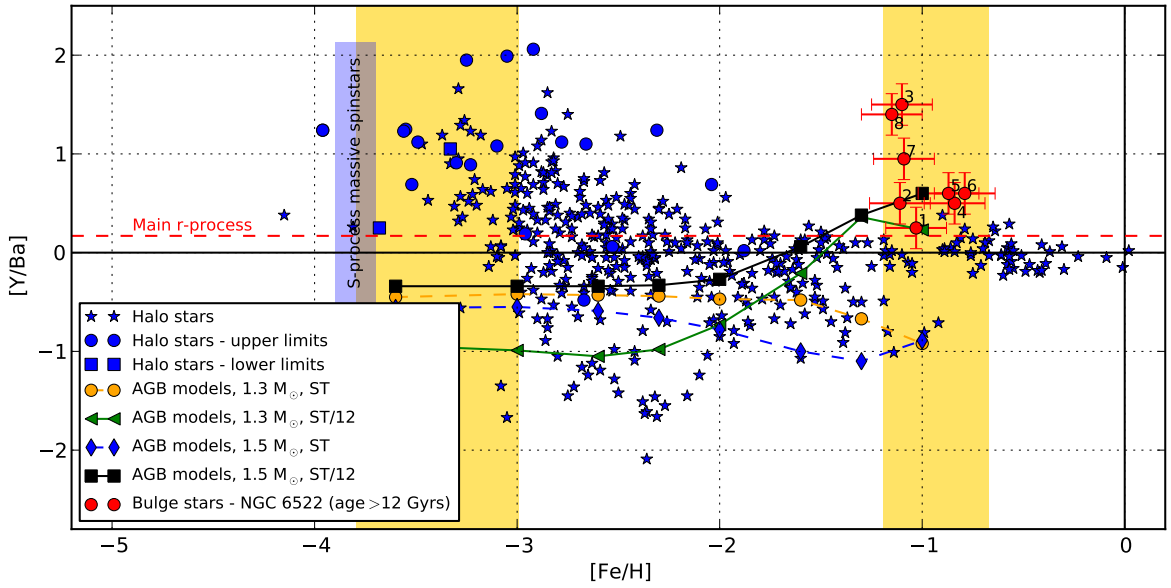

Figure 5.1: The [Y/Ba] scatter observed in the early Universe. Observed [Y/Ba] scatter in the NGC 6522 stars, which have a metallicity of around [Fe/H] = −1 (Barbuy et al. 2009) (red circles with s.d. error bars) compared to that observed in extremely metal-poor halo stars (Frebel 2010) with [Fe/H] < −3. The two yellow shaded areas mark the 'early Universe phase' sampled by halo and Bulge stars. We note the similar scatter in [Y/Ba] between the most metal-poor halo stars and our Bulge stars (compare the scatter inside the two yellow zones). Also shown is the [Y/Ba] scatter predicted for the very earliest phases of the chemical enrichment owing to 'spinstars' (indicated by the blue column). The dashed line indicates the [Y/Ba] ratio predicted from pure r process (Sneden et al. 2008). Finally, the curves show the predictions for the [Y/Ba] ratio by recent AGB models (Bisterzo et al. 2010), at different metallicities. The lowest ^{13}C-pocket efficiencymodel considered here (Bisterzo et al. 2010) is 'ST/12' (where ST is for standard, and ST/12 means the efficiency of the standard case reduced by a factor of 12; the ^{13}C-pocket is a tiny radiative layer of material in the He-rich region just below the H shell, responsible formost of the s process in AGB stars). We do not consider AGB models with lower efficiencies (showing higher [Y/Ba] ratios) because the corresponding [Ba/Fe] and [Y/Fe] ratios would be too low (Bisterzo et al. 2010) (approximately solar) compared to the large enhancements observed in the NGC 6522 stars (Table 5.1). Finally, we note that whereas AGB mass-transfer and 'spinstar' models can explain stars with slightly sub-solar [Y/Ba] ratios (−1 < [Y/Ba] < 0), both scenarios have difficulties in explaining stars with [Y/Ba] ratios below −1.

et al. 2008).

We have calculated extremely metal-poor 'spinstar' models ([Fe/H] = −3.8) with a reaction network including 613 isotopes up to Bi (Frischknecht et al. in preparation). Rotational mixing increases the s-process yields by about four orders of magnitude (Fig. 5.2 a and b; see also Supplementary Information in section 5.2). The efficiency of this process depends on the rotation rate. A lower rotation rate leads to a more efficient production of the Sr peak compared to heavier species (for instance, in our models the upper limit of [Y/Ba] is about +2), whereas strong mixing driven by a high rotation rate boosts the peak of s-process products towards heavier elements, decreasing the [Y/Ba] ratio (we obtain a lower limit for [Y/Ba] of around −1), even producing non-negligible quantities of Pb. Hence, one of the main predictions of our 'spinstar' scenario is that the early Universe composition should exhibit not only a large scatter in several [s-process element/Fe] ratios, but also a large scatter in the abundance ratios of elements belonging to the different s-process peaks.

Figure 5.1 compares the scatter in the [Y/Ba] ratio predicted by models of 'spinstars' in the very earliest phases of the chemical enrichment of the Universe with the scatter observed in extremely-metal poor halo field stars (Frebel 2010) (with [Fe/H] < −3) and in the stars of NGC 6522 (with [Fe/H] = −1; see Supplementary Information in section 5.2 for a discussion on other abundance ratios). Two important conclusions can be drawn. First, the observed scatter in [Y/Ba] in the early Universe (both in the Bulge and in the very-metal-poor halo stars) is compatible with the expected scatter from 'spinstar' models, apart from very few objects with [Y/Ba] ratios below −1, in the case of the halo field stars. Second, whereas 'spinstars' can produce a large scatter in the [Y/Ba] ratios, covering a range of $-1 < [Y/Ba] < +2$, AGB models (Bisterzo et al. 2010) at [Fe/H] = −1 (compatible with the observed high [Y/Fe] and [Y/Ba] ratios in Table 5.1) cover a smaller [Y/Ba] range ($-1 < [Y/Ba] < 0.5$), and cannot account for the large [Y/Ba] ratios of stars number 3, 7 and 8 in Fig. 5.1 (see Supplementary Information for more details). In addition, if we take into account the results shown in Fig. 5.1 together with the other element ratios presented in the Supplementary Information, a combination of the s-process component from 'spinstars' and the explosive r-process component may explain the heavy elements in all the stars observed in NGC 6522. Predictions from AGB models may explain the abundances in five out of eight stars (not reproducing those with the highest [Y/Ba]). However, the AGB mass-transfer scenario might have difficulty in explaining low [C/Fe] ratios. Hence it is of primary importance to obtain precise [C/Fe] ratios for the NGC 6522 stars, not just upper limits, in order to distinguish between 'spinstars' and AGB mass-transfer scenarios.

A possible observational test to confirm our scenario would be to look for the scatter in the [Pb/Fe] ratios in the early Universe. Low-metallicity AGB mass-transfer models (Karakas 2010; Bisterzo et al. 2010) have quite a robust prediction for the minimum expected [Pb/Eu] ratios, but 'spinstar' models predict a large scatter in the [Pb/Eu] ratios. Therefore, if Pb could also be measured for stars with known abundances of Sr,Y, Zr, Ba and La, it would be possible to distinguish between the two scenarios. Unfortunately, the useful Pb lines are in the ultraviolet part of the spectrum and thus are highly extinct for bulge stars.

Other processes besides fast rotation have been invoked in the literature to explain the large overabundances with respect to Fe of the light s-process elements (Y, Sr and Zr) in the very-metal-poor Universe (Qian & Wasserburg 2008; Travaglio et al. 2004; Farouqi et al. 2009), but it is unclear if they could also account for the abundances observed in NGC 6522. Here we propose that 'spinstars' offer another plausible explanation for this signature, both in the Bulge and in extremely metal-poor halo stars.

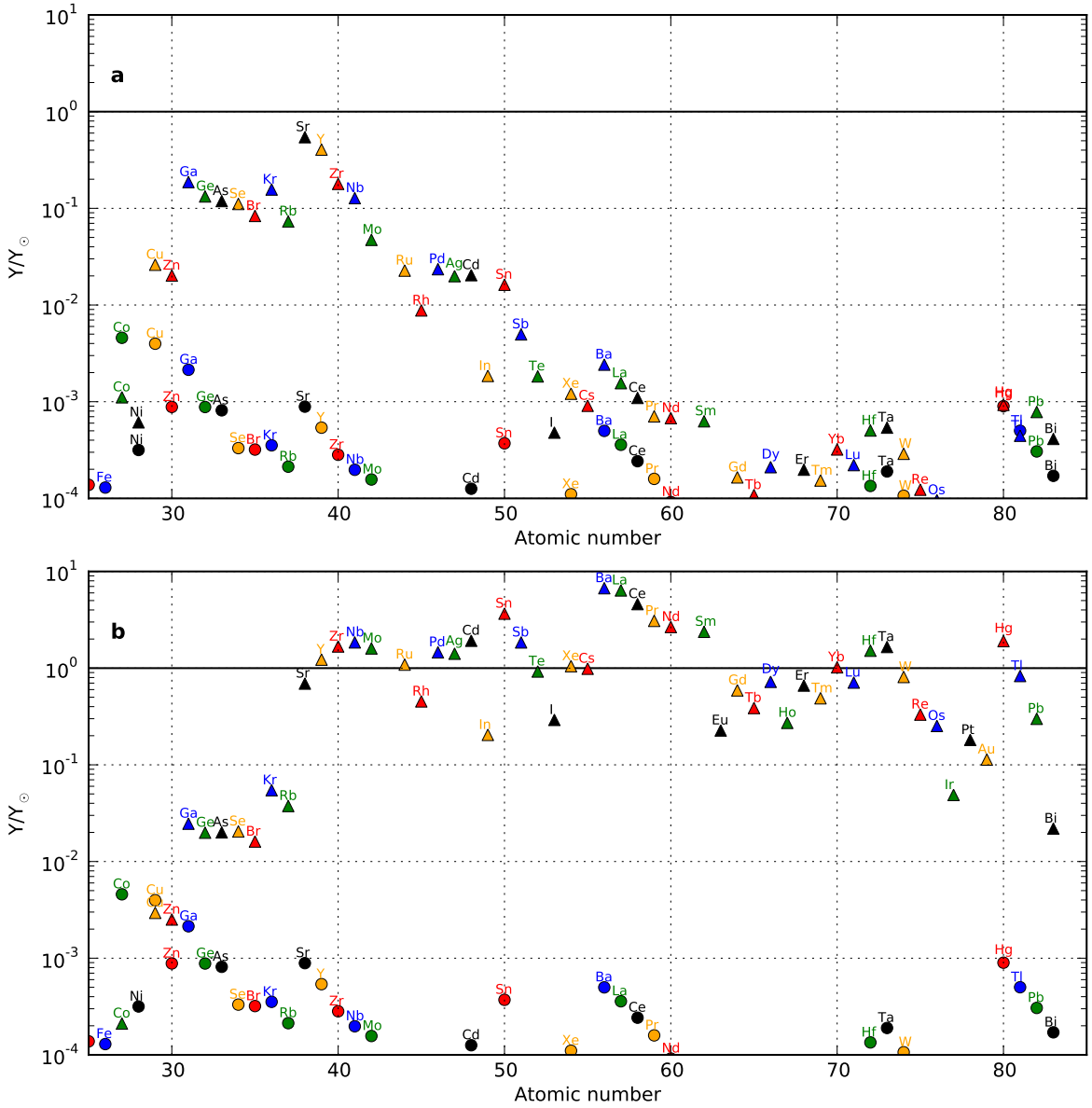

Figure 5.2: Impact of rotation on s-process element production in very-metal-poor massive stars. The models show the production of s-process elements (where $X/X_{\odot}$ is the mass fraction of atoms normalized to solar) predicted in a 40 $M_{\odot}$ star with [Fe/H] $= -3.8$, which does not rotate (circles), and with an initial rotational velocity of 500 km s^{-1} (triangles). These models are shown at two different phases of He burning: a, at the beginning of the s process (about 127′000 years before He exhaustion); and b, at the end of the central He-burning phase. Rotation boosts production of the s-process elements by four orders of magnitude. $X_{\odot}$ solar abundance of given element.

The impact of having had an early generation of 'spinstars' in the Universe is manifold. They may have contributed to the primary nitrogen production in the early Universe Chiappini et al. (2006, 2008). The fast spins of the stars could have led to more mass loss than expected at these very low metallicities and thus could have prevented the first stars fromdying as pair-instability supernovae (Ekström et al. 2008), which would explain why halo stars do not bear the chemical signature of pair-instability supernovae. In addition, even if the more-massive 'spinstars' were to collapse into black holes without a supernova explosion, they would have been able to contribute to the chemical enrichment of the interstellar medium in the very early Universe via stellar mass-loss triggered by rotation. This also has implications for the fate of the stars, leading possibly to more gamma-ray bursts than previously thought, and more generally to magneto-hydrodynamic explosions (Ekström et al. 2008). Finally, 'spinstars' have longer lifetimes (Ekström et al. 2008) and possibly higher surface temperatures and luminosities than non-rotating stars. It will therefore be worthwhile to study the impact of rotation on the ionizing power of the first stars. The fast rotation of the first stars is now also supported by the latest hydrodynamic simulations of the formation of the first stars (Stacy et al. 2011).

5.2 Supplementary material

In the first section more details are given on the observations and the associated uncertainties. In the second section more details are given on why massive stars at extremely low metallicities are different than their present day counterparts. Finally, in the third section we complement the manuscript discussion of the [Y/Ba] vs. [Fe/H] plot (Fig. 5.1) with a discussion of other abundance ratios, namely: [Eu/Ba], [Sr/Ba], [C/Fe], and [Sr/Fe].

5.2.1 The new abundances for the NGC 6522 stars

The abundance ratios were obtained by means of line-by-line spectrum synthesis calculations compared to the observed line. The adopted line lists of O, Mg, Si, Ca, Ti, Ba, La, Eu, and Na can be found in the literature (Barbuy et al. 2009). In the present work we obtained new [Y/Fe], [Sr/Fe] and upper limits for [C/Fe]. The adopted lines are described below.

A clear Y II line at 6′613.733 Å is present in the spectra of the 8 studied stars in NGC 6522, indicating large overabundances of this element with respect to iron. The robustness of this result is shown here for the NGC 6522-128 star (star number 6 in Table 5.1). Supplementary Fig. 5.3 shows the observed spectrum indicated by the red circles, whereas the solid lines indicate the resulting synthetic spectra computed with different [Y/Fe] ratios (see figure caption). As it can be clearly seen, the uncertainties in the determination of the [Y/Fe] ratio of this star is below 0.15 dex. The same is true for the other 7 stars.

The Sr abundances have been obtained from the Sr I line at 6′503.991 Å. In this case the lines are weak and subject to non-LTE effects. We estimate uncertainties of the order of 0.3 dex for this element.

For the [C/Fe] ratio only upper limits could be obtained by studying the C_2 Swan system (i.e. C_2 (0,2) at $\lambda = 6'191.27$ Å, C_2 (5,8) $\lambda = 6'481.81$ Å, and C_2 (2,5) $\lambda = 6'675.90$ Å band-heads), besides several CN red band-heads.

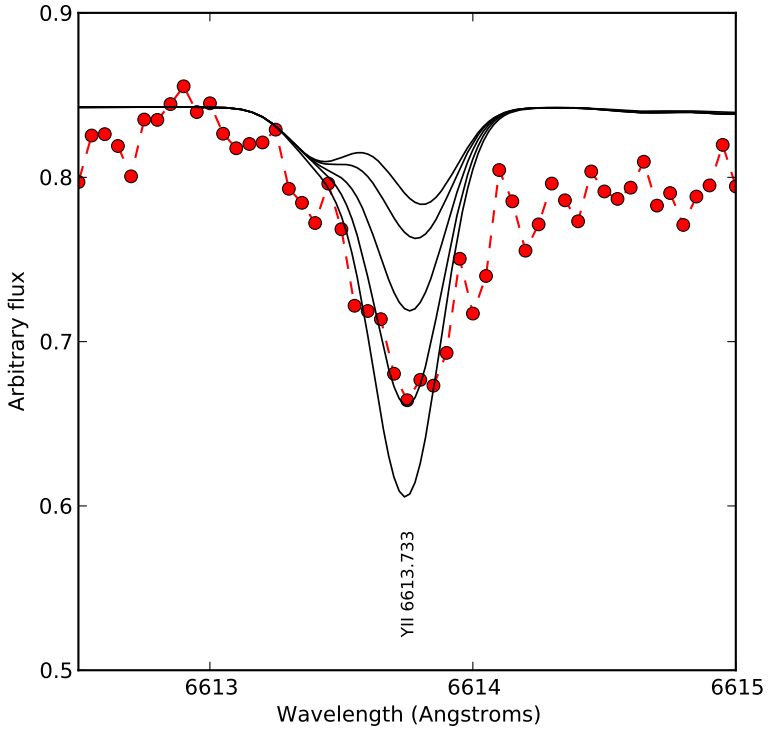

Figure 5.3: The large overabundance of Y observed in one of the studied NGC 6522 stars. A clear Y II line at 6′613.73 Å is present in the spectra of the 8 studied stars (Barbuy et al. 2009) indicating large overabundances of this element with respect to iron. The robustness of this result is shown here for the NGC 6522-128 star. The observed spectrum is indicated by the red circles, whereas the solid lines indicate the resulting synthetic spectra computed with [Y/Fe] = 0.0, +0.5, +1.0, +1.5 and +2.0 (from top to bottom). This comparison indicates a ratio [Y/Fe] = +1.5 for this particular star (see Table 5.1).

5.2.2 The special case of extremely metal-poor stars

The first stellar generations are believed to have been radically different from present-day massive stars because they were metal-poor and even metal-free for the first stars (i.e. were formed from a gas whose composition was the one left by the Big Bang primordial nucleosynthesis). The lack (or only traces) of metals leads to faster surface rotation velocities, as metal-poor stars are more compact than metal rich ones. Stars formed from a gas whose global metallicity is below $\approx 1/2000$ the one in the Sun, could attain rotational velocities of 500-800 km s^{-1} (depending on the stellar mass, Hirschi 2007) if their initial angular momentum content was similar to that of Solar vicinity stars. Note that the constancy of angular momentum with metallicity is a conservative assumption. In fact, metal poorer stars could have had larger amounts of angular momentum since braking by proto-stellar winds may be less efficient at lower metallicities.

Two important effects arise in fast rotating very metal-poor stars (hereinafter 'spinstars'). The first one is that rotation triggers mixing processes inside the star, which leads to the production of important quantities of primary ^{14}N, ^{13}C and ^{22}Ne. Second, the strong mixing

caused by rotation enriches the stellar surface, thus increasing the opacity of the outer layer, and possibly driving line driven winds. In addition, fast rotation can also lead mass losses. Both mechanisms are able to trigger non-negligible mass-loss already at very low metallicities (Meynet & Maeder 2002; Meynet et al. 2010, a result not achieved by standard models without rotation).

The efficiency of the mixing generated by rotation increases with stellar mass and rotational velocity, and with decreasing metallicity (Meynet & Maeder 2002). This last trend is true except for strictly metal-free ($Z = 0$) stars11, which produce systematically lower quantities of primary ^{14}N than $Z = 10^{-8}$ stars (but still much larger quantities than what is predicted in models without rotation). Hence, 'spinstars' can significantly enrich the early interstellar medium in primary ^{14}N and ^{13}C via stellar winds and supernovae explosion, providing the best explanation at present for the high N/O and low ^{12}C/^{13}C observed in very metal poor halo stars (Chiappini et al. 2006, 2008).

5.2.3 Abundances in the NGC 6522 stars versus that of extremely metal-poor halo stars

A small contribution from r process has been invoked in the literature to explain some extremely halo metal-poor stars with non negligible abundances of Ba (Truran 1981; Sneden et al. 2008). The expected [Eu/Ba] ratio from pure r process is 0.8 (Sneden et al. 2008). Fig. 5.4 shows [Eu/Ba] vs. [Fe/H] for halo field stars (Frebel 2010) and the studied NGC 6522 stars. The low [Eu/Ba] ratios observed in stars 1, 2, 4, 5 and 6 of NGC 6522 (with values between -0.9 and -0.3 – see Table 5.1) clearly show the necessity of invoking additional contribution of the s process to explain the Ba abundances.

When comparing Fig. 5.4 with Fig. 5.1, it can be seen that stars 1, 2, 4, 5, 6 ($-1 <$ [Eu/Ba] < 0, $0 <$ [Y/Ba] < 0.8) can be reproduced by both AGB nucleosynthesis predictions, or a combination of the r-process component (Sneden et al. 2008) and 'spinstars' s-process component reported in this work. These last two components are produced in massive stars, and hence are consistent with the early bulge enrichment. On the other hand, stars 3, 7, 8 ($0.5 <$ [Eu/Ba] < 1, $0.8 <$ [Y/Ba] < 1.5) cannot be reproduced by AGB pollution, and are best explained with a massive star origin (where most of the observed Eu is made from the r-process, and Y from pre-supernova 'spinstars' s process). Notice that in case of AGB models, stellar envelope abundances are compared with observations. Therefore, in this case the initial envelope abundance of Eu for the given metallicity ([Fe/H] $= -1$) is already included, and it is barely modified by third dredge up events along the AGB evolution, enriching the envelope mostly in carbon and typical s-process elements (Bisterzo et al. 2010; Busso et al. 2001).

Figure 5.5 shows the [Sr/Ba] vs [C/Fe] ratios for field halo stars (Frebel 2010). It can be seen that stars with [Sr/Ba] < 0 tend to be C-rich, as expected in the AGB mass-transfer models, which are often invoked to explain the Carbon Enhanced metal-poor stars (CEMPs Lucatello et al. 2006). On the other hand, stars with positive [Sr/Ba] ratios tend to show moderate C enhancements ($[C/Fe] < 1$), with rare exceptions. The stars in NGC 6522 that we studied do have [C/Fe] $\lesssim 0.0$ (see Table 5.1), hence being again compatible with the expectations of an interstellar medium enriched by 'spinstars'. In fact, a large C enhancement is not predicted for 'spinstars', except in special cirscunstances (Busso et al. 2001).

On the other hand, we need to keep in mind that the present upper limit for carbon abundance is not ruling out the AGB mass-transfer scenario for stars with compatible [Y/Ba] and [Eu/Ba] (see Fig. 5.4). Indeed, mass transfer mechanism between the primary AGB star

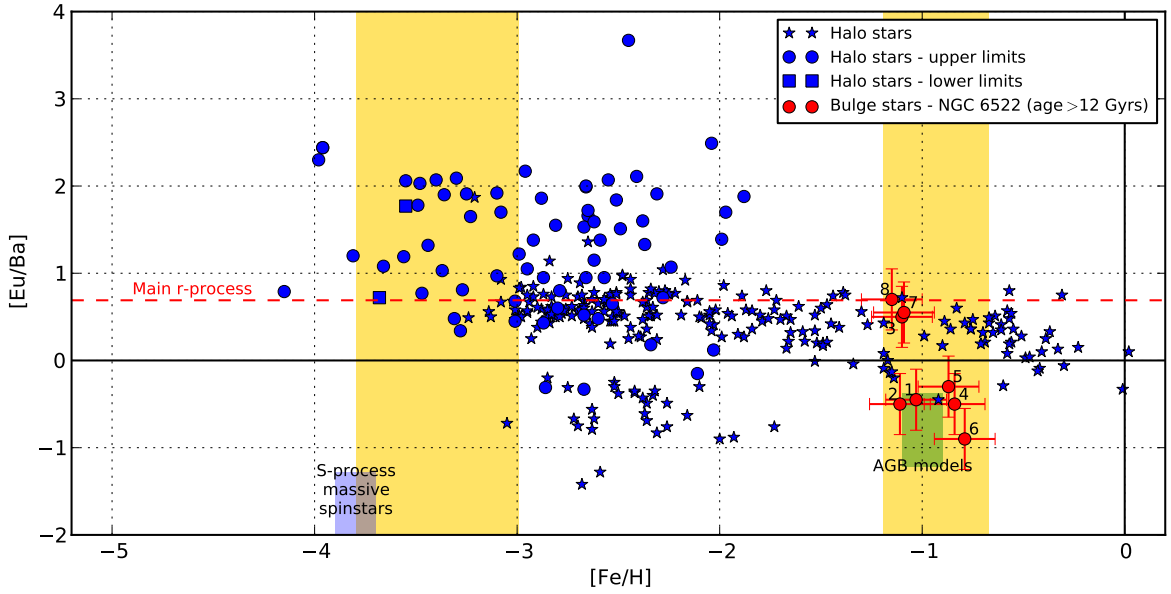

Figure 5.4: The signature of s process seen in stars of NGC 6522. Observed [Eu/Ba] vs. [Fe/H] in the 8 NGC 6522 stars (Barbuy et al. 2009, red circles with error bars) compared to that observed in field halo stars (Frebel 2010). The two yellow shaded areas mark the "early Universe phase" (as in Fig. 5.1 of the main manuscript). The red dashed line indicates the predicted [Eu/Ba] ratio from pure r process (Sneden et al. 2008). Also shown are the locus of recent AGB model predictions (Bisterzo et al. 2010) for the s process (with initial abundances which include species mostly produced by the r process), and the locus of our 'spinstar' models (without considering in this case a contribution from the explosive r process).

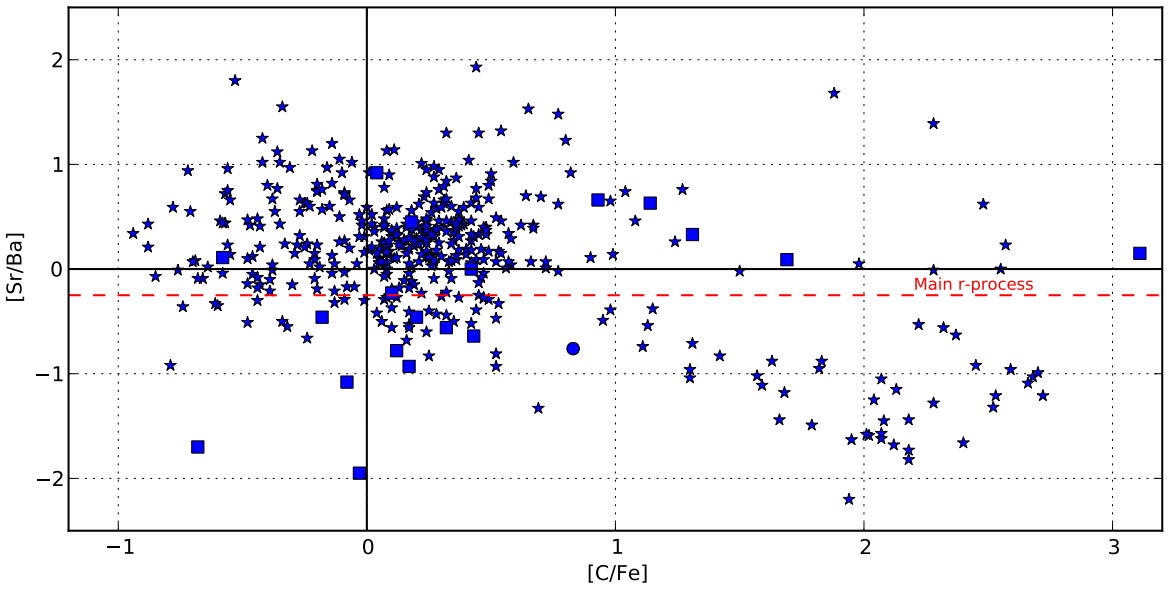

Figure 5.5: The observed [Sr/Ba] vs [C/Fe] in halo field stars. The red dashed line indicates the [Sr/Ba] ratio from pure r process (Sneden et al. 2008). It can be seen that stars with [Sr/Ba] ratios lower than that predicted by the r process tend to be strongly C-enhanced with respect to iron, pointing to the AGB-mass transfer scenario. On the other hand, the stars we studied in NGC 6522 have at most solar [C/Fe] (see Table 5.1).

and the secondary companion in the binary system is still uncertain, and a dilution factor of the original AGB abundances need to be is considered (Bisterzo et al. 2010), which might lower the final predicted [C/Fe] ratios to the levels observed in the NGC 6522. Furthermore, all the 8 observed stars are giants1 and hence their surface abundances have been exposed to the first dredge up (Nollett et al. 2003) and later to the Red Giant Branch evolutionary phase. In particular, during this later phase extra-mixing processes between envelope material and the underlying hydrogen shell (generally called Cool Bottom Processing) may further reduce the surface carbon abundance. The physics mechanism driving such process is still uncertain (Nollett et al. 2003; Palmerini et al. 2011; Denissenkov & Merryfield 2011), but its existence is confirmed by observations (Nollett et al. 2003; Denissenkov & Merryfield 2011). For this reason, a more precise definition of the C abundance is mandatory in order to further constrain the AGB mass transfer scenario.

Finally, in Fig. 5.6 we report the [Sr/Ba] versus [Fe/H] diagram, for completeness. However, the present measurements of Sr have large uncertainties (0.3 dex), and they are not observed in all the stars in our sample. Therefore, we postpone a more detailed discussion involving Sr production and comparison when more detailed measurements are available.

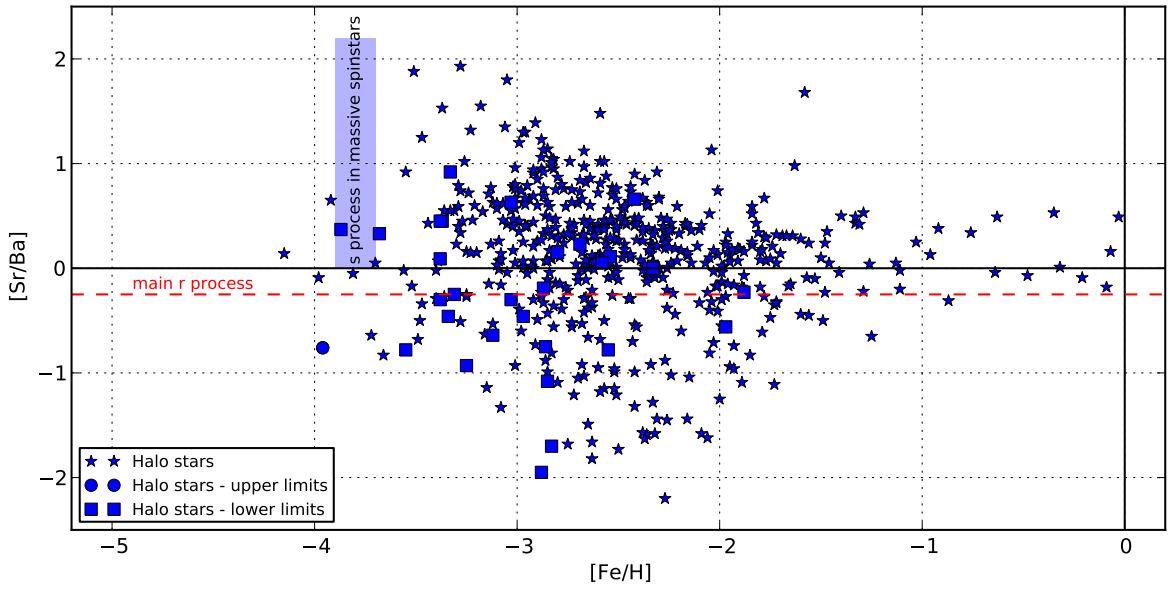

Figure 5.6: The observed [Sr/Ba] ratios in NGC 6522. Observed [Sr/Ba] scatter in 6 NGC 6522 stars, which have a metallicity around [Fe/H] = −1 (Barbuy et al. 2009, red circles with s.d. error bars) to be compared to that observed in extremely metal-poor halo stars (Frebel 2010). The two yellow shaded areas mark the 'early Universe phase' sampled by halo and bulge stars, similarly to Fig. 5.1. Unfortunately the Sr abundances are very uncertain (here we give only the formal error bars, but this do not take into account the possible effects due to non-LTE corrections). The red dashed line indicates the [Sr/Ba] ratio from pure r process Sneden et al. (2008).

6 Constraints on rotational mixing from surface evolution of light elements in massive stars

This chapter was published in Frischknecht et al. (2010) and is therefore also structured as a journal publication.

6.1 Abstract

Context: Light elements and nitrogen surface abundances together can constrain the mixing efficiencies in massive stars on the main sequence, because moderate mixing in the surface layers leads to depletion of light elements but only later to enrichment in nitrogen.
Aims: We want to test the rotational mixing prescriptions included in the Geneva stellar evolution code (GENEC) by following the evolution of surface abundances of light isotopes in massive stars.
Methods: The GENEC is a 1D code containing sophisticated prescriptions for rotational mixing. We implemented an extended reaction network into this code including the light elements Li, Be, and B, which allowed us to perform calculations testing the rotation-induced mixing.
Results: We followed 9, 12, and 15 $M_{\odot}$ models with rotation from the zero age main sequence up to the end of He burning. The calculations show the expected behaviour with faster depletion of light isotopes for faster rotating stars and more massive stars.
Conclusions: We find that the mixing prescriptions used in the present rotating models for massive single stars can account for most of the observations; however, the uncertainties are quite large, making it hard to draw a firm conclusion on the mixing scenario.

6.2 Introduction

Rotation is beside the stellar mass and the initial chemical composition a key parameter in the evolution of single stars. It affects the physical and chemical structures of the stars and therefore quantities such as lifetime, luminosity, effective temperature $T_{\rm eff}$ etc. Recent models including rotation reproduce a wide range of observations better than those without as for example, the nitrogen surface enrichment (Heger & Langer 2000; Meynet & Maeder 2000), the Wolf-Rayet to O-type star number ratio (Meynet & Maeder 2003, 2005; Vázquez et al. 2007), the ratio of blue to red supergiants in the Small Magellanic Cloud (Maeder & Meynet 2001),

or the variation with the metallicity of the number ratio of type Ibc to type II supernovae (Georgy et al. 2009). Still, the treatment of transport of angular momentum and chemical species is thought to be one of the main uncertainties in stellar evolution models. New observational data of late O and B-type stars from the VLT-FLAMES survey (Evans et al. 2005, 2006; Hunter et al. 2007; Trundle et al. 2007) lead to an intense discussion about how well the models with rotation can explain the observed nitrogen surface abundances (Hunter et al. 2008; Hunter et al. 2009; Maeder et al. 2008) and about whether or not binaries are needed to explain some groups of the observed O and B-type stars (Langer et al. 2008). Light elements and in particular boron can constrain the mixing induced by rotation and help distinguish between single stars and interacting binaries (Brott et al. 2009). Boron is destroyed at relatively low temperatures ($\approx 6 \cdot 10^6$ K) where the CNO-cycles are not yet efficient. Therefore modest mixing due to rotation leads to a depletion of light elements at the surface without considerable nitrogen enrichment. This effect can not be explained by mass transfer in a binary system, since there the accreted material is depleted in boron and enriched in nitrogen (Fliegner et al. 1996).

Boron is produced in spallation process of CNO atoms in the interstellar medium (ISM) by galactic cosmic rays (GCRs). In massive stars boron is only destroyed. It is the only light element out of Li, Be and B which is observed at the surface of massive stars (OB-type). Despite the difficulties to measure boron surface abundances an increasing number of boron surface abundances from O and early B-type stars became available in the last few years (Mendel et al. 2006; Venn et al. 2002; Proffitt & Quigley 2001; Proffitt et al. 1999). The comparison in Mendel et al. (2006) of observational data with the models of Heger & Langer (2000) shows a good agreement with the exception of three stars (HD 30836, HD 36591, HD205021). The strong boron depletion in these young stars raises the question if the efficiency of surface mixing due to rotation should be stronger or if there are other mixing processes at work. We reexamined this question because the Geneva stellar evolution code (hereafter GENEC) includes the effect of rotation in a different way with respect to the codes which were used in previous works to examine that question. The most important difference comes from the fact that in GENEC the transport of the angular momentum is properly accounted for as an advection process and not as a diffusion process.

In this paper we present correlations of the surface boron abundances with nitrogen as in Mendel et al. (2006), Venn et al. (2002) and also with other interesting quantities such as the $^{12}C/^{13}C$ number ratio or observable physical quantities such as the gravity and the surface velocity. In Sect. 6.3 we give a short description of the model ingredients and present the set of simulations performed. In Sect. 6.4, we discuss the results from our models. In Sect. 6.5 we compare them to observations and in Sect. 6.6 we summarise the results.

6.3 Stellar model description

6.3.1 Rotation-induced mixing

The Geneva code (GENEC) used for the calculation of our models is described in detail in many previous publications as for example in Hirschi et al. (2004) and more recently Eggenberger et al. (2008). Since the mixing efficiency is tested by the light element surface depletion, we will briefly describe here the mixing prescription implemented in GENEC. The horizontal transport of matter is assumed to be much faster than the vertical one, which leads

to almost constant angular velocity on isobars. This in turn enables to describe the stellar structure by shellular rotation, which allows to keep the stellar structure equations in one dimension (Zahn 1992; Meynet & Maeder 1997). The transport of angular momentum in the radiative zones is then described by

$$\rho \frac{d}{dt}\left(r^2\Omega\right)_{M_r} = \frac{1}{5r^2}\frac{\partial}{\partial r}\left(\rho r^4 \Omega U(r)\right) + \frac{8}{5r^2}\frac{\partial}{\partial r}\left(\rho D_{\rm shear} r^4 \frac{\partial \Omega}{\partial r}\right) \tag{6.1}$$

where ρ is the density, Ω the angular velocity of a shell, $D_{\rm shear}$ the diffusion coefficient due to the vertical shear turbulence (see Eq. 6.4 below) and $U(r)$ the quantity intervening in the expression of the radial component of the meridional velocity which is expressed by $u(r,\theta) = U(r)\cdot P_2(\cos\theta)$. Meridional mixing is an advective process. In contrast with diffusive processes which always smooth gradients, advection can both build up gradients or smooth them. It is therefore important to account for this process not as a diffusive process but as an advective one. This has been properly done in the present work during the main-sequence (MS) phase. After the MS, the impacts of meridional currents are much less important because the evolutionary timescales become shorter. During the post MS, the main effect governing the evolution of the angular velocity in the radiative zone is simply the local conservation of the angular momentum.

The transport of chemical composition in the convective core is treated as instantaneous. The size of the convective core is determined by the Schwartzschild criterion to which an overshooting distance $d_{\rm ov}$, which is set by $d_{\rm ov} = \alpha_{\rm ov}\min(H_p, r_{\rm core})$, is added. We adopted $\alpha_{\rm ov} = 0.1$ for all calculations.

The change of the mass fraction, $\dot{X}_i$, of a nuclide i due to rotation-induced mixing is described by a diffusion equation (note that nuclear burning and mixing are treated separately).

$$\left(\frac{dX_i}{dt}\right)_{M_r} = \left(\frac{\partial}{\partial M_r}\right)_t \left[\left(4\pi r^2 \rho\right)^2 D_{\rm mix}\left(\frac{\partial X_i}{\partial M_r}\right)_t\right] \tag{6.2}$$

where $D_{\rm mix} = D_{\rm eff} + D_{\rm shear}$ with $D_{\rm shear}$ accounting for the vertical mixing introduced by shear turbulence and $D_{\rm eff}$ the diffusion coefficient resulting from the interaction of the strong horizontal mixing induced by shear turbulence and the meridional currents (see Chaboyer & Zahn 1992). The expression of $D_{\rm eff}$ is given by

$$D_{\rm eff} = \frac{|rU(r)|^2}{30 D_{\rm h}}. \tag{6.3}$$

For the vertical shear diffusion coefficient we use the expression of Talon & Zahn (1997) which accounts for the effects of horizontal turbulence:

$$D_{\rm shear} = \frac{(K + D_{\rm h})}{\left[\frac{\varphi}{\delta}\nabla_\mu\left(1 + \frac{K}{D_{\rm h}}\right) + \left(\nabla_{\rm ad} - \nabla_{\rm rad}\right)\right]} \frac{\alpha H_{\rm p}}{g\delta}\left(0.8836\,\Omega \frac{d\ln\Omega}{d\ln r}\right)^2, \tag{6.4}$$

where K is the thermal diffusivity, the diffusion coefficient $D_{\rm h}$ describes horizontal turbulent transport. As a standard, we used the $D_{\rm h}$ derived by Maeder (2003).

6.3.2 Nuclear reaction network

The nuclear reaction network used previously in the Geneva stellar evolution code included a limited number of isotopes and reaction rates. This prevented the investigation of the evolution of different isotopes as for example the light isotopes lithium, beryllium and boron. We

therefore implemented into GENEC the Basel reaction network developed originally by F.-K. Thielemann, which is more flexible in terms of choice of nuclei followed and corresponding reaction rates. This reaction network was previously used in a wide range of astrophysical nucleosynthesis calculations, e.g. Thielemann & Arnett (1985), Fröhlich et al. (2006), etc. The equations describing the abundance changes and the method how these equations are solved are described in Hix & Thielemann (1999). The reaction rates are used in their analytical form in the so-called REACLIB-format (see Rauscher & Thielemann 2000).

The two reactions which determine the burning timescales of H and He burning, $^{14}\mathrm{N}(p,\gamma)^{15}\mathrm{O}$ and 3α were taken from Imbriani et al. (2005) and Fynbo et al. (2005) respectively. The analytical fits of these two rates were provided by the JINA reaclib website (`http://groups.nscl.msu.edu/jina/reaclib/db`). The rates of the (p,α) and (p,γ) reactions involved in the different CNO-cycles were taken from NACRE (Angulo et al. 1999). Also all the (p,α) and (p,γ) reactions on the isotopes of lithium, beryllium and boron which are responsible for their destruction come from this source. The involved β^+-decays are experimental rates which can also be found in the JINA reaclib database (under label "bet+").

We included 43 isotopes from hydrogen up to silicon in the reaction network. These isotopes are listed in Table 6.1. ^{8}Be is included implicitly, i.e. assumed to decay instantaneously into two α-particles.

6.3.3 Model grid

The most recent abundance determinations of boron were based on the B III 2065.8 Å line strength. Venn et al. (2002) found a plateau of the line strength for $T_{\rm eff}$ between 18′000 and 29′000 K. Such surface temperatures are reached by MS stars between about 9 to 15 $M_\odot$. Therefore we chose models with initial masses of 9, 12 and 15 $M_\odot$ to investigate the effect of mixing. For each mass, models with different rotational velocities were calculated. All models were started from the zero age main sequence (ZAMS) and followed up to the end of He-core burning. The time averaged equatorial velocities on the MS phase $\langle v_{\rm eq}\rangle$ are between 0 to 350 km s^{-1} (see Table 6.2). The models with rotation were started at ZAMS with a flat angular velocity profile.

Most of our models were started with a solar like composition, since the observations of boron in B-type stars have been made for stars in the solar neighbourhood. As initial composition we chose $X = 0.72$, $Y = 0.266$ and $Z = 0.014$ with the elemental composition from Asplund et al. (2005) but the neon abundance from Cunha et al. (2006) and the isotopic percentage from Lodders (2003). Three models were computed with $X = 0.7$, $Y = 0.28$, $Z = 0.02$ for comparison with models of Heger & Langer (2000). To investigate the influence of lower metallicity on the surface mixing an additional 12 $M_\odot$ model was calculated with $X = 0.736$, $Y = 0.257$, $Z = 0.007$.

In Table 6.2 some parameters of the performed models are presented. In the first column the initial stellar mass $M_{\rm ini}$ is listed and thereafter, equatorial velocity over critical velocity $v_{\rm ini}/v_{\rm crit}$, initial angular momentum $J_{\rm ini}$, MS life time $\tau_{\rm H}$, equatorial velocity $v_{\rm eq}$, and the surface mass fractions of p, ^{3}He, ^{4}He, ^{10}B, ^{11}B,^{12}C, ^{13}C, and ^{14}N at different times of the evolution.

Table 6.1: Isotopes considered in the reaction network and their initial abundance in mass fractions.

Isotope	Mass Fraction	Isotope	Mass Fraction
n	0.000E-00	^{17}O	2.266E-06
p	7.200E-01	^{18}O	1.290E-05
D	1.397E-05	^{17}F	0.000E-00
^{3}He	4.415E-05	^{18}F	0.000E-00
^{4}He	2.660E-01	^{19}F	5.407E-07
^{6}Li	4.004E-12	^{20}Ne	1.877E-03
^{7}Li	5.689E-11	^{21}Ne	4.724E-06
^{7}Be	0.000E-00	^{22}Ne	1.518E-04
^{8}Be	0.000E-00	^{21}Na	0.000E-00
^{9}Be	1.692E-10	^{22}Na	0.000E-00
^{8}B	0.000E-00	^{23}Na	2.666E-05
^{10}B	7.786E-10	^{24}Mg	5.035E-04
^{11}B	3.465E-09	^{25}Mg	6.641E-05
^{11}C	0.000E-00	^{26}Mg	7.599E-05
^{12}C	2.283E-03	^{25}Al	0.000E-00
^{13}C	2.771E-05	^{26}Al	0.000E-00
^{14}C	0.000E-00	^{27}Al	4.961E-05
^{13}N	0.000E-00	^{27}Si	0.000E-00
^{14}N	6.588E-04	^{28}Si	6.550E-04
^{15}N	2.595E-06	^{29}Si	3.445E-05
^{15}O	0.000E-00	^{30}Si	2.349E-05
^{16}O	5.718E-03		

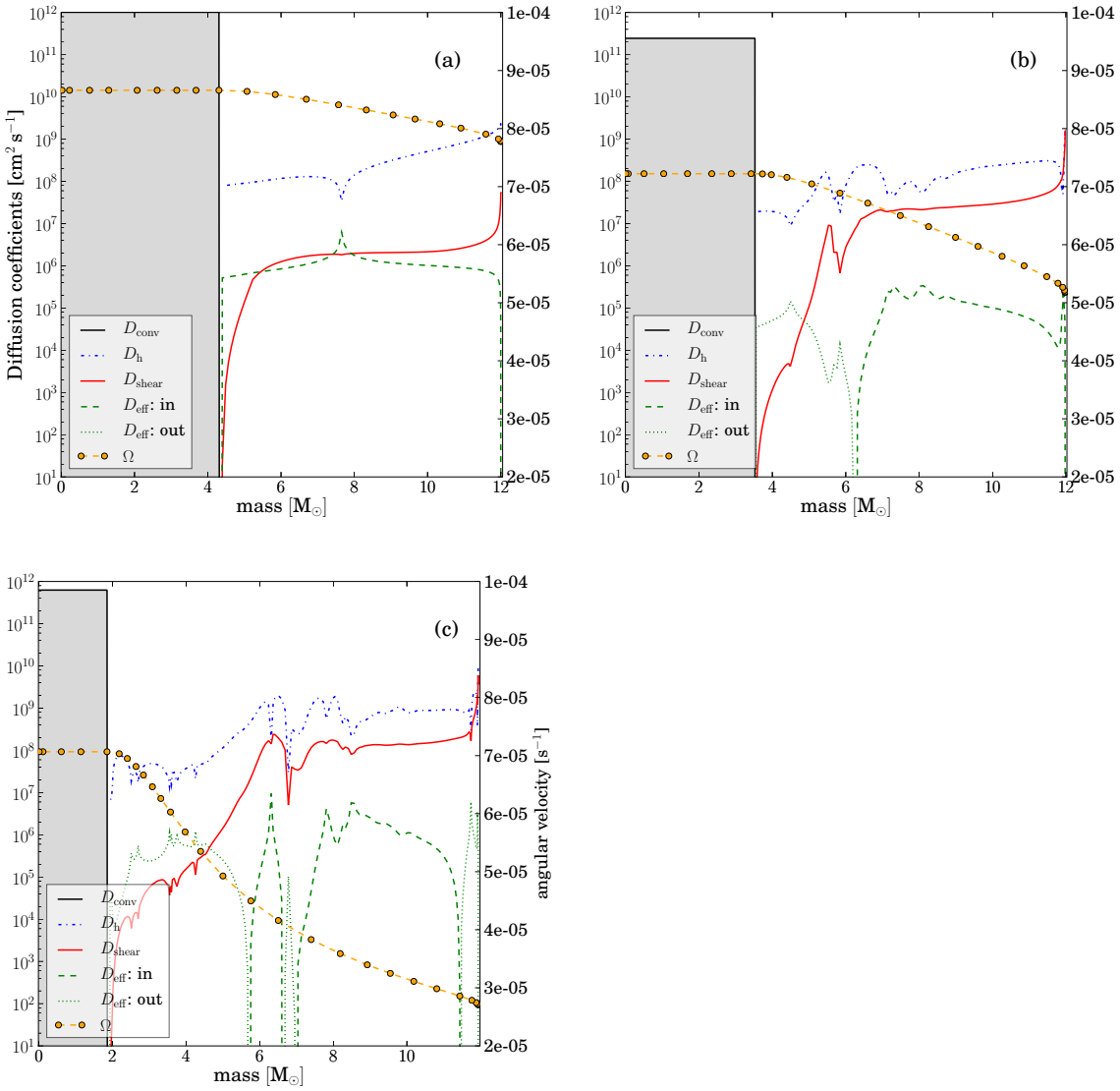

Figure 6.1: Diffusion coefficients and angular velocity versus mass for a 12 $M_\odot$ star with $\upsilon_{\rm ini}/\upsilon_{\rm crit} = 0.4$ at the start of hydrogen burning (a) when central hydrogen mass fraction is 0.48 (b) and $5 \cdot 10^{-3}$ (c). The area below the convective diffusion coefficient $D_{\rm conv}$ is grey shaded to depict the convective core. The diffusion coefficient describing meridional circulation $D_{\rm eff}$ is plotted with two different lines to distinguish between $U(r) < 0$ (green dotted line) and $U(r) > 0$ (green dashed line), i.e. the zones transporting angular momentum outwards and inwards respectively.

6.4 Models

6.4.1 Rotation and mixing

In Fig. 6.1 the diffusion coefficients in a 12 $M_\odot$ model with intermediate rotation velocity ($\langle \upsilon_{\rm eq} \rangle \approx 200$ km s^{-1}) are plotted for three different times on the MS. When meridional circulation currents descend at the equator and ascend at the pole, i.e. when it transports momentum towards the centre, $D_{\rm eff}$ is drawn as (green) dashed line and for the opposite circulation direction as dotted line.

All the models begin their evolution on the ZAMS with a flat angular velocity profile (Ω =constant). The profile of Ω converges rapidly towards an "equilibrium" profile where the advection of angular momentum towards the inner layers is compensated by the diffusion of angular momentum towards the outer layers (see Denissenkov et al. 1999; Meynet & Maeder 2000). The slow expansion of the stellar outer layers during the MS phase, the core contraction and the effects of meridional currents and shear diffusion, lead to a continuous and slow change of Ω.

Very early in the evolution, a situation with two cells of meridional currents sets in: an inner shell which brings angular momentum towards the surface and an outer cell which transport angular momentum inwards (see Fig. 6.1b). Close to the end of the MS even more meridional current cells appear (see Fig. 6.1c). Except for a short while at the very beginning of the evolution, the transport of the chemical species is mainly due to $D_{\rm eff}$ near the convective core and to $D_{\rm shear}$ in the outer part of the radiative zone. $D_{\rm shear}$ is thus the key parameter responsible for boron depletion at the surface. The nitrogen enhancement at the surface is due to the effects of both $D_{\rm eff}$ and $D_{\rm shear}$ since nitrogen is enhanced in the convective core and thus must be transported through the whole radiative envelope.

6.4.2 Evolution of surface composition

In Fig. 6.2 the variations with the Lagrangian mass coordinate of various elements are shown. At the beginning of the evolution, on the ZAMS, there is a thin surface layer containing Li, Be and B. The mass of this surface layer is between 0.3 and 2 $M_\odot$ depending on the isotope and the model considered. We see that the isotopes of Be and Li disappear very rapidly from the surface (and therefore from the whole star!). The boron isotopes are also rapidly depleted at the surface although on a longer timescale than Li. Changes of the abundances of ^{3}He and ^{14}N at the surface take still more time.

The physical reasons for these different timescales associated to the changes in surface abundances are the different temperatures required to change the abundances of these elements by nuclear reactions: the Li isotopes are destroyed at about $3 \cdot 10^6$ K, Be and B isotopes start to be depleted as soon as the temperature reaches about 5 and $6 \cdot 10^6$ K respectively, ^{3}He and ^{14}N still need higher temperatures to be destroyed/synthesized (in case of nitrogen) of the order of $1.4 \cdot 10^7$ (for ^{3}He) and of $1.7 \cdot 10^7$ K (for nitrogen). In the absence of any mixing in the radiative zones, as would be the case in standard non-rotating models, the surface abundances of these elements would not change. When some mixing processes are at work, as those induced by rotation, one expects changes of the surface abundances, more rapid for those elements whose abundances are changed at low temperatures, near the surface (such as Li, Be, and B), than for those which are depleted/synthesized in deeper layers (such as ^{3}He and ^{14}N). For instance, boron depletion is obtained by transport processes in a much smaller

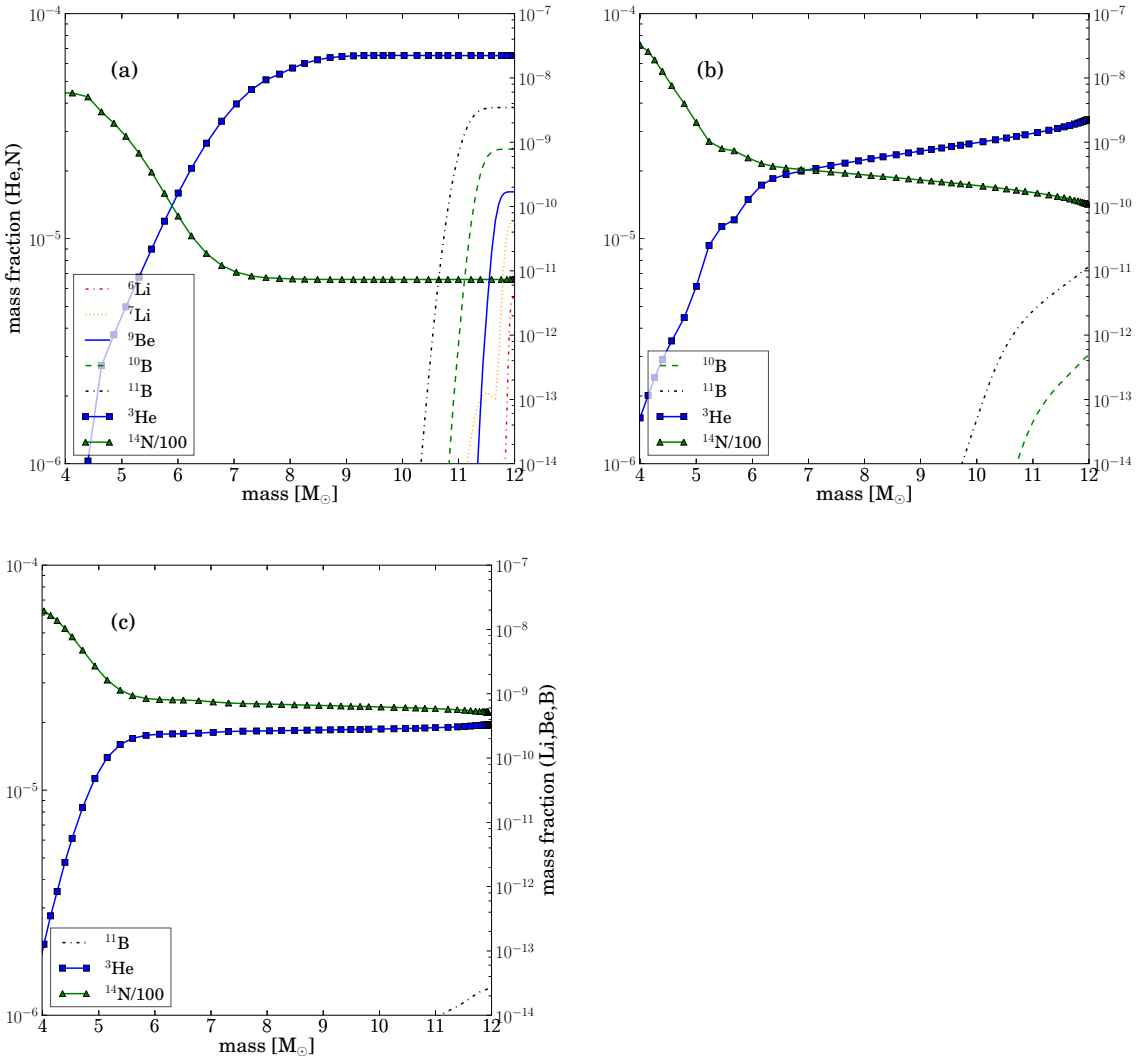

Figure 6.2: Mass fractions of light isotopes versus mass for a 12 $M_\odot$ star with $v_{\rm ini}/v_{\rm crit} = 0.4$ at the start of hydrogen burning (a) when central hydrogen mass fraction is 0.48 (b) and $5 \cdot 10^{-3}$ (c). In this model the mixing is strong enough to deplete boron almost completely at the end of the MS, lithium and beryllium are depleted at much earlier times.

portion of the star than the one required to obtain nitrogen enhancement. Nitrogen indeed needs to be transported through the whole radiative envelope, while boron only needs to be transported through a small part of it. Therefore present models predict the existence of boron depleted stars with no nitrogen enrichments. From Fig. 6.2, we see also that the ratio of $^{11}B/^{10}B$ increases when evolution goes on, because ^{10}B is destroyed closer to the surface than ^{11}B but this features is probably not observable since it occurs when both isotopes are already strongly depleted.

Figure 6.3 shows how boron depletion occurs at the surface when different initial rotation velocities (and therefore angular momentum content) are considered. In this diagram, evolution proceeds from right to left. Non-rotating models would show non-depleted boron surface abundances during the whole MS phase. Only when the star is at the red supergiant stage the model predicts a lowering of the surface abundance in boron ($\log \epsilon(B)$[1] drops down to 1.59). This is due to the dilution of the boron-rich outer layer with deeper boron depleted layers when an external convective zone appears. The evolution in Fig. 6.3 of rotating models is quite different with depletion of boron already during the MS evolution. We can see a first phase during which the surface velocity decreases, while no changes of the surface boron abundance occur. The time spent during that phase depends on the initial rotation. As a numerical example, this first phase lasts about 6 Myr for the 12 $M_\odot$ model with $\upsilon_{\rm ini}/\upsilon_{\rm crit} = 0.1$ and about 0.6 Myr for the 12 $M_\odot$ model with $\upsilon_{\rm ini}/\upsilon_{\rm crit} = 0.6$. During a second phase, the surface abundance decreases. The decrease occurs nearly at constant surface velocity in the case of the $\upsilon_{\rm ini}/\upsilon_{\rm crit} = 0.6$ model, indicating that the mixing timescale is very rapid. It occurs on a longer timescale for lower initial rotation rates. Interestingly, we see that stars with a low initial rotation (below about $\upsilon_{\rm ini}/\upsilon_{\rm crit} = 0.2$) still have observable boron surface abundances ($\log\epsilon(B)\geq 1$) at the end of the MS phase. This is an interesting feature. Indeed boron on the surface of stars in the HR gap would tell us that these stars had a small rotation rates during the previous phases. Another important point is that boron depletion is very sensitive to the metallicity. Stars with sub-solar metallicity are more compact and undergo enhanced mixing. They end up with a stronger boron depletion for the same evolutionary stage on the MS. Our 12 $M_\odot$ model with half solar metallicity reaches a lower boron surface abundance by 2 dex at the end of its MS life.

Beyond the MS all models develop a convective zone at the surface, in which the remaining boron is diluted but not burned, since the temperature at the bottom of the convective zone is only about $6 \cdot 10^5$ K. For the very slow rotators ($\upsilon_{\rm ini}/\upsilon_{\rm crit} \leq 0.1$, $\langle \upsilon_{\rm eq} \rangle \leq 50$ km s^{-1} on the MS) our models predict observable boron abundances ($\log \epsilon(B) > 1$) even in the red supergiant phase.

The evolution of boron and nitrogen abundances at the surface of our stellar models is drawn in Fig. 6.4. The 12 $M_\odot$ models with $\upsilon_{\rm ini}/\upsilon_{\rm crit}$ between 0.1 and 0.7 follow a similar path (see Fig. 6.4a), with the exception that the faster rotators have larger changes in nitrogen and boron by the end of the MS. Thus we see that a change in the initial velocity mainly affects the timescales for the changes of the surface abundances (more rapid with higher rotation rates) but not the correlation much between the abundances of these two elements during the MS phase.

We also see that similar correlations are found for stars of different initial masses (see Fig. 6.4b). We can, however, note that the lower the initial mass, the stronger the nitrogen surface enrichment at a given boron abundance. This is because a given boron abundance is

[1] $\log \epsilon(X) := \log(Y(X)/Y(H) + 12$ with $Y(X)$ the number abundance of element X

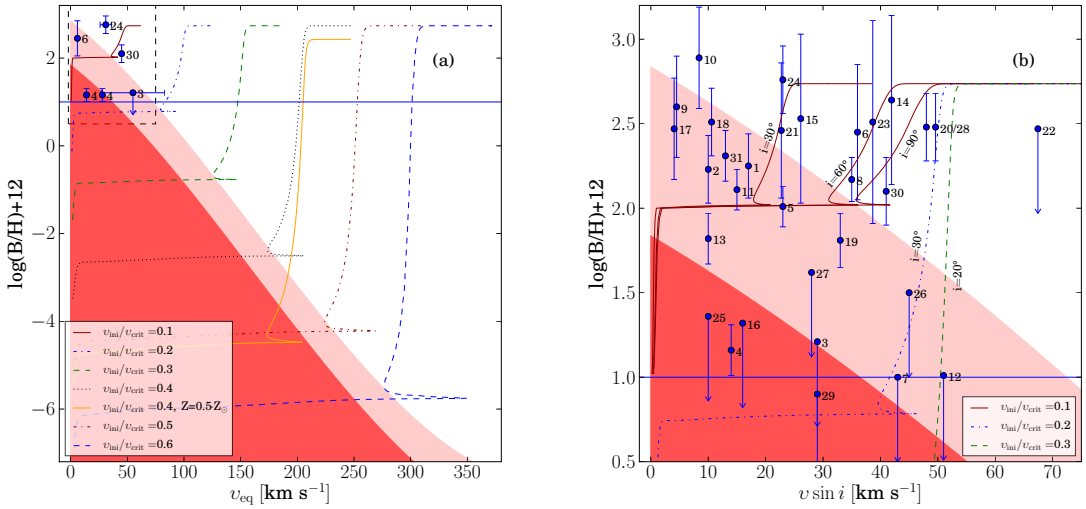

Figure 6.3: Boron versus equatorial velocity for 12 $M_\odot$ models with different rotation velocities. The stars from the chosen sample with known rotational velocities are shown in (a) and all stars with their $v \sin i$ in (b). The horizontal line indicates the minimum boron abundance that can still be detected. In (a) the dashed rectangle illustrates the section shown in (b). The red hatched area shows the evolution region for the post MS phases of our models (assuming i=90°), whereas the light red area could still be on the MS for models with sub-solar Z. The stars are labelled by the number given in the first column of Tables 6.3 and 6.4. Star 4 has either v_{eq} = 14 or 28 km s^{-1} (see Aerts et al. 2006). In (b) the curves depict models with different inclination angles.

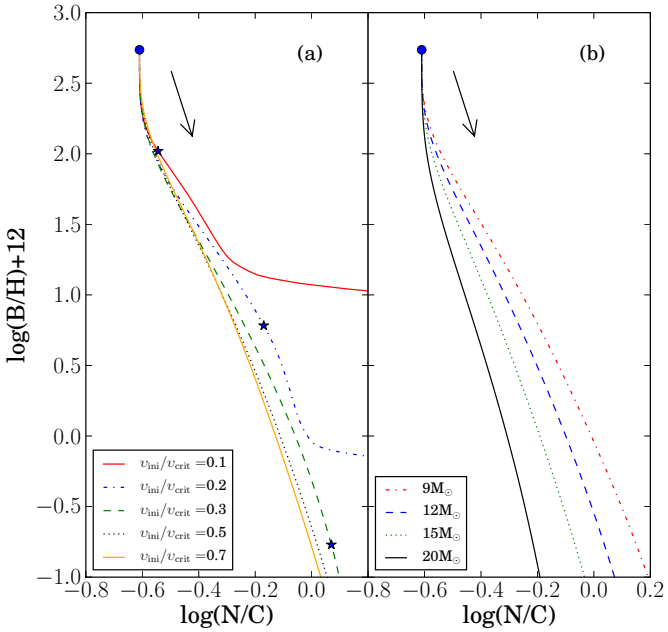

Figure 6.4: Boron versus log(N/C) for 12 $M_\odot$ models with different rotation velocities (a) and of 9, 12, 15, and 20 $M_\odot$ models with $v_{\rm ini}/v_{\rm crit} = 0.4$ (b). In the left hand plot, the end of the MS of the slow rotators ($v_{\rm ini}/v_{\rm crit} = 0.1$-$0.3$) is marked by a star symbol. The ZAMS position is indicated by a circle.

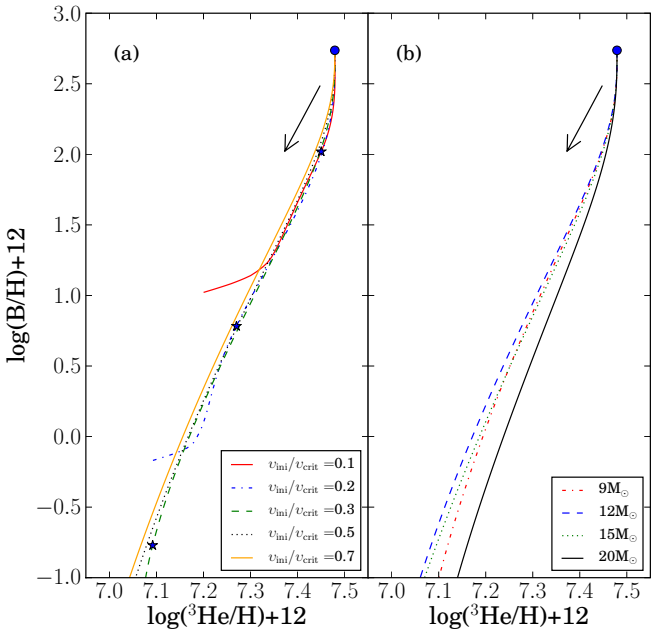

Figure 6.5: Boron versus log(^{3}He/H) for 12 $M_\odot$ models with different rotation velocities (a) and of 9, 12, 15, and 20 $M_\odot$ models with $v_{\rm ini}/v_{\rm crit} = 0.4$ (b). In the left hand plot, the end of the MS of the slow rotators ($v_{\rm ini}/v_{\rm crit} = 0.1$-0.3) is marked by a star symbol. The ZAMS position is indicated by a circle.

reached after a significantly longer time in the 9 $M_\odot$ stellar model than in the 15 $M_\odot$ one, thus giving more time for changes in nitrogen in the surface layers of the 9 $M_\odot$ model.

The depletion of boron is also correlated with changes in other abundances. The case of ^{3}He is shown in Fig. 6.5. The nuclear reactions affecting ^{3}He occur at higher temperature than those affecting boron and at a lower temperature than those affecting nitrogen. Thus the changes on the surface of ^{3}He occur more rapidly than those of nitrogen but less rapidly than those of boron.

It is interesting to look at possible correlations between surface abundances of boron and ^{4}He since the abundances of these two elements can be obtained by spectroscopy for OB-type stars. Helium enrichments have, for instance, been obtained by Lyubimkov et al. (2004). From a theoretical point of view, one expects that the changes in surface helium abundance take much more time than changes in nitrogen. This comes from the fact that the abundance gradient of helium that builds up at the border of the convective core is quite shallow with respect to the gradient in the abundance of nitrogen, and the stronger the gradient, the more rapid the diffusion (see e.g. Eq. 3 in Meynet et al. 2004). The gradient of nitrogen is steeper than the one of helium because nitrogen is very rapidly enhanced in the core as a result of the CN cycle, while it takes much longer timescales to increase the central helium abundance. One consequence is that the present models predict that, as long as boron is observable at the surface on the MS, no helium enrichment is predicted.

In Fig. 6.6 the boron versus ^{12}C/^{13}C ratio shows the same property as for boron versus nitrogen; i.e., the curve is almost independent of the parameters velocity and stellar mass

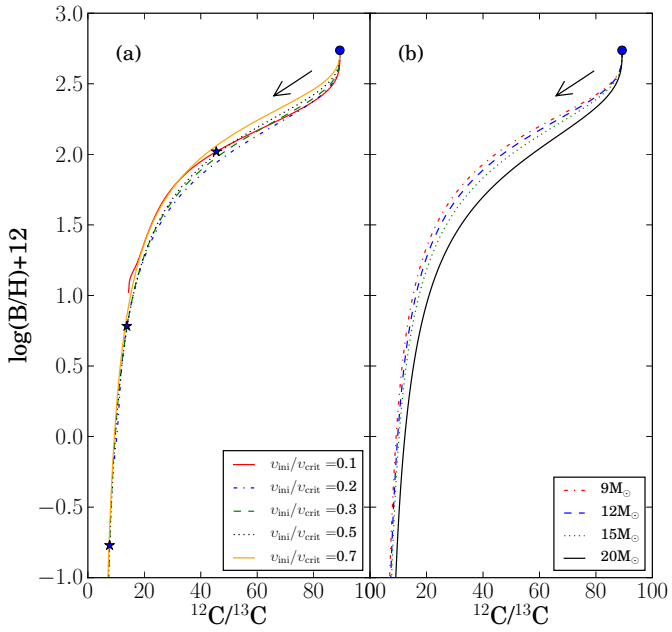

Figure 6.6: Boron versus ^{12}C to ^{13}C ratio for 12 $M_\odot$ models with different rotation velocities (a) and of 9, 12, 15, and 20 $M_\odot$ models with $v_{\rm ini}/v_{\rm crit} = 0.4$ (b). In the left hand plot, the end of the MS of the slow rotators ($v_{\rm ini}/v_{\rm crit}$ =0.1-0.3) is marked by a star symbol. The ZAMS position is indicated by a circle.

in the investigated parameter range. The initial value for the ^{12}C/^{13}C ratio is around 89 (Lodders 2003). The ratio continuously decreases during the MS phase. On the surface, the ^{12}C/^{13}C CNO-equilibrium value is only reached by the fastest rotators with a time-averaged equatorial velocity over 200 km s^{-1} on the MS.

A comparison with the models of Heger & Langer (2000) is shown in Fig. 6.7. For the purpose of comparison, we computed three 12 $M_\odot$ models with similar initial angular momentum and composition to the models of Heger & Langer (2000). We see that the present models show more boron depletion at the end of the MS phase than the ones of Heger & Langer (2000). The cause of this difference may be the different way of implementing the effects of rotation. An important difference is the way the advection of the angular momentum transport due to meridional currents is treated, as a diffusive process in the model by Heger & Langer (2000) and as an advective one in the present model. Also the counteractive effect of μ-gradient on the shear diffusion is not treated in the same way in both models (see Heger & Langer 2000; Meynet & Maeder 2000). We can also mention here that the models with solar like composition according to Asplund et al. (2005), i.e. with $Z = 0.014$, show even stronger surface mixing. Lower metal content makes rotational mixing more efficient (Maeder & Meynet 2001), since the stars are more compact. Beyond these differences, we obtain here similar qualitative results to Heger & Langer (2000), namely that boron depletion occurs much more rapidly than surface nitrogen enhancements.

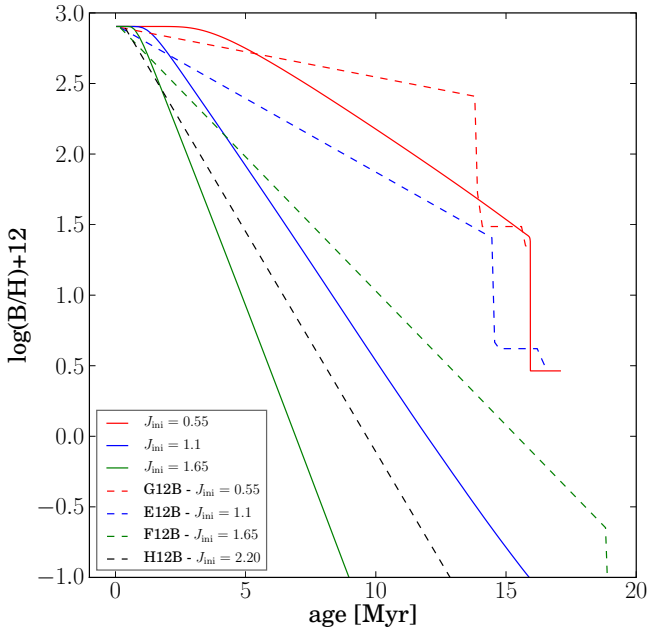

Figure 6.7: Boron versus time for 12 $M_\odot$ models with different rotation velocities, our models (solid lines) and models from Heger & Langer (2000) (dashed lines) with comparable initial angular momentum $J_{\rm ini}$ [10^{52} erg s]. Both sets of models were calculated with $Z = 0.02$.

6.5 Comparison with the observations

In Tables 6.3 and 6.4, the physical properties and the surface abundances of a selected sample of stars having boron determination are presented. Out of the available OB-type stars with boron detection from B III line at 2065.8 Å, we chose only those with $T_{\rm eff}$ between 18′000 and 29′000 K. The B III 2065.8 Å line strength has a plateau (Venn et al. 2002) in this temperature range, making the B-determination more precise. All stars of this selection have narrow line spectra (see e.g. Proffitt & Quigley 2001), which was a selection criterion to avoid blending effects. The $v \sin i$ is therefore low (< 70 km s^{-1}), meaning that either the equatorial velocity is low or that the star is seen nearly pole on.

The observations of boron in young massive stars show variations in $\log \epsilon$(B) from 2.9 down to unobservable quantities below 1 (Mendel et al. 2006; Venn et al. 2002; Proffitt & Quigley 2001). Their positions in the $\log(g_{\rm pol})$ versus $\log(T_{\rm eff})$ plane is shown in Fig. 6.8. For plotting the tracks, we used the polar gravity because it is not affected much by rotation and is a good indicator of the evolutionary stage of the stars. The "observed gravities", deduced from spectroscopy, of course do not necessarily correspond to the polar ones. There is equality between these two quantities when the star is slowly rotating. For the fast rotators, the observed gravity can be lower than the polar one if the star is, for instance, seen equator on (see the nice discussion of that topic in Huang & Gies 2006). Thus some points in Fig. 6.8 might be shifted towards higher values (downwards) if it were possible to deduce the polar gravity from the observations; however, this effect is only important for very fast rotators ($v_{\rm ini}/v_{\rm crit} > 0.7$).

We also see that there are stars below the ZAMS, with gravities above 4.3. Obviously, the above inclination effect cannot be invoked here since this effect would still push these stars to greater log$g$. But with the current uncertainties, this difference is not significant (see the sizes of the error bars in Fig. 6.8). From Fig. 6.8, we see that the majority of the observed stars have initial masses between 9 and 15 $M_{\odot}$. We also see that most of the nitrogen enriched stars are found in the upper part of the MS band. This is consistent with the idea that these surface enrichments result from an evolutionary process.

In Fig. 6.9 the boron abundances with respect to hydrogen are plotted as a function of gravity. The colour map illustrates the regions where our 12 $M_{\odot}$ models with initial solar-like composition show different values of log(N/C). The upper area represents log(N/C)< -0.4 (red/light grey) and the lower one log(N/C) ≥ -0.4 (green/dark grey). We see that most of the stars are accounted for well by the models with solar composition and slow-to-intermediate rotation rates ($\langle v_{\rm eq} \rangle$ = 0-100 km s^{-1}), assuming that the stars with highest gravities show their initial composition. The group of stars with $\log \epsilon$(B) below about 1.7 are all more evolved stars, which is consistent with mixing processes occurring during the course of their evolution. In that diagram, stars with different N/C surface abundance ratios are plotted with different symbols. We see that, in agreement with models, most of the non-depleted boron stars show no nitrogen enrichment, and most of the boron depleted stars show nitrogen enrichments. This is indeed encouraging and can be taken as support for the mixing scenario.

In Fig. 6.9, we see that two nitrogen-enriched stars (green diamonds) appear in the red area where models predict no or small nitrogen enrichment. But those stars have large error bars on their N/C, indicating that they may be normal N-rich stars (see also stars in Fig. 6.10 with logϵ(B) > 2 and log(N/C) > -0.4), therefore we shall not discuss them further in the present work.

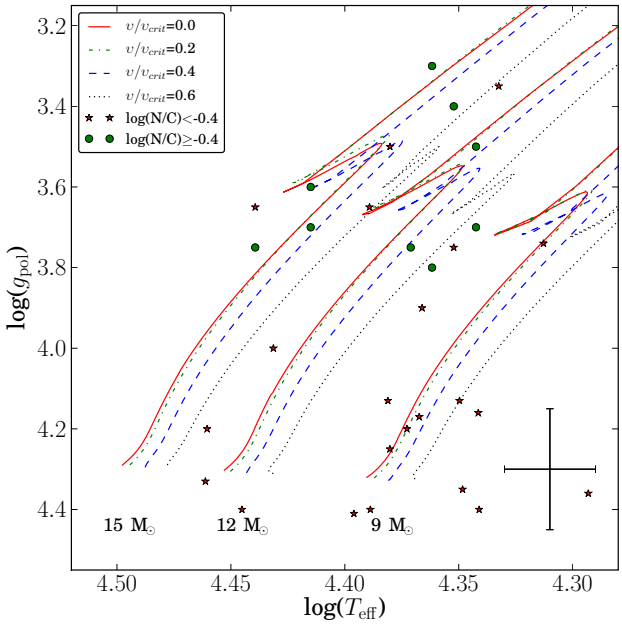

Figure 6.8: Evolutionary tracks of our models in the $\log g_{\rm pol}$ versus $\log T_{\rm eff}$ plane. For estimating the gravity of the theoretical track, we used the gravity at the pole. The gravities for the observed stars are those deduced from spectroscopy. Different kinds of points are used for stars with various surface nitrogen over carbon ratios. The stars labelled with numbers correspond to the objects, discussed in the text. The typical error bars are depicted in the lower right hand corner.

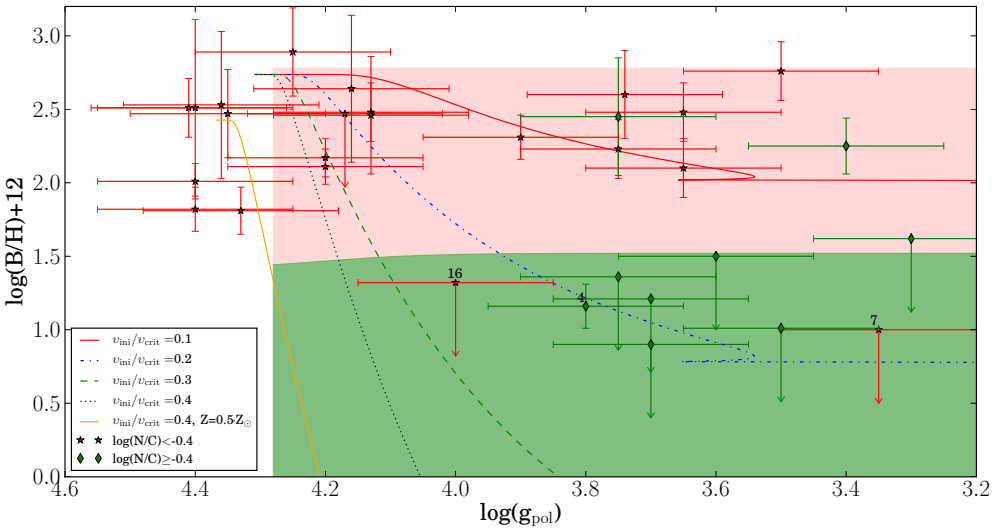

Figure 6.9: Surface boron abundances plotted versus polar gravity for 12 $M_\odot$ models with initial $v_{\rm ini}/v_{\rm crit}$ between 0 and 0.4. The orange continuous curve corresponds to the 12 $M_\odot$ with $Z = 0.007$. Different kinds of points are used for stars with various surface N/C ratios. The labelled stars correspond to objects discussed in the text. The colour map depicts the same division in log(N/C) regimes as the observations going from low (top) to high (bottom) values.

One also sees that two stars are B-depleted while showing no nitrogen enrichment (stars 7 and 16). Such stars can be explained if the timescale for boron depletion is much shorter than the timescale for the surface nitrogen enrichment. Present models, even those rotating very fast, have difficulties reproducing the surface abundances of the two stars belonging to this category. Probably here, another process than the processes studied in the present paper must be invoked. Binary mass transfer usually occurs in case B[2], allowing only transfer of B-depleted and N-enriched material. But in the less common case A[3], we might imagine transfer of B-depleted, but not yet N-enriched material. In close binaries, some mixing might also occur through tidal mixing, a process that has not yet been explored so far whether from an observational point of view or from theory. Another possibility would be that these stars present a strong differential rotation at the surface, triggered by some (magnetic?) braking mechanism of the surface layers. This would in turn trigger efficient mixing through shear instabilities in the layers with a strong differential rotation, explaining the rapid depletion of boron without any significant enhancement of nitrogen.

As just discussed, the bulk of the observations can be explained by our tracks with an average rotation on the MS between 0 and 100 km s^{-1}. Looking at Fig. 6.3, we see that the most B-depleted stars can be explained by 12 $M_\odot$ stellar models with a velocity on the MS superior to about 90 km s^{-1} and an inclination inferior or equal to 30 degrees[4].

[2]Mass transfer during the transition from MS to the red-giant phase.

[3]Roche lobe overflow already during the main sequence of the donor.

[4]The inclination angle fix the position of the boron depletion curve on the MS at a given $v \sin i$, while the rotation velocity governs the amplitude of the depletion.

What would be interesting is to know the fraction of stars showing a $\upsilon \sin i$ inferior to υ_1 having a velocity υ superior to a given limit, υ_2. To compute such a fraction, one has to apply the equation

$$P(\upsilon \sin i < \upsilon_1 \text{ with } \upsilon > \upsilon_2) = \frac{\int_{\upsilon_2}^{\upsilon_{\max}} \int_0^{\varphi} f(\upsilon) \sin\alpha d\upsilon d\alpha}{\int_0^{\upsilon_{\max}} \int_0^{\varphi} f(\upsilon) \sin\alpha d\upsilon d\alpha}, \tag{6.5}$$

where $f(\upsilon)$ is the velocity distribution function, $\upsilon_{\max}$ the upper limit of the rotation velocities, and φ the inclination angle between the rotation axis and the line of sight (equal to $\pi/2$ when the axis of rotation is perpendicular to the line of sight). $\varphi = \pi/2$ when $\upsilon \leq \upsilon_1$ and $\varphi = arcsin(\upsilon_1/\upsilon)$ when $\upsilon \geq \upsilon_1$, so that $\upsilon \sin i \leq \upsilon_1$. We suppose an isotropic distribution of inclination angles, so that the probability of having an inclination angle between α and $\alpha + d\alpha$ is proportional to $\sin\alpha d\alpha$. The denominator of Eq. 6.5 is proportional to the number of stars with $\upsilon \sin i \leq \upsilon_1$, whereas the numerator counts the subset of these stars with $\upsilon > \upsilon_2$.

For υ_1 we adopted 50 km s^{-1}, which is appropriate for the investigated sample, a value equal to 100 km s^{-1} was considered for υ_2 (see above), since this is the velocity required to reproduce the strongest B-depletion. The value of $\upsilon_{\max}$ has been chosen as equal to 400 km s^{-1} [5]. We assumed a Gaussian velocity distribution as proposed by Dufton et al. (2006) with the updated parameters, $\upsilon_0 = 225$ km s^{-1} and $\Delta\upsilon = 145$ km s^{-1}, from Hunter et al. (2009).

We find that 36% of stars with $\upsilon \sin i < 50$ km s^{-1} have velocities υ superior to 100 km s^{-1}. Considering that our model 12 $M_\odot$ with $\upsilon_{\rm ini}/\upsilon_{\rm crit} = 0.2$ only reaches the upper limits for B-depletion at the very end of its MS, $\upsilon_2 = 100$ km s^{-1} might seem too optimistic. But with stricter limits, such as $\upsilon_2 = 125$ or even 150 km s^{-1}, the probability is still 29% and 23%, respectively. This fits the 29% (9 of 31 stars) B-depleted stars in the sample.

If we take only the sample with $\upsilon \sin i < 20$ km s^{-1} ($\upsilon_1 = 20$ km s^{-1}), then we get $P = 0.21$, i.e. 21% whereas in the observational sample 25% (3 out of 12 stars) are B-depleted (compare Fig. 6.3b), which is also in good agreement for the size of this sub-sample. We can therefore conclude that the inclination effect is likely to play a role in the observational sample here and that the statistical properties fit our models of single rotating stars.

In Fig. 6.10, we have plotted the observations of the B/H versus N/C ratio, as well as the evolutionary tracks obtained in the present work. This diagram tests whether the concomitant changes of boron and nitrogen are reproduced by the rotating stellar models. In Fig. 6.10a we plotted models with $\upsilon_{\rm ini}/\upsilon_{\rm crit} = 0.4$ to show the typical B-N/C relation. We see that these models could explain a large fraction of the observations, but they correspond to an average velocity on the MS of around 180 km s^{-1}, while the observational sample mainly consists of slow rotators ($\upsilon \sin i \leq 50$ km s^{-1}). On the other hand, in panel b of Fig. 6.10, models with lower velocities are shown. We see that they would provide a good fit to the points with boron abundances between 0.9 and 1.5 and N/C ratios of the order of -0.2. These models have difficulty explaining stars that are more depleted in boron and more enriched in nitrogen.

The two stars 7 and 16 (see Fig. 6.10) present no or little surface nitrogen enrichment and are strongly boron-depleted. The range of values spanned by the different initial mass and initial velocity models barely explain these values, therefore these stars challenge our models even though the difference in N/C is within 2-σ of the models at the upper limit. These two

[5] The results only marginally depend on the upper integration limit as long $\upsilon_{\max} \gtrsim$400km s^{-1}.

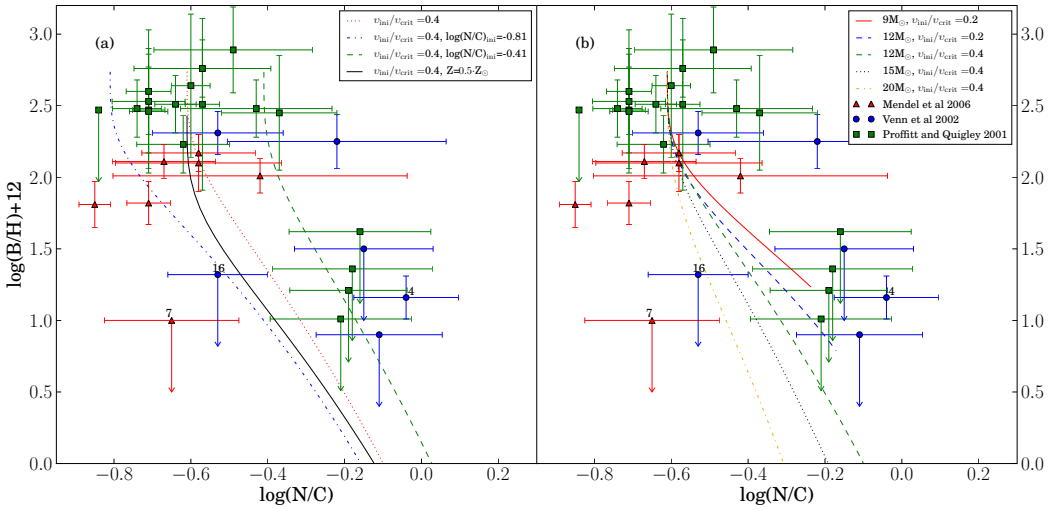

Figure 6.10: Boron versus nitrogen over carbon for the observations and in (a) $12M_{\odot}$ models with different initial compositions and in (b) models with different masses and low-to-intermediate velocities to show the possible spread in MS evolution. The labelled stars correspond to objects that challenge the present theoretical predictions (see text).

stars were also found to be a problem for single-star models by other authors (Morel et al. 2008; Mendel et al. 2006; Venn et al. 2002).

Apart from these few difficult cases, the above comparisons are very encouraging on the whole and support the predictions of the rotating models. At this stage it is also interesting to note that star 7, which cannot be reproduced by the present models, is a spectroscopic binary with a period of 9.5 days (Pourbaix et al. 2004), so it might well be that this star was slowed down by spin-orbit coupling in the course of its MS evolution. Such a braking mechanism would also slow down or even stop the N-enrichment process.

Are there any other indications that the changes in surface abundances we observe here are linked to rotation? To answer that question, measurements of surface velocities would be welcome. At the moment only a few stars (5) have estimates of their surface velocity (see Table 6.3). These stars are plotted in Fig. 6.3. Let us make a few comments on each of them.

- Stars 3 and 4: for those stars, the present rotating models show too high surface velocity for their boron surface abundances. In other words, in Fig. 6.3a, the theoretical MS tracks that go through the observed B/H ratio *during the MS phase* are too much to the right. This may indicate that mixing in those stars is more efficient than predicted by the present models[6]. This is supported by the high N surface content and that they are still on the MS. Models computed with a lower initial metal content may help to improve the situation (see yellow track and light red shaded area in Fig. 6.3a). Indeed, as can be seen looking at the track for the $12M_{\odot}$, $v/v_{\rm crit} = 0.4$, $Z = 0.5\ Z_{\odot}$, the MS band extends well into the post-MS regions defined by the more metal-rich models. In that case there would be no difficulty at least reproducing star 3. But the iron content of these stars is

[6]In case those stars were post MS stars, which is not confirmed by their present observed gravities (see Fig. 6.9), then there would be no difficulty for the present models to explain those stars.

not significantly different from the solar value. In general, most stars in the sample have Fe surface abundance consistent with the solar value[7]. Star 4 is the most extreme case in showing B-depletion while rotating slowly and is therefore positioned in the shaded area of Fig. 6.3a. It cannot be explained even with a low-metallicity track.

- Stars 6, 24 and 30: for these stars, the present theoretical models present characteristics that agree with the observations. Looking at Fig. 6.3a, star 6 might be interpreted as a slowly rotating star at the beginning of its evolution, but its gravity indicates it is an evolved star that is rather at the end of the MS phase, if not beyond. Thus it seems that here the mixing was less efficient than shown by the present models. But the σ-error of boron is comparable to the boron depletion expected at this low rotation rate, so at the moment, this observation is not very constraining and is compatible with the present models.

Except for star 4, present models explain surface abundances, velocities and gravities simultaneously. The number of stars is, however, small, and it would be interesting to obtain more velocity measurements to set such a conclusion on firmer ground.

If we look at the projected velocities in Fig. 6.3b, it appears that all B-depleted stars are in the shaded regions, *i.e.* beyond the main sequence phase, which does not appear to be consistent with the $\log g$ values (see Fig. 6.9). This difficulty might be resolved by invoking the following reasons.

1. Initially rapidly rotating stars were suddenly slowed down at a given point by, for example, binary interaction.

2. The efficiency of mixing is underestimated, so that stars can be both boron-depleted and rotating at low velocities. Rotation is measured only at the surface, while the shear turbulence, which governs the changes in the surface abundances in rotating models depends on the gradient of the velocity inside the star. Effects like magnetic breaking could trigger mixing in the outer layers and slow the surface down.

3. The stars have low inclination angles (see the effect illustrated in Fig 6.3).

The last case was discussed at the start of this section and, from a statistical point of view, may indeed explain part of the discrepancy. Point 2 seems to be required at least for some stars (like 7 and 16) only on the basis of their position in the boron versus nitrogen plane. The impact of binarity still remains difficult to assess in part because this effect produces similar changes in the surface abundances to those expected from rotation, at least for those stars showing boron depletion and nitrogen enrichment[8].

A way to disentangle rotation and binary effect would be to look at the presence or not of a correlation between surface velocity and surface enrichments. In case binarity effects dominate, no correlation is expected between stellar rotation rate and boron depletion (Langer et al. 2010), while rotational mixing would lead to stronger depletion for faster rotation rates (for the same mass, metallicity, and age). In Fig. 6.3 no correlation can be seen. This might look like favouring binary mixing. But for such a conclusion to be valid, one needs to correct for the inclination effects and one should be sure that stars of similar initial masses and ages

[7]Stars 5 and 8 have a $\log \epsilon$(Fe) differing by more than 2 σ but do not show B-depletion.

[8]Models with intermediate-to-fast rotation ($\upsilon/\upsilon_{\rm crit} \geq 0.3$) show comparable boron depletion (> 3 dex) to binary mass transfer.

form the bulk of the sample[9], which is not the case here, looking at Fig. 6.8. From the present data, therefore, we have difficulty concluding about the nature of the process at work. Rotation does appear to provide a reasonable process for explaining at least part of the stars, but binarity can also play a role.

From an observational point of view, we may conclude that, to take a step further, the following informations would be needed:

- The boron abundances on the surface of stars with a high $\upsilon \sin i$. This is probably a real challenge to observe, but since $\upsilon \sin i$ is a lower limit to υ, any high values imply a fast rotator. Unless the observed stars are at the very beginning of the main sequence, rotational models would predict that all these stars should be boron-depleted.

- The abundances of ^{3}He and the values of the ^{12}C/^{13}C ratio in order to test the predictions of the present models shown in Figs. 6.5 and 6.6. Of course it would be interesting to have predictions of models invoking binary mass transfer and/or tidal mixing for comparison.

- Observations in star clusters or of eclipsing binaries, since they would allow stars of the same age to be compared, with those for which some (more) precise indications on the mass can be obtained.

- Asteroseismological data could probe the way rotation varies with depth, but it is only feasable for very slow rotators. Asteroseismology is also able, together with models, to provide some information on the previous rotational history of the star (Aerts 2008). This might offer very interesting hints to the processes at work here.

6.6 Conclusions

We implemented the Basel reaction network into the Geneva stellar evolution code (GENEC), which treats the meridional circulation as an advection process. This allowed us to predict the surface evolution of light elements in massive stars. We obtained the following results.

- The boron depletion is stronger than in models of Heger & Langer (2000). This is probably because we account for the effect of meridional currents on the transport of angular momentum as an advective process and not as a diffusive one, along with accounting for the effects of mean molecular weight gradients on the efficiency of rotational diffusion, which is different in both models.

- We present expected correlations based on rotating stellar models between boron surface abundances and the surface abundances of ^{3}He, and the surface number ratios ^{12}C/^{13}C. Further observations will be able to check whether these correlations are present in real stars.

- We confirm the general conclusion obtained by Mendel et al. (2006) and Venn et al. (2002) that rotational mixing can account for most of the observations of the boron and nitrogen surface abundances.

[9] Mixing efficiency depends not only on the rotation velocity alone but also on the age, mass, and metallicity.

- We confirm the existence of challenging cases that do not fit well in the present scenario: stars 4 and 7, which do appear to present a much more rapid B-depletion than presently allowed by the models.
- Even though our models can reproduce most of the observations, the current uncertainties do not allow us to draw a firm conclusion about the questions whether our models mix enough and whether another surface mixing mechanism has to be invoked. We proposed some possibilities for further observations that would help clarifying the situation.

Table 6.2: Model parameters

$M_{\rm ini}$	$\frac{v_{\rm ini}}{v_{\rm crit}}$	$J_{\rm ini}$	$\tau_{\rm H}$	$v_{\rm eq}$	p	^{3}He	^{4}He	^{10}B	^{11}B	^{12}C	^{13}C	^{14}N
$M_\odot$		10^{52}erg · s	10^7 yr	km s^{-1}	Mass fraction							
9	0.0	0.00	2.538	0 (0)[a]	0.720	6.51e-5	0.266	7.79e-10	3.46e-09	2.28e-3	2.77e-5	6.59e-4
				0[b]	0.720	6.51e-5	0.266	7.79e-10	3.46e-09	2.28e-3	2.77e-5	6.59e-4
				0[c]	0.703	4.40e-5	0.283	3.84e-11	2.66e-10	1.36e-3	7.01e-5	2.18e-3
9	0.2	0.35	2.632	88 (115)[a]	0.720	6.00e-5	0.266	5.85e-11	5.25e-10	2.13e-3	5.97e-5	8.09e-4
				76[b]	0.720	4.96e-5	0.266	1.14e-11	1.38e-10	1.76e-3	1.03e-4	1.20e-3
				1[c]	0.696	3.07e-5	0.290	1.05e-12	1.53e-11	1.05e-3	1.11e-4	2.59e-3
9	0.4	0.67	2.663	182 (231)[a]	0.720	3.37e-5	0.266	2.83e-13	7.42e-12	1.31e-3	1.55e-4	1.67e-3
				163[b]	0.719	2.63e-5	0.267	1.04e-14	4.68e-13	9.48e-4	1.56e-4	2.15e-3
				1[c]	0.692	1.97e-5	0.294	9.25e-16	5.09e-14	6.71e-4	1.28e-4	3.03e-3
9	0.6	0.95	2.692	275 (348)[a]	0.719	2.22e-5	0.267	1.50e-15	1.01e-13	8.25e-4	1.53e-4	2.28e-3
				256[b]	0.717	1.84e-5	0.269	1.07e-17	1.57e-15	5.49e-4	1.28e-4	2.74e-3
				2[c]	0.687	1.47e-5	0.298	6.87e-19	1.48e-16	4.04e-4	1.01e-4	3.43e-3
12	0.0	0.00	1.605	0 (0)[a]	0.720	6.51e-5	0.266	7.79e-10	3.46e-09	2.28e-3	2.77e-5	6.59e-4
				0[b]	0.720	6.51e-5	0.266	7.79e-10	3.46e-09	2.28e-3	2.77e-5	6.59e-4
				0[c]	0.684	3.77e-5	0.302	2.30e-11	2.35e-10	1.33e-3	7.15e-5	2.42e-3
12	0.1	0.31	1.619	44 (62)[a]	0.720	6.51e-5	0.266	3.05e-10	1.89e-09	2.28e-3	2.92e-5	6.60e-4
				36[b]	0.720	6.09e-5	0.266	9.37e-11	7.25e-10	2.19e-3	5.21e-5	7.43e-4
				0[c]	0.680	3.25e-5	0.306	7.51e-12	7.06e-11	1.23e-3	9.24e-5	2.57e-3
12	0.2	0.62	1.638	94 (123)[a]	0.720	5.33e-5	0.266	2.37e-11	2.56e-10	2.02e-3	8.10e-5	9.18e-4
				79[b]	0.720	4.02e-5	0.266	2.94e-12	4.49e-11	1.61e-3	1.26e-4	1.36e-3
				1[c]	0.678	2.49e-5	0.308	2.57e-13	4.71e-12	1.02e-3	1.17e-4	2.81e-3
12	0.3	0.91	1.663	144 (184)[a]	0.720	3.63e-5	0.266	9.93e-13	1.98e-11	1.56e-3	1.47e-4	1.40e-3
				125[b]	0.719	2.67e-5	0.267	3.92e-14	1.31e-12	1.19e-3	1.68e-4	1.85e-3
				1[c]	0.677	1.88e-5	0.309	3.32e-15	1.34e-13	8.39e-4	1.38e-4	2.98e-3
12	0.4	1.20	1.669	194 (246)[a]	0.719	2.55e-5	0.266	2.50e-14	1.03e-12	1.20e-3	1.74e-4	1.80e-3
				173[b]	0.718	1.95e-5	0.268	2.97e-16	2.43e-14	9.05e-4	1.73e-4	2.23e-3
				1[c]	0.676	1.47e-5	0.310	2.38e-17	2.38e-15	6.67e-4	1.39e-4	3.19e-3
12	0.5	1.46	1.676	245 (309)[a]	0.719	1.96e-5	0.267	7.29e-16	5.69e-14	9.57e-4	1.76e-4	2.12e-3
				224[b]	0.716	1.56e-5	0.269	2.42e-18	4.73e-16	6.98e-4	1.60e-4	2.55e-3
				1[c]	0.676	1.24e-5	0.310	8.87e-20	4.36e-17	5.33e-4	1.29e-4	3.35e-3
12	0.6	1.68	1.681	295 (371)[a]	0.719	1.62e-5	0.267	3.51e-17	4.47e-15	7.85e-4	1.68e-4	2.36e-3
				276[b]	0.715	1.34e-5	0.271	2.72e-22	1.39e-17	5.51e-4	1.42e-4	2.80e-3
				1[c]	0.692	1.18e-5	0.293	4.15e-24	1.21e-18	4.65e-4	1.23e-4	3.24e-3
12	0.7	1.87	1.698	344 (431)[a]	0.718	1.41e-5	0.267	3.19e-18	5.71e-16	6.81e-4	1.63e-4	2.50e-3
				337[b]	0.713	1.20e-5	0.273	7.73e-27	5.07e-20	4.54e-4	1.27e-4	2.98e-3
				2[c]	0.660	9.22e-6	0.326	8.21e-29	5.38e-22	3.39e-4	9.72e-5	3.79e-3
12	0.4	1.20	1.667	195 (248)[a,d]	0.735	1.95e-5	0.258	3.48e-16	3.11e-14	4.17e-4	7.33e-5	1.16e-3
				173[b,d]	0.733	1.52e-5	0.260	7.39e-19	2.67e-16	2.83e-4	6.38e-5	1.38e-3
				1[c,d]	0.727	1.41e-5	0.266	1.32e-20	2.91e-17	2.47e-4	5.89e-5	1.50e-3
15	0.0	0.00	1.128	0 (0)[a]	0.720	6.51e-5	0.266	7.79e-10	3.46e-09	2.28e-3	2.77e-5	6.59e-4
				0[b]	0.720	6.51e-5	0.266	7.78e-10	3.46e-09	2.28e-3	2.77e-5	6.59e-4
				0[e]	0.680	3.14e-5	0.305	2.99e-16	6.92e-11	1.17e-3	6.73e-5	2.70e-3
15	0.2	0.96	1.197	97 (129)[a]	0.720	4.88e-5	0.266	8.58e-12	1.19e-10	1.95e-3	9.93e-5	9.84e-4
				80[b]	0.719	3.56e-5	0.267	6.82e-13	1.48e-11	1.56e-3	1.45e-4	1.43e-3
				0[e]	0.661	2.01e-5	0.325	4.68e-14	1.24e-12	9.18e-4	1.19e-4	3.17e-3
15	0.4	1.85	1.209	203 (257)[a]	0.719	2.23e-5	0.267	3.59e-15	2.15e-13	1.22e-3	1.96e-4	1.80e-3
				179[b]	0.716	1.69e-5	0.270	2.07e-17	2.68e-15	9.54e-4	1.94e-4	2.22e-3
				0[e]	0.650	1.21e-5	0.336	1.26e-18	2.13e-16	6.78e-4	1.47e-4	3.42e-3
15	0.6	2.61	1.224	308 (387)[a]	0.718	1.42e-5	0.268	1.72e-18	3.86e-16	8.55e-4	1.93e-4	2.29e-3
				286[b]	0.712	1.14e-5	0.274	6.07e-28	4.13e-20	6.24e-4	1.65e-4	2.76e-3
				1[e]	0.642	8.30e-6	0.344	4.15e-30	2.82e-22	4.49e-4	1.22e-4	3.79e-3

[a] The surface velocity and mass fractions when the central hydrogen abundance $X_c \approx 0.36$ is given on the first line for each model. The velocity values in brackets are the values at ZAMS.
[b] The surface velocity and mass fractions at the end of hydrogen burning ($X_c \approx 10^{-5}$) is given on the second line for each model. The velocity was not taken exactly when the hydrogen was depleted but when it reached its minimum, i.e., a little bit earlier.
[c] The third line for the 9 and 12 $M_\odot$ models corresponds to the surface values during the RGB phase.
[d] model with lower initial metallicity $Z = 0.5 \cdot Z_\odot$.
[e] The third line for the 15 $M_\odot$ models corresponds to the surface values at the end of He burning.

Table 6.3: Stellar parameters

No	Star	Cluster	Binary	logg^a	T^b_{eff}	$\upsilon \sin i$ [km s^{-1}]	Ref.	$\upsilon_{\rm eq}$ [km s^{-1}]	Ref.	Mass^c [$M_\odot$]
1	BD +56°576	χ Per	Eclipse	3.40	22500	17	1	...		13.5
2	HD 886	...	...	3.75	22500	10±1	2	...		10.7
3	HD 3360	CasTau OB1	...	3.70	22000	19±1	3	55±28	7	10.6
4	HD 16582	CasTau OB1	...	3.80	23000	14±1	2	14/28	8	10.7
5	HD 22951	Per OB	Visual	4.40	27900	23	4	...		11
6	HD 29248	Ori OB1	...	3.75	23500	36±3	2	6	9	11.5
7	HD 30836	Ori OB1	Spect.	3.35	21500	43±3	5	...		13.0
8	HD 34816	Ori runaway	...	4.20	28900	35	4	...		13.5
9	HD 35039	Ori OB1a	Spect.	3.74	20600	4	6	...		9.0
10	HD 35299	Ori OB1a	...	4.25	24000	8	6	...		9.1
11	HD 35337	Ori OB1c	...	4.20	23600	15	4	...		9.0
12	HD 35468	Ori OB1	...	3.50	22000	51±4	5	...		11.8
13	HD 36285	Ori OB1c	...	4.40	21900	10	4	...		<9
14	HD 36351	Ori OB1a	Visual	4.16	22000	42	6	...		<9
15	HD 36430	Ori OB1c	...	4.36	19600	26	6	...		<9
16	HD 36591	Ori OB1b	Visual	4.00	27000	16±2	5	...		12.8
17	HD 36629	Ori OB1c	...	4.35	22300	4	6	...		<9
18	HD 36959	Ori OB1c	...	4.41	24900	11	6	...		9
19	HD 36960	Ori OB1c	Visual	4.33	28900	33	4	...		12
20	HD 37209	Ori OB1c	...	4.13	24000	50	6	...		9.7
21	HD 37356	Ori OB1c	...	4.13	22400	23	6	...		<9
22	HD 37481	Ori OB1c	...	4.17	23300	67	6	...		<9
23	HD 37744	Ori OB1b	...	4.40	24500	39	6	...		9
24	HD 44743	...	...	3.50	24000	23±2	2	31±5	10	14.5
25	HD 46328	Coll. 121	...	3.75	27500	10±2	2	...		15.5
26	HD 50707	Coll. 121	...	3.60	26000	45±3	5	...		15.6
27	HD 52089	...	...	3.30	23000	28±2	5	...		15.3
28	HD 111123	Sco Cen	...	3.65	27500	48±3	5	...		16.6
29	HD 205021	Cep OB1	Spect.	3.70	26000	29±2	2	...		14.5
30	HD 214993	Lac OB1	...	3.65	24500	42±4	2	45	11	13.5
31	HD 216916	Lac OB1	Eclipse	3.90	23200	13	1	...		9.7

[a]The typical 1-σ error for $\log g$ is between 0.15 and 0.2 (see e.g Morel et al. 2008).
[b]The typical 1-σ error for T_{eff} is about 1000 K (see e.g Morel et al. 2008).
[c]The masses of the stars are only rough estimates from the comparison of the models and the stellar positions in the $\log g$-$\log T_{\rm eff}$ diagram under the assumption of slow rotation.
References: [1] Venn et al. (2002); [2] Morel et al. (2006); [3] Briquet & Morel (2007); [4] Mendel et al. (2006); [5] Morel et al. (2008); [6] Proffitt & Quigley (2001); [7] Neiner et al. (2003); [8] Aerts et al. (2006); [9] Pamyatnykh et al. (2004); [10] Mazumdar et al. (2006); [11] Aerts (1996)

Table 6.4: Surface abundances

No	Star	logϵ(C)	logϵ(N)	log(N/C)	Ref.	logϵ(Fe)	Ref.	logϵ(B)	Ref.
1	BD +56°576	7.84±0.18	7.62±0.22	-0.22±0.28	1[a]	7.34±0.17	1	2.25±0.19	1
2	HD 886	8.20±0.05	7.58±0.11	-0.62±0.12	2	7.25±0.16	2	2.23±0.20	6
3	HD 3360	8.16±0.08	7.97±0.13	-0.19±0.15	3	7.31±0.16	3	<1.21	6
4	HD 16582	8.09±0.08	8.05±0.11	-0.04±0.14	2	7.32±0.18	2	1.16±0.15	1
5	HD 22951	8.11±0.21	7.69±0.32	-0.42±0.38	1[a]	7.03±0.10	4	2.01±0.12	4
6	HD 29248	8.24±0.12	7.87±0.09	-0.37±0.15	2	7.36±0.19	2	2.45±0.40	6
7	HD 30836	8.19±0.09	7.54±0.15	-0.65±0.18	5	7.11±0.18	5	<1.00	4
8	HD 34816	8.17±0.07	7.59±0.13	-0.58±0.15	1[a]	7.12±0.11	4	2.17±0.13	4
9	HD 35039	8.36±0.03	7.65±0.05	-0.71±0.06	1[a]	7.24	6	2.60±0.30	6
10	HD 35299	8.19±0.19	7.70±0.08	-0.49±0.21	1[a]	7.19	6	2.89±0.30	6
11	HD 35337	8.31±0.09	7.64±0.10	-0.67±0.13	1[a]	7.38±0.10	4	2.11±0.12	4
12	HD 35468	8.11±0.09	7.90±0.16	-0.20±0.19	5	7.23±0.14	5	<1.01	6
13	HD 36285	8.48±0.04	7.77±0.04	-0.71±0.06	1[a]	7.23±0.09	4	1.82±0.15	4
14	HD 36351	8.28±0.04	7.68±0.03	-0.60±0.05	1[a]	7.28	6	2.64±0.50	6
15	HD 36430	8.38±0.03	7.67±0.09	-0.71±0.09	1[a]	7.54	6	2.53±0.50	6
16	HD 36591	8.19±0.05	7.66±0.12	-0.53±0.13	5	7.32±0.19	5	≤1.32	1
17	HD 36629	8.32±0.03	7.61±0.03	-0.71±0.04	1[a]	7.39	6	2.47±0.30	6
18	HD 36959	8.37±0.02	7.73±0.05	-0.64±0.05	1[a]	7.29	6	2.51±0.20	6
19	HD 36960	8.39±0.01	7.54±0.04	-0.85±0.04	1[a]	7.22±0.10	4	1.81±0.16	4
20	HD 37209	8.29±0.04	7.55±0.05	-0.74±0.06	1[a]	7.32	6	2.48±0.20	6
21	HD 37356	8.41±0.03	7.70±0.04	-0.71±0.05	1[a]	7.32	6	2.46±0.40	6
22	HD 37481	8.39	7.55±0.02	-0.84	1[a]	7.40	6	<2.47	6
23	HD 37744	8.37±0.02	7.80±0.04	-0.57±0.04	1[a]	7.36	6	2.51±0.60	6
24	HD 44743	8.16±0.11	7.59±0.14	-0.57±0.18	2	7.17±0.19	2	2.76±0.20	6
25	HD 46328	8.18±0.12	8.00±0.17	-0.18±0.21	2	7.30±0.22	2	<1.36	6
26	HD 50707	8.18±0.10	8.03±0.15	-0.15±0.19	5	7.23±0.19	5	≤1.50	1
27	HD 52089	8.09±0.12	7.93±0.14	-0.16±0.19	5	7.16±0.15	5	<1.62	6
28	HD 111123	8.04±0.10	7.61±0.17	-0.43±0.20	5	7.23±0.24	5	2.48±0.20	6
29	HD 205021	8.02±0.10	7.91±0.13	-0.11±0.17	2	7.24±0.23	2	≤0.90	1
30	HD 214993	8.22±0.12	7.64±0.18	-0.58±0.22	2	7.30±0.20	2	2.10±0.20	4
31	HD 216916	8.17±0.13	7.64±0.11	-0.53±0.17	1[a]	7.66±0.14	1	2.31±0.15	1

[a]N and C values are from the compilation in Venn et al. (2002) where most N and C values are corrected values originally from Gies & Lambert (1992) and Cunha & Lambert (1994).
References: the numbers correspond to the same references as in Table 6.3.

7 Conclusion and Outlook

7.1 Summary & Conclusion

In this work I investigated the impact of rotation on the nucleosynthesis in hydrostatic burning stages of massive stars. For this purpose an extended nuclear reaction network based on the BasNet code was implemented into the Geneva stellar evolution code (GenEC). Two grids of massive star models were performed with this code and the three following subjects were investigated.

1. An extended grid of models of 15 to 40 $M_\odot$ models was performed, with various rotation rates and compositions, to investigate the impact of rotation and rotation induced mixing, respectively, on the s process in massive stars (see Chapter 4).

2. We found possible signature of such a rotation boosted s process in the Galactic bulge (see Chapter 5), which was probably a site of early and strong star formation in the Milky Way.

3. The second grid of stellar models was performed for 9 to 15 $M_\odot$ stars at solar metallicity and with various rotation rates to investigate the depletion of boron in the stellar envelopes (see Chapter 6). With such a study one can constrain the rotation induced mixing in particular secular shear.

From these three parts of this work the following conclusions were drawn.

1. In Chapter 4 we have investigated the impact of rotation on the s-process nucleosynthesis in massive stars.

   - Rotation was found to boost the s process in massive stars, on the one hand by affecting the stellar structure and on the other and by the production of ^{22}Ne caused by rotation induced mixing between the shell H-burning layers the and He-core.
   - The s process from He core is enhanced at all metallicities, but in particular at $Z < Z_\odot$ where massive rotating stars can produce 10^2 to 10^4-times higher over-production factors.
   - The s process from C-shell burning on the other hand is still limited to $Z \gtrsim Z_\odot$, because of the limited iron seeds.
   - Even with very high neutron to seed ratios at $Z = 10^{-5}$ and $Z = 10^{-7}$ no primary production of the seeds is possible. And the s process in massive stars is limited by seeds in $Z \lesssim 10^{-3}$ stars.

- The exhaustion of the seeds leads to a peak production of Kr to Sr at $Z = 10^{-3}$ (initial [Fe/H]$= -1.8$) in stars with rotation. The lighter nuclei from $A = 60$ to 80 still have a secondary like behaviour. Yields from rotating massive stars with $Z > 10^{-5}$ have therefore to be considered in particular for Kr, Sr, Y, and Zr in the chemical enrichment leading to a solar composition. Hence, for the galactic chemical enrichment of heavy elements (60-90), yields of massive rotating stars with $Z > 10^{-5}$ should be adopted.
- Rotating stars typically produce [Sr/Ba]$\approx +2$ and an intrinsic upper limit of about $+2.3$, but [Sr/Ba] goes towards 0 around $Z = 10^{-5}$. Also intrinsic would be a scatter in the absolute Sr and Ba production as well as in the Sr/Ba at $Z < 10^{-3}$, which could be a possible solution for the [Sr/Ba] scatter in metall poor halo stars.
- Rotation induced mixing also provides the primary neutron source, ^{22}Ne, in the He-shell for explosive nucleosynthesis. A reinvestigation of the n-process (Rauscher et al. 2002) in massive rotating stars at various metallicities might therefore be interesting.
- Primary ^{25}Mg and ^{26}Mg from massive rotating stars could provide the missing fraction of these isotopes, which was missing from previous nucleosythesis calculations of massive stars (Yong et al. 2003).

2. In Chiappini et al. (2011) we have found stars with the enrichment of s-process elements in one of the oldest globular clusters in the Galactic Bulge, NGC 6522. By comparing the abundance pattern of the eight stars studied to massive star and AGB star models, have found the following conclusions.

   - The eight stars studied in NGC 6522 are enriched in α-elements, and neutron capture nucleosynthesis elements: Sr, Y, Ba, La and Eu.
   - On the one hand, five of these stars show [Y/Ba] ratios, which could be explained by the AGB models or the r process, three stars show [Y/Ba]$\gtrsim 1$ (B-108, B-130 and F-121), which is neither consistent with a main r-process component nor with the s process in low Z AGB stars. On the other hand, the same three stars show [Eu/Ba] ratios, which are consistent with a main r process and the other five stars values of the same ratio, which rather match mixture of r and "weak" s process.
   - We concluded that, at least for the three stars B-108, B-130 and F-121, a possible scenario to explain the chemical signature is a rotation boosted s process, which accounts for the enhancment in Sr and Y.
   - Moreover the intrinsic scatter in [Y/Ba] and [Sr/Ba] of such a rotation boosted s process is consistent with the scatter found in metal-poor halo stars as well as the Bulge stars from NGC 6522 studied.

3. The Geneva stellar evolution code (GenEC) treats the meridional circulation as an advection process. This allowed us to predict the surface evolution of light elements in massive stars. We obtained the following results.

   - The boron depletion is stronger in GenEC than in models of Heger & Langer (2000). This is probably because we account for the effect of meridional currents on the transport of angular momentum as an advective process and not as a diffusive one,

along with accounting for the effects of mean molecular weight gradients on the efficiency of rotational diffusion, which is different in both models.

- We present expected correlations based on rotating stellar models between boron surface abundances and the surface abundances of ^{3}He, and the surface number ratios ^{12}C/^{13}C. Further observations will be able to check whether these correlations are present in real stars.
- We confirm the general conclusion obtained by Mendel et al. (2006) and Venn et al. (2002) that rotational mixing can account for most of the observations of the boron and nitrogen surface abundances.
- We confirm the existence of challenging cases that do not fit well in the present scenario: stars 4 and 7 in Frischknecht et al. (2010), which do appear to present a much more rapid B-depletion than presently allowed by the models.
- Even though our models can reproduce most of the observations, the current uncertainties do not allow us to draw a firm conclusion about the questions whether our models mix enough and whether another surface mixing mechanism has to be invoked. We proposed some possibilities for further observations that would help clarify the situation.

7.2 What to do next?

In an ideal world of modelling stellar structure and nucleosynthesis, we could follow the full stellar structure in three spacial dimensions and with a full reaction network over the whole stellar lifetime including the collapse and explosion phase. And one would be able to run models in a reasonable time for a large parameter space of initial stellar masses, metallicities and rotation rates to explain the status of the universe observed today.

However, even though the numerical tools used in this work were and are involved in world leading science, they are far from this "ideal world". With the limitation to 1D for the stellar structure, parametrisations of transport mechanisms for energy, angular momentum and chemical elements had to be applied, which impose important uncertainties. Also the size of the network used in this work is at the moment too large for a full evolution from main sequence till collapse when the network is coupled to the stellar structure and a large set of models should be calculated. Hence, on a roadmap for a more complete picture of stellar evolution and nucleosynthesis, work on many aspects is needed.

- One of the projects we want to progress is to use the yields of rotation boosted s process in GCE models, to see the possible impacts it has on the chemical enrichment of the different components of the Galaxy. In particular also the Mg isotopic ratios should be studied. Inhomogeneous GCE study, made in Argast et al. (2004), could also shed some more light on the observed and modeled scatter of elemental abundances.
- In the framework of GenEC with included BasNet, we should be able to follow now the stellar evolution until the onset of the iron core collapse, because the network includes electron captures, which will lead to a lowering of Y_e and hence of the electron degeneracy pressure. This part has to be tested and eventually the time step management of GenEC might have to be changed. The final goal is to provide SN-progenitor models to the SN modelling community.

- The successful calculation of SN-progenitors would allow us to apply simple explosion models and would allow us to study the impact of the rotation modified s process on the p process, which has s-process nuclei as seeds.
- A further study could then also investigate the explosive neutron capture nucleosynthesis in the He-shell, in case the α captures on the primary ^{22}Ne could be activated by the SN-shock.
- To improve the consistency with SN 3D hydro-models we should implement another EoS as mentioned in Section 2.7. A good candidate for an implementation is the Helmholtz EoS of Timmes & Swesty (2000) (available on cococubed.asu.edu).
- Full 3D stellar evolution not feasable but mixing prescriptions guided by multi-D hydrodynamic models should increase the accuracy of 1D models. Such work is now done in several groups and publications start to appear, as e.g. by Arnett et al. (2009), and hopefully will soon lead to an application in the parametrised prescriptions of transport phenomena of 1D stellar evolution codes.
- Dr. T. Rauscher, Dr. R. Hirschi, Dr. C. Winteler and I have developed a thermonuclear Monte-Carlo network, as mentioned in Section A.2. It puts us into the position to make reaction rate sensitivity studies of all astrophysical nucleosynthesis processes. As a first project a p-process study is planned.

8 Curriculum vitæ

Urs Stefan Frischknecht

Date of Birth: January 29, 1980
Citizenship: Swiss

Research interests

Nucleosynthesis in massive stars, stellar evolution, nucleosynthesis in general, galactic chemical evolution

Academic education

December 2011	Ph.D. summa cum laude in Theoretical Physics, Basel University Thesis title: *'Nucleosynthesis in Massive Rotating Stars'* Supervisors: Prof. Dr. F-K. Thielemann, Dr. R. Hirschi (Keele University, UK) External expert: Prof. Dr. G. Meynet (Geneva Observatory, CH)
2007 - 2011	Ph.D. student, Department of Physics, Basel University
2007 - 2010	Member of the European Graduate School Basel-Graz-Tübingen: *'Hadrons in vacuum, in nuclei and stars'*

November 2007	M.Sc. summa cum laude in Physics, Basel University Thesis title: *'S-Process Nucleosynthesis in Massive Stars'* Supervisor: Prof. Dr. M. Liebendörfer. Examination topic: *'General relativity, Nuclear Astrophysics'* Examiners: Prof. Dr. D. Trautmann, PD Dr. T. Rauscher
2005 - 2007	Master student, Department of Physics, Basel University
November 2005	B.Sc. in Physics, Basel University
2002 - 2005	Bachelor student, Department of Physics, Basel University
December 2001	High school Graduation: Matura Type C
1999 - 2001	Gymnasium (Grammar school), Münchenstein
1987 - 1999	Steiner School, Aesch

During my studies I heard lectures by the following persons:
Prof. Dr. C. Alewell, Prof. Dr. G. Baur, Prof. Dr. B. Binggeli, Prof. Dr. C. Bruder, Prof. Dr. H. Burkhart, Prof. Dr. R. Buser, PD Dr. T. Christen, Prof. Dr. O. Gerhard, Prof. Dr. S. Goedecker, Prof. Dr. E. Grebel, Prof. Dr. H.-J. Güntherodt, Prof. Dr. B. Hecht, PD Dr. M. Hofmann-Riedinger PD Dr K. Hencken, Prof. Dr. H.-J. Hug, Prof. Dr. H.-C. Im Hof, PD Dr. J. Jourdan, Prof. Dr. B. Krusche, Prof. Dr. M. Liebendörfer, Prof. Dr. D. Loss, Prof. Dr. D. Masser Prof. Dr. E. Meyer, Prof. Dr. P. Nagel, Prof. Dr. P. Oelhafen, Prof. Dr. E. Parlow, PD Dr. T. Rauscher, PD Dr. D. Rohe, Prof. Dr. R. Schneider-Sliwa, Prof. Dr. C. Schönenberger, Prof. Dr. I. Sick, Prof. Dr. F.-K. Thielemann, Prof. Dr. D. Trautmann

Languages

German (native), English (fluent), French (basic)

A Publications

A.1 List of publications

A.1.1 Refereed journals

- U. Frischknecht, R. Hirschi, F.-K. Thielemann, Non-standard s process in low metallicity massive rotating stars, A&A letters, 2012
- S. Ekström, C. Georgy, P. Eggenberger, G. Meynet, N. Mowlavi, A. Wyttenbach, A. Granada, T. Decressin, R. Hirschi, U. Frischknecht, C. Charbonnel, Grids of stellar models with rotation - I. Models from 0.8 to 120 Msun at solar metallicity (Z = 0.014), A&A, 2012
- C. Chiappini, U. Frischknecht, G. Meynet, R. Hirschi, B. Barbuy, M. Pignatari, T. Decressin, A. Maeder, Imprints of fast-rotating massive stars in the Galactic Bulge, Nature, 472, 2011
- U. Frischknecht, R. Hirschi, G. Meynet, S. Ekström, C. Georgy, T. Rauscher, C. Winteler, F.-K. Thielemann, Constraints on rotational mixing from surface evolution of light elements in massive stars, A&A, 2010

A.1.2 Conference Proceedings

- R. Hirschi, U. Frischknecht, F.-K. Thielemann, Chemical signature of GRB progenitors at low metallicities, Memorie della Societa Astronomica Italiana, 2012
- U. Frischknecht, R. Hirschi, T. Rauscher, F.-K. Thielemann, Impact of rotation on the weak s process, NiC XI, 2011
- U. Frischknecht, R. Hirschi, G. Meynet, S. Ekström, C. Georgy, T. Rauscher, C. Winteler, F.-K. Thielemann, Boron depletion in 9 to 15 solar mass stars with rotation, IAU Symposium, Volume 268, 2010
- R. Hirschi, U. Frischknecht, F.-K. Thielemann, M. Pignatari, C. Chiappini, S. Ekström, G. Meynet, A. Maeder, Stellar Evolution in the Early Universe, IAU Symposium, Volume 255, 2008
- T. Fischer, C. Winteler, U. Frischknecht, F.-K. Thielemann, M. Liebendörfer, The formation of the neutrino driven wind termination shock in spherically symmetric core collapse simulations, NiC X, 2008

- R. Hirschi, U. Frischknecht, M. Pignatari, F.-K. Thielemann, M. Bennet, S. Diehl, C. Fryer, F. Herwig, A. Hungerford, G. Magkotsios, G. Rockefeller, F. Timmes, P. Young, NuGrid: s process in massive stars, NiC X, 2008

PROCEEDINGS OF SCIENCE

Impact of rotation on the weak s process

Urs Frischknecht[*†]
Department of Physics, University of Basel, Switzerland
E-mail: urs.frischknecht@unibas.ch

Raphael Hirschi
Astrophysics Group, University Keele, UK
and Institute for the Physics and Mathematics of the Universe, University of Tokyo, Japan

Thomas Rauscher
Department of Physics, University of Basel, Switzerland

Friedrich-Karl Thielemann
Department of Physics, University of Basel, Switzerland

The weak s process takes place in massive stars and it produces the majority of s-only isotopes in the atomic mass range from 60 to 90. This process is qualitatively well understood. However, there are still large uncertainties remaining on the quantitative side. Rotation has a strong effect on the stellar structure and mixing, but its impact on the s process has not been studied yet. We implemented an extended and flexible reaction network inside the Geneva stellar evolution code (GENEC) to be able to study the influence of rotation on the s process. For a star with a particular initial mass and composition rotation increases the He core size and the central temperature enhancing the s-process efficiency during core helium burning. In turn the C-shell contribution is reduced since more ^{22}Ne has already been burnt during He-burning. Mixing induced by rotation also affects the contribution of the He-burning shell, since it leads to the production of primary ^{14}N and primary ^{22}Ne. ^{22}Ne and ^{4}He can again be transported to regions with higher temperatures below the convective He-shell, where $^{22}\mathrm{Ne}(\alpha,n)$ becomes an efficient neutron source. To investigate the influence of reaction rate uncertainties besides the uncertainties of stellar structure and mixing, we have developed a one-zone post-processing network including Monte Carlo variations of the rates.

11th Symposium on Nuclei in the Cosmos, NIC XI
July 19-23, 2010
Heidelberg, Germany

[*] Speaker.
[†] A footnote may follow.

1. Introduction

The weak s process in massive stars is qualitatively well understood (see e.g. [1 – 3], but there are still uncertainties on the nuclear as well as on the stellar model side. At the start of helium burning ^{14}N is converted to ^{22}Ne. The s process takes place at the end of helium burning when the temperatures are high enough to run ^{22}Ne$(\alpha,n)^{25}$Mg efficiently. Consequently s-process yields from central helium burning increase with increasing stellar mass. In C-shell burning again ^{22}Ne$(\alpha,n)^{25}$Mg is the main neutron source, its strength being limited by the amount of ^{22}Ne left over from helium burning. Therefore weak s process is a secondary process in the standard case of non-rotating stars, because of the need for CNO and Fe in the initial stellar composition. What might stellar rotation change? Rotation increases stellar core masses (see e.g. [4]) and it enables mixing in otherwise radiation dominated unmixed zones in stellar interiors. This leads to the production of primary ^{14}N and ^{22}Ne [5]. As a consequence the additional amount of neutrons released could boost the weak s process in particular at low Z [6].

2. Impact of rotation on weak s process

We calculated two 25 $M_\odot$ models at solar metallicity to study the effects of rotation on the s process. One model was calculated without and the other one with rotation. A typical rotation rate with $v_{\rm ini}/v_{\rm crit} = 0.4$ was chosen for the model including rotation, corresponding to an average velocity of about 240 km s^{-1} on the main sequence. As initial composition we used the solar chemical composition of [7]. With the Geneva stellar evolution code (GENEC) [8], we followed the evolution of these stars until after central Ne burning. We implemented the Basel Network (BasNet, used before extensively in astrophysical nucleosynthesis calculations, see e.g. [9 – 11]) inside GENEC, which enabled us to follow the s-process network coupled with the stellar structure. For these calculations a network including 613 nuclei was used, similar to the one adopted by [3].

Inclusion of rotation induces slightly lower densities but higher temperatures at the center of the star. The higher temperatures lead to an earlier activation of ^{22}Ne(α,n). Therefore more ^{22}Ne is burned in He burning and less left over for C-shell burning. As mentioned earlier, the rotating model has a larger convective He core. In our models the core size was different by $\approx$0.5 $M_\odot$ when s process occured, meaning that a larger mass is affected by s process due to rotation. The appearance of shear instabilities is another effect of rotation affecting s process in two ways. First, in non-convective regions above the He core the additional mixing transports freshly produced ^{12}C into H-rich layers where it is converted into ^{14}N by ^{12}C$(p,\gamma)^{13}$N$(\beta^+)^{13}$C$(p,\gamma)^{14}$N. This primary nitrogen is then converted into ^{22}Ne and is available as neutron source mainly in He-shell burning. Second, in our models the bottom of the convective He shell is not hot enough to burn ^{22}Ne efficiently, but in the rotating model the layers just below the convective zone are also mixed although on a longer timescale. The downward mixing of helium and neon boosts the s process in He shell and increases the He-shell contribution to the final s-process yields strongly.

Figure 1 displays abundance profiles of different isotopes for both models. ^{70}Ge (orange dotted line, diamond) and ^{88}Sr (red dashed line, cross) are plotted as indicators for the weak s process. The level of ^{22}Ne (green dashed line, filled circle) in the rotating model is considerably higher, consisting of primary and secondary neon, whereas without rotation only secondary neon is found

in He shell. The enhanced s-process activity in He shell appears as a bump in the ^{70}Ge and ^{88}Sr profiles of the rotating model at around 6 $M_\odot$.

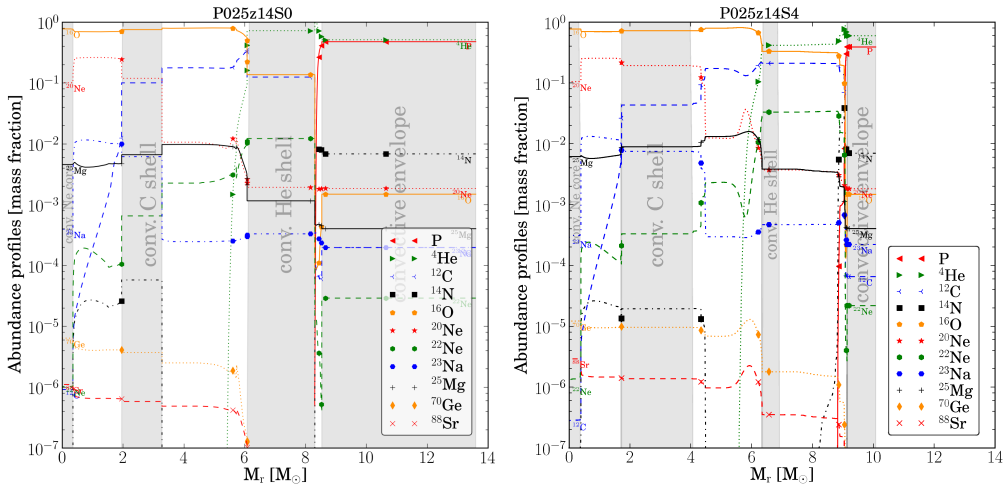

Figure 1: Abundance profiles (mass fraction versus mass) of the non-rotating (*left*) and rotating (*right*) 25 $M_\odot$ models during central Ne burning.

The s-process yields were estimated for both models by integrating from the bottom of the carbon shell up to the surface. Isotopes in the range of weak s process show in the rotating model higher yields by a factor 3 to 10. The contribution to the total weak s-process yields from He shell increased from below 10% to over 30%. The profile of weak s process (Y vs. A), did not change a lot due to rotation, since the s process is limited by the neutron source and not by the iron seeds at solar metallicity. The situation is reversed at low metallicities. Our models of rotating low Z stars show that a large production of primary ^{22}Ne is possible, even at low Z [5, 6]. This increases the ^{22}Ne to ^{56}Fe ratio and the neutron to seed ratio. This implies that in massive stars at low Z isotopes up to Ba or even heavier may be produced. The essential question will then be: how much primary ^{22}Ne can be produced by mixing induced by rotation on low metallicity stars? We will try to answer this question in our future work.

3. Nuclear reaction rate sensitivity study

Mainly the reaction rates including nuclei far from stability have large uncertainties. The astrophysical nucleosynthesis processes including such rates suffer therefore uncertainties accordingly. Such processes are e.g. p process, r process, etc. It is therefore useful to have a tool allowing the investigation of the combined effect of all rate uncertainties using Monte Carlo methods. This has been done already in Astrochemistry [12] and astrophysical nucleosynthesis calculations (see e.g. [13, 14]). But most of the previous sensitivity studies were based on manual rate by rate variation.

We have developed a one-zone post-processing reaction network code including Monte Carlo techniques for reaction rate variations. It can follow astrophysical trajectories (temperature, density) and allows us to investigate the sensitivity of different astrophysical processes on reaction rate

uncertainties. The reaction rates can be varied in different ways, for instance multiplied by a factor which is log-normal or normal distributed around one, i.e. around the standard rate.

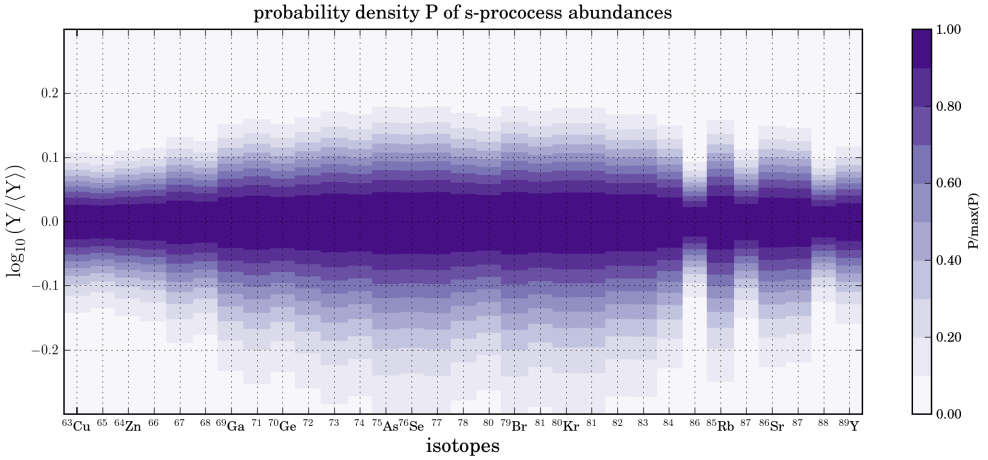

Figure 2: Normalised probability density function of s-process number abundances Y. For this calculation all (n,γ)-rates were allowed to vary between the upper and lower limits, which were in this case $\pm$20% of the standard rates (KADoNiS, www.kadonis.org). For the repeated calculations a trajectory from a 25 $M_\odot$ model was taken and chosen in a way that the ^{22}Ne burned is equal in the trajectory and the stellar model. In this particular calculation, 266 rates were varied and the trajectory was sampled ten thousand times.

We investigated first as a test case the sensitivity of s process in He burning to uncertainties in (n,γ)-rates. The abundance uncertainties after He burning are shown in Fig. 2. They grow from iron onwards up to Se. This is expected for weak s process, since the low neutron densities make the abundance of an isotope in this mass range dependent on the chain of n-captures and β-decays along the valley of stability from iron up to that particular isotope. This leads to a more or less linear behaviour of the uncertainties in s-process isotopes and makes it a good test case for such a Monte Carlo network.

Acknowledgments

This work was supported by grants of the Royal Society (IJP grant JP090091) and the Swiss National Science Foundation.

References

[1] M. Pignatari, R. Gallino, M. Heil, M. Wiescher, F. Käppeler, F. Herwig, and S. Bisterzo, *The Weak s-Process in Massive Stars and its Dependence on the Neutron Capture Cross Sections*, ApJ **710** (Feb., 2010) 1557–1577.

[2] L. S. The, M. F. El Eid, and B. S. Meyer, *s-process nucleosynthesis in advanced burning phases of massive stars*, ApJ **655** (Feb., 2007) 1058–1078, [arXiv:astro-ph/0609788].

[3] L. S. The, M. F. El Eid, and B. S. Meyer, *A new study of s-process nucleosynthesis in massive stars*, ApJ **533** (Apr., 2000) 998–1015.

[4] R. Hirschi, G. Meynet, and A. Maeder, *Yields of rotating stars at solar metallicity*, A&A **433** (Apr., 2005) 1013–1022, [arXiv:astro-ph/0412454].

[5] R. Hirschi, *Very low-metallicity massive stars:. pre-sn evolution models and primary nitrogen production*, A&A **461** (Jan., 2007) 571–583, [arXiv:astro-ph/0608170].

[6] M. Pignatari, R. Gallino, G. Meynet, R. Hirschi, F. Herwig, and M. Wiescher, *The s-Process in Massive Stars at Low Metallicity: The Effect of Primary ^{14}N from Fast Rotating Stars*, ApJ **687** (Nov., 2008) L95–L98, [0810.0182].

[7] M. Asplund, N. Grevesse, and A. J. Sauval, *The Solar Chemical Composition*, *Cosmic Abundances as Records of Stellar Evolution and Nucleosynthesis* (Sep., 2005) 25-+.

[8] P. Eggenberger, G. Meynet, A. Maeder, R. Hirschi, C. Charbonnel, S. Talon, and S. Ekström, *The Geneva stellar evolution code*, Ap&SS **316** (Aug., 2008) 43–54.

[9] C. Fröhlich, G. Martínez-Pinedo, M. Liebendörfer, F. K. Thielemann, E. Bravo, W. R. Hix, K. Langanke, and N. T. Zinner, *Neutrino-induced nucleosynthesis of a>64 nuclei: The νp-process*, *Physical Review Letters* **96** (Apr., 2006) 142502, [arXiv:astro-ph/0511376].

[10] W. R. Hix and F. K. Thielemann, *Computational methods for nucleosynthesis and nuclear energy generation.*, *Journal of Computational and Applied Mathematics* **109** (Sep., 1999) 321–351, [arXiv:astro-ph/9906478].

[11] W. D. Arnett and F. K. Thielemann, *Hydrostatic nucleosynthesis. i - core helium and carbon burning.*, ApJ **295** (Aug., 1985) 589–619.

[12] V. Wakelam, F. Selsis, E. Herbst, and P. Caselli, *Estimation and reduction of the uncertainties in chemical models: application to hot core chemistry*, A&A **444** (Dec., 2005) 883–891, [arXiv:astro-ph/0509194].

[13] J. A. Stoesz and F. Herwig, *Oxygen isotopic ratios in first dredge-up red giant stars and nuclear reaction rate uncertainties revisited*, MNRAS **340** (Apr., 2003) 763–770, [arXiv:astro-ph/0212128].

[14] A. Parikh, J. José, F. Moreno, and C. Iliadis, *The sensitivity of nucleosynthesis in Type I X-ray bursts to thermonuclear reaction-rate variations*, New A Rev. **52** (Oct., 2008) 409–411, [0806.2975].

PROCEEDINGS OF SCIENCE

NuGrid: s process in massive stars

R. Hirschi[*abc], U. Frischknecht[d], M. Pignatari[abe], F.-K. Thielemann[d], M. E. Bennett[ab], S. Diehl[afg], C. L. Fryer[af], F. Herwig[abh], A. Hungerford[ag], G. Magkotsios[aei], G. Rockefeller[ag], F. X. Timmes[ai], and P. Young[ai]

[a] *The NuGrid Collaboration*
[b] *Astrophysics Group, Keele University, ST5 5BG, UK*
[c] *IPMU, University of Tokyo, Kashiwa, Chiba 277-8582, Japan*
[d] *Theoretical Astrophysics Group, University of Basel, Basel, 4056, Switzerland*
[e] *Joint Institute for Nuclear Astrophysics, University of Notre Dame, IN, 46556, USA*
[f] *Theoretical Astrophysics Group (T-6), Los Alamos National Laboratory, Los Alamos, NM, 87544, USA*
[g] *Computational Methods (CCS-2), Los Alamos National Laboratory, Los Alamos, NM, 87544, USA*
[h] *Dept. of Physics & Astronomy, Victoria, BC, V8W 3P6, Canada*
[i] *School of Earth and Space Exploration, Arizona State University, Tempe, AZ 85287, USA*
E-mail: r.hirschi@epsam.keele.ac.uk

The s-process production in massive stars at very low metallicities is expected to be negligible due to the low abundance of the neutron source ^{22}Ne, to primary neutron poisons and decreasing iron seed abundances. However, recent models of massive stars including the effects of rotation show that a strong production of ^{22}Ne is possible in the helium core, as a consequence of the primary nitrogen production (observed in halo metal poor stars). Using the PPN post-processing code (developed within the NuGrid collaboration), we study the impact of this primary ^{22}Ne on the s process. We find a large production of s elements between strontium and barium, starting with the amount of primary ^{22}Ne predicted by stellar models including the effects of rotation. There are several key reaction rate uncertainties influencing the s-process efficiency. For example, within the nuclear reaction rate uncertainty, the ^{17}O(α,γ) reaction may either be critically important or negligible. We also report on the development of the new parallel (MPI) post-processing (MPPNP) variant of the PPN code designed to follow the complete nucleosynthesis in stars on highly resolved grids. We present here the first post-processing run from the ZAMS up to the end of helium burning for a 15 $M_{\odot}$ model.

10th Symposium on Nuclei in the Cosmos
July 27 - August 1 2008
Mackinac Island, Michigan, USA

[*] Speaker.

 http://pos.sissa.it/

PoS(NIC X)083

1. Introduction

Massive stars are known to produce elements heavier than the iron group via rapid neutron captures during their explosion, *r* process (see for example the contribution by Qian and Kratz et al. [1]) and also via slow neutron captures (*s* process) during the pre-supernova evolution, forming the so-called weak *s* component. The weak *s* process in massive stars with initial solar like composition is well understood. ^{22}Ne is the main neutron source and it is produced starting from the initial CNO isotopes (The et al. [2, 3], Raiteri et al. [4, 5], Pignatari et al. in prep.). The weak *s* process, producing mostly elements in the atomic mass range $60 \lesssim A \lesssim 90$, starts at the end of helium burning when the temperature is high enough to activate ^{22}Ne$(\alpha,n)^{25}$Mg. More massive stars reach higher temperatures at the end of He-burning and therefore burn more ^{22}Ne. Consequently *s*-process production during central helium burning increases with increasing stellar mass. The ^{22}Ne left over from helium burning is the main neutron source during the subsequent carbon shell burning. The carbon shell *s*-process contribution depends on the history of convective zones after the He-core burning and on several nuclear uncertainties (e. g. the rate of the ^{12}C$(\alpha,\gamma)^{16}$O reaction). The standard *s*-process production in massive stars depends on the initial metallicity. At low metallicity, the low iron seed abundance, the low ^{22}Ne content and the increasing strength of primary neutron poisons limits the *s*-process efficiency, permitting only negligible production of *s* elements (e. g. Raiteri et al. [6]).

2. Weak *s* process at low metallicity in rotating stars

At solar metallicity, the main effect of rotation on the *s*-process production is the enlargement of the convective helium core due to additional mixing and therefore a behaviour like non-rotating more massive stars [7]. Thus a 25 $M_\odot$ star with rotation behaves like a non-rotating star with mass between 30 and 40 $M_\odot$. Hence the *s*-process efficiency in He-core burning is enhanced in rotating stars (Frischknecht et al. in prep.).

At low metallicity, the impact of rotation is more important. Indeed, at the start of core He-burning, carbon and oxygen are mixed upward into hydrogen rich regions leading to a strong production of nitrogen (see Meynet et al. [8] and Hirschi [9]). Part of this primary nitrogen may enter the convective He core and be transformed into primary ^{22}Ne by α-captures. As a consequence, with respect to the non-rotating models, the ^{22}Ne available in the He-core is strongly enhanced. According to Hirschi et al. [10], about 1% in mass of the helium core is composed of ^{22}Ne at the *s*-process activation.

The stellar evolution calculations described above do not follow s-process nucleosynthesis. In this Section, we present simplified one-zone s-process calculations (using a thermodynamic trajectory that best mimics the full multi-zone evolution) following the nucleosynthesis up to the end of He-burning. For these calculations, we used the one-zone PPN code (see next Section and contribution by Herwig for more details) and an initial metallicity of Z$= 10^{-6}$. In order to reproduce the effect of rotational mixing on the helium burning core composition in the one-zone calculation, we replaced 1% in mass of ^{4}He by ^{22}Ne at the start of helium burning. The primary ^{22}Ne enhances the *s* process compared to the non-rotating case, where negligible amounts of *s* elements are produced. The highest nucleosynthesis efficiency is around Sr with overproduction

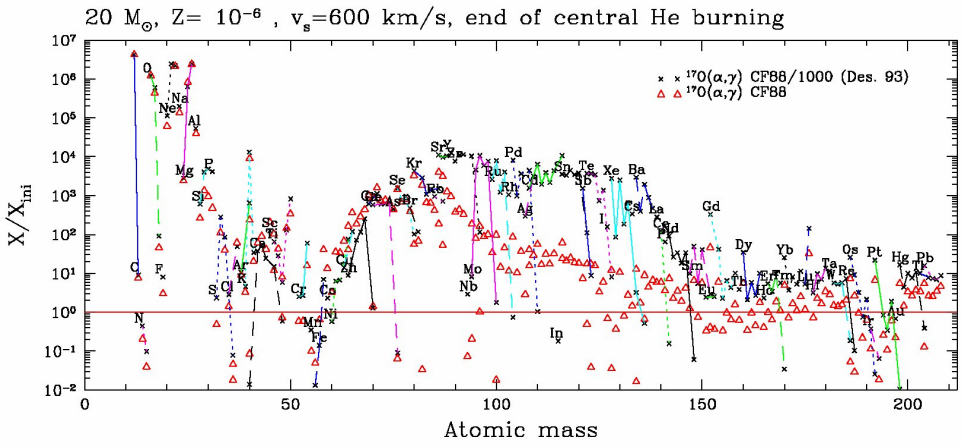

Figure 1: The overproduction factors after He-burning in the one-zone post-processing calculations. Using a low $^{17}O(\alpha,\gamma)$ rate (black crosses) leads to a strong increase of *s*-process overproduction between Sr and Ba. Isotopes with $X_i/X_{\rm ini}$ below the lower limit are not plotted.

factors ($X_i/X_{\rm ini}$) between thousand and ten thousand. As can be seen in Fig. 1, iron seeds and in general elements lighter than strontium feed the *s* nucleosynthesis in the mass region between strontium (Sr) and barium (Ba). Beyond Ba, the *s* efficiency rapidly falls, depending on the total neutron exposure. The major neutron poisons are ^{16}O, ^{25}Mg and ^{22}Ne, where ^{16}O is the strongest neutron absorber. Whether or not ^{16}O is an efficient poison depends on the ratio of $^{17}O(\alpha,\gamma)$ to $^{17}O(\alpha,n)$. According to the study of Descouvemont [11], the (α,γ) channel should be orders of magnitude weaker than the (α,n) channel, in which case the neutrons captured by ^{16}O are recycled by $^{17}O(\alpha,n)$. On the other hand, using the rates of Caughlan and Fowler [12], $^{17}O(\alpha,\gamma)$ is about a factor ten slower than $^{17}O(\alpha,n)$ and a significant fraction of neutrons captured by ^{16}O are not re-emitted. In this case, ^{16}O is the strongest neutron poison. In Fig. 1, we show the importance of the $^{17}O(\alpha,\gamma)$ rate by comparing the isotopic distributions obtained using the rate of Caughlan and Fowler [12] (red triangles) and using this same rate divided by a factor 1000 to reproduce the $(\alpha,\gamma)/(\alpha,n)$ ratio suggested by Descouvemont [11] (black crosses). The different *s*-process production between the two calculations demonstrates the importance of the $^{17}O(\alpha,\gamma)$ to $^{17}O(\alpha,n)$ ratio for the *s* process at low metallicity. This was also suggested by Rayet and Hashimoto [13] in standard *s*-process calculations in massive stars at low metallicity. However, because of the large primary ^{22}Ne production in rotating stars, in the present calculations the impact of the $^{17}O(\alpha,\gamma)$ to $^{17}O(\alpha,n)$ ratio on the *s*-process efficiency is much stronger than in Rayet and Hashimoto [13]. A better knowledge of these two rates at He-burning temperature is highly desirable in order to obtain more reliable *s*-process calculations at very low metallicity. The strong production of *s* elements between Sr and Ba is in agreement with Pignatari et al. [14], where the $^{17}O(\alpha,\gamma)$ rate of Descouvemont [11] is used and where the amount of primary ^{22}Ne is in agreement with Hirschi et al. [10]. The boosted *s* process due to primary ^{14}N production may provide a new *s*-process component with important implications for nucleosynthesis at low metallicity. Massive rotating

stars may therefore contribute considerable amounts of isotopic abundances between Sr and Ba to the Galactic chemical evolution at halo metallicities, which could provide a possibility to explain the high Sr enrichment and the high Sr/Ba ratio (see Pignatari et al. [14] for more details). In order to make a quantitative and more precise statement about the importance of this *s* process occurring in rotating low-metallicity stars, further investigations are needed.

3. Multi-zone parallel post-processing code, MPPNP

Although only a few isotopes are crucial for the energy generation in massive stars, many more are important for the nucleosynthesis, for example to determine how much *s* process is made in massive stars. Since it is not necessary to follow many of these species within a stellar evolution calculation, within the NuGrid collaboration (see contribution by Herwig for code details), we developed a post-processing network (PPN), that allows us to follow the complete nucleosynthesis taking place in massive stars. It also enables testing of the importance of various reaction rates and especially the use of the same set of nuclear reactions in different stellar environments. The multi-zone variant of the post-processing code, MPPNP, uses MPI and is therefore much faster than a serial code. Using MPPNP, we have post-processed a full stellar evolution model of 15 $M_{\odot}$ at Z$=0.01$ calculated with the Geneva code [15] from the ZAMS up to the end of helium burning with a 400-isotope network up to Ag. The overabundance pattern at the end of the core He-burning phase is shown in Fig. 2. As expected, the weak *s*-process production in a 15 $M_{\odot}$ star is modest, with overproduction factors up to 10 for *s*-only isotopes between iron and strontium. This is due to the low central temperature reached at the end of the core He-burning phase in a 15 $M_{\odot}$ star (compared to more massive stars) with a marginal activation of the ^{22}Ne$(\alpha,n)^{25}$Mg during He-burning. We are currently testing MPPNP in the advanced stages and we plan to calculate the full nucleosynthesis for a large range of masses and metallicities. The MPPNP code can also post-process AGB models (see contribution by Pignatari) and another variant of PPN, called TPPNP will follow trajectories of multi-dimensional simulations of supernova explosion and convective-reactive events in stars.

Acknowledgments

FH and MP acknowledge support from EU Marie Curie FP6 grant MIRG-CT-2006-046520 and NSF grant PHY 02-16783 (JINA).

References

[1] K.-L. Kratz, K. Farouqi, B. Pfeiffer, J. W. Truran, C. Sneden, and J. J. Cowan, *Explorations of the r-Processes: Comparisons between Calculations and Observations of Low-Metallicity Stars*, ApJ **662** (Jun., 2007) 39–52, [arXiv:astro-ph/0703091].

[2] L.-S. The, M. F. El Eid, and B. S. Meyer, *A New Study of s-Process Nucleosynthesis in Massive Stars*, ApJ **533** (Apr., 2000) 998–1015.

[3] L.-S. The, M. F. El Eid, and B. S. Meyer, *s-Process Nucleosynthesis in Advanced Burning Phases of Massive Stars*, ApJ **655** (Feb., 2007) 1058–1078, [arXiv:astro-ph/0609788].

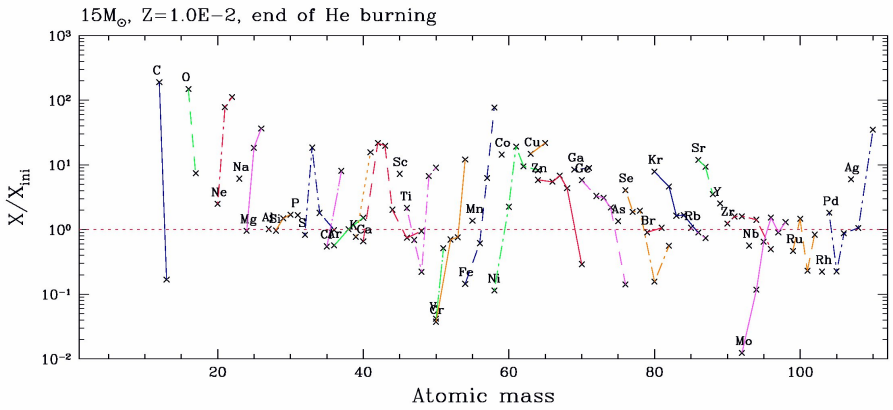

Figure 2: Overproduction factors in the convective core at the end of He-burning. Isotopes with $X_i/X_{\rm ini}$ below the lower limit are not plotted.

[4] C. M. Raiteri, M. Busso, G. Picchio, and R. Gallino, *S-process nucleosynthesis in massive stars and the weak component. II - Carbon burning and galactic enrichment*, ApJ **371** (Apr., 1991) 665–672.

[5] C. M. Raiteri, M. Busso, G. Picchio, R. Gallino, and L. Pulone, *S-process nucleosynthesis in massive stars and the weak component. I - Evolution and neutron captures in a 25 solar mass star*, ApJ **367** (Jan., 1991) 228–238.

[6] C. M. Raiteri, R. Gallino, and M. Busso, *S-processing in massive stars as a function of metallicity and interpretation of observational trends*, ApJ **387** (Mar., 1992) 263–275.

[7] R. Hirschi, G. Meynet, and A. Maeder, *Yields of rotating stars at solar metallicity*, A&A **433** (Apr., 2005) 1013–1022, [arXiv:astro-ph/0412454].

[8] G. Meynet, S. Ekström, and A. Maeder, *The early star generations: the dominant effect of rotation on the CNO yields*, A&A **447** (Feb., 2006) 623–639.

[9] R. Hirschi, *Very low-metallicity massive stars:. Pre-SN evolution models and primary nitrogen production*, A&A **461** (Jan., 2007) 571–583, [arXiv:astro-ph/0608170].

[10] R. Hirschi, C. Chiappini, G. Meynet, A. Maeder, and S. Ekström, *Stellar Evolution at Low Metallicity*, in *IAU Symposium*, vol. 250 of *IAU Symposium*, pp. 217–230, 2008.

[11] P. Descouvemont, *Microscopic three-cluster study of 21-nucleon systems*, Phys. Rev. C **48** (Dec., 1993) 2746–2752.

[12] G. R. Caughlan and W. A. Fowler, *Thermonuclear Reaction Rates V*, *Atomic Data and Nuclear Data Tables* **40** (1988) 283.

[13] M. Rayet and M.-a. Hashimoto, *The s-process efficiency in massive stars*, A&A **354** (Feb., 2000) 740–748.

[14] M. Pignatari, R. Gallino, G. Meynet, R. Hirschi, F. Herwig, and M. Wiescher, *The s process in massive stars at low metallicity. effect of primary ^{14}N from fast rotating stars.*, ApJ **687** (2008) L95.

[15] P. Eggenberger, G. Meynet, A. Maeder, R. Hirschi, C. Charbonnel, S. Talon, and S. Ekström, *The Geneva stellar evolution code*, Ap&SS (Jun., 2007) 263.

B Stellar initial composition tool

B.1 How to use

A little program was written to calculate stellar initial compositions with either solar scaled or α-enhanced metallicity dependence. It should work with any proper Fortran compiler (tested with ifort, gfortran, and pgf). In the current version there are two input files read. The first contains the elemental abundances and the second adopts the isotopic ratios from Lodders (2003).

When the program is started you will be asked which kind of abundances you want to produce. You can choose out of four sets of input abundances:

1. For solar abundances of Anders & Grevesse (1989) enter **1**.
2. For solar abundances of Grevesse & Noels (1993) enter **2**.
3. For solar abundances of Asplund et al. (2005)[1] enter **3**.
4. For solar abundances of Asplund et al. (2009) enter **4**.

After the abundance set is chosen tree options are available namely solar (**1**), proto-solar[2] (**2**) composition, or an arbitrary metallicity (**3**). If the last option (**3**) was chosen the metallicity $Z = 1 - X - Y$ has to be specified and how the input composition should be scaled to the chosen metallicity Z. There can either a scaled solar or an α-enhanced chemical composition be selected.

B.2 Abundance calculation

B.2.1 Solar abundances

For the choice "solar abundances" the program reads number abundances n_i (in astronomical log-scale: $A(H) = log\,(n(H)) = 12$) from the input files and normalise them according to the total mass conservation

$$\sum_i X_i = 1 \tag{B.1}$$

[1] Currently the composition of Asplund et al. (2005) is used with a changed neon abundance according to Cunha et al. (2006). If you don't want this change the input file from "elab_asplund05cunha06.txt" to "elab_asplund05.txt"

[2] This choice is only correct for the Asplund et al. (2005) composition, see also section B.2.2

The sum of read input abundances won't provide an exact value of one, since they are only given with a limited precision (3 decimal places of exponent). Thus this normalisation is always done regardless of which option was chosen.

B.2.2 Proto-solar abundances

With the notation for X and Y for hydrogen and helium mass fractions respectively and Z (metallicity) for the sum of the mass fractions of the remaining chemical species, Eq. B.1 is written in the following way

$$X + Y + Z = 1 \tag{B.2}$$

where Z is

$$Z = \sum_{Z_p>2} X_i \tag{B.3}$$

In this case $X = 0.72$, $Y = 0.266$ and $Z = 0.014$ is used, which was derived by calibrating the surface abundances of a 1 $M_\odot$ star model after 4.57 Gyr to the composition of Asplund et al. (2005) (private communication Sylvia Ekström) and to reproduce the solar radius and luminosity. This composition coincide also to massive stars in the solar neighbourhood (Asplund et al. 2009). Lodders (2003) calculated also a proto-solar composition which is $X = 0.7110$, $Y = 0.2741$ and $Z = 0.0149$, but it is not used here (commented out in the program). To get the full composition the solar abundances for the metals are scaled in the way that $Z = 0.014$ is fulfilled. If another particular composition is needed, the values X, Y and Z in the data vector "psol" can be chosen or the option in which the metallicity is set.

B.2.3 Free chosen metallicity

So with a new chosen metallicity Z, X and Y have to be recalculated and are simply given by the following relations

$$Y = Y_{prim} + \frac{dY}{dZ} Z \tag{B.4}$$

and the total mass conservation

$$X = 1 - Y - Z \tag{B.5}$$

In the relation between Y and the metallicity Z, where $Y_{prim} = 0.2484$ the primordial helium abundance was derived from the WMAP data (Cyburt et al. 2003) and $\frac{dY}{dZ} = 1.2571$[3]. For both options "scaled solar" and α-enhanced abundances X and Y are calculated in this way.

Scaled solar abundances

If this option was chosen the abundances for all elements beyond helium are scaled by the same factor. So the new abundances are given by

$$X_i = X_{i,\odot} \cdot S \tag{B.6}$$

where the scaling factor S is

$$S = \frac{Z_{new}}{Z_\odot} \tag{B.7}$$

[3]This value is calculated out of proto-solar Y, Z from subsection B.2.2 and Y_{prim}

α-enhanced abundances

In the *alpha*-enhanced case several isotopes which are multiples of α do not behave like the other isotopes. Instead, their abundances are enhanced compared to the one of iron. This is related to the production of these elements in massive stars, and the stronger relative contribution to the galactic chemical evolution in the early (metal poor) universe. As α-enhanced isotopes we assume here ^{12}C, ^{16}O, ^{20}Ne, ^{24}Mg, ^{28}Si, ^{32}S, ^{36}Ar, ^{40}Ca, ^{48}Ti. The abundance behaviour of these isotopes with $[Fe/H]$ is assumed to be

$$[\alpha/Fe] = A_\alpha \cdot [Fe/H] + B_\alpha \tag{B.8}$$

The parameters A_α and B_α are derived from observational data, details can be found the next section. The bracket value of elements a and b is defined by

$$[el(a)/el(b)] := log_{10}\left(\frac{X_a}{X_b}\right) - log_{10}\left(\frac{X_{a,\odot}}{X_{b,\odot}}\right) = log_{10}\left(\frac{Y_a}{Y_b}\right) - log_{10}\left(\frac{Y_{a,\odot}}{Y_{b,\odot}}\right) \tag{B.9}$$

and it is independent whether mass fractions X or number abundances Y are used. Kobayashi et al. (2006) observed a plateau in the α-enhancement below $[Fe/H] = -1$ for the halo and the thick disc of the Galaxy. So below this value Eq. B.8 is simply changed by setting $A_\alpha([Fe/H] < -1) = 0$ and $B_\alpha([Fe/H] < -1) = B_\alpha - A_\alpha$. The mass fraction of the α-isotopes is thus

$$X_\alpha = X_{Fe}\frac{X_{\alpha,\odot}}{X_{Fe,\odot}}\left(10^{B_\alpha}\left(\frac{X_{Fe}X_{H,\odot}}{X_H X_{Fe,\odot}}\right)^{A_\alpha}\right) \tag{B.10}$$

To get a simple function $Z(X_{Fe})$ also the assumption of the same downscaling like iron of all other isotopes is made.

$$X_i = \frac{X_{i,\odot}}{X_{Fe,\odot}}X_{Fe} \tag{B.11}$$

So with equations B.10 and B.11 we get the desired $Z(X_{Fe})$

$$\begin{aligned} Z &= \sum_\alpha X_\alpha + \sum_{i,rest} X_i \\ &= \sum_\alpha X_{Fe}\frac{X_{\alpha,\odot}}{X_{Fe,\odot}}\left(10^{B_\alpha}\left(\frac{X_{Fe}X_{H,\odot}}{X_H X_{Fe,\odot}}\right)^{A_\alpha}\right) + \sum_{i,rest}\frac{X_{i,\odot}}{X_{Fe,\odot}}X_{Fe} \end{aligned} \tag{B.12}$$

Since the mass fractions of hydrogen and helium are given by specifying Z and Eqs. B.4 and B.5), respectively, the only free parameter is the iron abundance X_{Fe}. If X_{Fe} is determined all other abundances are also fixed. So to find X_{Fe} the root of the following function has to be found

$$F(X_{Fe}) = X_{Fe}\left(\sum_\alpha \Gamma_\alpha X_{Fe}^{A_\alpha} + \Theta\right) - Z \tag{B.13}$$

This is done by the "secant method" (Press et al. 1992). The final abundances are calculated out of Eqs. B.10 and B.11.

B.3 Parameters for α-enhanced elements

For the α-enhanced isotopes the parameters A_α and B_α of a linear function shown in Eq. B.8 are needed to calculate α-enhanced compositions. These parameters are derived by making linear fits to the abundance data the halo and thick disc star from Reddy et al. (2006). The linear fits are made for data lying in the range $-1 \leq [Fe/H] \leq 0$. Two kind of fits were performed, the first with free parameters and the second one with B_α fixed to zero assuming the the sun represents a good mean chemical composition for solar metallicity. This second version of the fits was finally used. For Ne, S and Ar no data was fitted, but the model values from GCE models of Kobayashi et al. (2006) were taken. In Table B.1 the values of $[X_\alpha/Fe]$ at $[Fe/H] = -1$ are shown for different sources and for the fits.

Table B.1: Values [X/Fe] at [Fe/H]=-1 from different sources and own fits. From the galactic chemical evolution publications, the ranges given here include their theoretical results and the observational data cited therein.

	[X/Fe] at [Fe/H] $= -1$					adopted
element	Ko06[a]	Fr04[b]	GP00[c]	A_α*[Fe/H]+B_α	A_α*[Fe/H]	slope A_α
C	-0.2 to 0.4	-	-	0.458	0.562	-0.562
O	0.4 to 0.8	0.3 to 0.8	0.4 to 0.8	0.749	0.886	-0.886
Ne	≈0.5	-	-	-		-0.500
Mg	0.2 to 0.6	0.3 to 0.6	0.2 to 0.6	0.352	0.411	-0.411
Si	0.2 to 0.5	0.2 to 0.4	0.2 to 0.6	0.245	0.307	-0.307
S	0.37 to 0.5	-	≈0.1	-		-0.435
Ar	≈0.3	-	-	-		-0.300
Ca	0.1 to 0.45	0.1 to 0.4	0.1 to 0.5	0.194	0.222	-0.222
Ti	0.2 to 0.4	0.1 to 0.4	0.15 to 0.35	0.204	0.251	-0.251
Cr	-0.2 to 0.2	-0.5 to 0	-0.2 to 0	-0.059	-0.054	+0.054

References: [a]Kobayashi et al. (2006), [b]François et al. (2004), [c]Goswami & Prantzos (2000)

Figures including the two fits and the observational data of Reddy et al. (2006) can be found below.

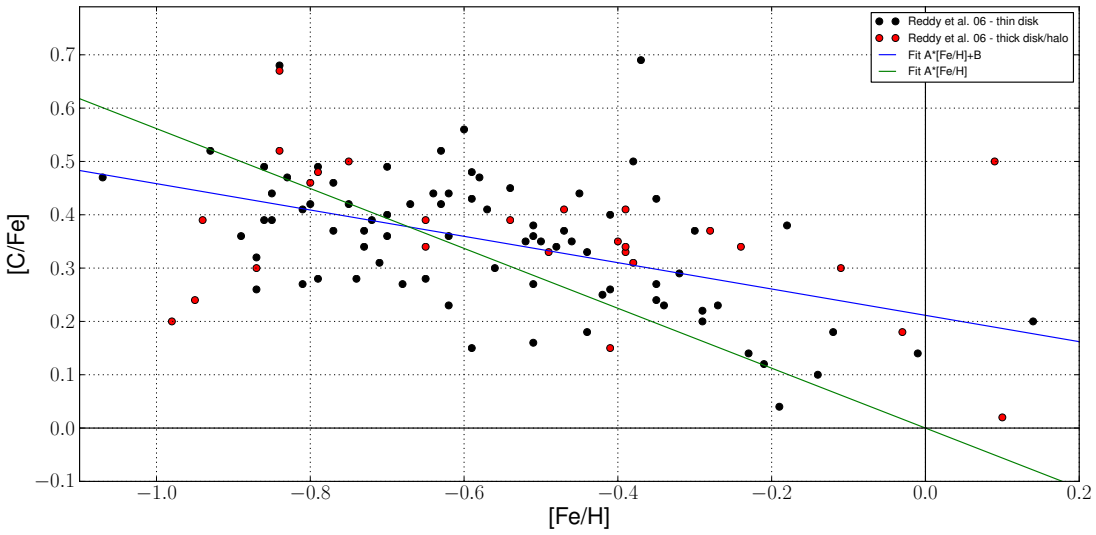

Figure B.1: The carbon versus iron content in F and G dwarfs of halo, thick and thin disc of the Galaxy (circles) Reddy et al. (2006) and the linear fits.

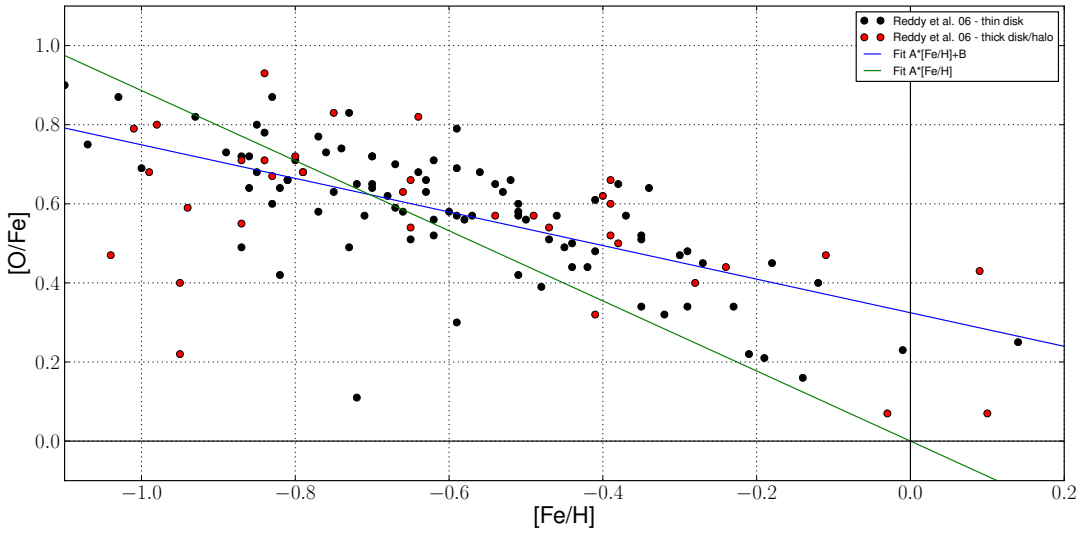

Figure B.2: The oxygen versus iron content in F and G dwarfs of halo, thick and thin disc of the Galaxy (circles) Reddy et al. (2006) and the linear fits.

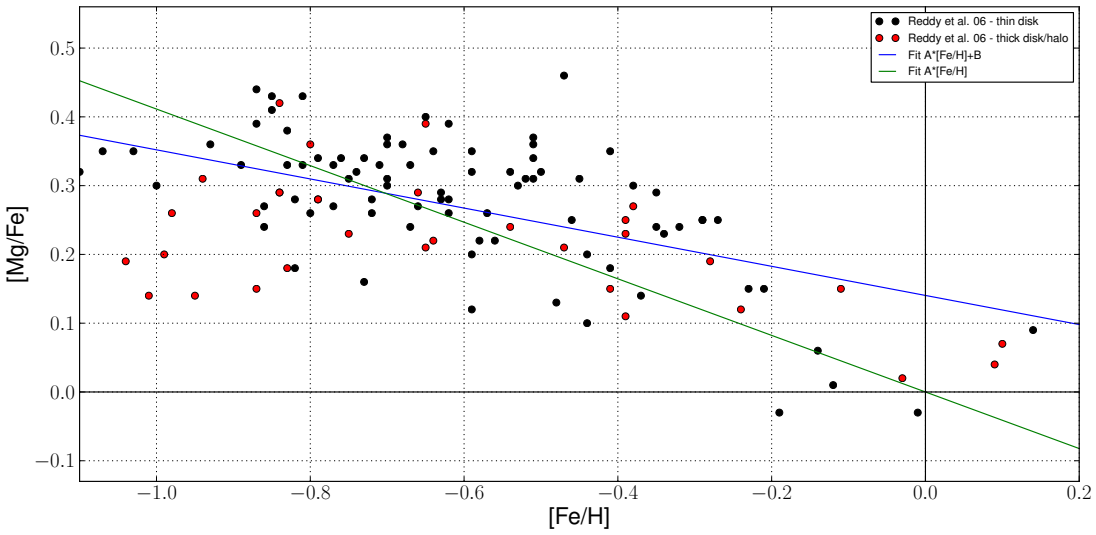

Figure B.3: The magnesium versus iron content in F and G dwarfs of halo, thick and thin disc of the Galaxy (circles) Reddy et al. (2006) and the linear fits.

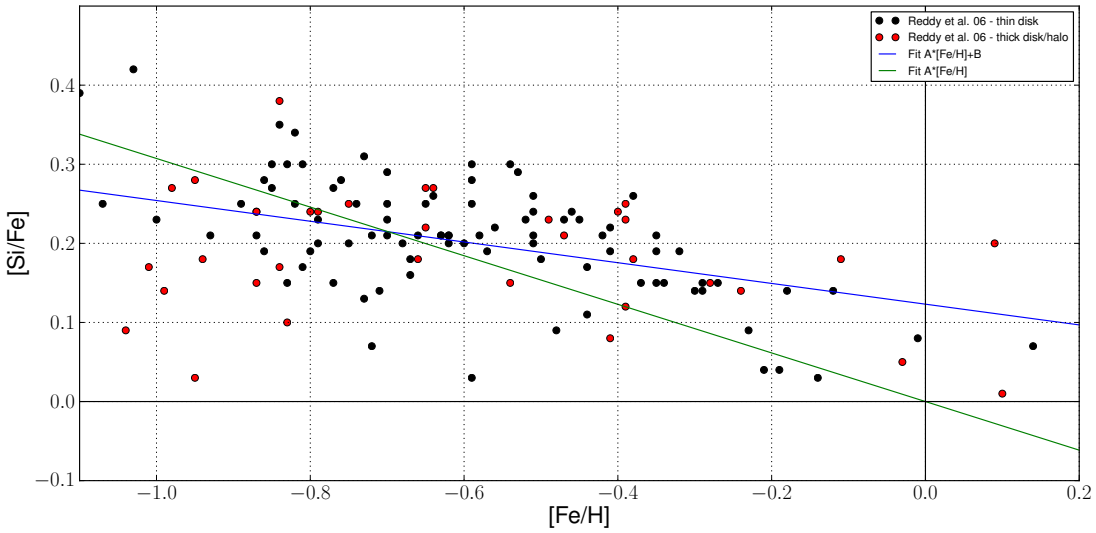

Figure B.4: The silicon versus iron content in F and G dwarfs of halo, thick and thin disc of the Galaxy (circles) Reddy et al. (2006) and the linear fits.

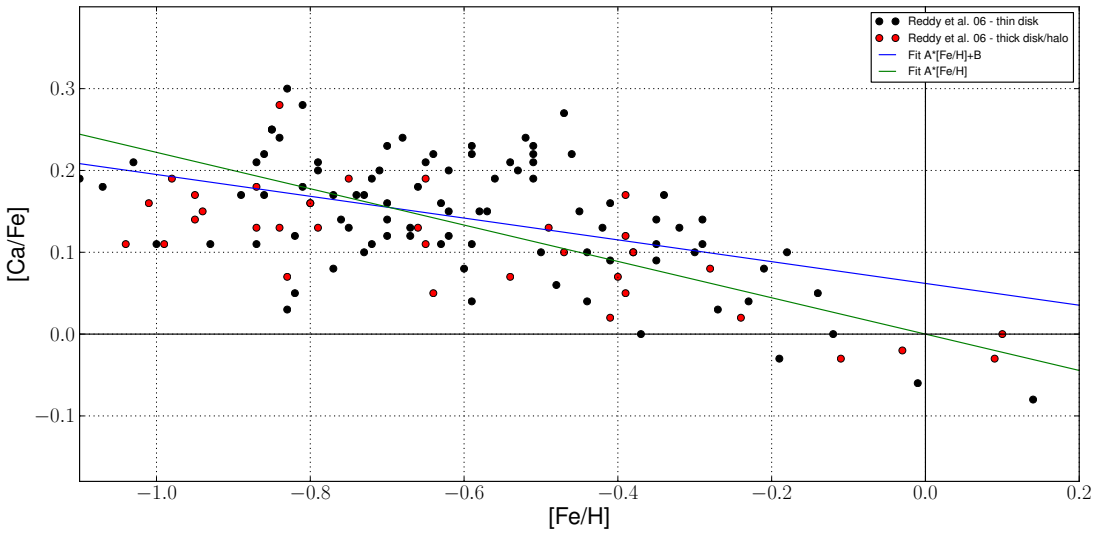

Figure B.5: The calcium versus iron content in F and G dwarfs of halo, thick and thin disc of the Galaxy (circles) Reddy et al. (2006) and the linear fits.

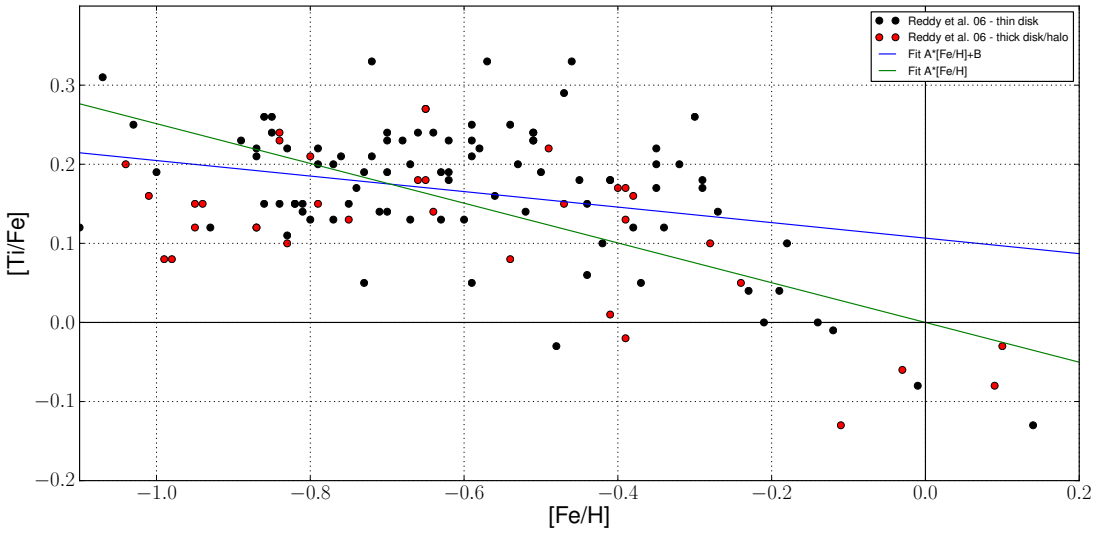

Figure B.6: The titanium versus iron content in F and G dwarfs of halo, thick and thin disc of the Galaxy (circles) Reddy et al. (2006) and the linear fits.

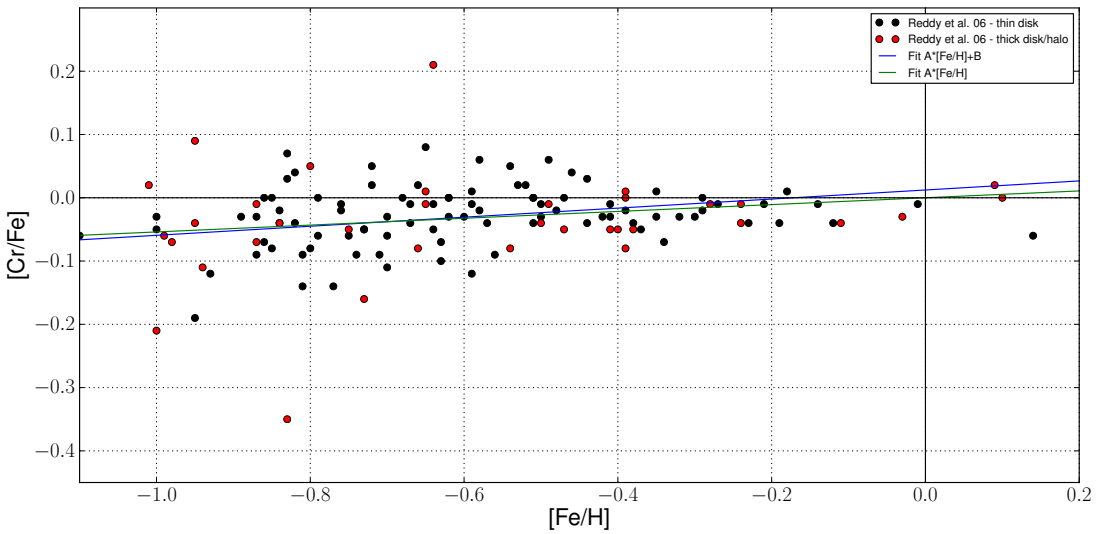

Figure B.7: The chromium versus iron content in F and G dwarfs of halo, thick and thin disc of the Galaxy (circles) Reddy et al. (2006) and the linear fits.

C Reaclib fitting tool

In this documentation you will find a little "how to" for a simple fitting tool based on least squares to obtain the seven parameter fit (see equations 3.12 and 3.13) of a reaction rate. It is written in *python* and the graphical output is based on *python-matplotlib*. The graphical output is not necessarily needed but highly recommended for an easier analysis of the fit quality. This documentation only shortly describe how to prepare good fits of astrophysical reaction rates. If there is more information needed about this subject have a look at (nucastro.org) of Dr. T. Rauscher.

C.1 How to fit rates

Several points have to be kept in mind to obtain the best result, while fitting rates to the seven parameter format. The temperature range of about $T_9 = 0.001$ to 10 (the lowest temperature depends on the strength of the rate) would ideally be given. This temperature range gives rise to the challenge of fitting values differing by many orders of magnitudes. In order to do so the $least - squares$ algorithm is probably the best method. The possibility of splitting the rate into several contributions of seven parameters makes this difficulty feasible. One should pay attention to the following points while fitting the rates.

- If available the rates with positive Q-value should be fitted and not the reverse rates or else it can cause numerical troubles. This is due to the fact that photodisintegration rates are negligible in low to intermediate temperature environments, whereas the forward rates are not.

- The reverse rate has to be calculated from the forward rate and is not fitted, to be sure to get the correct ratio of forward and reverse rate in equilibrium situations (NSE[1]). When calculating the reverse rates out of the forward rates by detailed balance (see section 3.6.2) this is automatically fulfilled.

- When fitting rates one has to keep in mind that these seven parameter fits should not only be usable for the current task but also for a wide range of astrophysical applications. Therefore it is important that the fitted rates behave well outside the fitting range, i.e. they must not diverge or oscillate non-physically otherwise this can cause numerical problems. This is important for models using the nuclear network in low as well as high temperature conditions. At high temperatures above $T_9 \approx 6$ the astrophysical plasma is in NSE wherefore it is not important that the fit of the rate have physical values, but

[1]Nuclear Statistical Equilibrium

the ratio of the forward and the reverse rate has to be correct. One can see that if the fit coefficients $a_1 \leq 0$ and $a_2 \leq 0$ an exploding rates is automatically prevented at low energies. Not every fit will satisfy this condition, but since no astrophysical environment with temperature below $T_6 = 1$ this is not really a constraint as long as the rate only explodes below T_6.

- More complex rates with resonances have to be split in several contributions to get a reasonable accuracy. The procedure is to fit one contribution and subtract it subsequently from the data. Afterwards we can try to fit the next contribution. Often this procedure have to be repeated several times to gain good results. The more fit contributions (sets of seven parameter fits) are needed, the more challenging it can be to find decent splits into the temperature regions. This problem can be avoided by taking the analytical part of the contributed reaction rates. Near resonances are described (see for example NACRE paper I Angulo et al. 1999) almost in the same analytical form as the *reaclib*-format

$$N_A < \sigma v >_{res} = N_A \left(\frac{2\pi}{\mu k_B}\right)^{3/2} \hbar^2 \omega\gamma T^{-3/2} exp\left(-\frac{E_r}{k_B T}\right) \tag{C.1}$$

where $\omega\gamma$ is defined as

$$\omega\gamma = \omega \frac{\Gamma_i \Gamma_f}{\Gamma(E_r)} \tag{C.2}$$

Γ_i is the entrance and Γ_f the exit channel particle width. $\Gamma(E_r)$ is the total width at the resonance energy E_r in MeV and ω the statistical factor

$$\omega = (1 + \delta_{i,j}) \frac{(2J+1)}{(2J_i+1)(2J_j+1)}, \tag{C.3}$$

where J_i, J_j are the spins of the interacting particles and J the spin of the resonance. One can then easily calculate the coefficients out of the resonance parameters E_r and $\omega\gamma$.

$$\begin{aligned} a_0 &= log\left(N_A \left(\frac{2\pi}{\mu k_B}\right)^{-3/2} \hbar^2 \omega\gamma\right) \\ &= log\left(1.5394 \times 10^{11} A^{-3/2} \omega\gamma\right) \\ a_1 &= -11.6045 E_r \\ a_6 &= -1.5 \end{aligned}$$

The other coefficients are zero. A is the reduced mass in amu. In the case of high resonance density, when the energy spacing $\Delta E \lesssim \Gamma$, these resonances can also be described by just one contribution with coefficients a_0, a_1 and a_6. When calculating the resonant contributions as described one has to fit only the non-resonant part of the rate.

- Nevertheless it should be avoided to describe one rate with too many contributions, since it could slow down the network.

C.2 List of files and description

In this section the different files which are necessary and their content is described.

C.2.1 Input files

config The *config* file is needed to configure your fit procedure. In this file the input information is specified and you can change the range of points from 'datafile', from which you want to get the fit. You can also change the weights for each point or add additional points.
Basic specifications for the fit:

- **line 2**: Input file name.
- **line 3**: The source label, which should be stated in the reaclib. This label should have a length of maximal four characters.
- **line 4**: Reaction specified in the reaclib format, but with at least one space between the isotope names. Example: for the $^{200}\mathrm{Au}(n,\gamma)^{201}\mathrm{Au}$ reaction the correct label here is **n au200 au201**, but NOT nau200au201, which would be correct in the reaclib format and will be given in the output file!
- **line 5**: The total Q-value in MeV.
- **line 6**: Number of the contribution which should be calculated. This integer starts with 0, so to get the first function put a 0 for the second a 1 and so on. So for example: if you set it to 1, at least one fit has to be present in the log-file. If there is more than one fit only the first is kept and all others are lost. If you put it to 2 at least two fits have to be present in the log-file, etc.
- **line 7**: This integer should be 0, if the complete set of data points should be fitted or 1 if the fit should only be taken from the points in between the point range specified below (next two lines).
- **line 8**: Integer specifying the lower limit in the data array taken for the fit procedure. It starts from 0.
- **line 9**: Integer specifying the upper limit. If it is larger than the number of available data points it just takes the last value in the list.

Plot options:

- **line 12**: If this integer is 0 no figure is shown. This is handy if you did not install *python-matplotlib*.
- **line 13**: Plot label of the rate vs. T_9 and the relative difference vs. T_9 plot written in TEX.
- **line 14**: Floating point number: without giving a number here the rate plot would just be given in the range between the maximum $y_{\max}$ and the minimum $y_{\min}$ of the data. However sometimes it is useful to see what the fit is doing above or below these values. So this number f gives the lower extension of y-axis by $y_{\min} \cdot f$.

- **line 15**: Floating point number specifying the upper extension of the y-axis in magnitudes $y_{\max} \cdot f$.

Additional configuration parameters:

- **line 18**: If this integer iw is set to 1, it allows to give the weight σ_i of each point i in the fitting range in the following way.

  $$\sigma_i = \frac{|data_i - F_{prev}(T_9(i))|}{data_i} \cdot k$$

  This only works if already a fit F_{prev} was done for the same data range. The idea is to give the less precise points a larger weight. Be aware, if you repeat this procedure more than once, F_{prev} is used which was obtained in the preceding execution of *refit.py*. So make sure that iw is set back to 0 after one execution.

- **line 19**: This floating point number is the factor k.

- **line 22**: Integer n is the number of additional data points. If $n \neq 0$ the data points on the following n lines are used additionally.

- **line 23-x**: At least n data points have to be given by three numbers, the temperature T_9, rate and its weight. This can be useful to force a fit to the intended behaviour, like avoiding exploding functions.

- **(x+2)th line**: Integer specifies if the weight of some points should be placed by hand.

- **following lines**: Index i and weight of the point i. If no weight σ_i is set by hand or no relative weight (see line 17) is defined, it is 1 for data points above 10^{-20} and below $\sigma_i = (data_i/10^{-20})^{0.03}$. The idea of this last relation is to give rates with low values a smaller weight.

data file The data input file should have the following format: The first two lines in the data file are left for documentation and comments to define for example the data source. Below two columns should be given, the first one containing the temperature in units of $10^9 K$ and the second one with the corresponding reaction rate.

C.2.2 Main program

refit.py This is the main program, which is written in python but it needs additionally an installation of the plot package *python-matplotlib* otherwise the plot part won't work. If *python-matplotlib* is not available you can turn the plot part off (see config file). Let it run, it works!

C.2.3 Output files

"rate".log This file is created after the first start of the fit procedure (execution of refit.py). On the first lines you will find first fits in the reaclib formate. If the number of the fitted contributions in config is n (line 6 in the config file) you will find $n + 1$ contributions in the log file. After line '- - - - -' some information about the fit and the chosen options. In fact this is also an input file if you need to do more than one contribution for a certain reaction rate.

plot file There is a plot file **"rate".png** produced, and renewed after each execution of the program. The upper figure shows the reaction rate between $T_9 = 0.001$ and 10, which is convenient to check whether the reaction rate explodes or not. The lower figure shows the relative difference between the data and the fit in the same temperature range. This helps to reach the desired accuracy.

C.3 Calculating the reverse rates

Calculating the backwards reactions are in most cases very easy. For the theoretical part you should have a look at Rauscher & Thielemann (2000) and/or section 3.6.2.

C.3.1 2to2 and 2to1 reactions

These were originally written by F.-K. Thielemann and calculate the reverse rate fits for reactions of type $i(j,o)m$ and $i(j,\gamma)m$.

r12.f90 Calculates the reverse rate of the rate type $i(j,\gamma)m$. It reads the rate fits from the file **rate21**, which is identical to the log-file, but only with the REACLIB fit. The type of the rate is automatically checked and if it is a different type of reaction nothing happens. The output is written into file **rate21-rev**.

r22.f90 Calculates the reverse rate of the rate type $i(j,o)m$. It reads the rate fits from the file **rate22**, which is identical to the log-file, but only with the REACLIB fit. The type of the rate is automatically checked and if it is a different type of reaction nothing happens. The output is written into file **rate22-rev**

winvn File **winvn** contains the isotopic information as A, Z, N, spin of ground state and the partition function $G(T)$. It has to be present were **r12** and **r22** are executed.

C.3.2 Different reaction types

For more complicated reactions like the 3α-rate one has to calculate the coefficients for the reverse rate almost the same way (see section 3.6.2), but there exists no routine, which does this. So it has to be calculated by hand.

Bibliography

Aerts, C. 1996, A&A, 314, 115

Aerts, C. 2008, in IAU Symposium, Vol. 250, IAU Symposium, ed. . J. P. F. Bresolin, P. A. Crowther, 237–244

Aerts, C., Marchenko, S. V., Matthews, J. M., et al. 2006, ApJ, 642, 470

Aikawa, M., Arnould, M., Goriely, S., Jorissen, A., & Takahashi, K. 2005, A&A, 441, 1195

Anders, E. & Grevesse, N. 1989, Geochim. Cosmochim. Acta, 53, 197

Angulo, C., Arnould, M., Rayet, M., et al. 1999, Nuclear Physics A, 656, 3

Argast, D., Samland, M., Thielemann, F.-K., & Qian, Y.-Z. 2004, A&A, 416, 997

Arnett, D., Meakin, C., & Young, P. A. 2009, ApJ, 690, 1715

Arnett, W. D. & Thielemann, F.-K. 1985, ApJ, 295, 589

Arnould, M., Goriely, S., & Takahashi, K. 2007, Phys. Rep., 450, 97

Asplund, M., Grevesse, N., & Sauval, A. J. 2005, in Astronomical Society of the Pacific Conference Series, Vol. 336, Cosmic Abundances as Records of Stellar Evolution and Nucleosynthesis, ed. T. G. Barnes III & F. N. Bash, 25–+

Asplund, M., Grevesse, N., Sauval, A. J., & Scott, P. 2009, ARA&A, 47, 481

Audi, G., Wapstra, A. H., & Thibault, C. 2003, Nuclear Physics A, 729, 337

Baker, N. & Kippenhahn, R. 1959, ZAp, 48, 140

Baker, N. & Kippenhahn, R. 1962, ZAp, 54, 114

Bally, J., Moeckel, N., & Throop, H. 2005, in Astronomical Society of the Pacific Conference Series, Vol. 341, Chondrites and the Protoplanetary Disk, ed. A. N. Krot, E. R. D. Scott, & B. Reipurth, 81–+

Bao, Z. Y., Beer, H., Käppeler, F., et al. 2000, Atomic Data and Nuclear Data Tables, 76, 70

Baraffe, I., El Eid, M. F., & Prantzos, N. 1992, A&A, 258, 357

Barbuy, B., Zoccali, M., Ortolani, S., et al. 2009, A&A, 507, 405

Beer, H. & Macklin, R. L. 1989, ApJ, 339, 962

Beer, H., Voss, F., & Winters, R. R. 1992, ApJS, 80, 403

Beers, T. C. & Christlieb, N. 2005, ARA&A, 43, 531

Best, A., Görres, J., Couder, M., et al. 2011, Phys. Rev. C, 83, 052802

Bisterzo, S., Gallino, R., Straniero, O., Cristallo, S., & Käppeler, F. 2010, MNRAS, 404, 1529

Bisterzo, S., Pompeia, L., Gallino, R., et al. 2005, Nuclear Physics A, 758, 284

Böhm-Vitense, E. 1958, ZAp, 46, 108

Briquet, M. & Morel, T. 2007, Communications in Asteroseismology, 150, 183

Bromm, V., Yoshida, N., Hernquist, L., & McKee, C. F. 2009, Nature, 459, 49

Brott, I., Hunter, I., de Koter, A., et al. 2009, Communications in Asteroseismology, 158, 55

Brüggen, M. & Hillebrandt, W. 2001, MNRAS, 320, 73

Burbidge, E. M., Burbidge, G. R., Fowler, W. A., & Hoyle, F. 1957, Reviews of Modern Physics, 29, 547

Busso, M., Gallino, R., Lambert, D. L., Travaglio, C., & Smith, V. V. 2001, ApJ, 557, 802

Busso, M., Gallino, R., & Wasserburg, G. J. 1999, ARA&A, 37, 239

Cameron, A. G. W. 1955, ApJ, 121, 144

Cameron, A. G. W. 1957, PASP, 69, 201

Cameron, A. G. W. 1960, AJ, 65, 485

Canuto, V. M. 2002, A&A, 384, 1119

Caughlan, G. R. & Fowler, W. A. 1988, Atomic Data and Nuclear Data Tables, 40, 283

Caughlan, G. R., Fowler, W. A., Harris, M. J., & Zimmerman, B. A. 1985, Atomic Data and Nuclear Data Tables, 32, 197

Chaboyer, B. & Zahn, J.-P. 1992, A&A, 253, 173

Chandrasekhar, S. 1939, An introduction to the study of stellar structure, ed. Chandrasekhar, S.

Chiappini, C., Ekström, S., Meynet, G., et al. 2008, A&A, 479, L9

Chiappini, C., Frischknecht, U., Meynet, G., et al. 2011, Nature, 472, 454

Chiappini, C., Hirschi, R., Meynet, G., et al. 2006, A&A, 449, L27

Chugunov, A. I., Dewitt, H. E., & Yakovlev, D. G. 2007, Phys. Rev. D, 76, 025028

Clayton, D. D., Fowler, W. A., Hull, T. E., & Zimmerman, B. A. 1961, Annals of Physics, 12, 331

Clayton, D. D. & Ward, R. A. 1974, ApJ, 193, 397

Couch, R. G., Schmiedekamp, A. B., & Arnett, W. D. 1974, ApJ, 190, 95

Cowan, J. J. & Sneden, C. 2006, Nature, 440, 1151

Cowan, J. J., Sneden, C., Beers, T. C., et al. 2005, ApJ, 627, 238

Crowther, P. A., Schnurr, O., Hirschi, R., et al. 2010, MNRAS, 408, 731

Cunha, K., Hubeny, I., & Lanz, T. 2006, ApJ, 647, L143

Cunha, K. & Lambert, D. L. 1994, ApJ, 426, 170

Cyburt, R. H., Fields, B. D., & Olive, K. A. 2003, Physics Letters B, 567, 227

de Jager, C., Nieuwenhuijzen, H., & van der Hucht, K. A. 1988, A&AS, 72, 259

de Wit, W. J., Testi, L., Palla, F., & Zinnecker, H. 2005, A&A, 437, 247

Decressin, T., Meynet, G., Charbonnel, C., Prantzos, N., & Ekström, S. 2007, A&A, 464, 1029

Denissenkov, P. A., Ivanova, N. S., & Weiss, A. 1999, A&A, 341, 181

Denissenkov, P. A. & Merryfield, W. J. 2011, ApJ, 727, L8

Descouvemont, P. 1993, Phys. Rev. C, 48, 2746

Diehl, R., Halloin, H., Kretschmer, K., et al. 2006, Nature, 439, 45

Diehl, R., Lang, M., Kretschmer, K., & Wang, W. 2008, New A Rev., 52, 440

Diehl, R., Lang, M. G., Martin, P., et al. 2010, A&A, 522, A51+

Dillmann, I., Heil, M., Käppeler, F., et al. 2008, ArXiv e-prints

Dillmann, I., Heil, M., Käppeler, F., et al. 2006, in American Institute of Physics Conference Series, Vol. 819, Capture Gamma-Ray Spectroscopy and Related Topics, ed. A. Woehr & A. Aprahamian, 123–127

Domiciano de Souza, A., Kervella, P., Jankov, S., et al. 2003, A&A, 407, L47

Domiciano de Souza, A., Kervella, P., Jankov, S., et al. 2005, A&A, 442, 567

Drake, J. J. & Testa, P. 2005, Nature, 436, 525

Dufton, P. L., Smartt, S. J., Lee, J. K., et al. 2006, A&A, 457, 265

Eggenberger, P., Meynet, G., Maeder, A., et al. 2008, Ap&SS, 316, 43

Ekström, S., Georgy, C., Eggenberger, P., et al. 2012, A&A, 537, A146

Ekström, S., Meynet, G., Chiappini, C., Hirschi, R., & Maeder, A. 2008, A&A, 489, 685

El Eid, M. F., Meyer, B. S., & The, L.-S. 2004, ApJ, 611, 452

Eldridge, J. J. & Vink, J. S. 2006, A&A, 452, 295

Endal, A. S. & Sofia, S. 1976, ApJ, 210, 184

Evans, C. J., Lennon, D. J., Smartt, S. J., & Trundle, C. 2006, A&A, 456, 623

Evans, C. J., Smartt, S. J., Lee, J. K., et al. 2005, A&A, 437, 467

Farouqi, K., Kratz, K.-L., Mashonkina, L. I., et al. 2009, ApJ, 694, L49

Ferguson, J. W., Alexander, D. R., Allard, F., et al. 2005, ApJ, 623, 585

Filippenko, A. V. 1997, ARA&A, 35, 309

Fliegner, J., Langer, N., & Venn, K. A. 1996, A&A, 308,

Fowler, W. A., Caughlan, G. R., & Zimmerman, B. A. 1967, ARA&A, 5, 525

François, P., Matteucci, F., Cayrel, R., et al. 2004, A&A, 421, 613

Frebel, A. 2010, Astronomische Nachrichten, 331, 474

Frischknecht, U., Hirschi, R., Meynet, G., et al. 2010, A&A, 522, A39+

Fröhlich, C., Martínez-Pinedo, G., Liebendörfer, M., et al. 2006, Physical Review Letters, 96, 142502

Fynbo, H. O. U., Diget, C. A., Bergmann, U. C., et al. 2005, Nature, 433, 136

Gallino, R., Busso, M., Lugaro, M., et al. 2000, Memorie della Societa Astronomica Italiana, 71, 771

Georgy, C., Meynet, G., Walder, R., Folini, D., & Maeder, A. 2009, A&A, 502, 611

Getman, K. V., Feigelson, E. D., Luhman, K. L., et al. 2009, ApJ, 699, 1454

Gies, D. R. & Lambert, D. L. 1992, ApJ, 387, 673

Goriely, S. 1999, A&A, 342, 881

Goswami, A. & Prantzos, N. 2000, Bulletin of the Astronomical Society of India, 28, 305

Graboske, H. C., Dewitt, H. E., Grossman, A. S., & Cooper, M. S. 1973, ApJ, 181, 457

Grevesse, N. & Noels, A. 1993, in Origin and Evolution of the Elements, ed. S. Kubono & T. Kajino, 14

Heger, A., Fryer, C. L., Woosley, S. E., Langer, N., & Hartmann, D. H. 2003, ApJ, 591, 288

Heger, A. & Langer, N. 2000, ApJ, 544, 1016

Heger, A., Langer, N., & Woosley, S. E. 2000, ApJ, 528, 368

Heger, A. & Woosley, S. E. 2010, ApJ, 724, 341

Heger, A., Woosley, S. E., & Spruit, H. C. 2005, ApJ, 626, 350

Henyey, L. G., Forbes, J. E., & Gould, N. L. 1964, ApJ, 139, 306

Herwig, F. 2005, ARA&A, 43, 435

Hirschi, R. 2004, PhD thesis, University of Geneva

Hirschi, R. 2007, A&A, 461, 571

Hirschi, R., Frischknecht, U., Thielemann, F., et al. 2008, in IAU Symposium, Vol. 255, IAU Symposium, ed. L. K. Hunt, S. Madden, & R. Schneider, 297–304

Hirschi, R. & Maeder, A. 2010, A&A, 519, A16+

Hirschi, R., Meynet, G., & Maeder, A. 2004, A&A, 425, 649

Hirschi, R., Meynet, G., & Maeder, A. 2005, A&A, 433, 1013

Hix, W. R. & Thielemann, F. K. 1999, Journal of Computational and Applied Mathematics, 109, 321

Huang, W. & Gies, D. R. 2006, ApJ, 648, 591

Hunter, I., Brott, I., Langer, N., et al. 2009, A&A, 496, 841

Hunter, I., Brott, I., Lennon, D. J., et al. 2008, ApJ, 676,

Hunter, I., Dufton, P. L., Smartt, S. J., et al. 2007, A&A, 466, 277

Hunter, I., Lennon, D. J., Dufton, P. L., et al. 2008, A&A, 479, 541

Hunter, I., Lennon, D. J., Dufton, P. L., et al. 2009, A&A, 504, 211

Iben, Jr., I. 1976, ApJ, 208, 165

Iglesias, C. A. & Rogers, F. J. 1996, ApJ, 464, 943

Iliadis, C., Longland, R., Champagne, A. E., Coc, A., & Fitzgerald, R. 2010, Nuclear Physics A, 841, 31

Imbriani, G., Costantini, H., Formicola, A., et al. 2005, European Physical Journal A, 25, 455

Itoh, N., Adachi, T., Nakagawa, M., Kohyama, Y., & Munakata, H. 1989, ApJ, 339, 354

Itoh, N., Hayashi, H., Nishikawa, A., & Kohyama, Y. 1996, ApJS, 102, 411

Itoh, N., Kuwashima, F., & Munakata, H. 1990, ApJ, 362, 620

Itoh, N., Totsuji, H., Ichimaru, S., & Dewitt, H. E. 1979, ApJ, 234, 1079

Jaeger, M., Kunz, R., Mayer, A., et al. 2001, Physical Review Letters, 87, 202501

Käppeler, F. 1996, Mem. Soc. Astron. Italiana, 67, 749

Käppeler, F., Beer, H., & Wisshak, K. 1989, Reports on Progress in Physics, 52, 945

Käppeler, F., Beer, H., & Wisshak, K. 1992, s-process nucleosynthesis-nuclear physics and the classical model (Stellar Astrophysics), 1

Käppeler, F., Gallino, R., Bisterzo, S., & Aoki, W. 2011, Reviews of Modern Physics, 83, 157

Käppeler, F., Gallino, R., Busso, M., Picchio, G., & Raiteri, C. M. 1990, ApJ, 354, 630

Käppeler, F., Wiescher, M., Giesen, U., et al. 1994, ApJ, 437, 396

Karakas, A. I. 2010, MNRAS, 403, 1413

Karakas, A. I., Lugaro, M. A., Wiescher, M., Görres, J., & Ugalde, C. 2006, ApJ, 643, 471

Kennicutt, R. C. 2005, in IAU Symposium, Vol. 227, Massive Star Birth: A Crossroads of Astrophysics, ed. R. Cesaroni, M. Felli, E. Churchwell, & M. Walmsley, 3–11

Kippenhahn, R. & Thomas, H.-C. 1970, in IAU Colloq. 4: Stellar Rotation, ed. A. Slettebak, 20–+

Kippenhahn, R. & Weigert, A. 1990, Stellar Structure and Evolution, ed. Kippenhahn, R. & Weigert, A.

Kippenhahn, R., Weigert, A., & Hofmeister, E. 1967, Methods in computational physics - Methods for calculating stellar evolution, ed. B. Alder, S. Fernbach, & M. Rotenberg (Academic Press)

Kobayashi, C., Umeda, H., Nomoto, K., Tominaga, N., & Ohkubo, T. 2006, ApJ, 653, 1145

Kudritzki, R. P. & Puls, J. 2000, ARA&A, 38, 613

Kunz, R., Fey, M., Jaeger, M., et al. 2002, ApJ, 567, 643

Langer, N., Arcoragi, J.-P., & Arnould, M. 1989, A&A, 210, 187

Langer, N., Brott, I., Cantiello, M., et al. 2010, 268, 411

Langer, N., Cantiello, M., Yoon, S. C., et al. 2008, 250, 167

Lattanzio, J. C. 1992, Proceedings of the Astronomical Society of Australia, 10, 99

Lattanzio, J. C. & Lugaro, M. A. 2005, Nuclear Physics A, 758, 477

Limongi, M. & Chieffi, A. 2006, ApJ, 647, 483

Limongi, M., Straniero, O., & Chieffi, A. 2000, ApJS, 129, 625

Lodders, K. 2003, ApJ, 591, 1220

Lucatello, S., Beers, T. C., Christlieb, N., et al. 2006, ApJ, 652, L37

Lyubimkov, L. S., Rostopchin, S. I., & Lambert, D. L. 2004, MNRAS, 351, 745

Maeder, A. 1992, A&A, 264, 105

Maeder, A. 1997, A&A, 321, 134

Maeder, A. 2003, A&A, 399, 263

Maeder, A. 2009, Physics, Formation and Evolution of Rotating Stars, ed. Maeder, A.

Maeder, A., Grebel, E. K., & Mermilliod, J.-C. 1999, A&A, 346, 459

Maeder, A. & Meynet, G. 2000, ARA&A, 38, 143

Maeder, A. & Meynet, G. 2001, A&A, 373, 555

Maeder, A. & Meynet, G. 2004, A&A, 422, 225

Maeder, A. & Meynet, G. 2005, A&A, 440, 1041

Maeder, A., Meynet, G., Ekstrom, S., & Georgy, C. 2008, ArXiv e-prints

Maeder, A. & Zahn, J.-P. 1998, A&A, 334, 1000

Martayan, C., Floquet, M., Hubert, A. M., et al. 2007, A&A, 472, 577

Mazumdar, A., Briquet, M., Desmet, M., & Aerts, C. 2006, A&A, 459, 589

McAlister, H. A., ten Brummelaar, T. A., Gies, D. R., et al. 2005, ApJ, 628, 439

Mendel, J. T., Venn, K. A., Proffitt, C. R., Brooks, A. M., & Lambert, D. L. 2006, ApJ, 640, 1039

Meynet, G., Eggenberger, P., & Maeder, A. 2011, A&A, 525, L11+

Meynet, G., Ekström, S., & Maeder, A. 2006, A&A, 447, 623

Meynet, G., Hirschi, R., Ekstrom, S., et al. 2010, A&A, 521, A30+

Meynet, G. & Maeder, A. 1997, A&A, 321, 465

Meynet, G. & Maeder, A. 2000, A&A, 361, 101

Meynet, G. & Maeder, A. 2002, A&A, 390, 561

Meynet, G. & Maeder, A. 2003, A&A, 404, 975

Meynet, G. & Maeder, A. 2005, A&A, 429, 581

Meynet, G., Maeder, A., & Mowlavi, N. 2004, A&A, 416, 1023

Mezzacappa, A. 2005, Annual Review of Nuclear and Particle Science, 55, 467

Miyaji, S., Nomoto, K., Yokoi, K., & Sugimoto, D. 1980, PASJ, 32, 303

Mochkovitch, R. & Nomoto, K. 1986, A&A, 154, 115

Montes, F., Beers, T. C., Cowan, J., et al. 2007, ApJ, 671, 1685

Morel, T., Butler, K., Aerts, C., Neiner, C., & Briquet, M. 2006, A&A, 457, 651

Morel, T., Hubrig, S., & Briquet, M. 2008, A&A, 481, 453

Neiner, C., Geers, V. C., Henrichs, H. F., et al. 2003, A&A, 406, 1019

Nollett, K. M., Busso, M., & Wasserburg, G. J. 2003, ApJ, 582, 1036

Nomoto, K. 1987, ApJ, 322, 206

Nomoto, K., Tanaka, M., Tominaga, N., & Maeda, K. 2010, New A Rev., 54, 191

Nomoto, K., Tominaga, N., Umeda, H., Kobayashi, C., & Maeda, K. 2006, Nuclear Physics A, 777, 424

Nugis, T. & Lamers, H. J. G. L. M. 2000, A&A, 360, 227

Ogata, S. 1997, ApJ, 481, 883

Palmerini, S., La Cognata, M., Cristallo, S., & Busso, M. 2011, ApJ, 729, 3

Pamyatnykh, A. A., Handler, G., & Dziembowski, W. A. 2004, MNRAS, 350, 1022

Paxton, B., Bildsten, L., Dotter, A., et al. 2011, ApJS, 192, 3

Peters, J. G. 1968, ApJ, 154, 225

Pignatari, M., Gallino, R., Heil, M., et al. 2010, ApJ, 710, 1557

Pignatari, M., Gallino, R., Meynet, G., et al. 2008, ApJ, 687, L95

Pourbaix, D., Tokovinin, A. A., Batten, A. H., et al. 2004, A&A, 424, 727

Pradhan, A. K. & Nahar, S. N. 2009, in American Institute of Physics Conference Series, Vol. 1171, American Institute of Physics Conference Series, ed. I. Hubeny, J. M. Stone, K. MacGregor, & K. Werner, 52–60

Prantzos, N., Hashimoto, M., & Nomoto, K. 1990, A&A, 234, 211

Preibisch, T. & Zinnecker, H. 2007, in IAU Symposium, Vol. 237, IAU Symposium, ed. B. G. Elmegreen & J. Palous, 270–277

Press, W. H., Teukolsky, S. A., Vetterling, W. T., & Flannery, B. P. 1992, Numerical recipes in FORTRAN. The art of scientific computing (Cambridge: University Press, —c1992, 2nd ed.)

Proffitt, C. R., Jönsson, P., Litzén, U., Pickering, J. C., & Wahlgren, G. M. 1999, ApJ, 516, 342

Proffitt, C. R. & Quigley, M. F. 2001, ApJ, 548, 429

Przybilla, N., Firnstein, M., Nieva, M. F., Meynet, G., & Maeder, A. 2010, A&A, 517, A38+

Qian, Y. & Wasserburg, G. J. 2008, ApJ, 687, 272

Raiteri, C. M., Busso, M., Picchio, G., & Gallino, R. 1991a, ApJ, 371, 665

Raiteri, C. M., Busso, M., Picchio, G., Gallino, R., & Pulone, L. 1991b, ApJ, 367, 228

Raiteri, C. M., Gallino, R., & Busso, M. 1992, ApJ, 387, 263

Rauscher, T. 2010, ArXiv e-prints

Rauscher, T., Heger, A., Hoffman, R. D., & Woosley, S. E. 2002, ApJ, 576, 323

Rauscher, T. & Thielemann, F.-K. 2000, Atomic Data and Nuclear Data Tables, 75, 1

Rayet, M. & Hashimoto, M. 2000, A&A, 354, 740

Reddy, B. E., Lambert, D. L., & Allende Prieto, C. 2006, MNRAS, 367, 1329

Salpeter, E. E. 1954, Australian Journal of Physics, 7, 373

Salpeter, E. E. 1955, ApJ, 121, 161

Schwarzschild, M. & Härm, R. 1967, ApJ, 150, 961

Seeger, P. A., Fowler, W. A., & Clayton, D. D. 1965, ApJS, 11, 121

Smartt, S. J. 2009, ARA&A, 47, 63

Sneden, C., Cowan, J. J., & Gallino, R. 2008, ARA&A, 46, 241

Spite, M., Cayrel, R., Plez, B., et al. 2005, A&A, 430, 655

Spruit, H. C. 1999, A&A, 349, 189

Stacy, A., Bromm, V., & Loeb, A. 2011, MNRAS, 142

Sugimoto, D. 1970, ApJ, 159, 619

Taggart, M., Hager, U., Laird, A., et al. 2011, in Nuclei in the Cosmos (NIC XI)

Takahashi, K. & Yokoi, K. 1987, Atomic Data and Nuclear Data Tables, 36, 375

Talon, S. & Zahn, J.-P. 1997, A&A, 317, 749

Tammann, G. A., Loeffler, W., & Schroeder, A. 1994, ApJS, 92, 487

Tassoul, J.-L. 1978, Theory of rotating stars, ed. Tassoul, J.-L.

The, L.-S., El Eid, M. F., & Meyer, B. S. 2000, ApJ, 533, 998

The, L.-S., El Eid, M. F., & Meyer, B. S. 2007, ApJ, 655, 1058

Thielemann, F., Arnould, M., & Hillebrandt, W. 1979, A&A, 74, 175

Thielemann, F., Dillmann, I., Farouqi, K., et al. 2010, Journal of Physics Conference Series, 202, 012006

Thielemann, F., Nomoto, K., & Hashimoto, M. 1996, ApJ, 460, 408

Thielemann, F.-K., Arcones, A., Käppeli, R., et al. 2011, Progress in Particle and Nuclear Physics, 66, 346

Thielemann, F. K. & Arnett, W. D. 1985, ApJ, 295, 604

Thielemann, F.-K., Rauscher, T., Freiburghaus, C., et al. 1998, in Neutrino Physics and Astrophysics, ed. J. G. Hirsch & D. Page, 27–78

Timmes, F. X. & Swesty, F. D. 2000, ApJS, 126, 501

Timmes, F. X., Woosley, S. E., & Weaver, T. A. 1995, ApJS, 98, 617

Travaglio, C., Gallino, R., Arnone, E., et al. 2004, ApJ, 601, 864

Trundle, C., Dufton, P. L., Hunter, I., et al. 2007, A&A, 471, 625

Truran, J. W. 1981, A&A, 97, 391

Truran, J. W., Cowan, J. J., & Cameron, A. G. W. 1978, ApJ, 222, L63

Tur, C., Heger, A., & Austin, S. M. 2009, ApJ, 702, 1068

Turatto, M. 2003, Lecture Notes in Physics, Berlin Springer Verlag, Vol. 598, Classification of Supernovae, ed. K. Weiler, 21–36

Vázquez, G. A., Leitherer, C., Schaerer, D., Meynet, G., & Maeder, A. 2007, ApJ, 663, 995

Venn, K. A., Brooks, A. M., Lambert, D. L., et al. 2002, ApJ, 565, 571

Vink, J. S., de Koter, A., & Lamers, H. J. G. L. M. 2001, A&A, 369, 574

Wagoner, R. V. 1969, ApJS, 18, 247

Weigert, A. 1966, ZAp, 64, 395

Woosley, S. E. & Bloom, J. S. 2006, ARA&A, 44, 507

Woosley, S. E., Heger, A., & Weaver, T. A. 2002, Reviews of Modern Physics, 74, 1015

Woosley, S. E. & Weaver, T. A. 1995, ApJS, 101, 181

Yong, D., Lambert, D. L., & Ivans, I. I. 2003, ApJ, 599, 1357

Zahn, J. P. 1992, A&A, 265, 115

Zinnecker, H. & Yorke, H. W. 2007, ARA&A, 45, 481